

EXPERIMENTAL AND THEORETICAL STUDY OF
CONVECTIVE INSTABILITY IN AN ENCLOSURE

by

KWANG JONG WON

B.S., Seoul National University
(1966)

S.M., Massachusetts Institute of Technology
(1974)

Submitted in Partial Fulfillment
of the Requirements for the
Degree of

DOCTOR OF SCIENCE

at the

MASSACHUSETTS INSTITUTE OF TECHNOLOGY

January, 1979

© Massachusetts Institute of Technology, 1979

Signature of Author:
Department of Chemical Engineering
January 12, 1979

Certified by:
A. F. Sarofim, Thesis Supervisor

Certified by:
L. A. Clomburg, Jr., Thesis Supervisor

Accepted by:
G. C. Williams, Chairman,
Departmental Committee on Graduate Theses

MASSACHUSETTS INSTITUTE OF TECHNOLOGY Archives

MAY 23 1979

LIBRARIES

EXPERIMENTAL AND THEORETICAL STUDY OF
CONVECTIVE INSTABILITY IN AN ENCLOSURE

by

Kwang Jong Won

Submitted to the Department of Chemical Engineering on January 12th, 1979, in partial fulfillment of the degree of Doctor of Science at the Massachusetts Institute of Technology.

ABSTRACT

An experimental and theoretical investigation was undertaken to characterize a localized convective instability in a rectangular enclosure, in which the principal source (of uniform heat flux) and sink (isothermal) are two-dimensionally (in the longitudinal direction) arranged along the top horizontal surface. The instability is of interest in understanding the mechanisms of homogenization and heat transfer enhancement in the melter section of an industrial glass-melting furnace.

In the experiment using glycerine as a working fluid, the instability was identified to occur only under the isothermal sink in the form of longitudinal roll motion with persistent transverse wavelengths and with penetrative growth. Detailed temperature measurements for a pair of roll cells and close-up streak photographs in various transverse planes were taken to characterize the three-dimensional nature of the instability.

A linear stability analysis, based on the predominance of the longitudinal circulation currents and some simplifying assumptions, was used to show that the Rayleigh number and the wave number of the cells at the onset of roll motion are given by

$$R_c \equiv \frac{g \cdot \beta \cdot \Delta T_m^* \cdot l_t^{*3}}{\nu_o^* \cdot \alpha_o} \approx 500 \quad \text{and} \quad a_c \approx 1.88.$$

This onset criterion, which requires only the maximum temperature and its position in the unstable layer, agreed quite well with the experimental data. In addition, prediction based on the two-dimensional longitudinal numerical solutions also indicated a satisfactory agreement with the observed onset condition of the roll motion.

Department of Chemical Engineering
Massachusetts Institute of Technology
Cambridge, Massachusetts 02139

January 12, 1979

Professor George C. Newton, Jr.
Secretary of the Faculty
Massachusetts Institute of Technology
Cambridge, Massachusetts 02139

Dear Professor Newton:

In accordance with the regulations of the Faculty, I herewith submit a thesis, entitled "Experimental and Theoretical Study of Convective Instability in an Enclosure", in partial fulfillment of the requirements for the degree of Doctor of Science in Chemical Engineering at the Massachusetts Institute of Technology.

Respectfully submitted,

Kwang J. Won

ACKNOWLEDGEMENTS

The author gratefully acknowledges the guidance and encouragement of Professors Adel F. Sarofim and Lloyd A. Clomburg, Jr., who suggested the problem and provided valuable advice throughout the course of this thesis investigation.

The experimental work was done in the Fuels Research Laboratory and the contributions of its fellow doctoral candidates are acknowledged. In particular, the author is indebted to Dr. Nigel W. E. Curlet for his helpful counsel in the early stage of this work and his cooperative efforts in operating the experimental apparatus. The use of the facilities at the Information Processing Center is also acknowledged. In addition, thanks are due to Mr. Stanley Mitchell for preparing final figures and providing helpful advice in the photographic processing and to Ms. Rachel Collister for typing a part of this thesis.

This work was sponsored through a grant from the National Science Foundation and, later, supported by Owens-Corning Fellowship.

* * *

It is only through the continual encouragement of the author's wife that this effort was at all possible. No perfunctory uxorial reference of "devotion" can do justice to her arduous efforts for bringing up our sons, David and William. I am indebted to her and the other members of our family.

TABLE OF CONTENTS

	<u>Page</u>
I. SUMMARY	1
1.1 Introduction	1
1.2 Thesis Objectives	4
1.3 Theory	5
1.3.1 Linear Stability Analysis	7
1.3.2 Amplitude Specification Method	9
1.4 Experimental Observation of the Longitudinal Roll Motion	10
1.4.1 On the Two-Dimensional Nature of Circulation Patterns	12
1.4.2 Temperature Data and Flow Visualization of the Longitudinal Roll Motion	20
1.5 Comparison of Experimental and Theoretical Onset Conditions for the Roll Motion	38
1.6 Rayleigh-Bénard Problem with Large Temperature Dependent Viscosity Variation	50
1.7 Concluding Remarks	53
II. INTRODUCTION	58
2.1 Natural Convection Currents in Glass Melts	58
2.2 The M.I.T. Program for Flow Simulation in Glass Furnace	62
2.3 Current Status of Cellular Convection Instability Theory	65
III. MATHEMATICAL FORMULATION OF THE NATURAL CONVECTION PROBLEM	74
3.1 The Governing Equations for Natural Convection	75
3.1.1 Equations in Dimensionless Form	77
3.2 Nature of the Physical Problem	81
3.2.1 Description of Overall Convection Motion	82

TABLE OF CONTENTS (CONT.)

	<u>Page</u>	
3.2.2	Origin of Convective Instability	83
3.3	The Source-Sink Approximation Method	85
IV.	THE THEORY OF STABILITY ANALYSIS	88
4.1	Linear Stability Analysis	89
4.1.1	On the Principle of Exchange of Stability	92
4.1.2	Onset Criterion for Longitudinal Roll Motion	93
4.1.3	Galerkin Procedure	94
4.1.4	Variational Principles Based on Adjoint Differential Systems	97
4.2	Finite Amplitude Convection	99
4.2.1	Amplitude Specification Method	101
V.	EXPERIMENTAL OBSERVATIONS OF CONVECTIVE INSTABILITY: LONGITUDINAL ROLL MOTION	105
5.1	Experimental Procedure and Operating Conditions	105
5.2	Two-Dimensional Nature of the Overall Circulation Pattern	109
5.2.1	The Two-Dimensional Circulation Pattern Without Roll Motion	112
5.2.2	Two-Dimensional Numerical Simulation for the Experiment	117
5.3	The Thermocouple Net and Roll Cell Visualization	123
5.4	Physical Nature of Roll Motion	126
5.4.1	Three Distinct Stages in the Development of Roll Motion	126
	The Unstably Stratified Stage	127
	Onset of Roll Motion	129

TABLE OF CONTENTS (CONT.)

	<u>Page</u>
The Growth Stage	134
The Fully Developed Stage	144
Recapitulation	152
5.4.2 Reproducibility of Temperature Data	152
5.5 Comparison of Experimental Temperature Data and Two-Dimensional Numerical Solutions	155
VI. THE ONSET CRITERIA OF THE ROLL MOTION	160
6.1 Basic Assumptions in Linear Stability Analysis	160
6.2 Nonlinear Source Distribution under the Batch Sink	161
6.3 Results of the Linear Stability Analysis	167
6.4 Comparison of Theoretical and Experimental Onset Condition for Roll Motion	180
VII. THE RAYLEIGH-BÉNARD PROBLEM WITH LARGE TEMPERATURE DEPENDENT VISCOSITY VARIATION	189
7.1 Introduction	189
7.2 The Principle of Exchange of Stability	192
7.3 Linear Stability Analysis	194
Method of Solution	194
Results and Discussion	197
7.4 Finite Amplitude Convection	201
Finite Difference Formulation	201
Numerical Results and Discussions	204
7.5 Summary	213
VIII. CONCLUDING REMARKS	214

TABLE OF CONTENTS (CONT.)

	<u>Page</u>
APPENDICES	
A. INTERFACE HEAT TRANSFER OF BATCH MELTING PROCESS	217
Chemical Reaction Sequence of Batch Material	217
Physical Process of Batch Melting	220
Heat Transfer Modeling at the Interfaces of Batch Blanket	223
The Lower Fused Layer Model	225
The Upper Fused Layer Model	230
B. THE TEMPERATURE DATA FOR TRANSVERSE PLANES	234
C. ESTIMATION OF TEMPERATURE INCREASE IN THERMOCOUPLE LINES DUE TO FLUID MOTION	242
D. ANALYTIC GALERKIN SOLUTION OF LINEAR STABILITY EQUATION FOR A CONSTANT VISCOSITY CASE	247
E. THE FINITE DIFFERENCE FORMULATION OF CONVECTION EQUATIONS	250
Energy Equation	253
Biharmonic Equation	255
F. PROGRAM LISTING FOR LINEAR STABILITY ANALYSIS	257
NOMENCLATURE	268
BIBLIOGRAPHY	274
BIOGRAPHICAL NOTE	280

-x-
LIST OF FIGURES

<u>Figure</u>	<u>Title</u>	<u>Page</u>
1.1	Schematic of Glass Furnace Melt Section; Representative Flow Fields	2
1.2	Schematic of Experimental Model Tank	11
1.3	The Thermocouple Net in the Model Tank	13
1.4	Experimental Flow Field Without the Roll Motion (Heater Input of 15 Volts)	17
1.5	Experimental Flow Fields with the Roll Motion	18
1.6	Experimental Streak Lines and Computed Streamlines for Longitudinal Plane ($z = 0$)	19
1.7	Comparison of Experimental and Computed Temperature Profiles in the Roll Region	21
1.8	Experimental Isotherms at the 8" Transverse Plane ($y = 1.6$) (Run 611)	23
1.9	Experimental Isotherms in the Roll Cells at the 7" Transverse Plane ($y = 1.4$) (Run 609)	24
1.10	Experimental Streak Lines for the 7" Transverse Plane ($y = 1.4$)	25
1.11	Experimental Streak Lines for the Roll Motion at the 6" Transverse Plane ($y = 1.2$)	27
1.12	Experimental Isotherms in the Roll Cells at the 6" Transverse Plane ($y = 1.2$) (Run 607)	28
1.13	Experimental Streak Lines of the Roll Motion at the 5" Transverse Plane ($y = 1.0$)	29
1.14	Experimental Streak Lines of the Roll Motion at the 4" Transverse Plane ($y = 0.8$)	30
1.15	Experimental Isotherms in the Roll Cells at the 5" Transverse Plane ($y = 1.0$) (Run 622)	32
1.16	Experimental Isotherms in the Roll Cells at the 4" Transverse Plane ($y = 0.8$) (Run 616)	33

<u>Figure</u>	<u>-xi-</u> <u>Title</u>	<u>Page</u>
1.17	Experimental Streak Lines of the Roll Motion at the 3" Transverse Plane ($y = 0.6$)	34
1.18	Experimental Streak Lines of the Roll Motion at the 2" Transverse Plane ($y = 0.4$)	35
1.19	Experimental Isotherms in the Roll Cells at the 3" Transverse Plane ($y = 0.6$) (Run 618)	36
1.20	Experimental Isotherms in the Roll Cells at the 2" Transverse Plane ($y = 0.4$) (Run 620)	37
1.21	Reproducibility Test for Experimental Temperature in the Roll Cells at the 5½" Transverse Plane ($y = 1.1$) (Run 606 and 623)	39
1.22	Similarity Curve for Source-sink Functions	41
1.23	Critical Conditions for the Onset of Roll Motion: $R_{S,l}$ vs η_s	45
1.24	Critical Conditions for the Onset of Roll Motion: $R_{T,l}$ vs η_t	46
1.25	Comparison of Theoretical and Experimental Onset Condition for the Roll Motion	48
1.26	Prediction of the Onset of Roll Motion from Two-dimensional Numerical Solution	49
1.27	Observed Wave Number and Prediction of Critical Wave Number for the Onset of Roll Motion	51
1.28	Stability Diagram - R_M vs Wave Number at Fixed Viscosity Ratio Number	54
1.29	Asymptotic Behavior of Nusselt Number and Stream Function	55
1.30	Finite Amplitude Behavior of Nusselt Number and Stream Function	56
2.1	Schematic of Glass Furnace Melt Section; Representative Flow Fields	59
5.1	Schematic of Experimental Model Tank	106
5.2	Schematic of Experimental Apparatus	108

<u>Figure</u>	<u>Title</u>	<u>Page</u>
5.3	Experimental Flow Field without the Roll Motion (Heater Input 15 Volts)	113
5.4	Experimental Flow Fields with the Roll Motion	116
5.5	Experimental Streak Lines and Computed Streamlines for Longitudinal Plane ($z = 0$)	120
5.6	Computed Isotherm Plot for Longitudinal Plane ($z = 0$)	121
5.7	The Thermocouple Net in the Model Tank	124
5.8	Experimental Isotherms at the 8" Transverse Plane ($y = 1.6$) (Run 611)	128
5.9	Experimental Isotherms in the Roll Cells at the 7" Transverse Plane ($y = 1.4$) (Run 609)	130
5.10	Experimental Streak Lines for the 7" Transverse Plane ($y = 1.4$)	131
5.11	Experimental Streak Lines of the Roll Motion at the 6" Transverse Plane ($y = 1.2$)	133
5.12	Experimental Isotherms in the Roll Cells at the 6" Transverse Plane ($y = 1.2$) (Run 607)	135
5.13	Experimental Streak Lines of the Roll Motion at the 5" Transverse Plane ($y = 1.0$)	138
5.14	Experimental Streak Lines of the Roll Motion at the 4" Transverse Plane ($y = 0.8$)	139
5.15	Experimental Isotherms in the Roll Cells at the 5" Transverse Plane ($y = 1.0$) (Run 622)	142
5.16	Experimental Isotherms in the Roll Cells at the 4" Transverse Plane ($y = 0.8$) (Run 616)	143
5.17	Experimental Streak Lines of the Roll Motion at the 3" Transverse Plane ($y = 0.6$)	145
5.18	Experimental Streak Lines of the Roll Motion at the 2" Transverse Plane ($y = 0.4$)	146
5.19	Experimental Streak Lines for the 3" Transverse Plane ($y = 0.6$) showing Roll Cells close to the Side Wall	148

<u>Figure</u>	<u>Title</u>	<u>Page</u>
5.20	Experimental Isotherms in the Roll Cells at the 3" Transverse Plane ($y = 0.6$) (Run 618)	149
5.21	Experimental Isotherms in the Roll Cells at the 2" Transverse Plane ($y = 0.4$) (Run 620)	150
5.22	Experimental Streak Lines in the Roll Motion Region for the Longitudinal Plane ($z = 0$)	151
5.23	Reproducibility Test for Experimental Temperature in the Roll Cells at the 5½" Transverse Plane ($y = 1.1$) (Run 606 and 623)	153
5.24	Comparison of Experimental and Computed Temperature Profiles in the Roll Region	156
5.25	Experimental Penetration Depth of Maximum Temperature Layer in the Roll Region	158
6.1	Similarity Curve for Source-sink Functions	163
6.2	Expansion Coefficients of Characteristic Functions ($N = 1.0$)	173
6.3	Characteristic Functions for Source Depth 0.1 and 0.5	175
6.4	Critical Conditions for the Onset of Roll Motion: $R_{S,\lambda}$ vs η_s	178
6.5	Critical Conditions for the Onset of Roll Motion: $R_{T,\lambda}$ vs η_t	179
6.6	Comparison of Theoretical and Experimental Onset Condition for the Roll Motion	181
6.7	Temperature Profiles Normalized with the Source Strength	184
6.8	Prediction of the Onset of Roll Motion from Two-dimensional Numerical Solution	185
6.9	Observed Wave Number and Prediction of Critical Wave Number for the Onset of Roll Motion	187
7.1	Stability Diagram - R_M vs Wave Number at Fixed Viscosity Ratio Number	199
7.2	Critical Rayleigh Number vs Viscosity Ratio Number	200
7.3	Profiles of Characteristic Functions	202

<u>Figure</u>	<u>Title</u>	<u>Page</u>
7.4	Flow and Temperature Contour Plots at a Constant Amplitude, $\epsilon = 5.0$	206
7.5	Finite Amplitude Behavior of Nusselt Number and Stream Function	208
7.6	Asymptotic Behavior of Nusselt Number and Stream Function	209
7.7	Two Distinct Finite Amplitude Solutions near the Critical Rayleigh Number ($\Gamma = 10^3$)	211
7.8	Convergence Behavior of the Conventional Numerical Technique	212
A.1	Phase Diagram for Soda-Lime-Silica Glass	218
A.2	Modeling of Batch Melting Process	224
A.3	Batch-Melt Heat Transfer	229
E.1	Non-uniform, Staggered Grid System	252

LIST OF TABLES

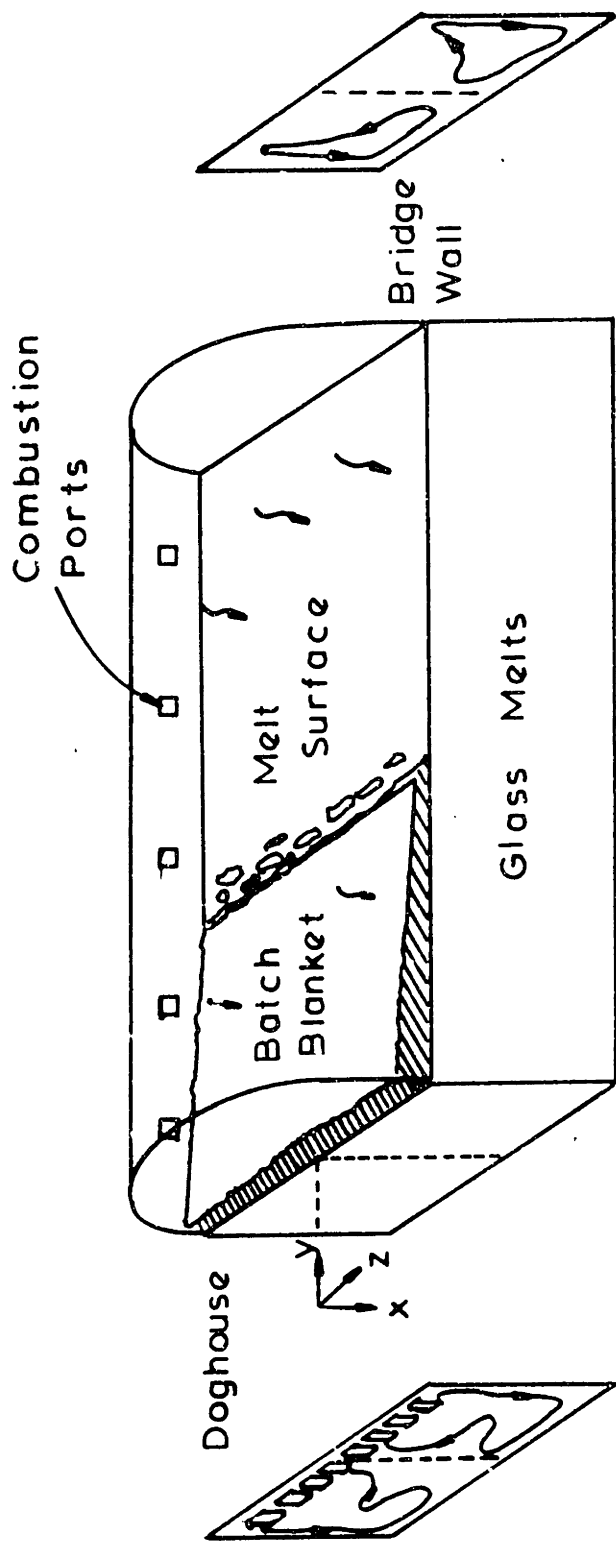
<u>Table</u>	<u>Title</u>	<u>Page</u>
1.1	Dimensionless Parameters for Two-dimensional Numerical Calculation	14
1.2	Comparison of Experimental and Numerical Energy Balance	15
1.3	Observed Wavelength (W) and Depth (D) of the Roll Motion	40
1.4	Maximum Source Strength and Source Depth from the Numerical Solution	42
3.1	Reference Scales for Various Rayleigh Numbers	79
5.1	Experimental Operating Conditions	110
5.2	Physical Properties of Glycerine at Batch Temperature, $T_s = 297.6$ K	111
5.3	Dimensionless Parameters for Two-dimensional Numerical Calculation	119
5.4	Comparison of Experimental and Numerical Energy Balance	122
5.5	Observed Wavelength (W) and Depth (D) of the Roll Motion	136
6.1	Maximum Source Strength and Source Depth from the Numerical Solution	164
6.2	Critical Parameters for Internal Source Problem	168
7.1	Numerical Results for Finite Amplitude Convection	205
B.1	Coordinates of the Thermocouple Net Positions	236
B.2	Thermocouple Emf Data	236
C.1	Representative Physical Properties and Experimental Conditions	243
D.1	The Critical Rayleigh Number derived by the Variational Method	249

I. SUMMARY

1.1 Introduction

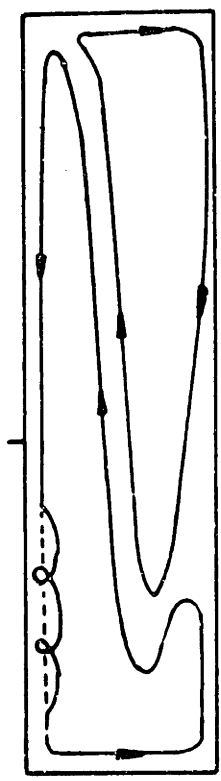
The purpose of this study was to provide a better understanding of a localized convective instability phenomenon (termed a longitudinal roll motion), which occurs in a rectangular parallelepiped the top surface of which is subdivided into a rectangular energy source abutting a rectangular energy sink. Such a system represents an idealized model of the melter section of an industrial glass-melting furnace. It is schematically shown in Figure 1.1 together with representative flow patterns for conditions simulating those occurring in glass furnaces. In a commercial glass furnace, a solid mixture of the glass ingredients (called the batch) is fed at one end (called the doghouse end), and floats on the melt surface as the batch blanket, before being transformed into the molten state. The energy required for the glass formation is provided to the batch either directly by radiative transfer to the top surface of the batch, or indirectly by convection currents within the melt to the bottom of the batch. A century long experience with industrial glass furnace operations has suggested that the flow path and temperature history of the glass melt significantly affects the quality of glass products.

Motivated by the premise, research work at the M.I.T. has been concerned with the fundamental understanding of the circulation patterns in the melter section. In an idealized enclosure model, the batch and melt surfaces have been treated as an isothermal sink and a uniform heat flux source, respectively, both to simplify the treatment of batch melting and to decouple the treatment of heat transfer from that in the melt. A two-



Transverse Motion
Under Sink
(with Roll Motion)

Transverse Motion
Under Source



Longitudinal Motion

Figure 1.1 Schematic of Glass Furnace Melt Section ; Representative Flow Fields

dimensional numerical algorithm was developed which has facilitated subsequent investigations for the problem (Clomburg, 1971). In addition, using glycerine as a working fluid, he validated the numerical prediction of the longitudinal circulation current (see Figure 1.1); the predicted temperature profiles, however, showed some systematic discrepancies. The predominance of this two-dimensional flow was exploited to devise the source-sink approximation method for the quantitative assessment of three-dimensional features due to the furnace boundary conditions (Won, 1974). Subsequent complementary experimental and numerical investigations for the problem were concentrated on the characterization of quality parameters related to the predominant two-dimensional current (Gamm, 1975) and on the three-dimensional features of the circulation currents in conjunction with the application of the source-sink method (Curlet, 1976). The results of both experiments confirmed that the circulation patterns are predominantly two-dimensional in the longitudinal direction and are little perturbed by the secondary motion in transverse planes (excluding the longitudinal roll motion) driven by the heat losses through the side walls. However, other experimental observations indicated the strong influence of three-dimensional motion; for example, the residence time distribution for Gamm's through-flow system and the core temperature in Curlet's enclosure system were significantly deviated from the numerical predictions based on the predominance of longitudinal motion.

The origin of these discrepancies was attributed to a tertiary motion, which exhibited a regular cellular pattern when observed in transverse plane. Moreover, the motion was identified as an instability phenomenon due to the unstable temperature gradient which exists under the isothermal

sink. Although Curlet presented a qualitative characterization of the roll motion as analogous to the Rayleigh-Bénard problem, this thesis demonstrates that the longitudinal circulation current which carries the roll motion downstream alters significantly the criterion for the onset condition of the roll motion. A definitive exposition of the roll motion constitutes one of major contributions of the present thesis. The major global effect of the roll motion, albeit a localized phenomenon, is to enhance the heat transfer to the sink surface and to promote mixing over the region.

In glass furnace operations, it is imperative to control the occurrence of the roll motion. While the promotion of the roll motion is desirable under the batch blanket to facilitate melting and homogenization, the same instability phenomenon should be suppressed in the final drawing stage of the melt. Any excessive cooling of the melt from above will undoubtedly induce cellular patterns in the final product glass, thereby resulting in optically inhomogeneous product. In this regard, the strong temperature dependence of the melt viscosity warrants a close examination in its effect on the instability phenomenon.

1.2 Thesis Objectives

Clearly, it is important to understand quantitatively this roll motion. Curlet extended the source-sink approximation method to predict the amplitude and the frequency (wavelength) of the roll motion and demonstrated the good agreement of experimental data with the numerical predictions. This observation suggested that the onset criterion for the roll motion might be predicted by utilizing the same source-sink approximation method. Since the analysis necessarily involves some approximations, the theoretical results are tested by comparison with experiments.

One of the features of the instability phenomenon is that the roll motion grows downstream after its onset but maintains a steady state. The assessment of this supercritical (i.e. finite amplitude) convection motion requires numerical calculations. However, conventional numerical procedures via finite difference technique is known to have severe convergence problems near the critical condition. A new method is necessary to resolve this convergence problems.

The objectives of this thesis are to provide

- (1) a theoretical criterion for the onset of the roll motion,
- (2) an experimental test of the criterion for conditions representative of a glass furnace tank, and
- (3) an assessment for the effect of a highly variable viscosity on the Rayleigh-Bénard, in particular on the finite amplitude convection.

1.3 Theory

Thermal convection in an enclosure is described by the continuity equation, the Boussinesq form of the Navier-Stokes equation and the energy equation:

$$\nabla \cdot \bar{V} = 0$$

$$P^{-1}(\partial_t \bar{V} + \bar{V} \cdot \nabla \bar{V}) = -\nabla \Pi - RT \hat{i} + \nabla \cdot 2\nu \bar{D} \quad (1.1)$$

$$\partial_t T + \bar{V} \cdot \nabla T = \nabla^2 T$$

where

$$\nu = \text{EXP}\left\{\gamma \left(\frac{1}{T} - \frac{1}{T_0}\right)\right\} \quad (1.2)$$

$$\bar{D} \equiv \frac{1}{2} (\nabla \bar{V} + \nabla \bar{V}^T)$$

and

$$R \equiv \frac{g \cdot \beta \cdot T_R \cdot \ell^{*3}}{v_o^* \cdot \alpha_o}$$

$$P \equiv \frac{v_o^*}{\alpha_o}$$

$$\gamma \equiv \frac{E}{T_R}$$

Scaling parameters selected for the dimensional variables

$$\{ t^*, \bar{x}^*, T^*, \Pi^*, \bar{V}^*, v^*, U^* \}$$

are

$$\left\{ \frac{\ell^{*2}}{\alpha_o}, \ell^*, T_R, \frac{\mu_o^* \alpha_o}{\ell^{*2}}, \frac{\alpha_o}{\ell^*}, v_o^*, \frac{k_o}{\ell^*} \right\},$$

where the reference scales, ℓ^* and T_R , are to be chosen according to the requirements of a specific problem. The pressure term, Π^* , denotes the deviation from the hydrostatic pressure corresponding to the reference temperature, T_o^* , for physical properties

$$\Pi^* \equiv \frac{p^*}{\rho_o} - g(1 - \beta T_o^*) \cdot x.$$

Note that the coordinate system is chosen such that the gravity vector points in the direction of the positive x coordinate.

The dominant two-dimensional nature of the convection motion allows one to obtain three-dimensional convective fields by coupling together two-dimensional fields. Specifically, the enclosure is decomposed into two sets of orthogonal planes, the longitudinal planes ($x - y$ planes) and the transverse planes ($x - z$ planes). Two-dimensional problems are readily solved with the introduction of the stream function concept:

$$\begin{aligned}\bar{\Psi} &\equiv \Psi \bar{n} \\ \bar{V} &\equiv \nabla \times \bar{\Psi}\end{aligned}\tag{1.3}$$

where \bar{n} denotes a unit vector normal to the chosen orthogonal plane. The overall convective fields can be obtained by the source-sink approximation method. For the transverse plane, the energy equation,

$$J_{\hat{j}}(\tilde{T}, \tilde{\Psi}) - \nabla^2 \tilde{T} = SI_T \equiv -\partial_x^2 T - \{J_{\hat{k}}(T, \Psi) - \nabla_{\hat{k}}^2 T\}, \tag{1.4}$$

involves the source-sink function SI_T and is solved simultaneously with the biharmonic equation. (See Won (1974) or Curlet (1976) for details.) When the source-sink function SI_T is evaluated from a longitudinal solution $T(x,y)$ for the experimental condition and is normalized with the maximum source strength and its position, the profiles under the sink can be represented by a single parabolic source curve (see Figure 1.22, Section 1.4.1). Accordingly, the onset of roll motion is determined from the linear stability analysis of a fluid layer heated internally with a parabolic heat source distribution.

1.3 Linear Stability Analysis

The linearized perturbation equations are described by

$$\sigma \begin{bmatrix} \Theta \\ P^{-1} \nabla^2 \Psi \end{bmatrix} = \begin{bmatrix} \nabla^2 & -h \partial_z \\ R_S \partial_z & \mathcal{L}_4 \end{bmatrix} \begin{bmatrix} \Theta \\ \Psi \end{bmatrix}, \tag{1.5}$$

with homogeneous boundary conditions

$$\Psi(0,z) = \Psi(1,z) = \partial_x \Psi(0,z) = \partial_x \Psi(1,z) = 0$$

$$\Theta(0,z) = (\partial_x + N) \cdot \Theta(1,z) = 0,$$

where $\mathcal{L}_4 \equiv -(\partial_z^2 - \partial_x^2) \{v(\partial_z^2 - \partial_x^2)\} - 4\partial_{xz}^2 (v \partial_{xz}^2)$

and
$$R_s \equiv \frac{g \cdot \beta \cdot S_m^* \cdot H^5}{\nu_o^* \cdot \alpha_o^2} .$$

The maximum strength of the heat source, S_m^* , is located at the midpoint of the source depth, l_s^* , which occupies only a fraction of the fluid layer depth, H . The function $h(x)$ is the vertical temperature gradient of the static solution for the parabolic internal source.

Invoking assumptions of the separation of variables and the principle of exchange of stability, the equations are reduced to a system of ordinary differential equations:

$$\begin{bmatrix} (D^2 - a^2) & -ah \\ aR_s & L_4 \end{bmatrix} \begin{bmatrix} \theta \\ \phi \end{bmatrix} = \begin{bmatrix} 0 \\ 0 \end{bmatrix} \quad (1.6)$$

with boundary conditions

$$\begin{aligned} \phi(0) = \phi(1) = D\phi(0) = D\phi(1) = 0 \\ \theta(0) = (D + N) \cdot \theta(1) = 0 \end{aligned} ,$$

where $L_4 \equiv (D^2 + a^2)\{\nu(D^2 + a^2)\} - 4a^2D(\nu D)$.

and a is a wave number arising as a separation constant.

To solve these equations, a Galerkin procedure is employed. A complete set of trial functions, θ_k , is obtained from the solution to the problem

$$(D^2 - a^2)\theta_k = -\lambda_k^2 \theta_k \quad (1.7)$$

with the temperature boundary conditions given above. The second equation of (1.6) is exactly solved for each θ_k to obtain corresponding trial function ϕ_k . Then these trial functions

$$\theta \equiv \sum_{k=1}^{\infty} A_k \theta_k \quad \text{and} \quad \phi \equiv \sum_{k=1}^{\infty} A_k \phi_k \quad (1.8)$$

are substituted into the first equation of (1.6). Multiplying by θ_j and integrating over the entire range of x , an infinite set of linear homogeneous equations for the A_k 's is obtained:

$$\bar{E} \bar{A} = R_S \bar{G} \bar{A} \quad , \quad (1.9)$$

where
$$\bar{E} \equiv [E_{jk}] = \left[\frac{\lambda_j^2}{a^2} \int_0^1 \theta_j^2 dx \delta_{jk} \right]$$

$$\bar{G} \equiv [G_{jk}] = \left[\int_0^1 h \theta_j \phi_k dx \right]$$

$$\bar{A} \equiv [A_k] \quad .$$

The critical condition, R_c and a_c , are determined by finding a minimum of the smallest positive eigenvalues R_S with respect to a (wave number) for a specified set of parameters. Since negative eigenvalues (corresponding to uninteresting physical situations) exist for the internal source problem, all the eigenvalues should be examined and the power method cannot be used. It can be shown that this procedure is equivalent to a variational principle:

$$R_c = \min_{(a, R_S > 0)} \frac{- \langle \theta, (D^2 - a^2) \theta^\dagger \rangle}{a \langle \phi, L_4 \phi^\dagger \rangle} \quad , \quad (1.10)$$

where θ^\dagger and ϕ^\dagger satisfy an adjoint system of equations to (1.6):

$$\begin{bmatrix} (D^2 - a^2) & -a \\ ahR_S & L_4 \end{bmatrix} \cdot \begin{bmatrix} \theta^\dagger \\ \phi^\dagger \end{bmatrix} = \begin{bmatrix} 0 \\ 0 \end{bmatrix} \quad . \quad (1.11)$$

1.3.2 Amplitude Specification Method

In finite amplitude convection problems, numerical solution procedures by finite difference techniques raise serious convergence problems near the

critical condition (Liang et al., 1969). A new method, called the amplitude specification method, was devised to resolve the convergence difficulties. In the method, the amplitude is specified as a parameter to obtain the corresponding Rayleigh number. For this purpose, the stream function is rescaled:

$$\Phi = \frac{\Psi}{R} . \quad (1.12)$$

Then, the velocity will be, by definition,

$$\bar{V} \equiv - R \|\Phi\| \nabla \times \left\{ \frac{\Phi}{\|\Phi\|} \hat{j} \right\} \quad (1.13)$$

where $\|\Phi\|$ denotes any norm of the stream function field. If an amplitude parameter, ϵ , is introduced such that

$$R = \frac{\epsilon}{\|\Phi\|} , \quad (1.14)$$

the finite amplitude equations are transformed to

$$\begin{bmatrix} \epsilon \cdot J(\Theta, \frac{\Phi}{\|\Phi\|}) \\ -P^{-1} \epsilon \cdot J(\nabla^2 \Phi, \frac{\Phi}{\|\Phi\|}) \end{bmatrix} = \begin{bmatrix} \nabla^2 & \frac{\epsilon}{\|\Phi\|} \partial_z \\ \partial_z & \mathcal{L}_4 \end{bmatrix} \begin{bmatrix} \Theta \\ \Phi \end{bmatrix} . \quad (1.15)$$

The calculation procedure is exactly the same as the conventional finite difference procedure, except that, after each iteration, the stream function field is normalized with the calculated $\|\Phi\|$ and multiplied by ϵ to provide a chosen amplitude for the convective field.

1.4 Experimental Observation of the Longitudinal Roll Motion

The experimental model constructed as a multiwalled plexiglas box (depicted in Figure 1.2) contained glycerine as a working fluid. Heat input

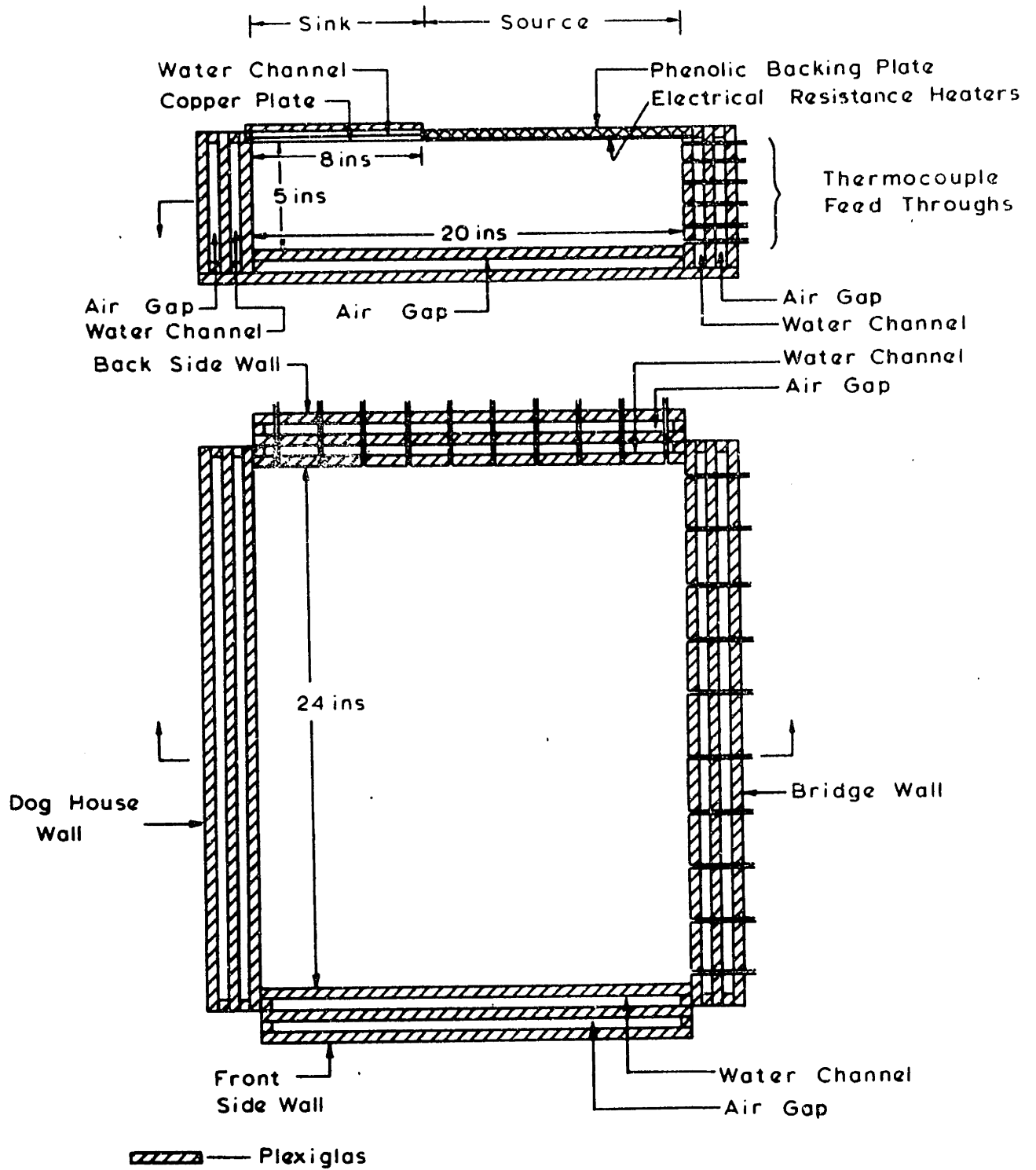


FIGURE 1.2

SCHEMATIC OF EXPERIMENTAL MODEL TANK

of ~88 watts (~300 Btu/hr) was provided by electrical resistance heaters, while the isothermal sink on the top surface (~297.6 K) was a water cooled copper plate. Additional heat losses at the bridgewall (end wall adjacent to the heat source) were controlled by water cooling.

For temperature measurements in the region of roll motion, a thermocouple net was designed to cover roughly a pair of roll cells. The thermocouple net consists of sixty junction beads (10 rows by 6 columns) in a square area of 0.0254 m x 0.0254 m. The thermocouples were made from copper - constantan wire of 1.27×10^{-4} m (5 mil.) diameter. Figure 1.3 shows the thermocouple net placed in a transverse plane. The positions of the beads in the net were determined both photographically and with a cathetometer. Flow visualization was achieved by taking streak photographs of neutrally buoyant anthracene particles illuminated with a planar light source.

The experiment was carefully controlled to maintain constant boundary conditions during the period (~3 weeks for the experiment reported here) of data acquisition. Temperatures in the roll region were collected with the thermocouple net being placed at the desired transverse planes. Roll motion corresponding to the transverse planes was recorded photographically. The operating conditions and design parameters are presented in dimensionless form in Table 1.1 and the energy balance of the experiment in Table 1.2.

1.4.1. On the Two-dimensional Nature of the Circulation Patterns

Curlet (1976) had previously characterized the dominance of the two-dimensional motion in the enclosure for different conditions of heat loss at the side walls. He found, for all the conditions he studied, that the major departure from the dominant two-dimensional motion was due to roll

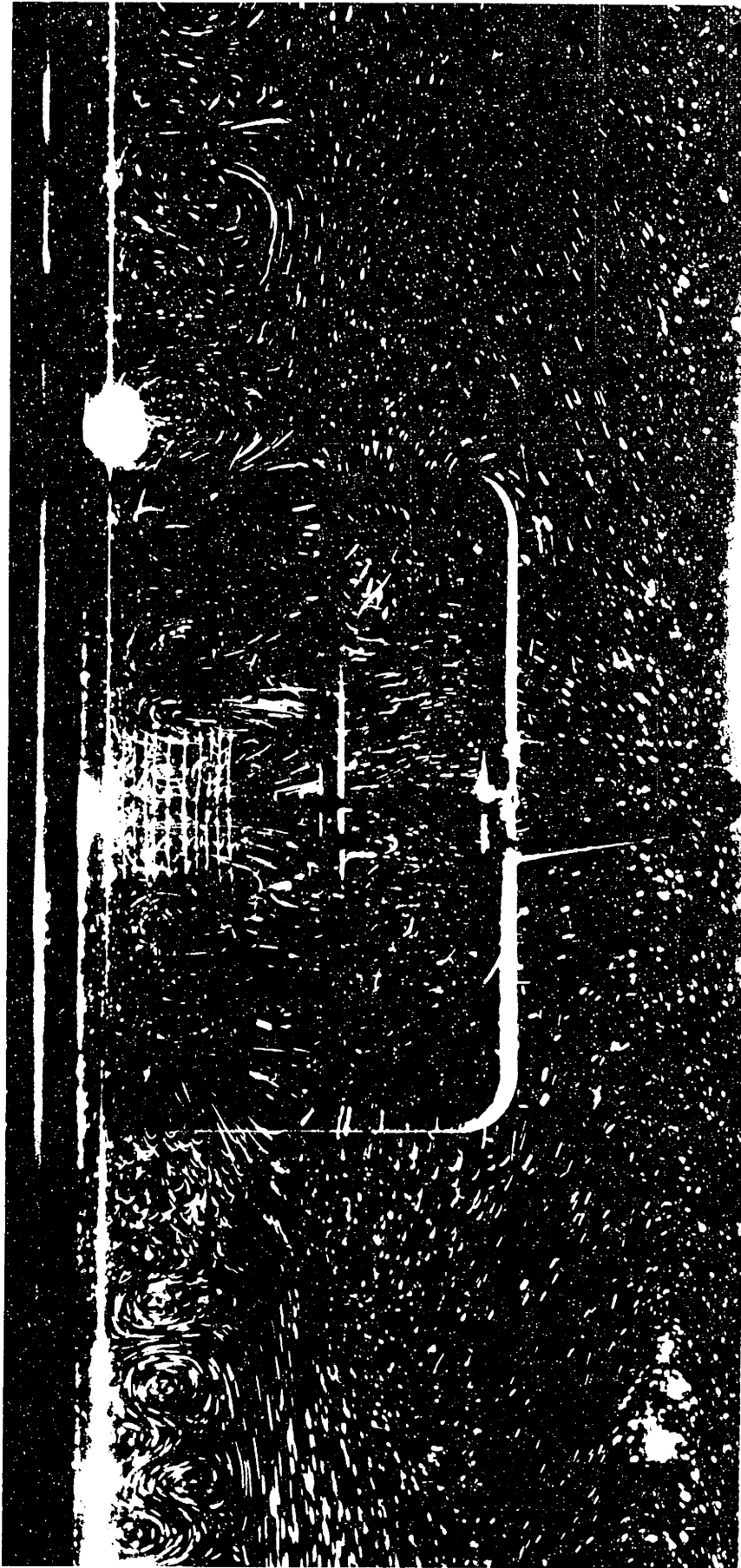


Figure 1.3 The Thermocouple Net in the Model Tank

TABLE 1.1

Dimensionless Parameters for Two-dimensional Numerical Calculation

<u>Parameter</u>	<u>Definition</u>	
Rayleigh Number, R	$\frac{g \cdot \beta \cdot T_R^* \cdot H^3}{\nu_o^* \cdot \alpha_o}$	2.87×10^7
Prandtl Number, P	ν_o^* / α_o	7.79×10^4
Viscosity Number, γ	E / T_R^*	32.14
Longitudinal Aspect	L / H	4.0
Batch Coverage	L_B / L	0.4
<u>Boundary Condition</u>	<u>Definition</u>	
Batch Temperature, T_s	T_s^* / T_R^*	1.4147
Source Heat Flux, q_F	$q^* H / \kappa_o T_R^*$	1.0000
Bridgwall Temperature		1.4082
Bridgwall Biot Number, N	$U^* H / \kappa_o$	7.35
Doghouswall Temperature		1.4188
Doghouswall Biot Number [§]		0.6358
Bottom Temperature		1.4180
Bottom Biot Number [§]		0.8610
Side Wall Heat Loss, T		-7.546×10^{-3} ¶
Reference Temperature, $T_R^* \equiv q^* H / \kappa_o$		210.4 K (378.7 R)
Heat Flux Density, q^*		471.6 J/m ² ·s (149.5 Btu/hr·ft ²)

¶ Uniform sink was assumed for the source-sink approximation method.

§ Estimated.

TABLE 1.2

Comparison of Experimental and Numerical Energy Balance

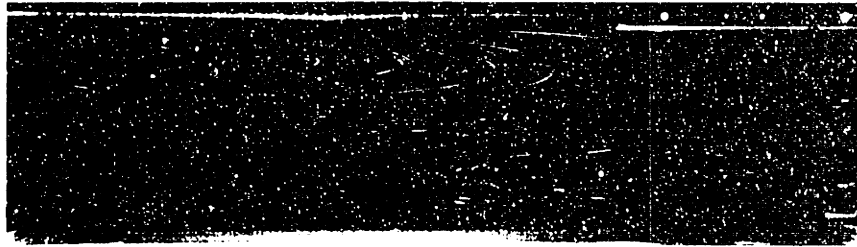
	<u>Experimental</u>			<u>Numerical</u> [¶]	
	Btu/hr	W	%	Dimensionless	%
INPUT					
Heater Input	305.9	89.65			
Leakage	(6.9)	(2.02)			
<u>Total Input</u>	<u>299.0</u>	<u>87.63</u>	<u>100.0</u>	<u>2.4000</u>	<u>100.0</u>
OUTPUT					
Batch	256.0	75.29	85.6	2.0278	84.5
Bridgewall	35.5	10.40			
Leakage	(1.3)	(0.38)			
	34.2	10.02	11.4	0.2721	11.3
Doghousewall	1.1	0.32	0.4	0.0116	0.5
Bottom	4.6	1.35	1.5	0.0493	2.1
Side Walls [¶]	3.8	1.11	1.3	0.0302	1.3
<u>Total Output</u>	<u>299.9</u>	<u>87.83</u>	<u>100.2</u>	<u>2.3910</u>	<u>99.6</u>
DISCREPANCY					
Input - Output	-0.7	-0.31	-0.2	0.0090	0.4

[¶] By the source-sink approximation method. (Heat losses at the side walls were assumed as uniform sink.)

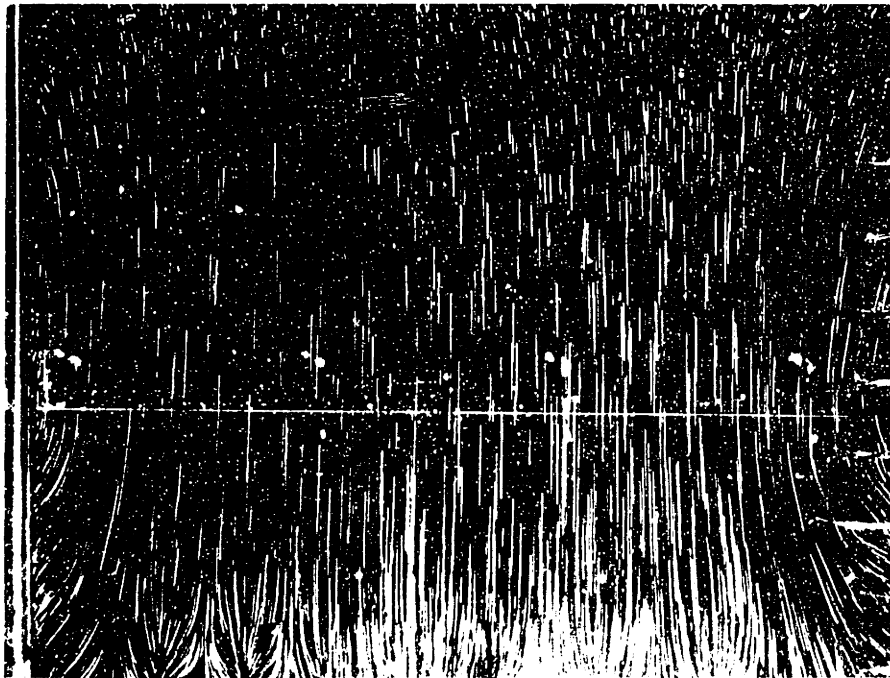
motion. That the roll motion, analogous to Rayleigh-Bénard instability, can be entirely suppressed if the magnitude of the unstable temperature gradients under the sink is reduced below the critical condition is demonstrated by the streak photographs shown in Figure 1.4, achieved by reducing the power input to the source into $\frac{1}{9}$ of the normal input (the voltage drop across the heaters was reduced from 45 volts to 15 volts). The pure two-dimensional nature of the motion is clearly evident in the parallel streak lines in the middle part of the horizontal planform (Figure 1.4.a). The longitudinal circulation pattern shows a perfect shape of elongated ellipsoid, slanted slightly toward the heater side (Figure 1.4.b).

Roll motion sets in with a slight increase in heat input (corresponding to a voltage drop of ~17 volts), as shown in Figure 1.5.a. The projected crossing of streak lines is clearly shown in the upper left-hand corner. Notice that a new circulation eye is formed closer to the doghouse end (left end). When the power input is further increased to a value (~40 volts across the heaters) comparable to the main experimental condition, the horizontal planforms in Figure 1.5.b and 1.5.c clearly shows the definite frequency of the regular structure of the roll motion in the lower parts of the photographs. The straight streak lines in the rest of the planforms indicate the dominant two-dimensional nature of flow.

The streak photograph taken in the main experiment is compared with computed streamlines in Figure 1.6. The boundary layer nature of the solution under the top surface is clearly indicated in the streamlines. The streamlines in the boundary layer flow evidently exhibit a "thermal Vena Contracta" at the leading edge of the isothermal sink. Being two-dimensional, the numerical solution cannot produce crossed streamlines in



(a) Longitudinal Motion at $z = 0$ (Exposure time 20 minutes)

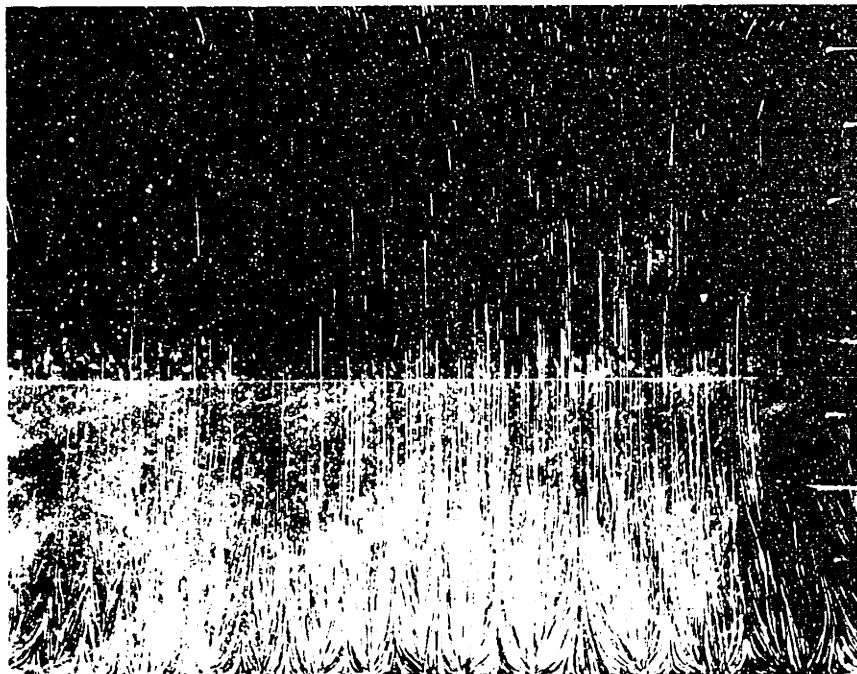


(b) Horizontal Motion at $x \approx 0.1$ (Exposure time 10 minutes)

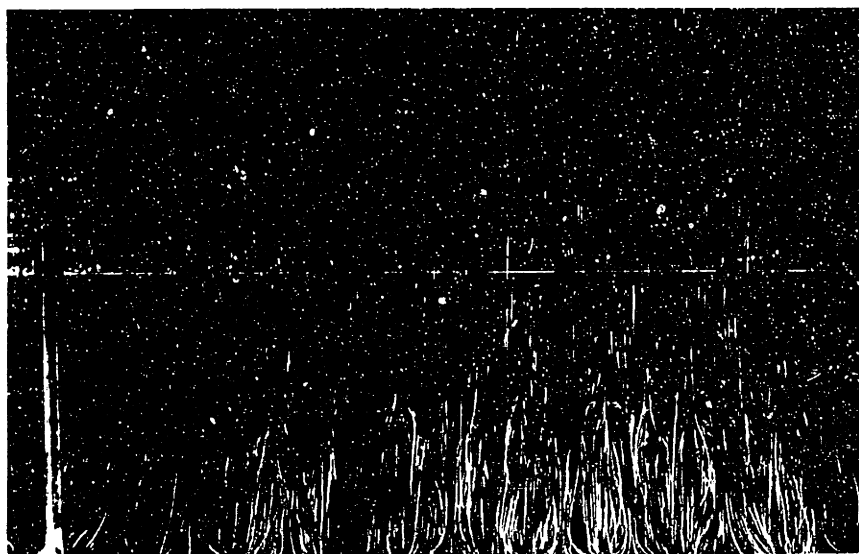
Figure 1.4
Experimental Flow Field without the Roll Motion (Heater
Input 15 Volts)



(a) Longitudinal Motion at $z = 0$ (17 Volts) (Exposure time 20 min.)

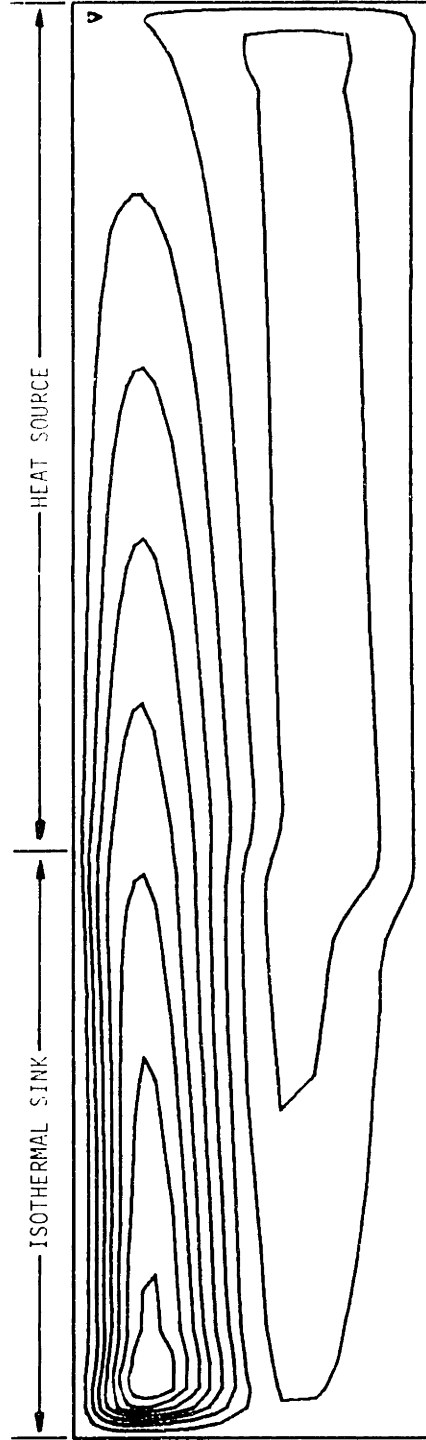


(b) Planform at $x = 0.1$ (40 Volts) (Exposure time 10 minutes)



(c) Planform at $x = 0.15$ (40 Volts) (Exposure time 8 minutes)

Figure 1.5 Experimental Flow Fields with the Roll Motion



STREAM FUNCTION FIELD FOR RUN NUMBER 6019

PSI MAX = 54.05 PSI MIN = -15.32 DELTA PSI = 6.938

Figure 1.6 Experimental Streak Lines and Computed Streamlines for Longitudinal Plane ($z = 0$)
(Exposure time 20 minutes)

the longitudinal plane.

To indicate the limitation of the two-dimensional numerical solution, the predicted temperature is directly compared with the experimental measurements of temperature in various transverse plane under the sink (Figure 1.7). Excess average temperatures from the sink temperature ($T-T_s$) are plotted. (The dimensionless scale of 0.01 is equivalent to an actual temperature difference of 2.1 K.) Systematically lower temperatures in the experimental measurements are due to the enhancement of the local heat transfer in the roll region. If this local enhancement were properly accounted for in the two-dimensional calculation, the deviation would disappear. This was qualitatively demonstrated by Curlet, using an enhanced thermal conductivity over the roll region (as much as a factor of three). Surprisingly enough, the fluid close to the top surface increases its temperature downstream, which is indicated in the dotted profile in Figure 1.7. This is, of course, a consequence of the fluid turnover due to the spirally advancing roll motion.

1.4.2 Temperature Data and Flow Visualization of the Longitudinal Roll Motion

This section is devoted exclusively to the characterization of the longitudinally traveling roll motion under the sink. Experimental temperatures are presented in the form of isotherm contour plots, in conjunction with streak photographs taken at the corresponding transverse planes. When the temperature data are combined with the information on the photographs, the development of roll motion reveals three distinctive stages: an unstably stratified stage prior to the onset of roll motion, a growth stage and a fully developed stage. To facilitate discussion, the isotherm plots and the photographs are sometimes referred to by the location of the trans-

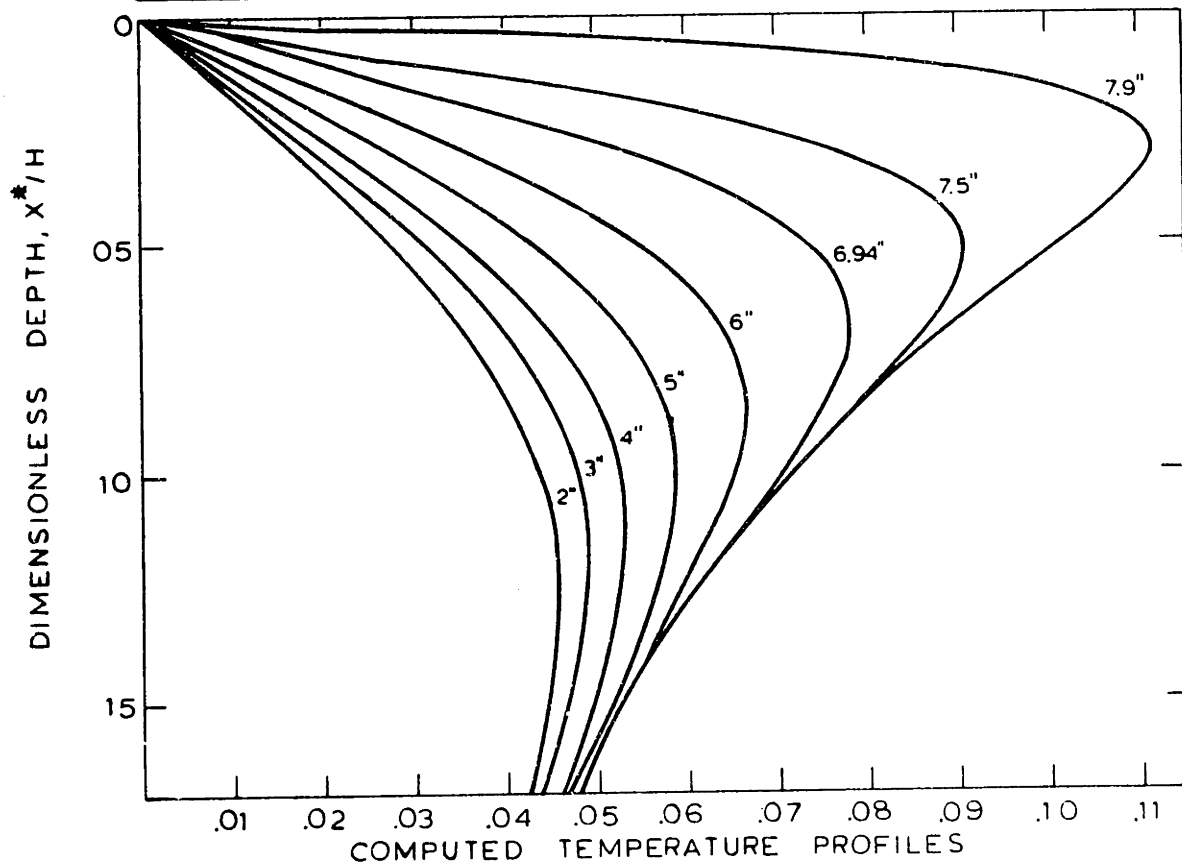
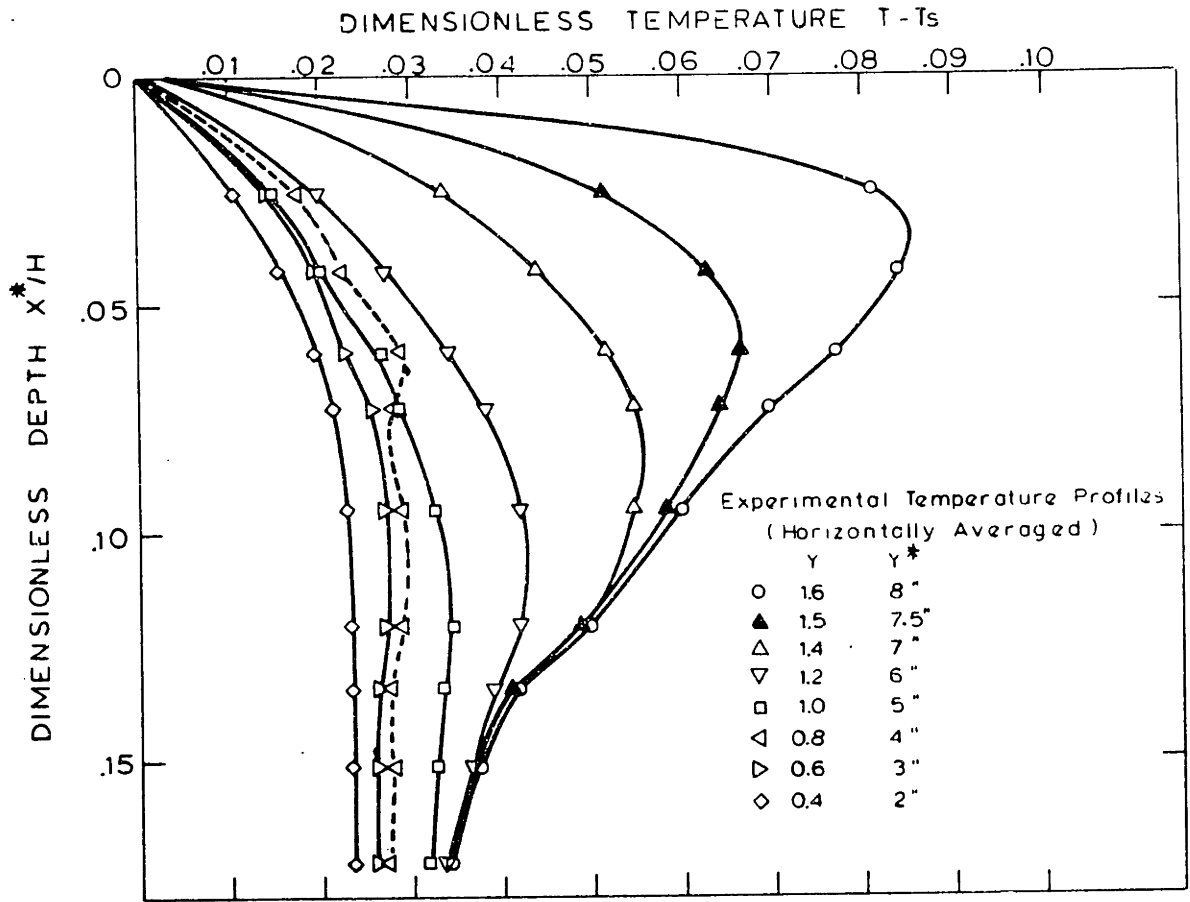


Figure 1.7 Comparison of Experimental and Computed Temperature Profiles in the Roll Region

verse plane in inch unit. (The leading edge of the batch is at 20 cm (8") from the doghouse end.) Note that each isotherm plot covers only one fifth (~2.54cm) of the total enclosure depth. In each photograph the wavelength is marked for a chosen pair of roll cells to indicate its relative position in the experimental model.

The unstably stratified stage covers roughly the first 2.5 cm (1") from the leading edge in this experiment. In this stage, no roll motion appears under the sink, although there exists an adverse temperature gradient in the fluid layer. The isotherm plot at the 8" plane (Figure 1.8) shows that the maximum temperature (~42°C) occurs slightly below the top surface. An adverse temperature gradient is already developed in the top layer and it is the steepest at this location. The nearly parallel horizontal isotherms indicate no disturbances in the transverse direction in the fluid layer, and, hence, the circulation current is two-dimensional. In Figure 1.9 showing isotherms at the 7" plane, the slightly wavy appearance of isotherm lines might be an indication of the flow disturbances at the location. The position of maximum temperature is enclosed within the 36°C isotherm line on the left side, which signifies a horizontal variation of temperature due to the disturbances. In contrast with Figure 1.8, the maximum temperature layer shows a penetration into the depth. The results of a linear stability analysis suggests the onset of roll motion around this location. On the other hand, the corresponding streak photograph shown in Figure 1.10 does not reveal any sign of a disturbance in the top layer. (The small circulation cells at the both corners are caused by the heat leak at the side walls and should not be confused with the roll motion resulting from the convective instability.) It is of course difficult to

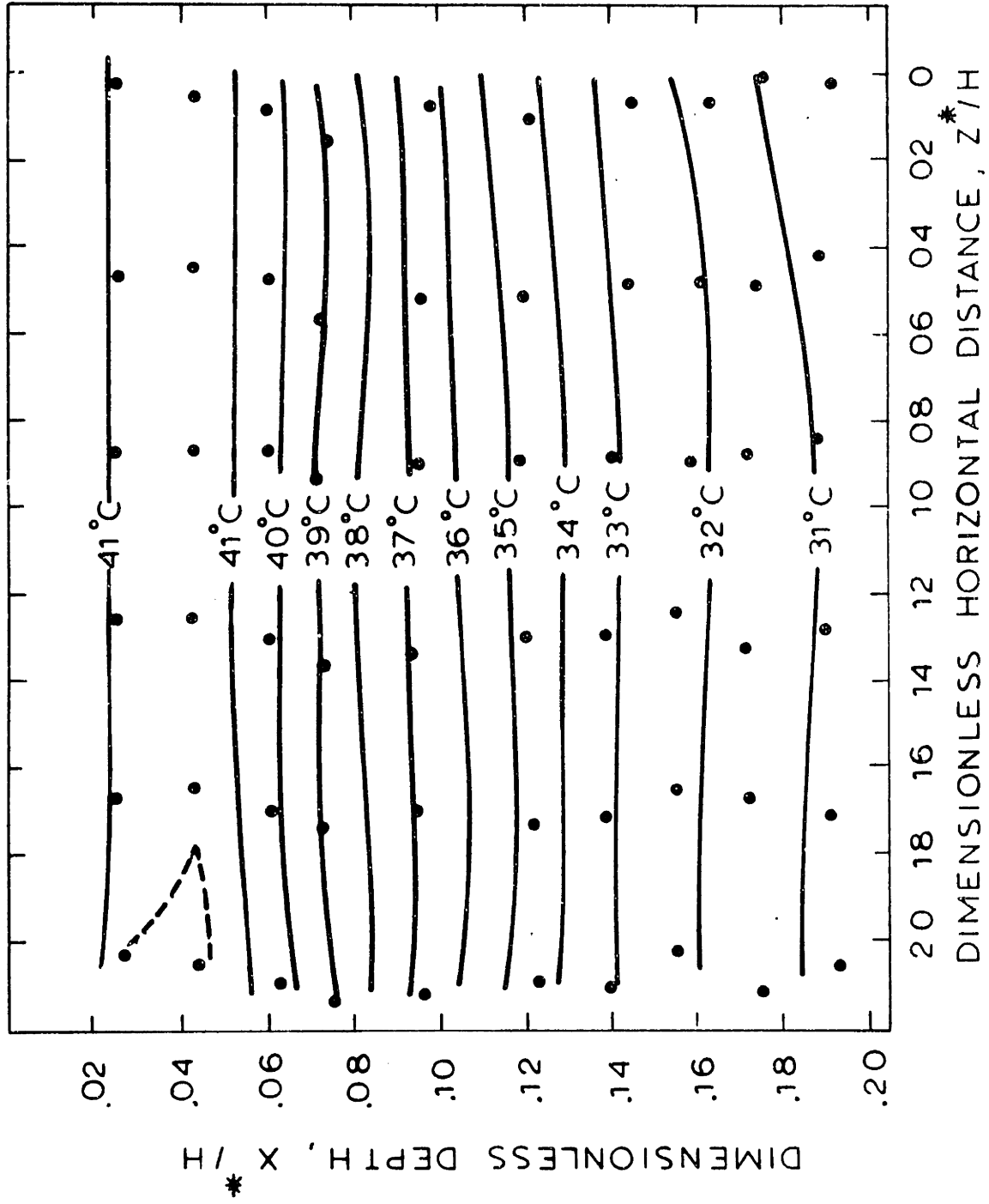


Figure 1.8 Experimental Isotherms at the 8" Transverse Plane ($Y=1.6$) (Run 611)

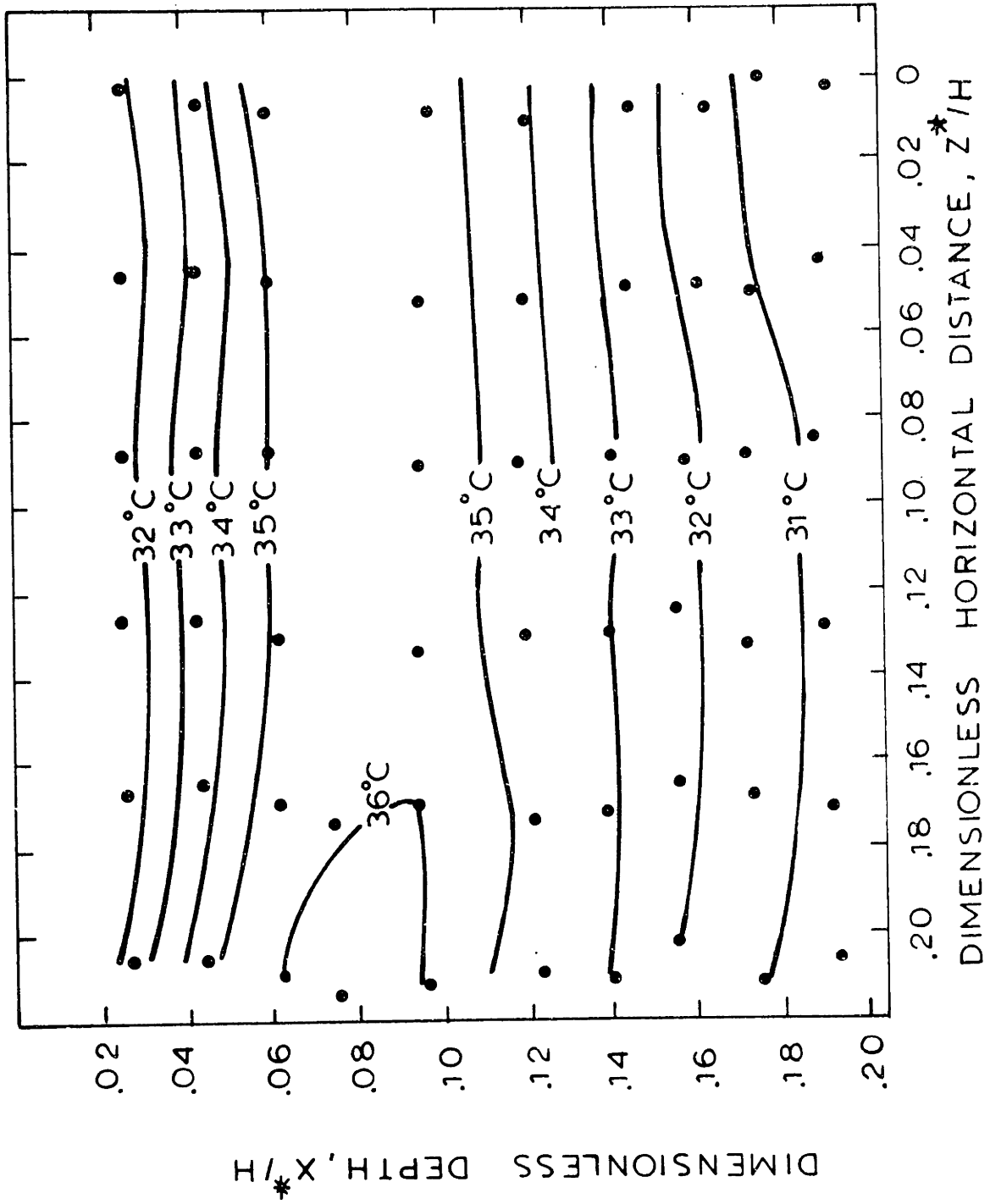


Figure 1.9 Experimental Isotherms in the Roll Cells at the 7" Transverse Plane (Y=1.4). (Run 609)



Figure 1.10 Experimental Streak Lines for the 7" Transverse Plane ($y= 1.4$)
(Exposure time 20 minutes)

identify the exact onset point from photographs, since the flow disturbances can only be observed after the amplitudes grow up to a certain finite magnitude.

The roll motion is clearly evident at the 6" plane, as shown in Figure 1.11. In the middle of top layer, a glimpse of a few pair of roll cells is easily detectable. In the layer, patterns of streak orientation are repeated with a regular interval, which contrast with the uniform upward orientation[¶] of streaks below the roll cells. Vortex eyes appear in staggered positions. A rough estimation indicates that the amplitude of disturbances is of at least two order of magnitude less than the maximum horizontal velocity of the longitudinal current. In the corresponding isotherm plot of Figure 1.12, the wavy appearance is more pronounced. The further penetration of the maximum temperature layer is evident and continues throughout the entire development of roll motion.

Once the roll motion sets in, the roll cells grow in depth within the boundary layer flow, as they are convected downstream by the longitudinal current. However, the growth rate in penetration is significantly slowed. This growth stage is depicted in Figure 1.13 and 1.14. Clear cellular structures reflect the growing amplitude of the disturbances. The upward turning flow of the longitudinal current, which appears as a narrow band of vertical streaks just below the roll cells in the photographs, tends to converge toward the ascending interfaces of the roll cells. These ascending interfaces appear as more natural cell boundaries than the descending inter-

¶ Aberration (due to the use of a close-up lens) is responsible for the slanted streaks towards the both sides of the photographs. However, the orientation of the streaks at the left side is real and is caused by the transverse motion.

λ

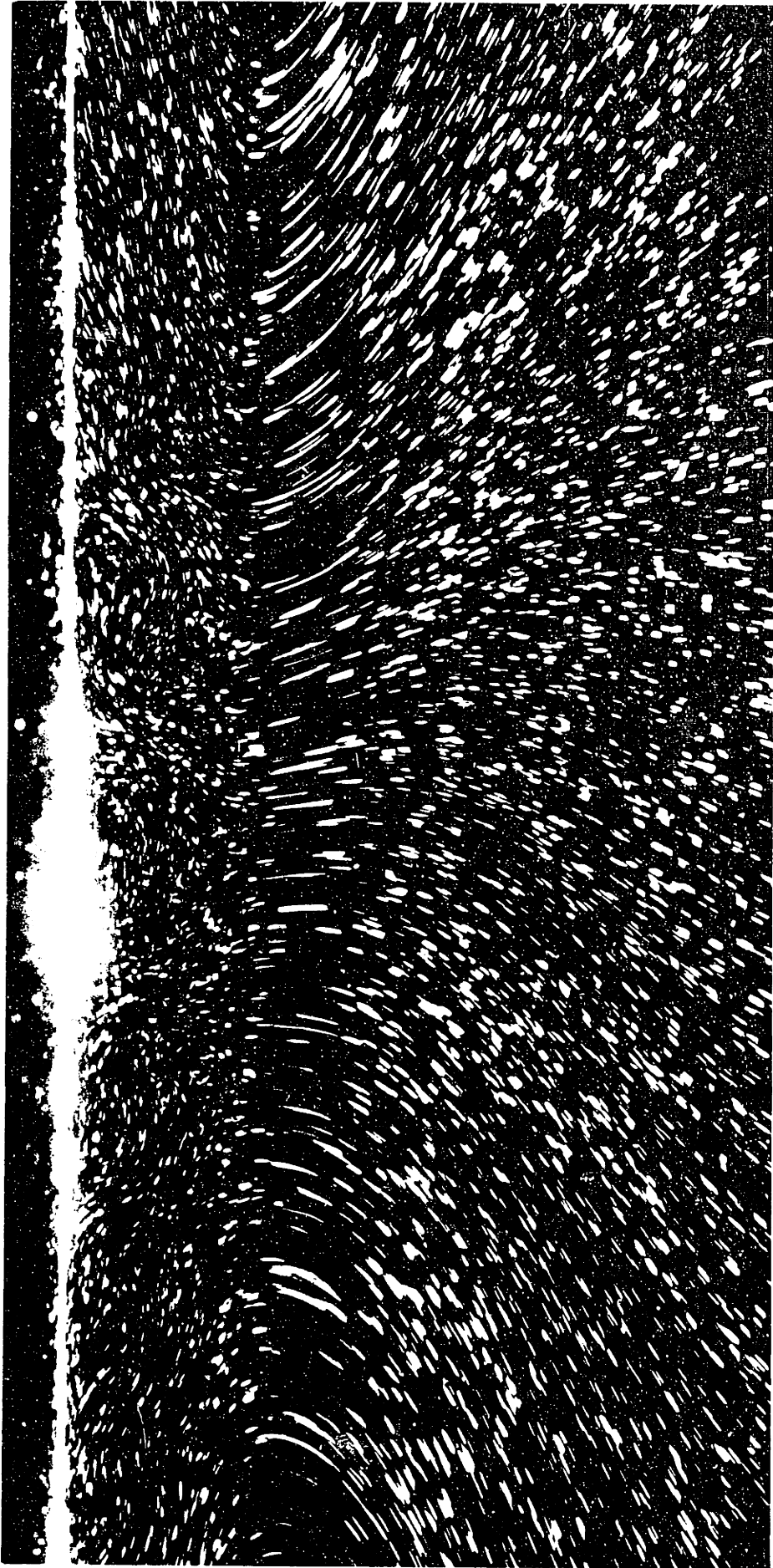


Figure 1.11 Experimental Streak Lines of the Roll Motion at the 6" Transverse Plane
($y = 1.2$) (Exposure time 20 minutes)

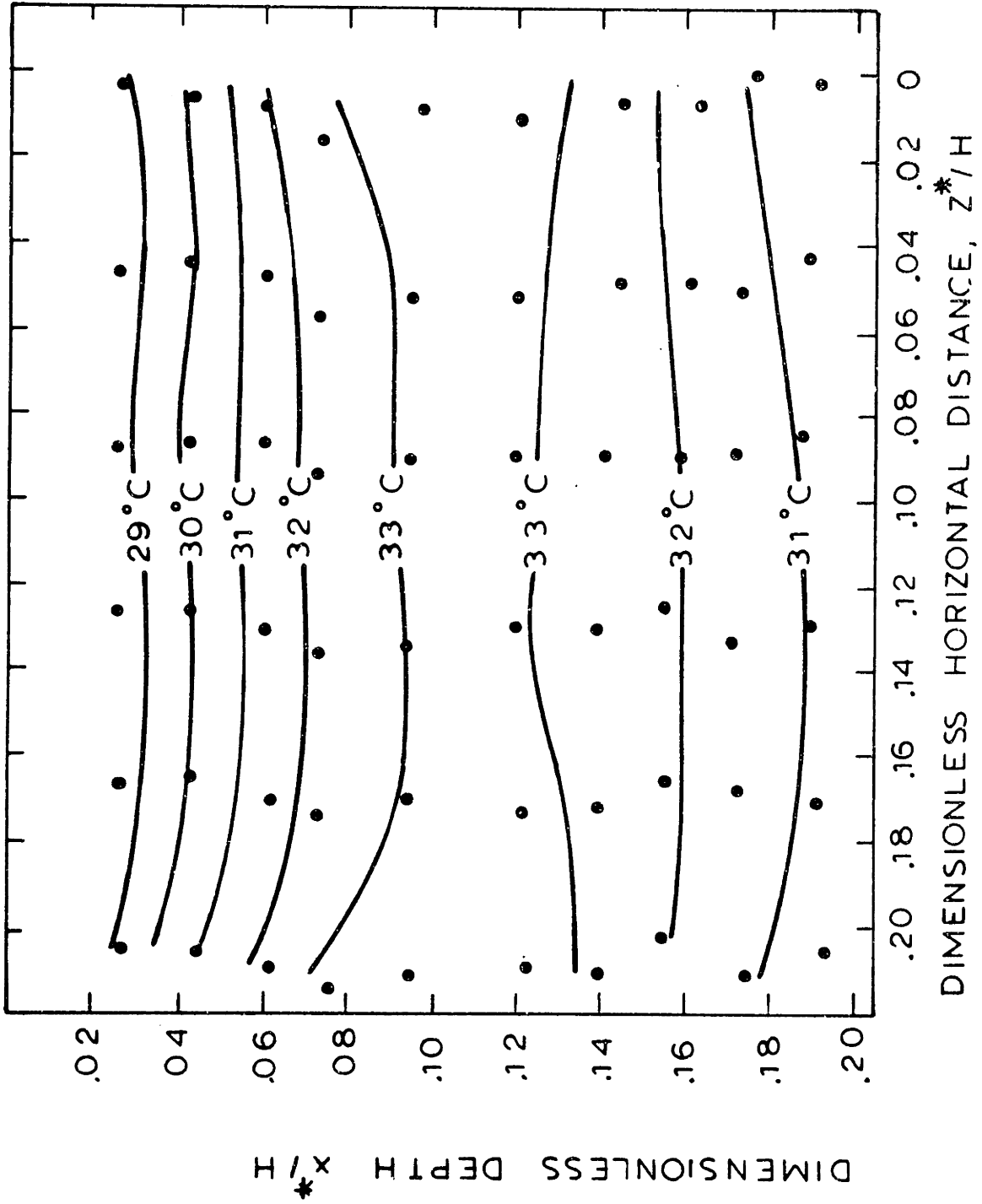


Figure 1.12 Experimental Isotherms in the Roll Cells at the 6" Transverse Plane ($Y=1.2$), (Run 607)

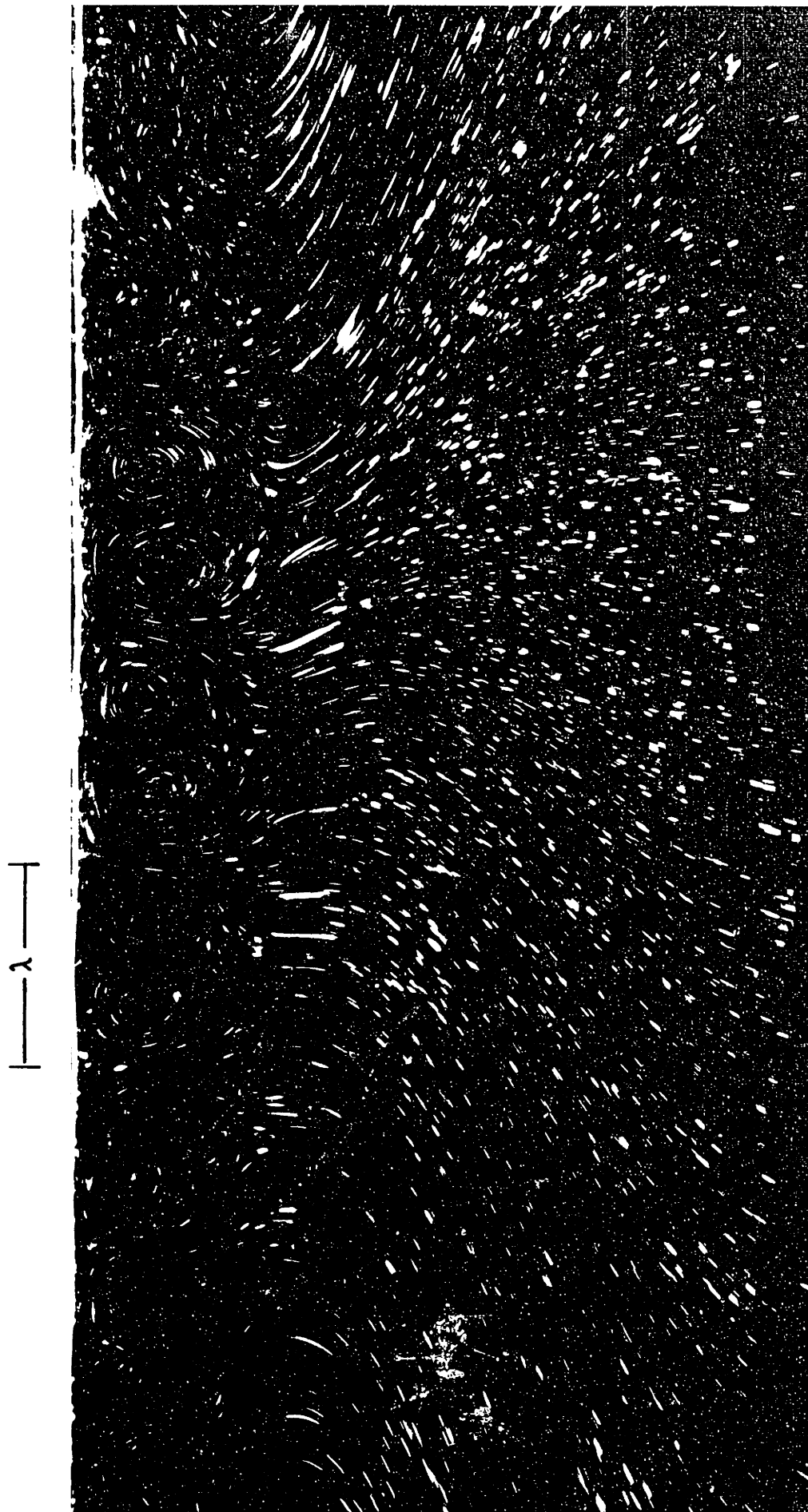


Figure 1.13 Experimental Streak Lines of the Roll Motion at the 5" Transverse Plane
($y = 1.0$) (Exposure time 20 minutes)

λ



Figure 1.14 Experimental Streak Lines of the Roll Motion at the 4" Transverse Plane
($y = 0.8$) (Exposure time 20 minutes)

faces do, which are conventionally accepted as cell boundaries for the Rayleigh-Bénard problem. The corresponding isotherm plots are shown in Figure 1.15 and 1.16. It should be noted that the fluid along the right side is in the ascending motion. Here, a few isotherms appear enclosed and heating occurs in a broad region, while the descending flow plunges down in a narrow area close to the left side. This is one of the features in the Rayleigh-Bénard roll cells with an internal heat source. This analogy is exploited in the linear analysis in conjunction with the source-sink approximation method. Fluid in the isotherm envelope of 32°C shows an upward displacement to the downstream of the longitudinal current. This temperature reversal has already been mentioned in Section 1.4.1 and is construed as fluid turnover due to the spiraling roll motion. In this stage, temperature fluctuations of a transient and random nature have been recorded, although they are quite small (maximum of $\sim 0.5^{\circ}\text{C}$). No fluctuations are detected in the other stages. It is conjectured that influence of the upward turning flow is responsible for this high frequency fluctuation.

When the roll motion reaches to the level of the circulation eye region, a transition to the fully developed stage occurs. Figures 1.17 and 1.18 represent this stage. The narrow band of streaks corresponding to the upward turning flow has completely disappeared. The bottom of the roll cells reaches down into the circulation eye region, where fluid is nearly stagnant. Streak lines in this region are suggestive of free slip in the lateral (transverse) direction. The roll cells still manage to grow and the corresponding isotherm plots of Figures 1.19 and 1.20 show continuous cooling of the fluid stream. Finally, the roll cells begin to disarray, coalesce and merge to the downward return flow along the doghouse wall.

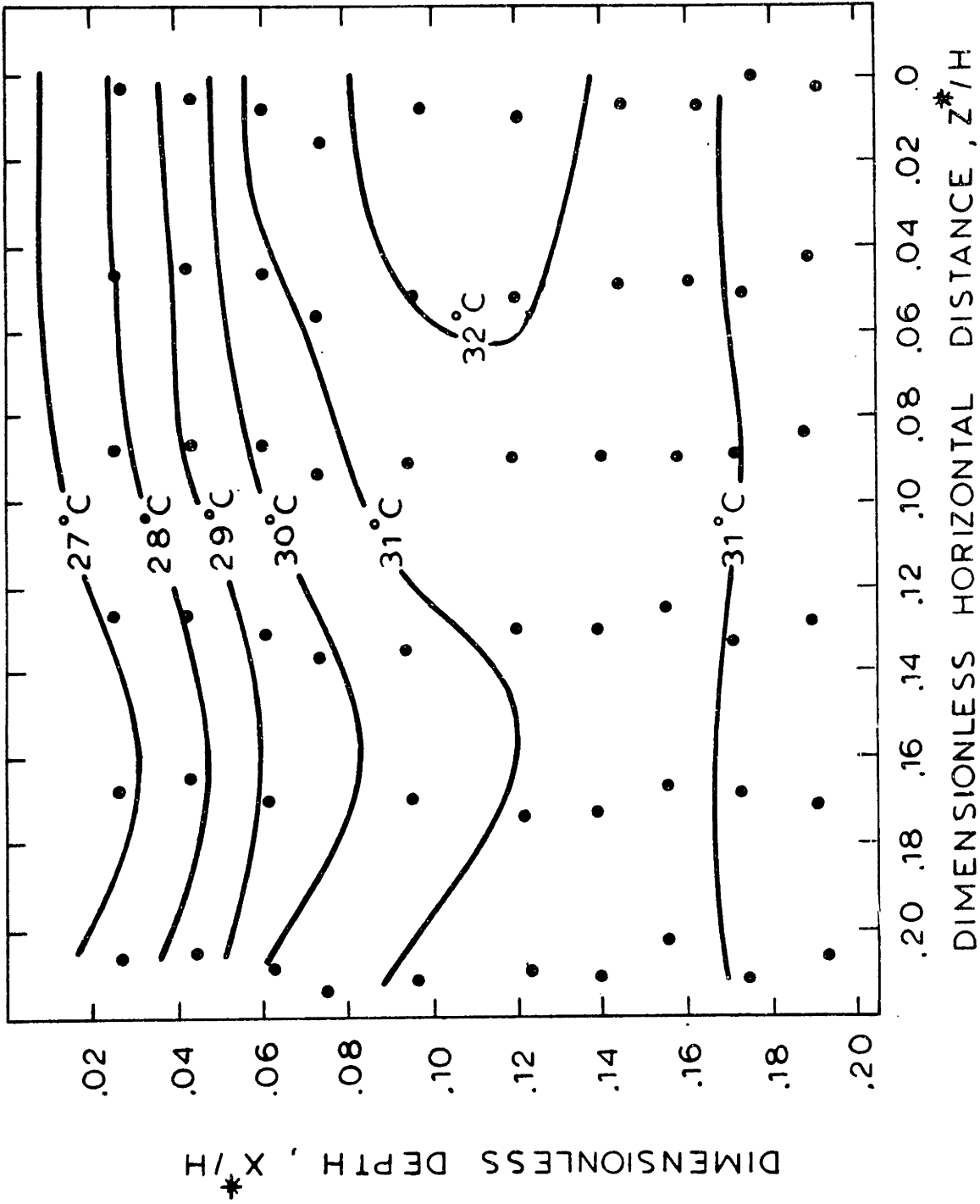


Figure 1.15 Experimental Isotherms in the Roll Cells at the 5" Transverse Plane (Y=1.0). (Run 622)

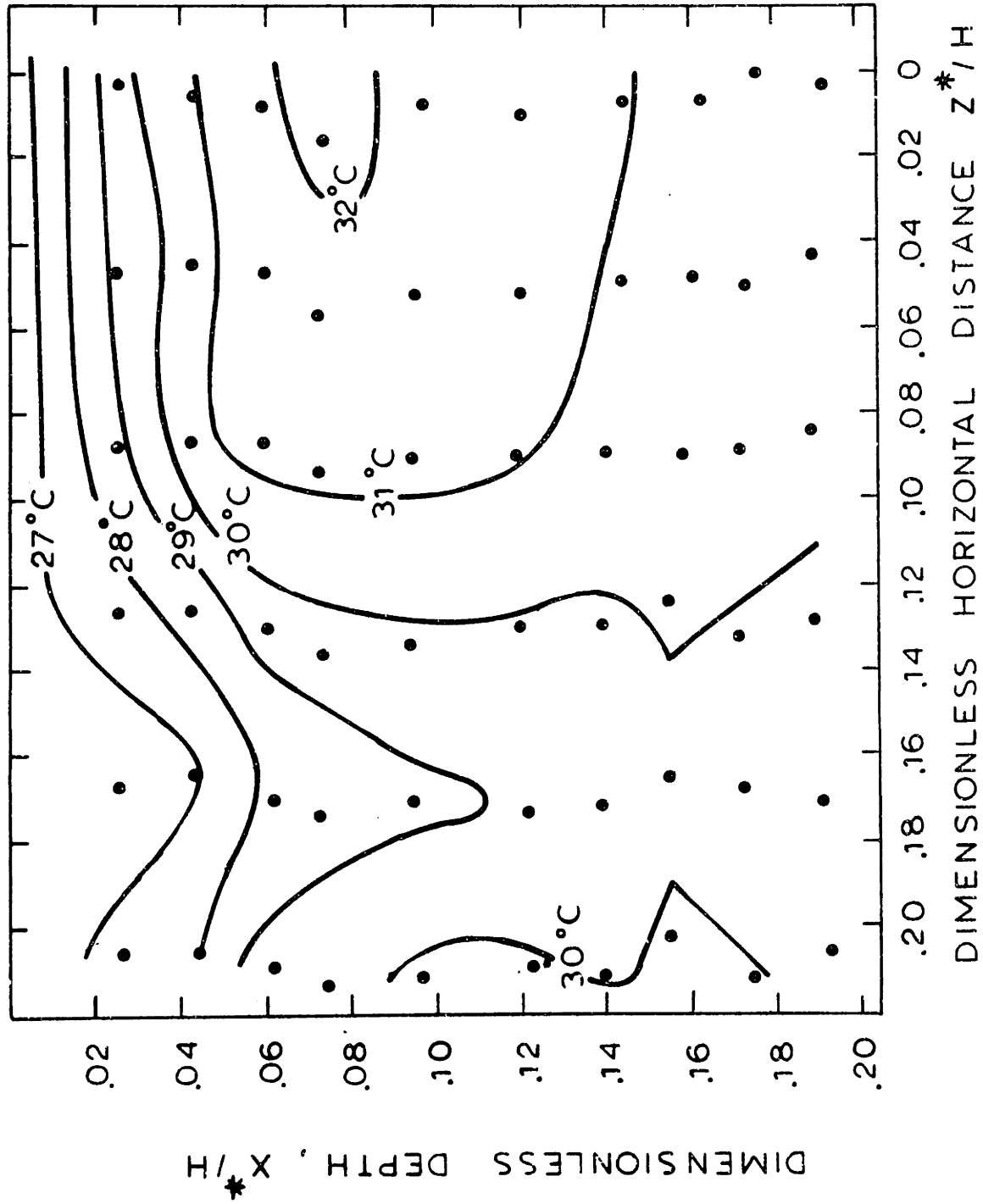


Figure 1.16 Experimental Isotherms in the Roll Cells at the 4" Transverse Plane (Y=0.8).(Run 616)

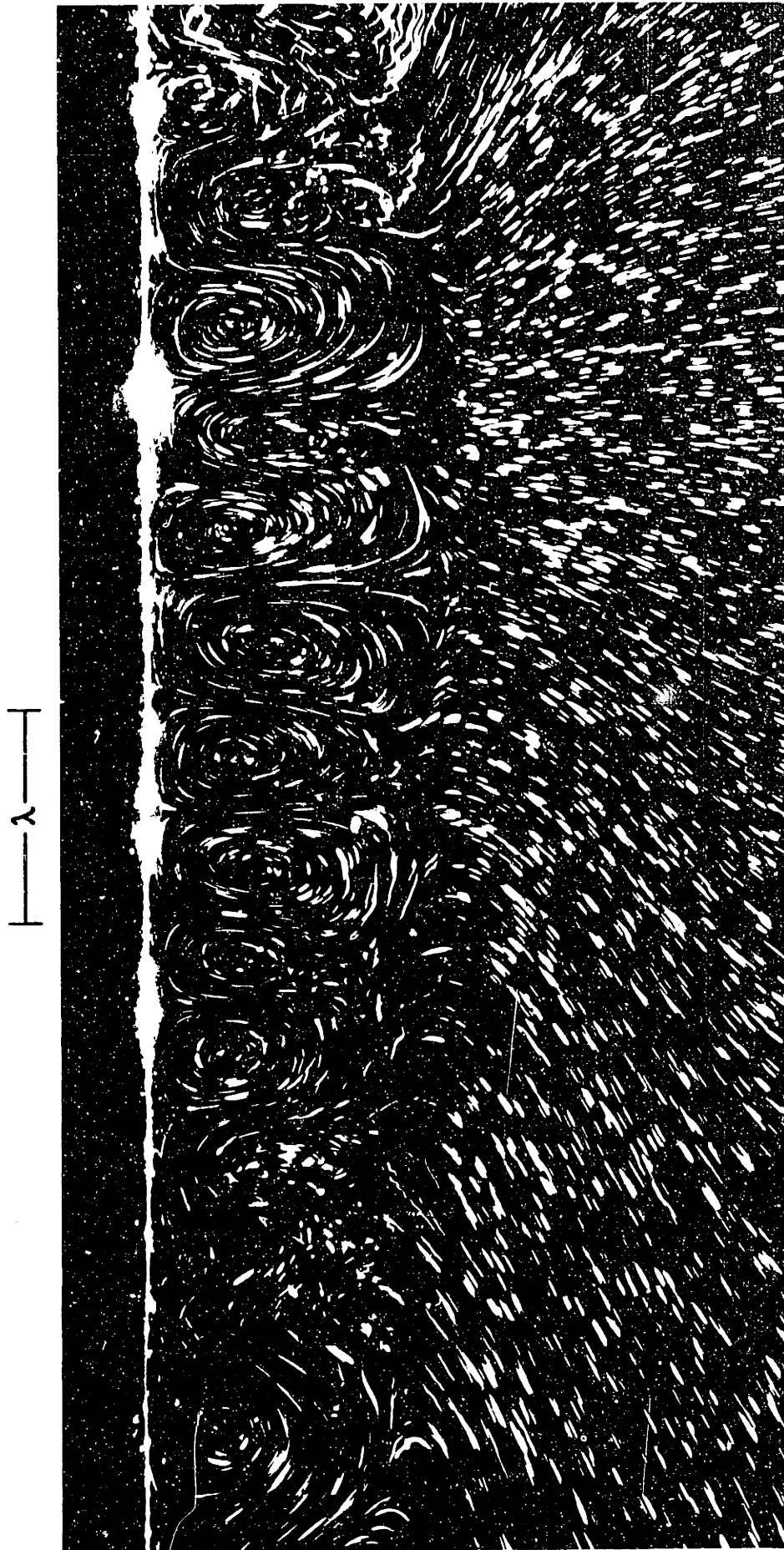


Figure 1.17 Experimental Streak Lines of the Roll Motion at the 3" Transverse Plane
($y = 0.6$) (Exposure time 20 minutes)

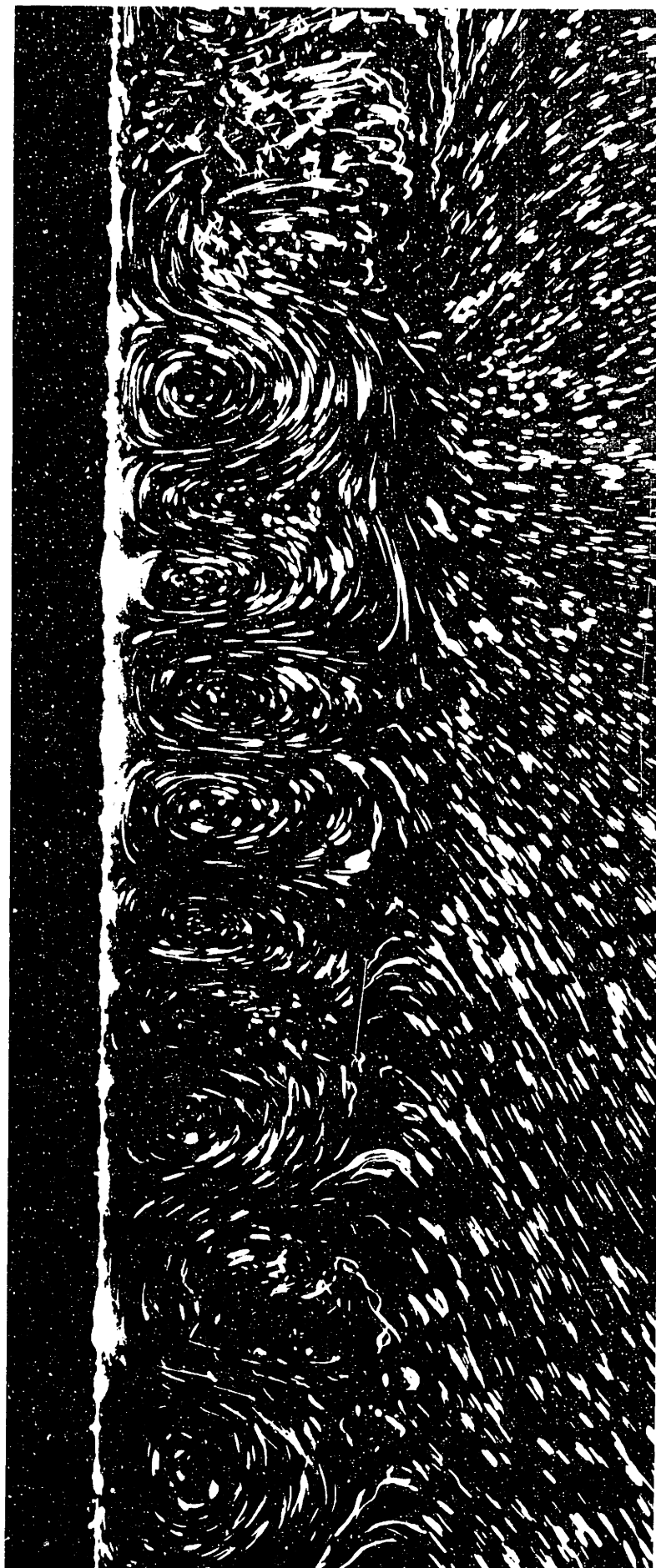


Figure 1.18 Experimental Streak Lines of the Roll Motion at the 2" Transverse Plane
($y = 0.4$) (Exposure time 20 minutes)

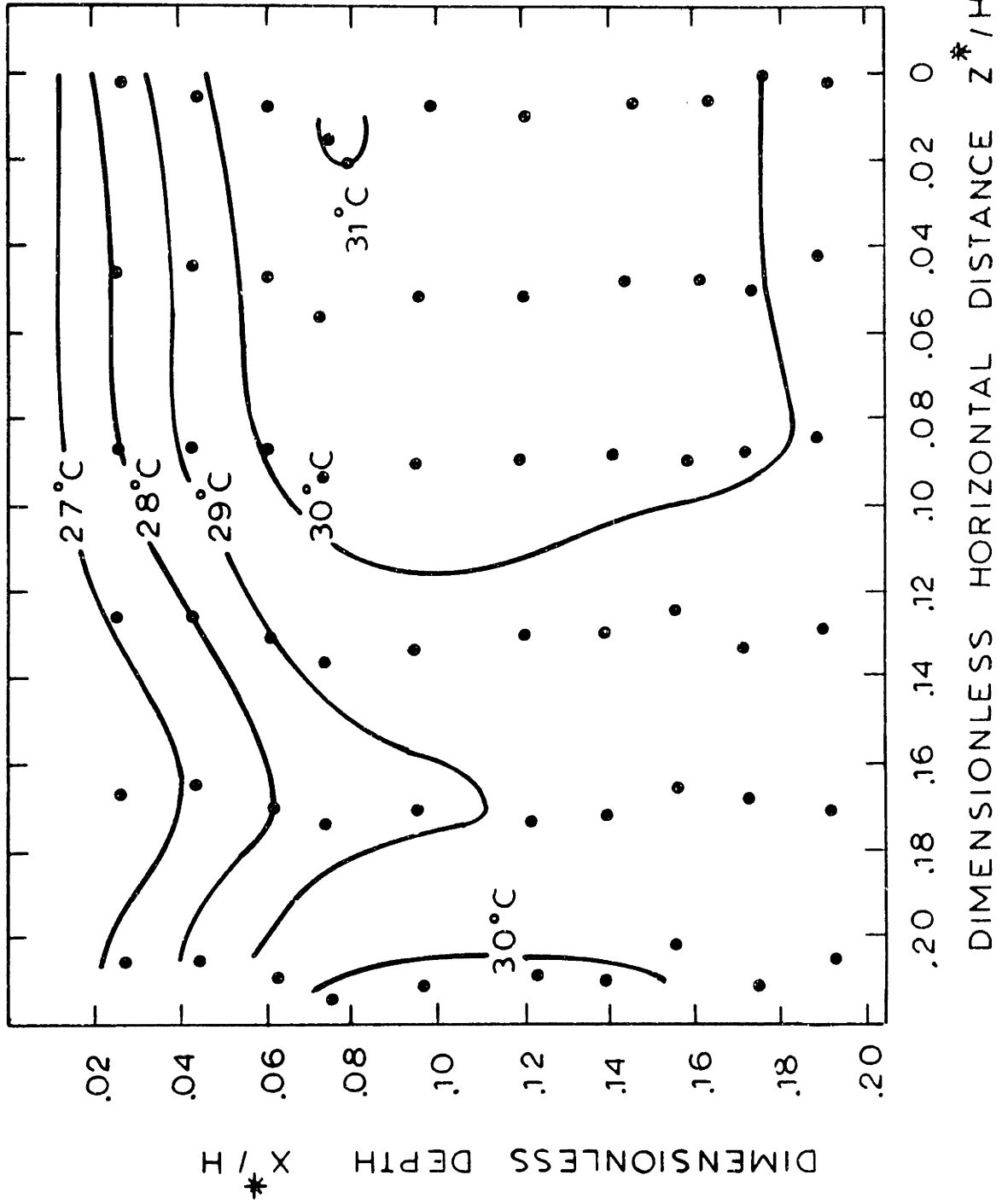


Figure 1.19 Experimental Isotherms in the Rolls at the 3" Transverse Plane ($Y=0.6$). (Run 618)

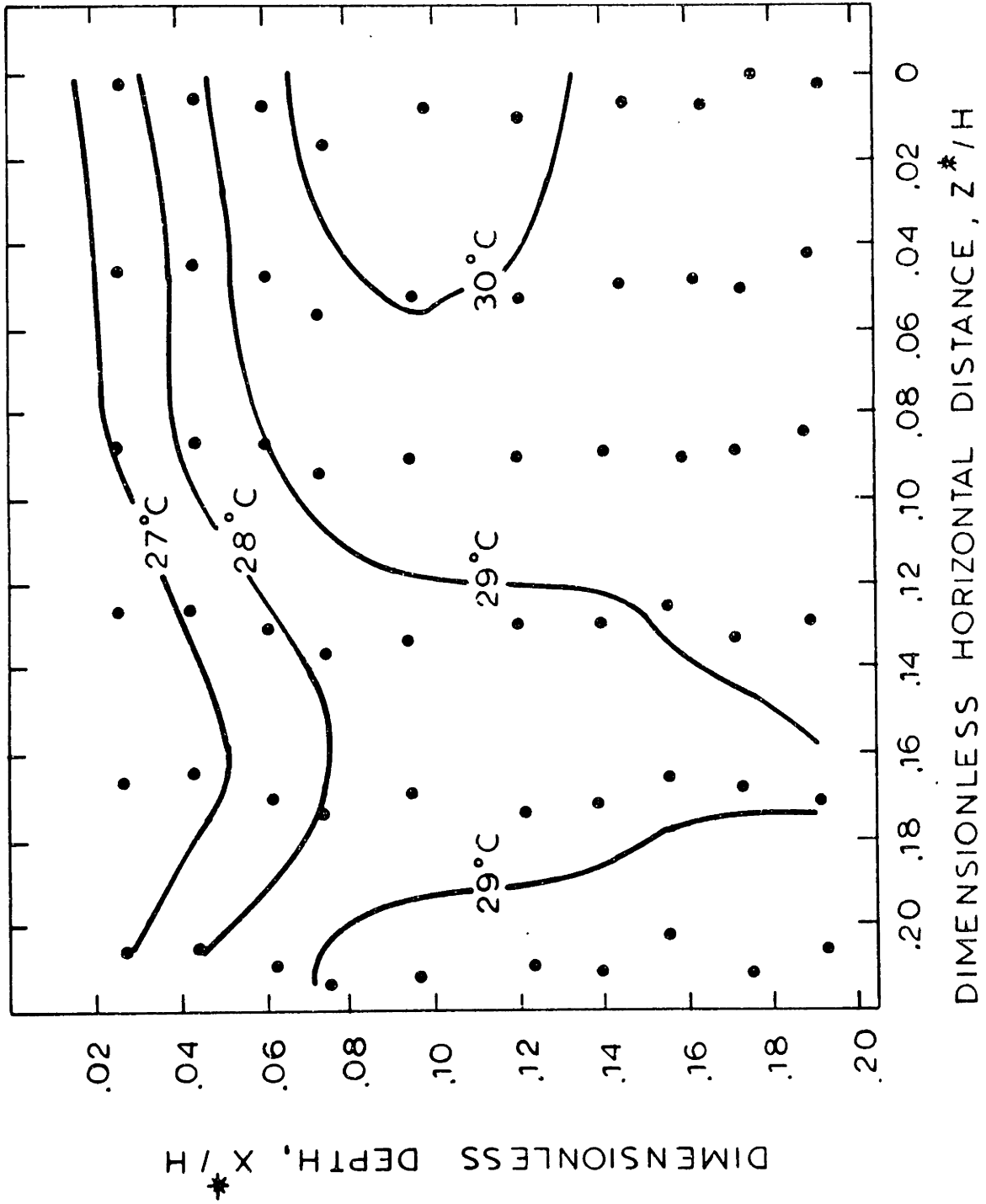


Figure 1.20 Experimental Isotherms in the Roll Cells at the 2" Transverse Plane (Y=0.4). (Run 620)

All the temperature data reported here are reproducible. In Figure 1.21, the two sets of isotherm plots represent data at the 5.5" plane taken 6.5 days apart. During the time between measurements the thermocouple net has been relocated more than a dozen times. The two sets of data show an excellent agreement.

The wavelengths of the roll cells has been determined from the streak photographs and are summarized in Table 1.3. Four pairs of roll cells were chosen from the middle of the photographs and the distance between the ascending interfaces measured together with its penetration depth. The data clearly shows that each individual roll preserves its wavelength throughout the entire development stages of roll motion. Even though variations in the wavelength of the roll cells are observed in a given transverse plane, the ratio of the wavelength to the penetration depth occupied by the roll motion remains constant. It is this ratio that linear stability analysis can predict at the onset condition of flow instability.

1.5 Comparison of Experimental and Theoretical Onset Condition for the Roll Motion

The normalized curve of source-sink functions discussed in Section 1.3.1 is shown in Figure 1.22. It was obtained from the temperature distribution of the two-dimensional numerical solution and relevant parameters are listed in Table 1.4. A total of 14 curves are well represented by a single parabolic profile

$$F \equiv \frac{4 \cdot x}{\ell^2} (\ell - x) \cdot H(\ell - x)$$

where ℓ is the dimensionless source depth corresponding to ℓ_s^* . The Heaviside step function, $H(\ell - x)$, is used to indicate that the source

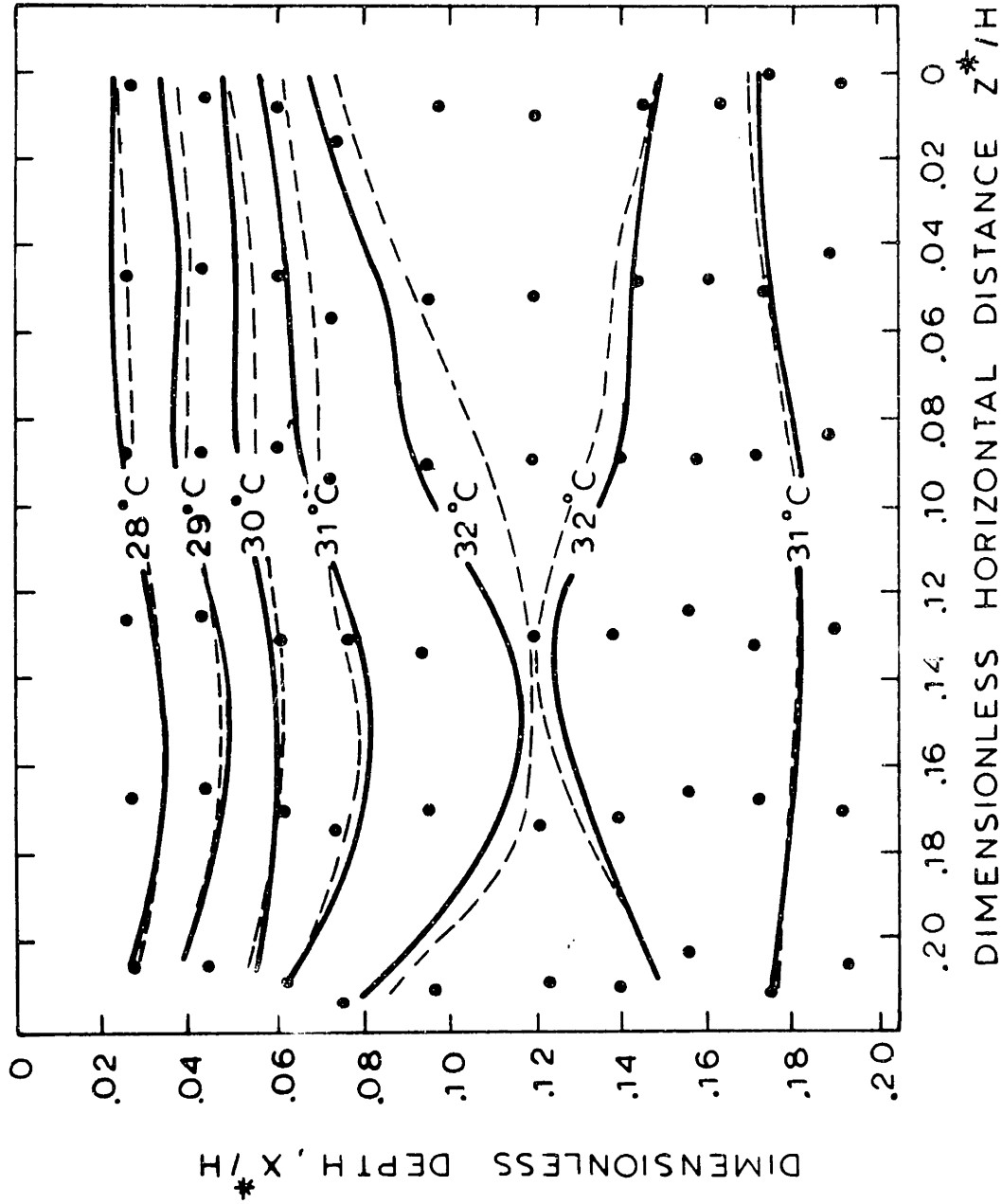


Figure 1.21 Reproducibility Test for Experimental Temperature in the Roll Cell at the $5\frac{1}{2}$ Transverse Plane ($Y=1.1$)

Run 606 - Solid Line Taken at 12.15. 1977

Run 623 - Dotted Line Taken at 12.21. 1977

2

TABLE 1.3

Observed Wavelength (W) and Depth (D) of the Roll Motion

(Unit in inch)

Plane Location	roll 1		roll 2		roll 3 [†]		roll 4		$\lambda \equiv \frac{W}{D}$	$a \equiv \frac{2\pi}{\lambda}$
	W	D	W	D	W	D	W	D		
6 "	0.90	0.42	0.89	0.43	0.88	0.42	-	-	2.10	2.99
5½"	-	-	0.92	0.50	0.90	0.49	0.86	0.48	1.82	3.45
5 "	0.90	0.61	0.91	0.60	0.88	0.61	0.83	0.56	1.48	4.25
4½"	-	-	0.94	0.84	0.91	0.82	0.86	0.74	1.13	5.56
4 "	0.95	0.97	0.94	0.94	0.91	0.94	0.84	0.87	0.98	6.38
3 "	0.93	1.23	0.93	1.27	0.90	1.17	0.85	1.03	0.77	8.16
2 "	0.93	1.22	0.91	1.29	0.92	1.24	0.85	1.14	0.74	8.49
Average	0.92		0.92		0.90		0.85			

[†] Wavelength of the roll 3 is marked in photographs.

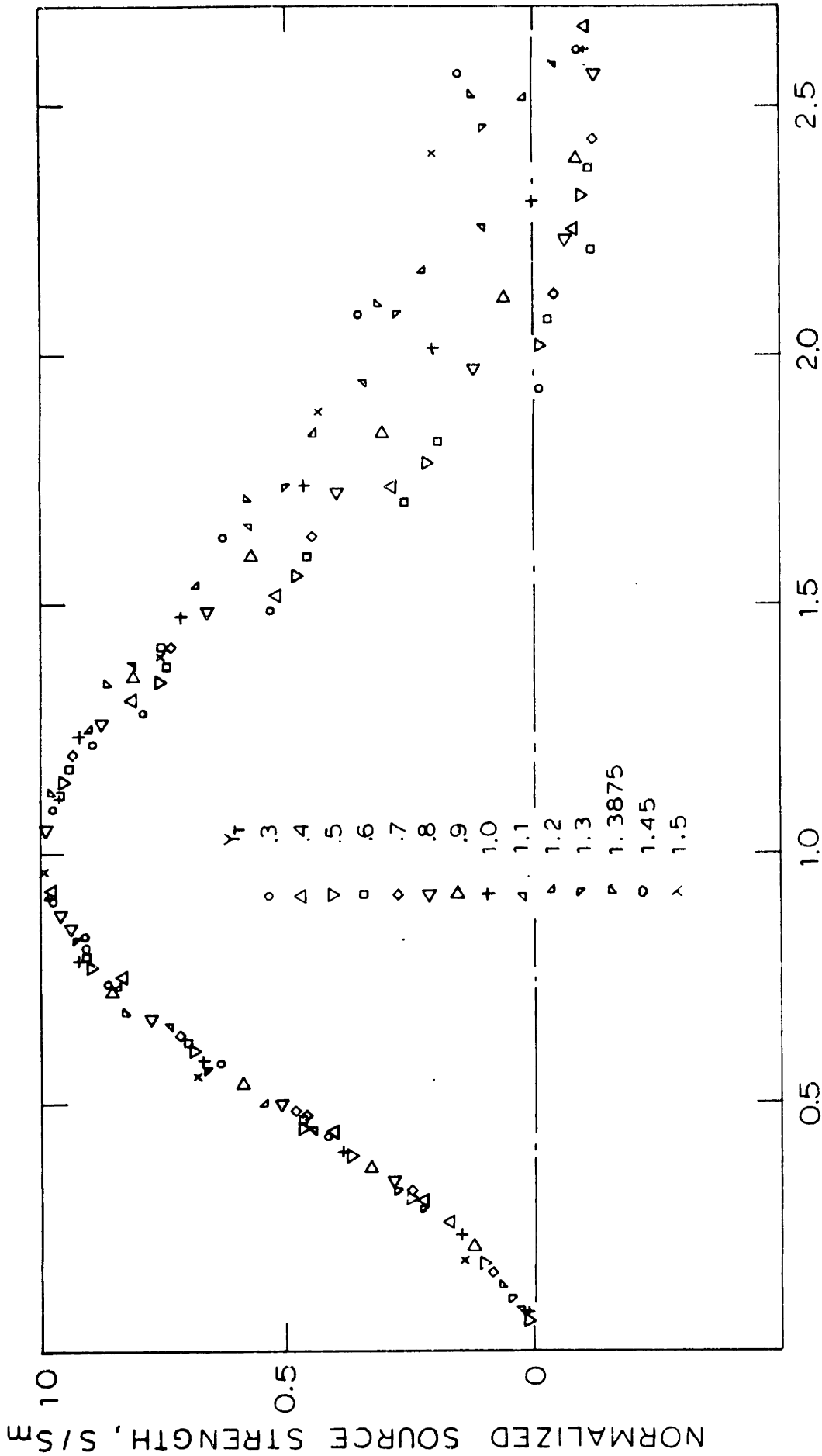


Figure 1.22 Similarity Curve for Source - Sink Functions

TABLE 1.4

Maximum Source Strength and Source Depth from the Numerical Solution

Plane Location (y)	Maximum Source Strength (S_m)	Source Depth (ℓ)	Temperature Gradient Parameter (η_s)
0.3	7.02	0.176	0.06677
0.4	7.17	0.173	0.07135
0.5	8.00	0.168	0.08265
0.6	8.67	0.164	0.08475
0.7	9.37	0.160	0.09205
0.8	10.52	0.156	0.09506
0.9	12.08	0.142	0.10056
1.0	14.29	0.130	0.10908
1.1	17.78	0.118	0.11004
1.2	22.31	0.104	0.11658
1.3	30.40	0.092	0.11030
1.3875	43.12	0.076	0.11429
1.45	66.20	0.062	0.10780
1.5	92.50	0.054	0.09844

distribution exists only in a part of the entire fluid layer ($0 < x < \ell$). Deviations appearing in the lower part of the parabolic source profile are accounted for by adjusting the parameter, η , defined below. The gradient function, $h(x)$, is easily obtained from the static temperature profile for the parabolic source distribution:

$$h(x) = -\eta + \frac{1}{3\ell^2}(4x^3 - 6\ell x^2 - 2\ell^3)H(\ell-x) \quad (1.16)$$

where
$$\eta \equiv \frac{N}{N+1} \left(\Delta T + \frac{\ell^2}{3} \right) .$$

N is the heat transfer coefficient at the bottom and ΔT is the temperature difference between the ambient and the sink ($T_S - T_A$), both parameters arising from the mixed type boundary conditions at the bottom. Physically, the parameter, η , signifies the stable temperature gradient in the deeper fluid layer ($\ell < x < 1$) where no source distribution is assigned. In the numerical calculations, viscosity is assumed to be constant.

It can be shown that the maximum temperature difference in the conduction solution is

$$\Delta T_m \equiv T_m - T_s = \frac{\ell_t^3}{\ell^2} \left(\frac{4}{3}\ell - \ell_t \right) , \quad (1.17)$$

where ℓ_t denotes the depth to the location of maximum temperature (T_m) and T_s is the sink temperature. This temperature difference can be used to define the temperature Rayleigh number:

$$R_T \equiv \frac{g \cdot \beta \cdot \Delta T_m^* \cdot H^{*3}}{\nu_o^* \cdot \alpha_o}$$

which is related to the source Rayleigh number

$$R_T = R_S \left\{ \frac{\ell_t^3}{\ell} \right\}^2 \cdot \left(\frac{4}{3}\ell - \ell_t \right) . \quad (1.18)$$

Since the source depth ℓ_s^* occupies only a small fraction of the total depth H , it is convenient to choose smaller length scales, ℓ_s^* or ℓ_t^* . Modified Rayleigh numbers based on these scales are defined as follow:

$$R_{S,\ell} \equiv R_S \cdot \ell^5$$
$$R_{T,\ell} \equiv R_T \cdot \ell_t^3$$

The results of the stability analysis are shown in Figure 1.23, where $R_{S,\ell}$ is plotted against the temperature gradient parameter in the stable deeper layer below the source region:

$$\eta_s \equiv \frac{\eta}{\ell}$$

These results indicate the importance of the parameter, η_s :

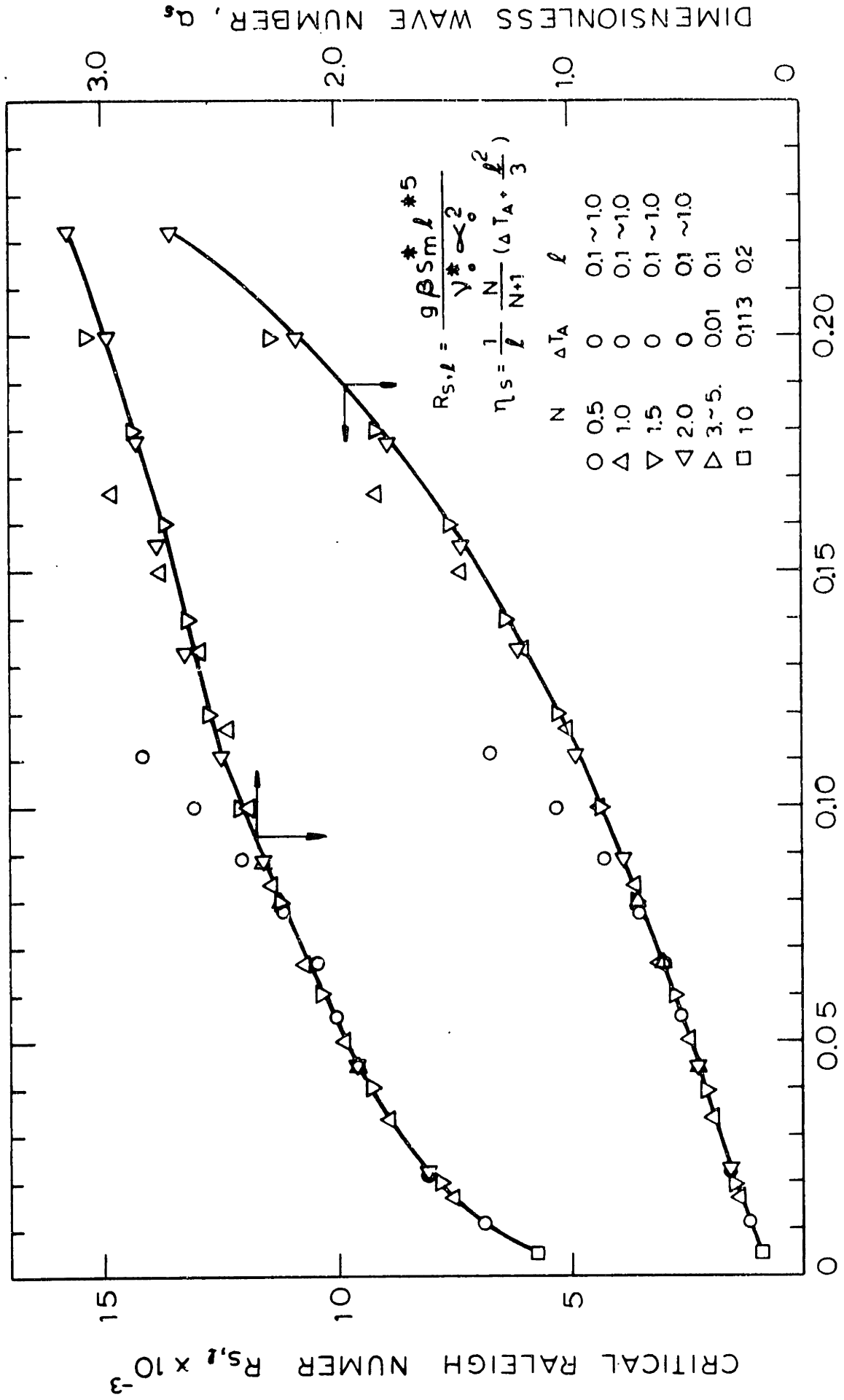
$$R_{S,\ell} = R_{S,\ell}(\eta_s) \quad (1.19)$$

This unique relationship is valid only when the source depth ℓ is small compared to the total depth of fluid layer. This result can be derived from a coordinate transformation, when the fluid disturbances due to the instability do not reach down to the bottom boundary. For a direct comparison with the experimental data, the temperature Rayleigh number plot shown in Figure 1.24 is more convenient. Theoretical consideration leads to a relationship in the form of

$$R_{T,\ell} = R_{T,\ell}(\eta_t, \frac{\ell}{\ell_t}) \quad (1.20)$$

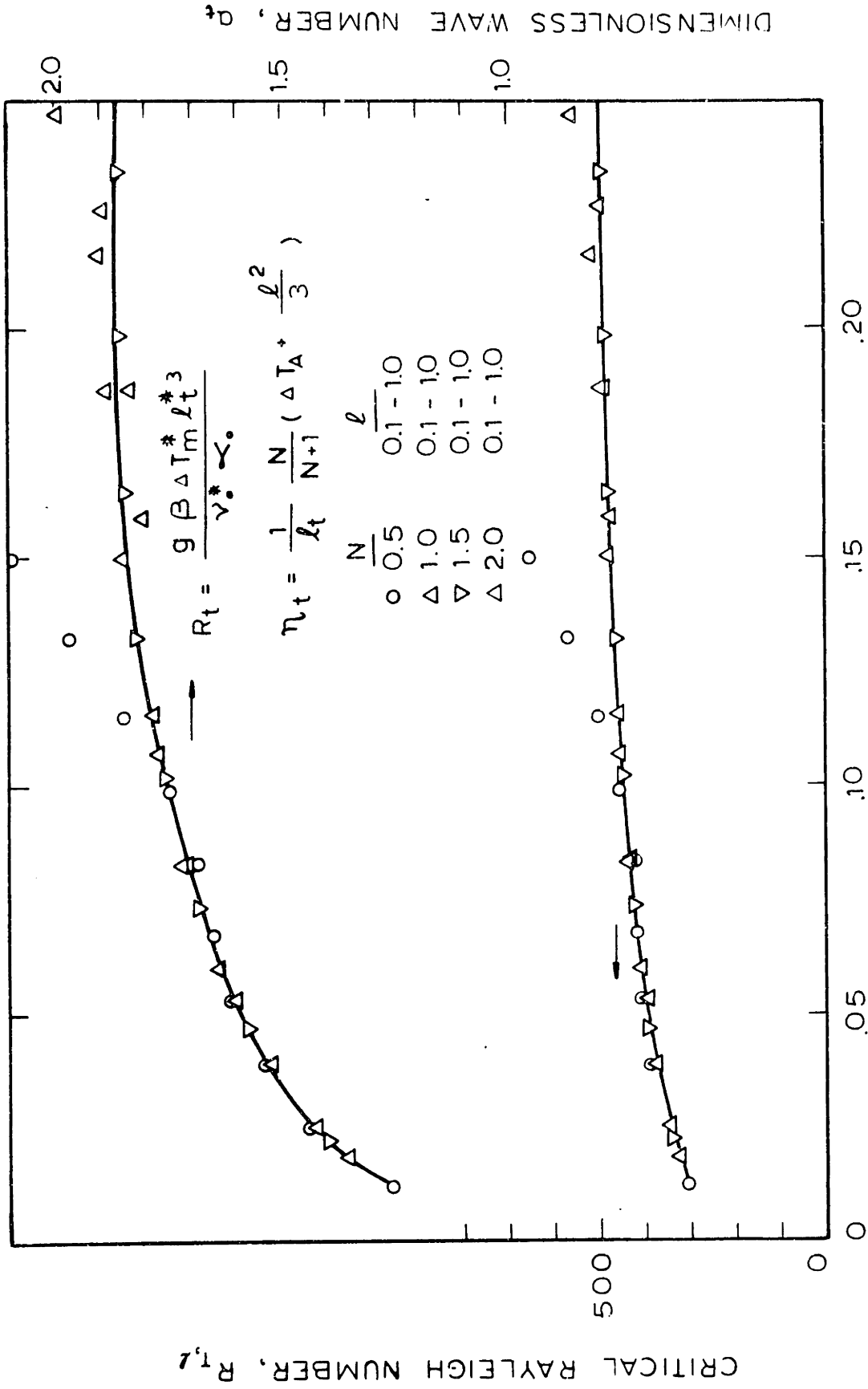
where

$$\eta_t \equiv \frac{\eta}{\ell_t}$$



RELATIVE TEMPERATURE GRADIENT IN THE STABLE LAYER, η_s

Figure 1.23 Critical Conditions for the Onset of Roll Motion $R_{s,l}$ vs η_s



RELATIVE TEMPERATURE GRADIENT IN THE STABLE LAYER, η_t

Figure 1.24 Critical Conditions for the Onset of Roll Motion:
 $R_{t,l}$ vs η_t

On the other hand, the numerical results in the Figure suggests that, as long as the parameter, η_t , is greater than the value of 0.1, the critical condition for the onset of roll motion can be generalized as follows:

$$R_{T,\ell} \approx 500$$

and (1.21)

$$a_c \approx 1.88 ,$$

with a deviation less than 5%.

For comparison, experimental Rayleigh numbers were obtained from the horizontally averaged temperature profile for each transverse plane. These are plotted as circled data in Figure 1.25. The Figure clearly shows that the onset for the roll motion in the experiment occurs at the $7 \frac{1}{4}$ " plane. This prediction is consistent with the experimental observations discussed earlier in Section 1.4.2. The experimental wave number at the onset can not be directly compared, because of the difficulty in obtaining the data photographically. However, the numerical solution for the longitudinal circulation motion and the derived source-sink functions from it can be utilized to test the theoretical results for the onset condition. The source Rayleigh number based on the numerical solutions is shown in Figure 1.26, together with predicted Rayleigh number obtained from the generalized stability curve (Figure 1.23) based on the parameter η_s . The two Rayleigh numbers coincide only when the fluid layer is in the critical condition. Therefore, the numerical solution predicts the onset of roll motion at the $6 \frac{3}{4}$ " transverse plain. Considering the systematic discrepancies in the numerical temperature solution, the prediction is remarkable. Finally, a comparison of wave number at the onset of roll motion is presented in

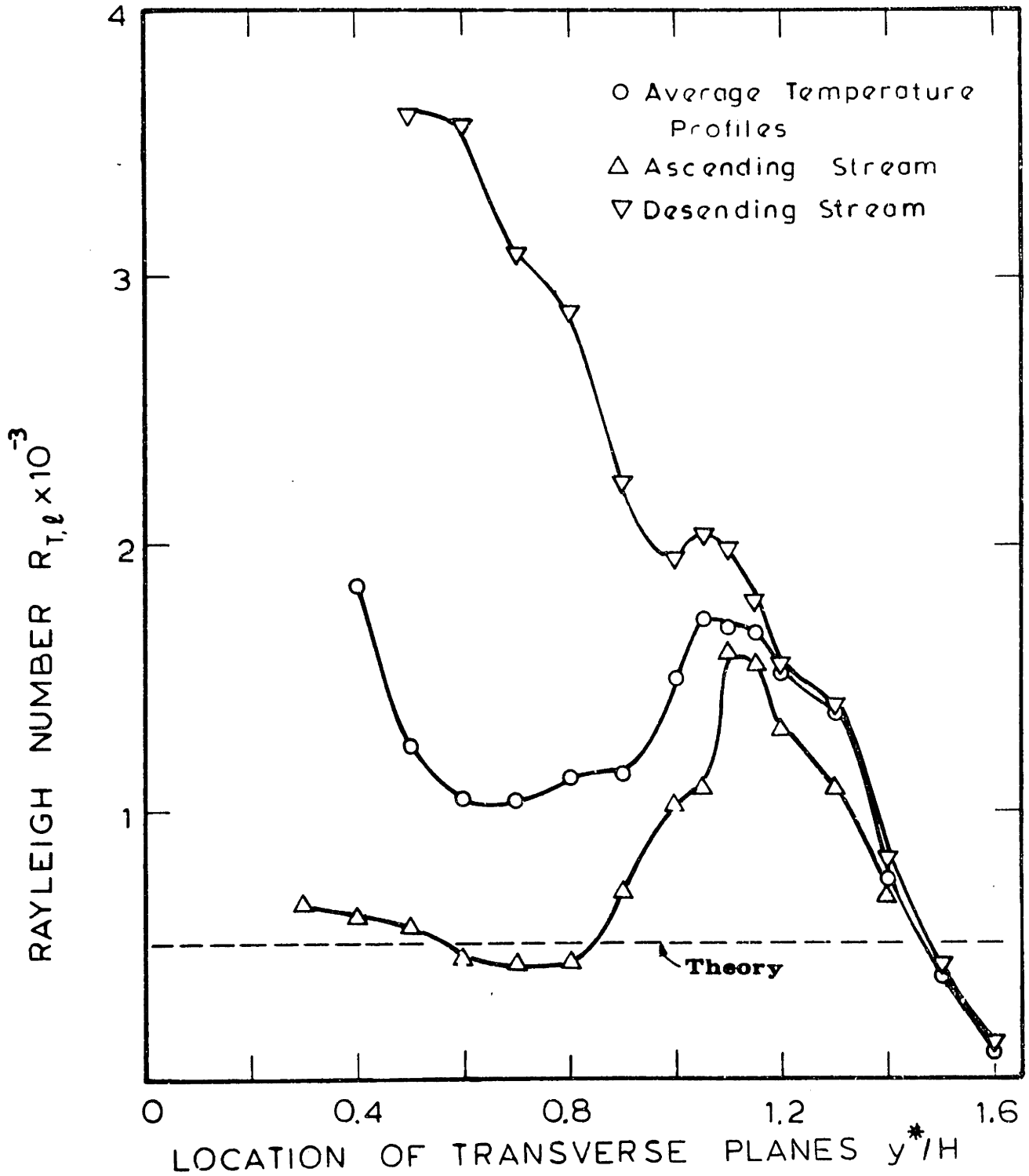


Figure 1.25 Comparison of Theoretical and Experimental Onset Condition for the Roll Motion

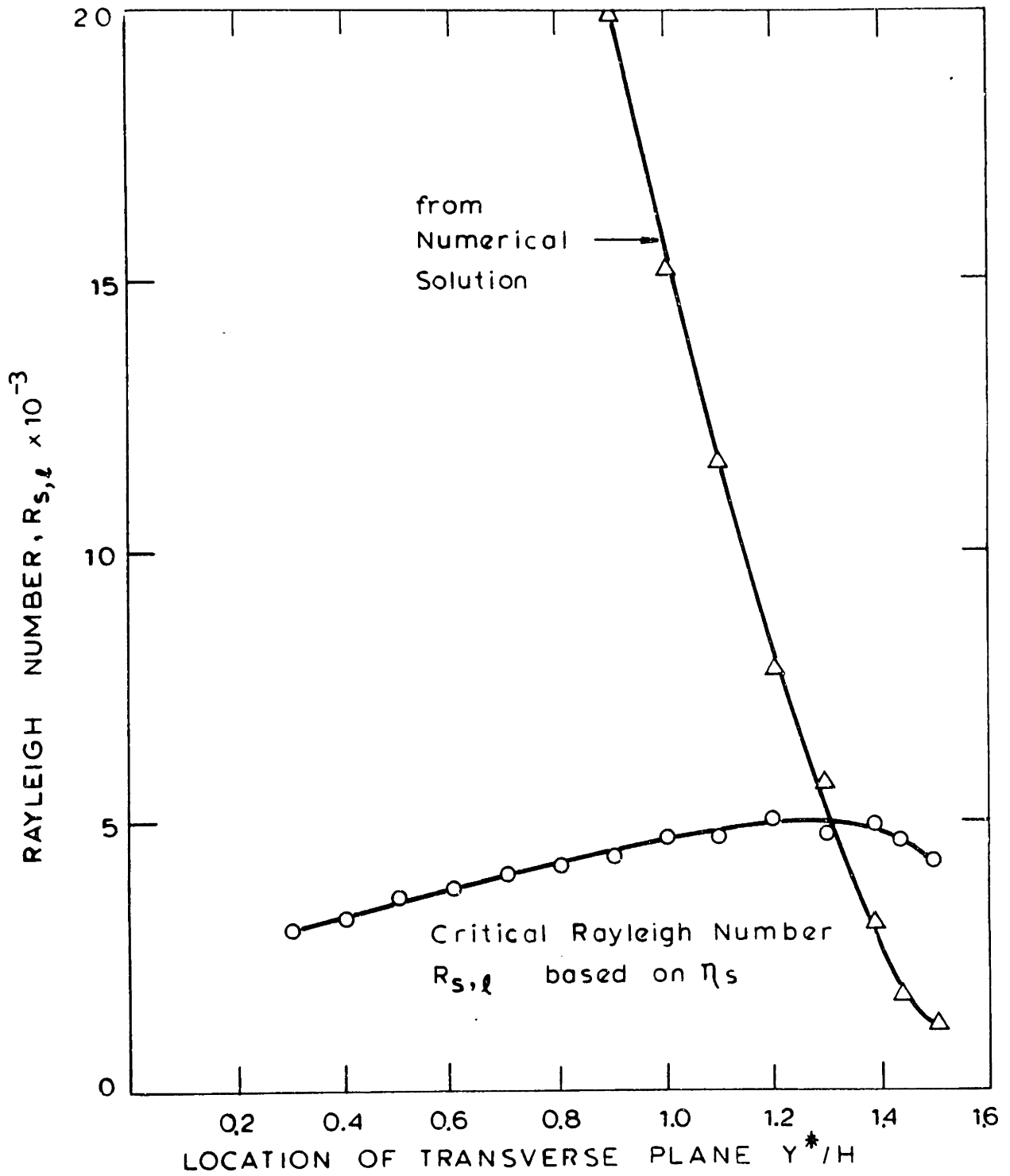


Figure 1.26 Prediction of the Onset of Roll Motion from Numerical Solution Two - Dimensional

Figure 1.27. The generalized stability curve of Figure 1.23 provides the critical wave number for each transverse plane, when the parameter η_s is evaluated from the numerical solution. Triangle symbols denote the wave numbers obtained in this way. If a Rayleigh number $R_{s,\ell}$ obtained from the numerical solution is assumed to be at the critical state, the corresponding wave number would be also found from the same generalized curve. Square symbols are used for the wave numbers predicted in this way. The crossing point of the two curves represents the critical state for the numerical solution. The critical wave number is about 2.5 (based on the source depth). Its location is, of course, identical to that predicted in Figure 1.26. In Figure 1.27, circled symbols represent the photographically determined wave numbers. The trend of these data clearly points to the same critical state predicted numerically. Moreover, the numerical prediction based on the $R_{s,\ell}$ (square symbols) prior to the onset point appears as a direct extension of the experimental curve. Interestingly enough, the experimental curve in the finite amplitude regime suggests wavelength elongation compared to the numerical prediction, in spite of the penetrative growth of the roll motion. The results clearly indicate the utility of the two-dimensional numerical solution for predicting the onset of roll motion.

1.6. Rayleigh-Bénard Problem with Large Temperature Dependent Viscosity Variation

In the early stages of this thesis investigation, it was believed that viscosity variations might have a significant impact on the roll motion. For this reason, its effect on the overall circulation and the heat transfer rates of the roll motion was investigated numerically. However, the effect of longitudinal motion was not considered. Thus, the problem is identical

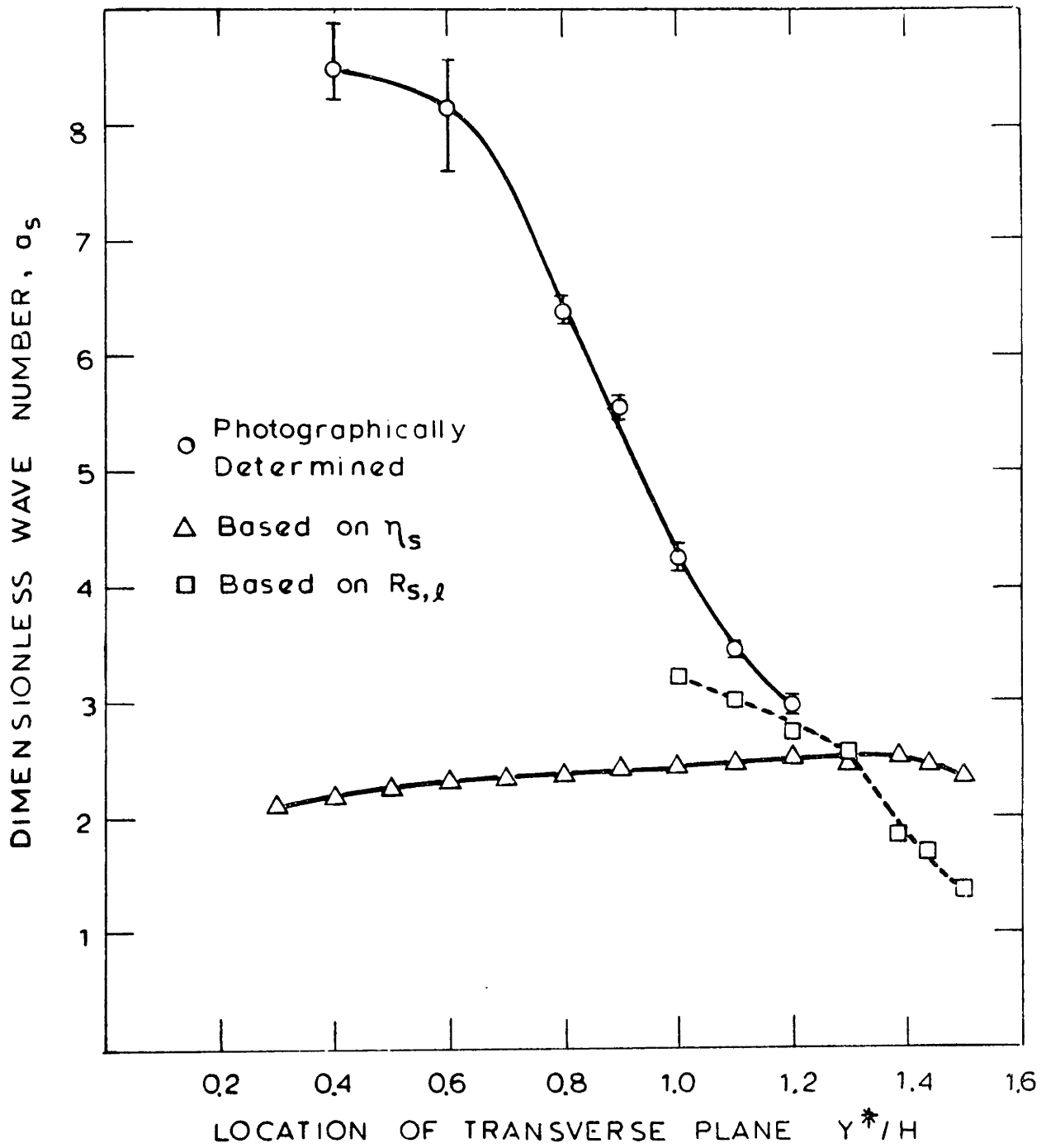


Figure 1.27 Observed Wave Number and Prediction of Critical Wave Number for the Onset of Roll Motion

to the Rayleigh-Bénard problem, except that the viscosity variation is allowed according to equation (1.2). The rigid top and the free bottom boundary surfaces are maintained at specified temperatures (1 and 2 in the dimensionless values, respectively). The Rayleigh number is defined:

$$R_M \equiv \frac{g \cdot \beta \cdot (T_h^* - T_c^*) \cdot H^3}{\nu_M^* \cdot \alpha_0}$$

where

$$\nu_M^* \equiv \sqrt{(\nu_h^* \cdot \nu_c^*)}$$

and the subscripts h and c denote the bottom (hot) and the top (cold) boundaries, respectively. This definition is in contrast to the selection of an arithmetic mean boundary temperature normally adopted for evaluating a reference viscosity, which gives a different Rayleigh number, R_θ . The two Rayleigh numbers are related:

$$R_M = \Gamma^{-1/6} \cdot R_\theta \quad (1.22)$$

where

$$\Gamma \equiv \frac{\nu_c^*}{\nu_h^*} : \text{the Viscosity Ratio number.}$$

The linear stability analysis follows a procedure identical to that described in Section 1.3.1. The major differences are in the boundary conditions and the absence of an internal heat source. Thus, the gradient function, $h(x)$, of the static temperature profile reduces to unity. For the resulting system of perturbation equations, the principle of exchange of stability can be proven to hold, when viscosity is a function of x only. Consequently, the numerical calculations are greatly simplified because all the eigenvalues are real positive, and the power method is applicable to finding the smallest eigenvalue.

The results for the assumed roll cells are summarized in Figure 1.28. It shows that the critical Rayleigh number, R_M , and the critical wave number decrease with increasing viscosity ratio numbers. These critical conditions are used to fix the cell sizes for calculating finite amplitude convection fields by the amplitude specification method. The asymptotic behavior of Nusselt number and the circulation rate is depicted in Figure 1.29. For the constant viscosity case, the result can be directly compared to the modified perturbation solution obtained by F. H. Busse (1967a). He predicted the relationship between the Nusselt number and the Rayleigh number near the critical condition as:

$$(Nu - 1) \frac{R}{R_C} = 1.628 \frac{R - R_C}{R_C}, \quad (1.23)$$

for an infinite Prandtl number fluid. The present result shows exactly the same relationship up to $1.5 R_C$. A noble feature of the new amplitude specification method lies in its capability of predicting even multiple stationary solutions associated with the hysteresis effect. The behavior that convection at a certain Rayleigh number depends on the path of Rayleigh number history is called the hysteresis effect. Figure 1.30 shows that the effect appears when the viscosity ratio number exceeds 100. Notice that the finite amplitude convection can exist even below the critical state (up to $0.965 R_C$ for $\Gamma = 1000$). In the limit of the critical condition, the finite amplitude solution obtained by the method is reduced to a functional shape identical to that predicted by the linear stability analysis.

1.7 Concluding Remarks

The longitudinal roll motion under the sink has been experimentally

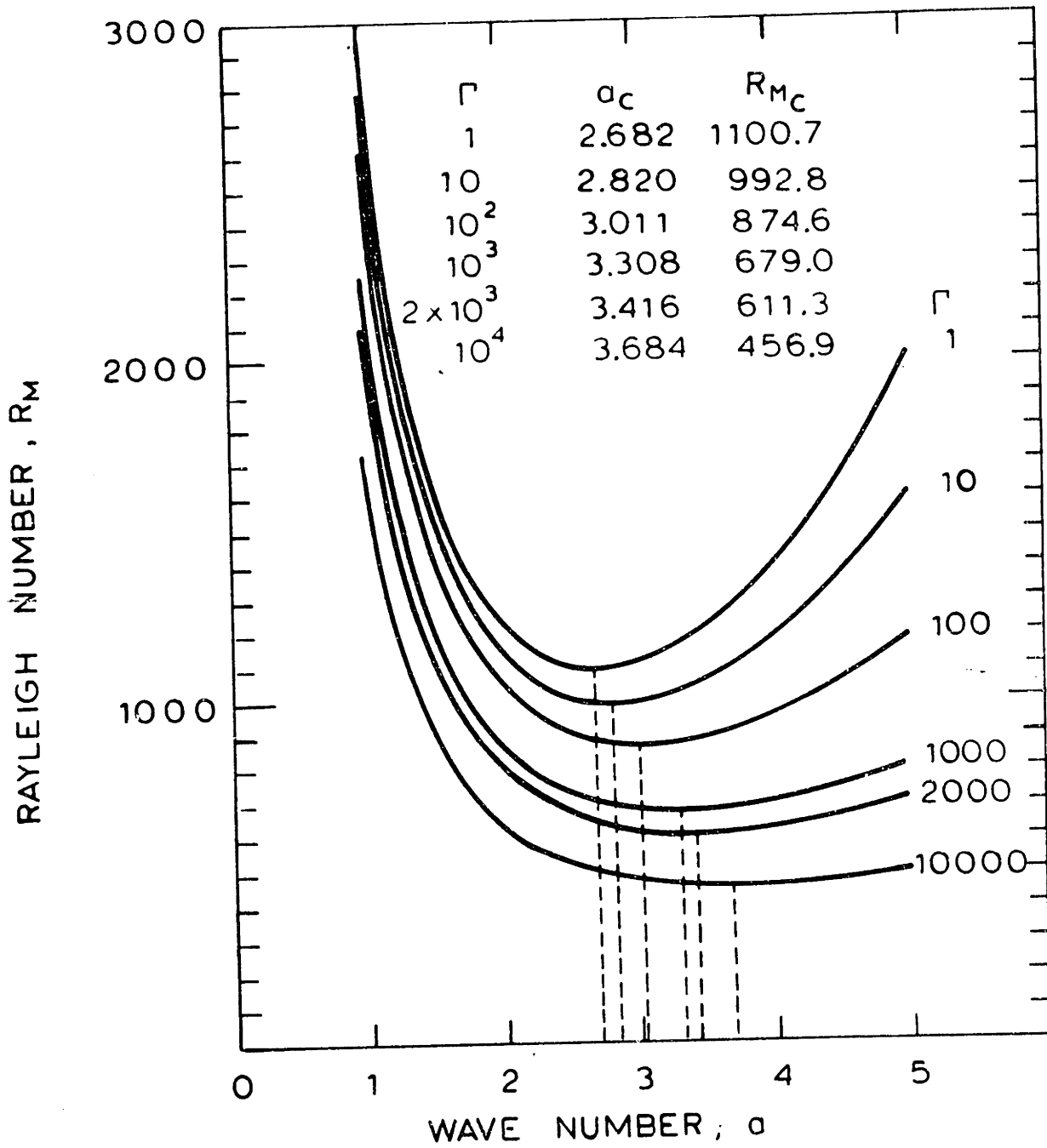


Figure 1.28 Stability Diagram - R_M vs Wave Number at Fixed Viscosity Ratio Number

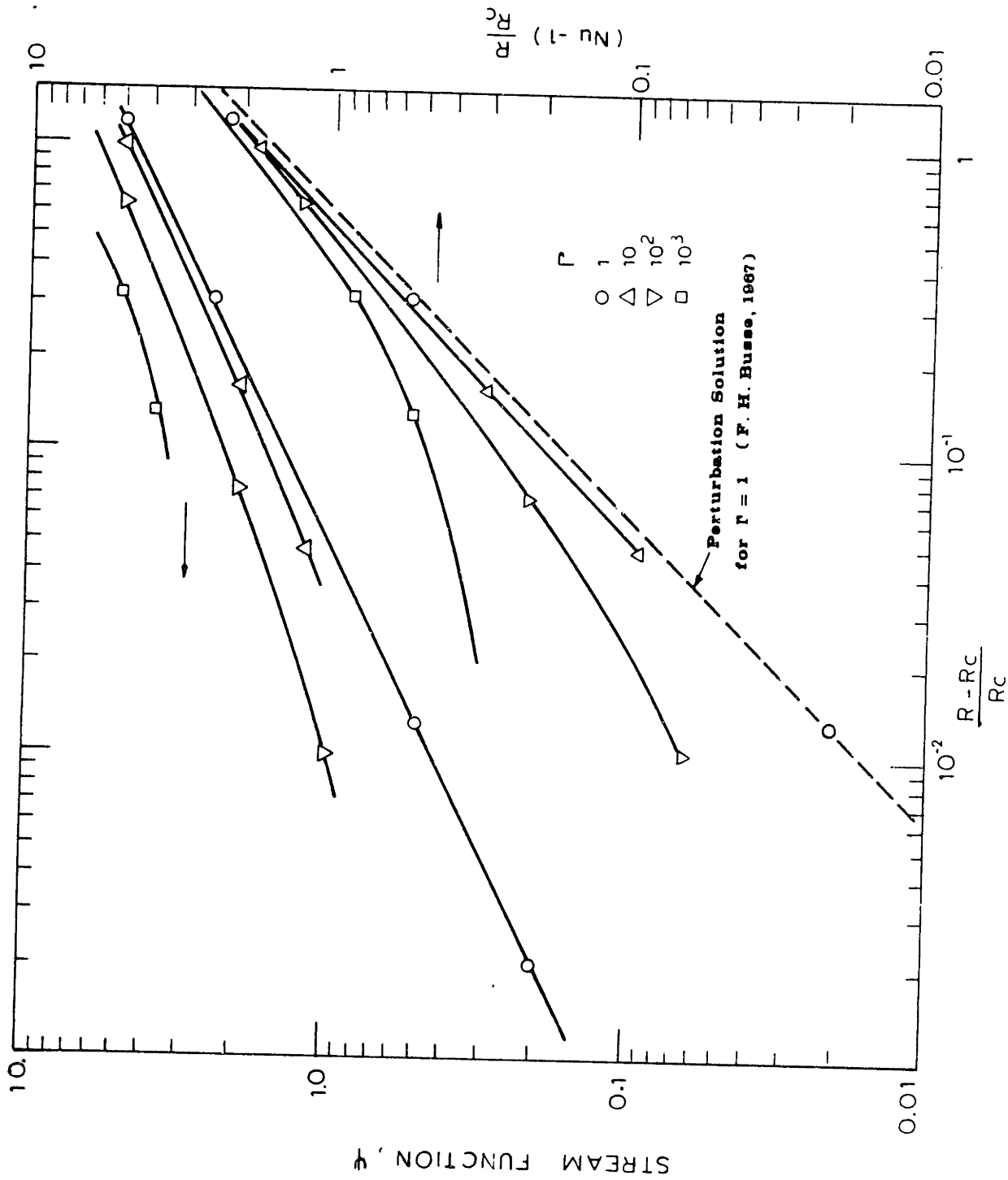


Figure 1.29 Asymptotic Behavior of Nusselt Number and Stream Function

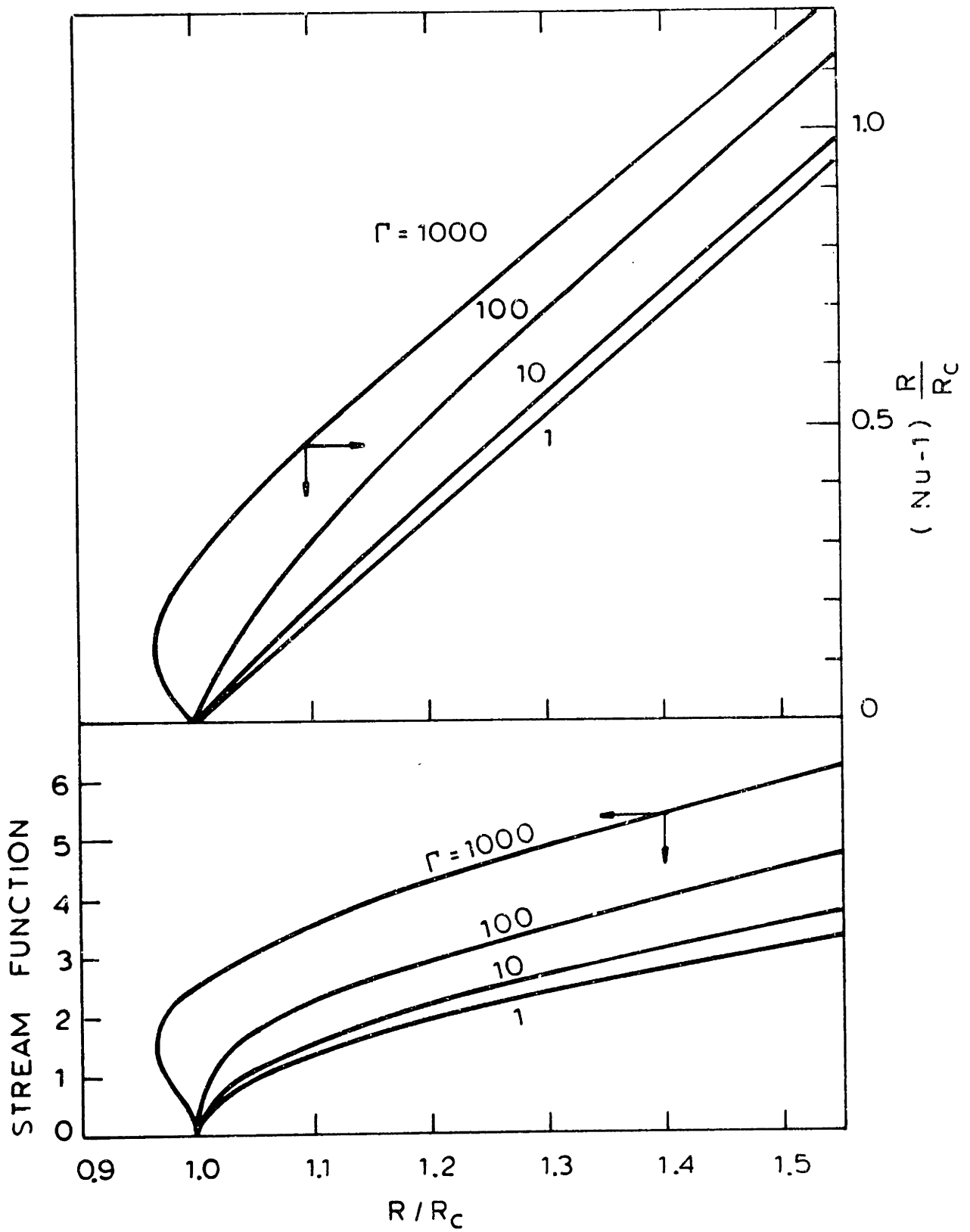


Figure 130 Finite Amplitude Behavior of Nusselt Number and Stream Function

characterized and its onset condition has been predicted by linear stability analysis. An excellent agreement between the experimental and the predicted results has been demonstrated. Thus, the source-sink approximation method can be used for the prediction of onset conditions. A new technique, the amplitude specification method, was developed as an efficient tool to evaluate the finite amplitude convection fields.

II. INTRODUCTION

2.1 Natural Convection Currents in Glass Melts

Nearly all of the world's commercial glass is now produced in large continuous tank furnaces. Of a rectangular bath shape, these may be 30-50 meters long, 6-9 meters wide, 0.9-1.5 meters deep, and contain up to 1300 tons of molten glass with a throughput (pull rate) up to 500 tons/day of product glass. Shown in Figure 2.1 is a sketch of a cross-fired tank furnace with representative convection currents that occur within the glass melt. Raw materials (batch) - a mixture in precise proportions of sand, soda ash, and limestone with oxide additives - are regularly charged through a feed port (doghouse) and form a batch blanket which floats on the melt. The energy required to melt the batch is provided by the combustion of natural gas or oil. The fuel is introduced with preheated air through combustion ports located above the melt surface. The direction of flow through the fuel ports is regularly reversed in intervals of 10 to 20 minutes to enable the use of regenerative heat exchangers for air preheating.

The batch melting process and most of the glass formation reactions (see Appendix A for more details) occur in the batch blanket in less than a couple of hours which is relatively short compared to the long residence time spent by the melts (a few days). During the melting process, enormous volumes of gases are released and the accompanying stirring motion is known to promote partial homogenization of glass components. The resulting glass melt has a density range of 2450-2550 kg/m³ depending on the bubble content (Jebsen-Marwedel, 1959). This contrasts with the original batch bulk den-

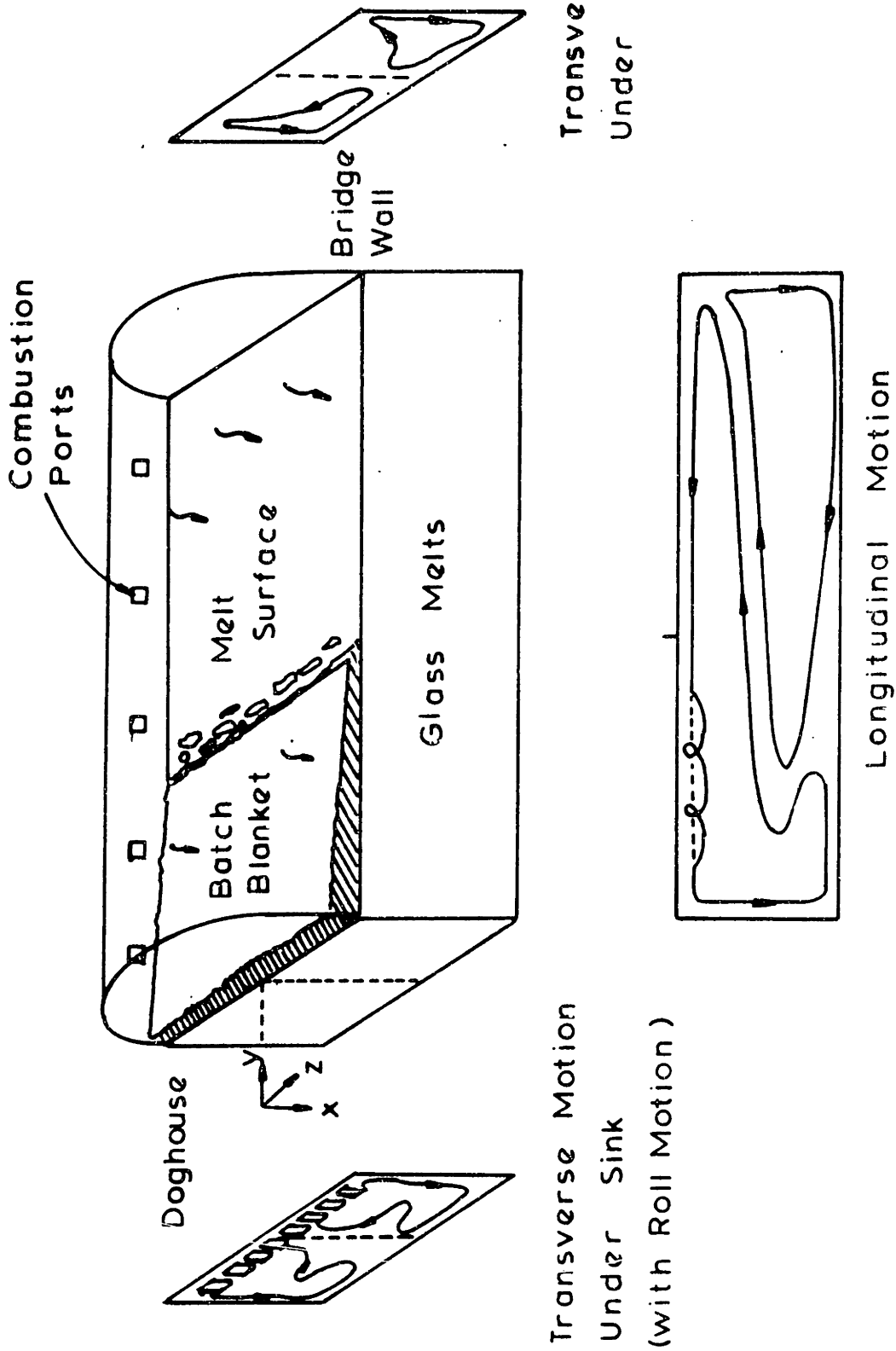


Figure 2.1 Schematic of Glass Furnace Melt Section ; Representative Flow Fields

sity of 1100-1300 kg/m³. Fresh melt enters the bulk under the batch, flows through the furnace, and is withdrawn at the far end for a subsequent forming stage. A long residence time is required to disengage small gas bubbles, to dissolve residual silica grains, and to refine melt inhomogeneities. The large volume of the tank provides for the long residence time.

The continuous glass-making tank furnace was invented in the sixties of the last century. Since then, many mass production processes have been developed and introduced through contributions of the chemist and physicist to the fundamental understanding of glass technology. In spite of major advances in glass technology, difficulties have been experienced in the scale-up of existing furnaces (Günther, 1958). While the glass industry has relied heavily on practical experience in the design and construction of furnaces, the importance of a correct manner of operation has not been overestimated. For example, once optimum operating conditions are determined, operating personnel strive to keep the batch extent at some predetermined position and to maintain steady temperatures at selected points on refractory walls and melt surface through the combined adjustment of feed rate and furnace firing details. The industry has clearly understood that the flow path and temperature history of the glass melt significantly affects the quality of the product. In the absence of mechanical mixing, these are determined by natural convection. The location of a strong heat source and sink along the top surface causes density gradients to exist which derive a large-scale longitudinal circulation pattern. This circulation pattern provides the means to transfer the energy supplied over the free melt surface to the underside of the batch blanket where raw materials

dissolve into the melt. On the other hand, heat losses at the side walls tend to disturb this strong two-dimensional motion. These lateral disturbances are small compared to the longitudinal motion when the side walls are effectively insulated. These are shown in Figure 2.1 as the transverse motions under the batch and the source (melt surface), respectively, which are separated from the longitudinal motion.

The mass transfer processes in the glass melt are least understood due to the lack of a theoretical understanding of the batch melting and its interaction with the glass melt. At the underside of the batch, mass is transferred from several different solid phases into a single liquid phase. While the mass transfer rate will be influenced by any mixing processes, the molecular diffusion will ultimately lead to a homogeneous product. Industry has suggested that the stirring motion due to bubble formation and disengagement is responsible for the mixing. Since the melt leaving the batch is still inhomogeneous in composition and the residual silica grains result in a high local concentration in the melt stream, it was believed that shear stresses produced by velocity gradients in the laminar stream could aid further mixing by stretching out and redistributing the inhomogeneities. However, it has been recently pointed out that an unstable temperature gradient can cause roll motions to develop under the batch. The roll motions (shown as spiral motion in Figure 2.1) can be envisioned as several dozens of screw machines imbedded in the melt stream under the batch. If these exist, they may profoundly influence the heat and mass transfer rates under the batch. The work of this thesis is exclusively devoted to characterize the roll motions.

In the rest of this chapter, previous work done on this problem at M.I.T. will be briefly summarized and a literature survey of the stability problem in natural convection will follow.

2.2 The M.I.T. Program for Flow Simulation in Glass Furnaces

Historically, the convection currents in glass melt had been studied mainly through the physical modeling (Psychés, 1948), until Trier (1965) first published the results of a numerical study which most represented transverse motions in a glass furnace. Since the main convection currents were known to occur along the longitudinal plane, the work was not useful from a practical point of view. The numerical difficulties in dealing with large Rayleigh numbers (order of 10^7 - 10^9 , employing a length scale equal to the liquid depth[¶]) were pointed out in the paper.

A decade of research work in the Department of Chemical Engineering at M.I.T. on numerical modeling combined with some physical modeling has been concerned with predicting the convective currents and accompanying heat transfer within glass melts. To overcome the numerical difficulties, Clomburg (1971) developed an efficient algorithm to solve the biharmonic form of the flow equation, utilizing the alternating direction implicit line over-relaxation scheme. He validated his algorithm by comparing predicted two-dimensional results with measurements of velocity and temperature obtained with an experimental model. He suggested that convection currents along the longitudinal plane in a glass melt were due

[¶] Clomburg (1976) pointed out that the relevant scale should reflect the magnitude of the boundary layer thickness which is only a fraction of the total liquid depth.

principally to the thermal driving force of the coupled heat source and sink. These are influenced negligibly by the effect of the material throughput (mechanical as opposed to thermal). The numerical algorithm of Clomburg has been the basis of subsequent studies on the glass furnace modeling problems.

In an effort to assess the effect of three-dimensional motion in glass melts, the predominance of the flow in the longitudinal plane was exploited to formulate an approximate numerical method (Won, 1974). Motion in transverse planes was predicted by introducing distribution of energy sources and sinks within that plane. The precise distribution, the longitudinal derivative of the energy flux rate, was computed directly from the results of a centerline longitudinal simulation. Since each orthogonal plane was solved by the two-dimensional algorithm, the "source-sink approximation" method provided detailed quantitative results without consuming excessive computational time. It was assumed that the method would be useful when the longitudinal flow was predominant, but predominance was not quantitatively defined.

Gamm (1975) explored the possibility of relating longitudinal plane predictions to expected glass quality. He computed the residence time distributions, the bubble path movement and the silica grain dissolution rates that would be associated with pure two-dimensional motion. An experiment to compare residence time distribution with the predictions exhibited a discrepancy in residence time history. Although minimum residence time was well-predicted, a considerable fraction of the material took a much longer time to pass through the experimental model.

A careful observation showed that roll motions existed under the sink (corresponding to the batch blanket) due to the unstable temperature gradient that existed in that location. Even though the roll motion occupied only a small fraction of the total volume, its mixing effect was so powerful that it was entirely responsible for the observed discrepancy in residence time history.

Curlet (1976) performed an experimental investigation on the effect of three-dimensional boundary conditions on the overall natural convection currents. He showed that the influence of three-dimensionality can be effectively evaluated by the source-sink method. Indeed, predicted results by the method for the transverse planes, as well as the longitudinal planes, were found in excellent agreement with experimental measurements in temperature and velocity. He obtained photographic evidence for the roll motions and attempted to define the onset point of the instability based on the well-known critical conditions of the Rayleigh-Bénard problem. This comparison turns out too simplistic and the photographic procedure is found inadequate to detect the onset point. The definite exposition of the onset criterion of the roll motion constitutes one of the major contributions of the present thesis. On the other hand, he showed that the source-sink approximation method could be extended to predict the wavelength and amplitude of roll motions, if sufficient number of grids were used to resolve the region of interest. Comparison with experimental temperature and velocity data was found satisfactory. Unfortunately, the collected data were limited only to a chosen transverse plane. He also

reported a concise review on glass furnace modeling and the numerical methods relevant to furnace simulation.

2.3 Current Status of Cellular Convection Instability Theory

There are several other physical systems in which a convective instability similar to roll motion under the sink is encountered; namely, earth mantle convection, atmospheric convection, cloud formation, and oceanic circulation. All of these physical phenomena have a common origin in their formation, that is, a thermally-induced flow instability. Much original and penetrating work has been done on the flow instability and the theoretical analysis of more complex related problems is an important area of ongoing research in fluid mechanics. Only the major papers of interest are selected and particular attention has been paid to the convective instability of gravitational cause (opposed to the surface-tension cause, known as Marangoni effect).

Flow motions which break up a fluid layer into a number of regular cellular structures are called cellular convection. Usually steady flow streamlines reflect in their shape the conditions imposed from the outside. However, cellular motion shows a peculiar property that its streamlines are confined to a number of regular cells which are not uniquely determined by the exterior conditions. Nevertheless, it is a stationary solution to the equation of motion. This indeterminacy is not caused by the lack of imposed conditions. Rather, the stationary solution has a bifurcation point in its dependence on a parameter of the problem. Below a critical value of the parameter, the stationary solution is uniquely determined (such as conduction solution at a static state in the Rayleigh-Bénard problem).

Above the value, multiple, even infinite, solutions are possible for a stationary state. Physically realizable solutions may be distinguished from others by investigating the stability of these solutions against disturbances. This is the principal difficulty faced in the theoretical analysis of finite amplitude convection. The current status of research work in this direction will be briefly summarized.

The best known and the best understood natural convection instability problem is the Rayleigh-Bénard problem, whether driven by buoyancy (Rayleigh, 1916) or by surface-tension gradients (Bénard, 1901; Pearson, 1958). The basic method of theoretical analysis, initiated by Rayleigh, is based on the assumption that the first disturbances to the basic motion are infinitesimal so that the equations may be linearized (hence the name of linear stability theory). The problem was thoroughly treated in the papers of Pellew and Southwell (1940) and of Reid and Harris (1958). The most comprehensive treatment of the linear stability analysis is presented in a book by Chandrasekhar, along with an extensive bibliography through 1961. The linear theory provides critical conditions for fluid stability. Above the critical point, linear theory suggests a broad band of horizontal wave numbers associated with a continuous spectrum of unstable modes. (This is contrary to experimentally realized regular cellular structure and its narrower band width of wave number.) A more critical defect of the theory is its inability to predict the amplitude of disturbances. This is a direct consequence of linearization process which results in an eigenvalue problem.

Chemical engineers, geologists and astrophysicists are most interested in the heat transfer enhancement and the structure of the

convection motion which results from the loss of stability. These finite amplitude effects are part of the field of nonlinear stability theory. The theory has received considerable attention in the past from both pure and applied mathematicians due to their interest in studying the nonlinear aspects of partial differential equations. The bifurcation phenomenon, in which one state of flow loses stability to a more stable state when a critical parameter changes, has inspired an interesting view that thermal turbulence motion is a series of discrete transition states (Malkus, 1954). Indeed, an ultimate object of the nonlinear stability theory has been directed to understand the evolution of laminar flow to turbulence in shear flow (Stuart, 1971) and in thermal convection flow (Palm, 1975).

Two different theoretical approaches have been advanced to understand the mechanism involved in the finite amplitude convection fields. One method suggested by Stuart (1960) and independently introduced to a thermal convection problem by Palm (1960) emphasizes the growth of the disturbance amplitude. The other method was first introduced by Malkus and Veronis (1958) to obtain stationary solutions for finite amplitude regime in the Rayleigh-Bénard problem by applying a modified perturbation technique. The essence of the method was elegantly presented by Millman and Keller (1969) for several examples of nonlinear boundary value problems. Major advances in understanding the mechanism of flow instability were reported in the papers of Schlüter et al. (1965) and the subsequent work of Busse (1967a,b). A generalization of the modified perturbation technique made it possible to determine simultaneously the entire spectrum of stationary solutions and to investigate the stability of the different stationary finite amplitude

solutions. These studies showed that the most stable planform of the Rayleigh-Bénard convection problem is two-dimensional roll cells, while the appearance of hexagonal cells is due to the variation of physical properties, for an infinite horizontal layer of fluid. Busse (1967b) provided the definite stability region for finite amplitude roll cells in the Rayleigh-Bénard problem by employing a Galerkin technique. The nonlinear stability theory, including the results of these authors, is presented in a book by Joseph (1967). A third approach, the energy theory of global stability, is also included in the book, as well as an extensive literature review current up to 1976. A wider range of application of interest to chemical engineers can be found in the book of Denn (1975), which also treats nonlinear problems. Tritton's book (1977) deals with the physical aspects of the stability problem.

Recently, thermal convection in a fluid layer with an internal heat source has received considerable attention. The problem, as a variant of the Rayleigh-Bénard problem, is of interest in geophysics, meteorology, and nuclear reactor design. For example, McKenzie et al. (1974) paid special attention to radioactive heat source as one of the driving forces in earth mantle motion. Even though the problem treated in this thesis does not contain any physical heat source, the contribution of longitudinal circulation current to the instability in transverse planes will be treated as a certain distribution of heat source.

The linear stability analysis first appeared in the paper of Sparrow et al. (1964) for a uniform heat source problem with the rigid, isothermal boundary condition. The results indicated that the presence of lower

boundary does not influence the stability of the layer when maximum temperature is sufficiently far removed from the lower boundary. Tritton and Zarraga (1967) performed a qualitative experiment using as a heat source the ohmic dissipation of an alternating electrolyte current. The bottom boundary was insulated to eliminate side effects and Rayleigh number range $4 R_C$ to $80 R_C$ was investigated. The observed motion was predominantly hexagonal cell and surprisingly, its motion at the cell center was downward, contrary to the case of the Rayleigh-Bénard problem. Furthermore, wave elongation was noticed. A theoretical study of the experiment was reported by Roberts (1967) for linear stability and finite amplitude analysis. The downward motion of hexagonal cell was correctly predicted, but wavelength elongation could not be predicted. Tveitereid and Palm (1976) reexamined the stability of hexagonal cell, employing the modified perturbation method. The only stable mode of finite amplitude convection was found to be the hexagonal cell ($R < 15 R_C$). (This is contrary to Roberts' finding which predicted that two-dimensional roll form is also a stable mode.) Again, the narrow band of the stability region around critical wavelength did not explain the observed wavelength elongation. Tveitereid (1978) performed a similar analysis for a constant temperature bottom boundary. In this case, the stability region for hexagonal cells ranged only up to $3.5 R_C$ (compared to $15 R_C$), while its wavelength band again indicated a decreasing trend in size. An extensive review of the wavelength elongation in experiments is found in Koschmieder (1974).

The internal heat source problem differs mathematically from the ordinary Rayleigh-Bénard problem, in its nonlinear static temperature

profile. The effect of this nonlinearity must be clearly pronounced near the critical condition. To examine this effect, Krishnamurti (1968) performed an intriguing experiment to confirm her theoretical analysis based on the modified perturbation method. A nonlinear mean temperature profile was established by a steady constant rate of change in the boundary temperatures. Depending on the history of the temperature change, the mean temperature profile played the role of either a heat source or a sink. As predicted, hexagonal cells were observed and the finite amplitude instability at subcritical region exhibited the so-called hysteresis effect. The fact that the convection at a certain Rayleigh number range (less than the critical value predicted by the linear theory) depends on the way in which the Rayleigh number has been reached is called the hysteresis effect in the literature. Therefore, the effect usually manifests two distinct steady states with one intermediate unstable state at a given Rayleigh number. Either of two steady states can be attained depending on the initial condition. Whitehead and Chen (1970) investigated the effect of various nonlinear static temperature problems. They found that when the unstable layer is confined by the underlying stable layer, the convection motion shows a penetrative behavior.

Another problem relevant to this thesis work is the effect of viscosity variations in the fluid layer on cellular motion, because glass in a melt may vary in viscosity by several orders of magnitude over the range of expected temperature in glass furnace tank. The problem will be separately treated in Chapter VII, as a variation of the Rayleigh-Bénard problem. One motivation of past investigation for the effect of viscosity on cellular motion was to explain preference of the hexagonal structure near the critical

point. Palm (1960) studied the effect of small viscosity variation in this context. The most comprehensive study was reported by Busse (1967a) to include the general effect of temperature dependent material properties. The results of these study show that hexagonal cells are the preferred mode in a certain range of supercritical Rayleigh numbers and that a hysteresis behavior in heat transfer is associated with the hexagonal cells. However, the results were restricted to small viscosity variations, mainly due to the nature of the analytic perturbation techniques used to solve the problem.

Recently, several attempts, both experimental and numerical, have been made to investigate the effect of large viscosity variations on the cellular motion. Foster (1969) solved numerically a time dependent theoretical model with variable viscosity and internal heat source to speculate on the history of the earth's mantle convection. Richter and Parsons (1975), based on experimental observation, suggested a small scale motion in longitudinal shear flow to explain the higher heat flux at the earth's surface than that predicted by Rayleigh-Bénard cell. Peychés and Zortea (1971), on somewhat dubious grounds, suggested glass tank as a model for the earth's mantle convection. Booker (1976) measured heat flux experimentally for viscosity variations up to a 300 fold change. He presented a purely empirical formula for the heat flux - Rayleigh number relationship. In a subsequent paper (Booker and Stengel, 1978), a new relationship was suggested after the authors realized that the critical Rayleigh number is dependent on the viscosity variation in the fluid layer. Anomalous high heat transfer data were reported for a high viscosity ratio number at a relatively low Rayleigh number.

Torrance and Turcotte (1971) obtained numerical solutions for two-

dimensional roll cells in an infinite Prandtl number fluid with an exponential viscosity variation. Using free surface boundary conditions, they choose the wavelength of the roll cell as the critical wavelength for a constant viscosity fluid. One of their numerical results is of special interest to this thesis work. Having started with a static isothermal initial condition for a Rayleigh number six times greater than the critical, they obtained, as a final solution, the conduction solution. Moreover, the number of iterations spent for the solution was reported four times greater than that for the correct final solution, which was obtained starting from the perturbed conduction solution at the same Rayleigh number. Liang et al., (1969) performed experiments in a cylindrical container to confirm the bifurcating solutions predicted through perturbation expansion. Numerical computations were also performed to predict the flow pattern by a finite difference scheme. Even though qualitative agreement was obtained, they reported specifically the difficulties encountered in obtaining finite difference solution near the critical states. This convergence problem has been resolved by a new technique, called the amplitude specification method, which is presented in Chapter VII.

It appears that the theoretical tools are indeed powerful for predicting the occurrence of various instability phenomena and providing information for the structures of cellular motion near the critical conditions. In the finite amplitude convection regime well beyond the critical conditions, the problems becomes fluid dynamics and numerical solution of the flow equations provides necessary information for the flow and temperature. In spite of the proliferation of research papers, no theoretical results exist which could be directly applied to the problem treated in this thesis. One of the

most unique features of the problem is that the instability phenomenon of the experimental roll motion is confined to a part of the longitudinal circulation current and the basic flow field is two-dimensional and of the recirculating nature. Consequently, the entire system exhibits an onset, a growth and a consolidation stage of the instability phenomenon altogether. Nevertheless, the entire flow motion exhibits a remarkable steady state behavior.

Finally, it should be mentioned that other research results which have direct bearing on the present work will appear throughout the text.

III. MATHEMATICAL FORMULATION OF THE NATURAL CONVECTION PROBLEM

When a fluid in an enclosure is subject to heating, internal or external, density gradients are induced due to a thermal expansion of the fluid. Under the influence of gravity, the density gradients will result in buoyancy forces. If the gravitational potential is in a stable orientation, the fluid tends to stratify itself thermally. Otherwise, motion will be generated to redistribute fluid so as to correct the potentially unstable field of density gradients. The fluid motion thus generated is called natural or free convection. It must be pointed out that the unstable orientation of density gradients in fluid is not a sufficient condition to induce the motion, because the tendency to a motion can be inhibited by the dissipative effects of fluid viscosity. The unstable density gradients which are maintained in the fluid must exceed a certain value before the instability can manifest itself as a convective motion. The principal theoretical question of determining the critical condition has been successfully treated by stability theory for a few simple problems.

In particular, the stability theory of cellular convection, such as Bénard convection, has been used with considerable success to understand the responsible physical processes involved in instability phenomenon. That very success has been founded on the fact that exact analytic solutions exist for the base state. Various mathematically sophisticated approaches have been possible. The modified perturbation technique has been particularly successful. A direct application of the technique to a

problem requires a correct zeroth order solution. Unfortunately, the problem considered in this thesis has the peculiarity that the instability phenomenon is only confined to a part of the overall convection motion. A search for an exact analytic solution for the overall motion is futile. If an approximate solution were known, the problem would require an examination of its stability in the entire motion, but instability should occur only in the region of the roll motion. The recirculating nature of the overall flow makes such an approach hopeless. Nevertheless, it seems possible to take some advantage of the basic directionality of the overall flow. In this chapter, the basic equations will be presented, which govern both the overall convection flow and the convective instability.

3.1 The Governing Equations for Natural Convection

The equations which describe general thermal convection are the continuity equation, the Boussinesq form of the Navier-Stokes equations, and the energy equation:

Continuity Equation:
$$\nabla \cdot \bar{V}^* = 0$$

Boussinesq Form of Momentum Equations:
$$\rho_0 (\partial_t \bar{V}^* + \bar{V}^* \cdot \nabla \bar{V}^*) = -\nabla p^* + \rho \bar{g} + \nabla \cdot \mu^* [\nabla \bar{V}^* + \nabla \bar{V}^{*T}] \quad (3.1)$$

Energy Equation:
$$\rho_0 c_p (\partial_t T^* + \bar{V}^* \cdot \nabla T^*) = \nabla \cdot \kappa_e \nabla T^* .$$

The Boussinesq approximation takes advantage of simplifying features which characterize thermal convection:

- (1) the density variations are neglected except in the body-force terms of the momentum equations; these are induced by change of temperature, but not by pressure; and,

(2) viscous dissipation is assumed negligible.

It was first used by Oberbeck (1888) in his study of the atmospheric Hadley regime.

The incompressible form of the continuity equation is a direct consequence of the first assumption. In turn, this simplifies the expression for deviatoric stress tensor (see Batchelor (1960), Chapter 3), that is,

$$2\mu^* \left\{ \frac{1}{2}(\nabla\bar{V}^* + \nabla\bar{V}^{*\top}) - \frac{1}{3}(\nabla \cdot \bar{V}^*)\delta_{ij} \right\} = \mu^*(\nabla\bar{V}^* + \nabla\bar{V}^{*\top})$$

The second part of the first assumption means that density change of single phase pure material is described as

$$\begin{aligned} \rho &= \rho_0 \left\{ 1 + \frac{1}{\rho_0} \left(\frac{\partial \rho}{\partial T^*} \right)_{p_0^*} (T^* - T_0^*) + \frac{1}{\rho_0} \left(\frac{\partial \rho}{\partial p^*} \right)_{T_0^*} (p^* - p_0^*) \right\} \\ &\approx \rho_0 \{ 1 - \beta(T^* - T_0^*) \} \end{aligned}$$

where β is the coefficient of thermal expansion. The value of β for glycerine is $1.5 \times 10^{-4} \text{ K}^{-1}$ which should be compared with its compressibility of $2.2 \times 10^{-5} \text{ atm}^{-1}$. As implied, the origin of the Boussinesq approximation is due to the smallness of the coefficient of thermal expansion and the large gravitational constant acting on it, when the motion is of thermal origin. See Tritton (1977) for details.

Temperature variation of viscosity and thermal conductivity may be allowed, particularly in the case of a glass melt problem. In glass melts, thermal conductivity is greatly enhanced by radiative transport. Estimates using a Rosseland mean absorption coefficient indicate that the effective

thermal conductivity is roughly a linear function of temperature in the range of interest (Hottel and Sarofim, 1967). However, its usage requires a modified treatment at boundaries (Clomburg, 1971). In the experiment, it is assumed constant for glycerine. The specific viscosity-temperature relationship of interest is chosen as that empirically found to describe the behavior of many fluids:

$$\mu^* = \mu_0^* \text{EXP} \left[E \left(\frac{1}{T^*} - \frac{1}{T_0^*} \right) \right] . \quad (3.2)$$

The coordinate system is chosen such that the gravity vector points to the direction of positive x coordinate. Then, the complete set of equations governing convection motion becomes

$$\begin{aligned} \nabla \cdot \vec{V}^* &= 0 \\ \partial_t \vec{V}^* + \vec{V}^* \cdot \nabla \vec{V}^* &= -\nabla \Pi^* - g\beta T^* \hat{i} + \nabla \cdot \nu^* (\nabla \vec{V}^* + \nabla \vec{V}^{*T}) \quad (3.3) \\ \partial_t T^* + \vec{V}^* \cdot \nabla T^* &= \alpha_0 \nabla^2 T^* , \end{aligned}$$

where Π^* is the deviation of the pressure from the hydrostatic pressure corresponding to the reference property temperature T_0^* :

$$\Pi^* = \frac{p^*}{\rho_0} - g(1 - \beta T_0^*) \cdot x .$$

3.1.1 Equations in Dimensionless Form

The system of equations is cast in dimensionless form for general parameteric study. The dimensional variables

$$\{ t^*, \bar{x}^*, T^*, \Pi^*, \vec{V}^*, \nu^* \}$$

are divided by the reference scale factors:

$$\left\{ \frac{\ell^{*2}}{\alpha_o}, \ell^*, T_R, \frac{\mu_o^* \alpha_o}{\ell^{*2}}, \frac{\alpha_o}{\ell^*}, \nu_o^* \right\},$$

where $\alpha_o \equiv \frac{\kappa_o}{\rho_o c_p}$ is a thermal diffusivity and $\nu_o^* \equiv \frac{\mu_o^*}{\rho_o}$ a kinematic viscosity. The scale factors for length and temperature are to be chosen later according to the specific problem requirements. See Table 3.1 for summary. The subscript, o, denotes the physical properties evaluated at a chosen temperature, T_o .

Then, the dimensionless equations become

$$\begin{aligned} \nabla \cdot \bar{V} &= 0 \\ P^{-1}(\partial_t \bar{V} + \bar{V} \cdot \nabla \bar{V}) &= -\nabla \Pi - RT \hat{i} + \nabla \cdot 2\nu \bar{D} \\ \partial_t T + \bar{V} \cdot \nabla T &= \nabla^2 T, \end{aligned} \quad (3.4)$$

where the dimensionless parameters are defined as

$$\begin{aligned} \text{Prandtl number: } P &\equiv \frac{\nu_o^*}{\alpha_o} \\ \text{Rayleigh number: } R &\equiv \frac{g \cdot \beta \cdot T_R \cdot \ell^{*3}}{\nu_o^* \cdot \alpha_o}, \end{aligned}$$

and the deviatoric stress tensor is expressed in terms of deformation tensor

$$\bar{D} \equiv \frac{1}{2} [\nabla \bar{V} + \nabla \bar{V}^T] \quad \text{¶} \quad (3.5)$$

¶ Throughout the thesis, vectors are denoted by a single overline and Cartesian tensors, dyads and matrix by a double overlines.

TABLE 3.1

Reference Scales for Various Rayleigh Numbers

Definition:
$$R \equiv \frac{g\beta T_R \ell^{*3}}{v_o^* \alpha_o}$$

Rayleigh Numbers	Reference Scales			Remarks
	T_R	ℓ^*	v_o^*	
R	$\frac{q_F^* \cdot H}{\kappa_o}$	H	v_o^*	Enclosure Model (Chapter V)
$R_{S,\ell}$	$\frac{S_m^* \cdot \ell_s^{*2}}{\alpha_o}$	ℓ_s^*	v_o^*	Internal Source (Chapters IV, VI)
$R_{T,\ell}$	$T_m^* - T_s^*$	ℓ_t^*	v_o^*	Internal Source (Chapters IV, VI)
R_M	$T_h^* - T_c^*$	H	$\sqrt{v_h^* \cdot v_c^*}$	Variable Viscosity (Chapter VII)
R_θ	$T_h^* - T_c^*$	H	v_θ^*	Variable Viscosity (Chapter VII)

Moreover, the viscosity law becomes

$$\nu \equiv \frac{\nu^*}{\nu_0^*} = \text{EXP} \left[\gamma \left(\frac{1}{T} - \frac{1}{T_0} \right) \right] \quad (3.6)$$

with the viscosity exponent: $\gamma = \frac{E}{T_R}$.

Boundary condition for the problem are

for temperature:

$$\begin{aligned} T &= T_s && \text{on } \Sigma_s \\ -\partial_x T &= q_F && \text{on } \Sigma_m \\ \bar{n} \cdot \nabla T &= N(T - T_A) && \text{on } \Sigma - \Sigma_s - \Sigma_m, \text{ and} \end{aligned} \quad (3.7)$$

for velocity:

$$\bar{V} = 0 \quad \text{on } \Sigma,$$

where Σ denotes enclosure surface, which is divided into the (simulated) batch sink (s), the melt surface (m), the side walls and the bottom, and \bar{n} denotes unit vector inward normal to the enclosure surfaces. In a glass furnace, the melt surface is shear free. The boundary conditions introduce two dimensionless parameters:

heat flux on melt surface: $q_F \equiv \frac{q^* \ell^*}{\kappa_0 T_R}$, and

Biot modulus: $N \equiv \frac{U^* \ell^*}{\kappa_0}$.

Biot modulus can have different values for different surfaces. An additional parameter, T_A , appears to reflect the ambient temperature.

Since a three-dimensional solution is impractical, we resort to a two-dimensional approximation solution. For the two-dimensional case, it is convenient to introduce stream function concept,

$$\bar{\psi} = \psi \bar{n} \quad (3.8)$$

where \bar{n} is the unit normal vector to the assumed two-dimensional planes. Then velocity and vorticity can be expressed in the form

$$\bar{V} = \nabla \times \bar{\psi} \quad (3.9)$$

$$\bar{\omega} = - \nabla^2 \psi \bar{n}$$

using the two-dimensional Laplacian.

3.2 Nature of the Physical Problem

In the previous experimental simulations of convection motion in glass melts (Gamm, 1975 and Curlet, 1976), spiral motion in the form of longitudinal roll cells were observed under the isothermal batch sink. As in the case of Rayleigh-Bénard roll cells, the origin of this instability is the unstable temperature gradient in the region. As the cells develop along the main flow direction, they show a penetrating growth in depth, while the lateral or transverse motions maintain a remarkable stability in their wavelength and regularity. If the same phenomenon can occur in a glass furnace, it might have a profound influence on the furnace operation. The principal concern of this thesis is to provide definite exposition on the roll cell phenomenon for its origin and onset conditions,

as well as its consequence. Fortunately, much original and penetrating work has been done on other thermal convection problems. Some of the results are relevant to this problem.

3.2.1 Description of the Overall Convection Motion

In the experimental models, a highly viscous fluid (glycerine) is contained in a shallow rectangular enclosure. The primary heat source and isothermal sink, located on the top horizontal surface, causes a circulation current of boundary layer nature close to the surface. Much of the core (below the circulation current) is largely motionless and isothermal, but may exhibit a weak countercurrent circulation depending on the other boundary conditions. A laterally uniform condition on the boundaries ensures that the resulting longitudinal circulation cell is largely two-dimensional.

Strong thermal stratification develops in the fluid of circulation current. Under the source, fluid is stably stratified and energy is being conducted downward from the boundary. To accept this energy, fluid is being entrained upward into the boundary layer at a nearly uniform rate. Fluid in the boundary layer moves toward the sink. Its horizontal velocity increases rapidly as the boundary layer thickness decreases slightly near the leading edge of the sink. An inner thermal boundary layer develops from the leading edge of the sink, as the hot fluid is cooled from above. Therefore, there appears suddenly a thermally unstable fluid stratification in the boundary layer. Meanwhile, fluid continues to be entrained into the layer up to a circulation cell center (eye), which normally appears near the upper left corner close to the doghouse. The flowing fluid then turns

downward and returns to form a recirculating current, rather than descending along the entire doghouse wall. This return flow is being entrained into the boundary layer, as described above.

3.2.2 Origin of Convective Instability

The boundary layer flow under the sink is always subject to cooling from both above and below. The stronger cooling from above develops the gravitationally unstable orientation of fluid density. The resulting temperature profile is nonlinear due to the current of boundary layer nature. As the boundary layer current proceeds across the leading edge of the sink, the maximum temperature point in the current begins to penetrate into the currents. On the other hand, the continuous cooling from above reduces its temperature difference from the sink temperature. When the combined effect of these two competing factors is strong enough to overcome the effect of viscous dissipation, convective instability manifests itself in the form of advective longitudinal roll motions.

In his study of roll motions, Curlet (1976) observed that maximum horizontal velocity over the region does not deviate much from the predicted two-dimensional motion, but temperature profiles in the core region show a constant displacement lower than that predicted. This suggests that the most energetic disturbances are independent of the basic longitudinal direction of the current and the principal instability mechanism might be of pure thermal origin (opposed to the so-called shear mode of instability due to the self-interaction of basic velocity profile).

This observation is perhaps not unexpected. In the heated plane

Couette flow problem, the most unstable disturbance is known to be independent of the direction of the basic motion (Joseph, 1966). It follows that the presence of shear flow gives the problem a basic directionality. The preference for longitudinal rolls was perhaps first pointed out by Kuo (1963). A linear analysis of the problem was performed by Deardroff (1965) using a finite-difference technique. The stabilizing effect of shear becomes increasingly strong with increasing Prandtl number. Linear analysis shows that instability has a pure thermal origin due to the intrinsic stability of plane Couette flow. On the other hand, linear analysis of the heated plane Poiseuille flow problem (Gage and Reid, 1965) indicated that a sharp transition is possible from a thermal mode of instability to a wave type instability. However, at low shear rates, thermal mode of instability is still dominant in the form of longitudinal rolls. Recently, a thermally-driven shear flow heated from below was analyzed by Weber (1978). The problem bears a close resemblance to the longitudinal circulation current in this thesis. Weber found that the main instability mechanism is of a thermal origin and that the preferred mode of the disturbance is determined by the effect of shear. It is interesting to note that longitudinal rolls were found to be the preferred mode at least for the large Prandtl number fluid.

In all of these studies, it was important that the correct first order base solution was available in analytic form. This is necessary, if one wishes to perform a theoretical analysis of nonlinear interaction problem, such as the modified perturbation theory. The enclosed system of this thesis does not possess a closed form of basic solution, due to the peculiar boundary conditions and the effect of the recirculating flow.

(An exception is the case where the boundary conditions are simple harmonic functions such as that reported by McKenzie, Moore, and Weiss, 1974.) In this regard, any attempt at an exact analysis to the problem would be a formidable, if not hopeless task. Moreover, the overall mechanism of convection motion in the problem is clearly one of a feedback system, where the boundary layer flow-core interaction is further complicated by the occurrence of the "localized" roll motions. Accordingly, some simplifications were introduced to analyze the onset condition of the roll motions. As such, the source-sink approximation method deserves a review.

3.3 The Source-Sink Approximation Method

The method has been developed as a heuristic approach to a three-dimensional natural convection problem by iterative solution procedure of coupled complementary two-dimensional problems (Won, 1974). Further description with the underlying assumptions can be found in the thesis by Curlet (1976), where extensive comparison with experimental data was also presented. The essence of the method lies in the decomposition of flow motion into the two sets of orthogonal planes, the longitudinal planes and the transverse planes.

The flow motion in each plane is obtained by solving the system of equations

for the longitudinal plane:

$$J_k(\theta, \psi) - \nabla_k^2 \theta = - \partial_x^2 \tilde{\theta} - \{ J_j(\tilde{\theta}, \tilde{\psi}) - \nabla_j^2 \tilde{\theta} \} \equiv SI_L$$

$$P^{-1} J_k(\theta, - \nabla_k^2 \psi) = Ra_y \theta + \nabla_k^4 (-\psi) \quad (3.10)$$

for the transverse plane:

$$\begin{aligned}
 J_j(\tilde{\theta}, \tilde{\psi}) - \nabla_j^2 \tilde{\theta} &= - \partial_x^2 \theta - \{ J_k(\theta, \psi) - \nabla_k^2 \theta \} \equiv SI_T \\
 P^{-1} J_j(\tilde{\theta}, - \nabla_j^2 \tilde{\psi}) &= R \partial_z \tilde{\theta} + \nabla_j^4(-\tilde{\psi})
 \end{aligned} \tag{3.11}$$

where J denotes a two-dimensional Jacobian independent of the component appearing in the index (j or k) and the tilde differentiates the transverse plane variables from the longitudinal. Two-dimensional Laplacians are defined as

$$\begin{aligned}
 \nabla_j^2 &\equiv \partial_x^2 + \partial_z^2 \\
 \nabla_k^2 &\equiv \partial_x^2 + \partial_y^2 .
 \end{aligned}$$

The right hand side of each energy equation defines energy source-sink functions. Physically, this represents the energy transfer contributed to a specified plane, when an advection current orthogonal to the plane passes through it. Since this contribution cannot be evaluated a priori, the computations are started with a representative longitudinal section for which the z average source-sink function is initially estimated from the wall heat losses. The longitudinal solution is then employed to estimate the source-sink functions for various transverse planes. In this way, the estimations are progressively improved. If completely converged, the final solution would result $\theta \approx \tilde{\theta}$ at the cross section of the two planes, but the stream functions are determined as completely independent entities.

Curlet (1976) extended the method to predict the roll motions in the transverse plane. The result showed that the predicted amplitude and wavelength of the roll motions are in good agreement with the experimental

data, even though limited only in one transverse plane. This surprising observation eventually led to a basis for formulating the linear analysis of the onset condition of the roll motion by utilizing the source-sink approximation method.

IV. THE THEORY OF STABILITY ANALYSIS

The theoretical framework of linear stability and finite amplitude convection is presented in this section. The linear stability theory will be applied for the longitudinal roll motion observed in the experiment (Chapter V) and its prediction will be critically tested against the experimental data (Chapter VI). A new method for predicting finite amplitude convection via finite difference procedure is formulated to obtain a Rayleigh number corresponding to a specified amplitude for the convection fields. This amplitude specification method will be applied to a Rayleigh-Bénard problem to assess the effect of large viscosity variation (Chapter VII).

In Chapter III, it was pointed out that transverse motion can be well represented using the heat source-sink distributions (determined from longitudinal computations) imbedded in that plane. In the experiment, a cross section of a transverse plane shows a strikingly regular vortex structure consisting of more than 25 pairs of roll cells under the sink. Moreover, the calculated distributions show that strong sources exist under the sink region. Therefore, the problem can be attacked through investigating the stability of an infinite fluid layer with nonlinear heat source distributions. Specifically, the stability of the transverse flow is examined, rather than the longitudinal flow, to predict an onset condition for the longitudinal roll motion. No attempt is made to explain why the longitudinal cell structure is preferred.

4.1 Linear Stability Analysis

Consider a fluid layer of an infinite horizontal extent. The layer is assumed as heated internally by a horizontally uniform heat source $Q^*(x)$ { (energy)/(Volume)(time) }. Moreover, the layer is bounded above by a rigid, perfectly conducting surface at constant temperature, T_s , and below by a rigid plane with the mixed type heat flux condition. Then the basic equations can be written

$$\begin{aligned} \nabla \cdot \bar{V} &= 0 \\ \rho^{-1}(\partial_t \bar{V} + \bar{V} \cdot \nabla \bar{V}) &= -\nabla \Pi - R_s T \hat{i} + 2\nabla \cdot \nu \bar{D} \\ \partial_t T + \bar{V} \cdot \nabla T &= \nabla^2 T + F \end{aligned} \quad (4.1)$$

with the boundary conditions

$$\begin{aligned} \bar{V} = 0 \quad T = T_s \quad \text{at } x = 0 \\ \bar{V} = 0 \quad -\partial_x T = N(T - T_A) \quad \text{at } x = 1 \end{aligned} \quad (4.2)$$

where

$$R_s \equiv \frac{g \cdot \beta \cdot S_m^* \cdot H^5}{\nu_o^* \cdot \alpha_o^2}$$

The normalized source function, F , has a unit maximum value and is defined

$$F(x) \equiv \frac{S^*(x)}{S_m^*} \quad (4.3)$$

where the dimensional source distribution is a function of x only

$$S^*(x) \equiv \frac{Q^*(x)}{\rho_o c_p}$$

with its maximum adiabatic heating rate, S_m^* , within the layer. Clearly, the reference scales chosen for the internal source problem are

$$T_R = \frac{S_m^* H^2}{\alpha_0} \quad \text{and} \quad \ell^* = H \quad (4.4)$$

with the depth of fluid layer being H . If no source exists in the layer, a different reference scale for T_R should be chosen to define an appropriate Rayleigh number, R .

When the heat generated, S_m^* , is sufficiently small, the layer will be in a static state and the heat transfer will be in a conduction mode. Thus this static state satisfies

$$\begin{aligned} \bar{V}_{SS} &= 0 \\ \nabla \Pi_{SS} + R_S T_{SS} \hat{i} &= 0 \\ D^2 T_{SS} + F &= 0 \end{aligned} \quad (4.5)$$

with the boundary conditions

$$T_{SS}(0) = T_S \quad \text{and} \quad -DT_{SS}(1) = N \{T_{SS}(1) - T_A\} .$$

The conduction solution will be

$$T_{SS}(x) = T_S + \int_0^x \left[\int_x^1 F(x') dx' - N \{T_{SS}(1) - T_A\} \right] dx . \quad (4.6)$$

For larger values of S_m^* , convective motion will set in and the layer will be disturbed with perturbation velocity \bar{V} . Temperature will deviate from the static solution with the perturbation temperature defined as:

$$\theta \equiv T - T_{SS} .$$

Then the perturbation variables will satisfy the following system of stability equations:

$$\nabla \cdot \bar{V} = 0$$

$$P^{-1}(\partial_t \bar{V} + \bar{V} \cdot \nabla \bar{V}) = -\nabla \Pi - R_S \theta \hat{i} + \nabla \cdot 2\nu \bar{D} \quad (4.7)$$

$$\partial_t \theta + \bar{V} \cdot \nabla \theta = \nabla^2 \theta - h(x) \bar{V} \cdot \hat{i}$$

with the boundary conditions

$$\bar{V} = \theta = 0 \quad \text{at } x = 0 \quad (4.8)$$

$$\bar{V} = (\partial_x + N) \theta = 0 \quad \text{at } x = 1 ,$$

where the gradient function, $h(x)$, denotes the vertical temperature gradient of the static solution:

$$h(x) = DT_{SS}(x). \quad (4.9)$$

When the disturbances are infinitesimal, both quadratic terms $\bar{V} \cdot \nabla \bar{V}$ and $\bar{V} \cdot \nabla \theta$ are dropped. When ν is a function of x only, the resulting equations are linear. Moreover, the operators and coefficients of the right hand side are time-independent. Then, the relative growth rate can be introduced in the exponential form:

$$\partial_t \bar{V} = \sigma \bar{V} .$$

4.1.1 On the Principle of Exchange of Stability

The linear stability theory assumes that the vertical and the horizontal dependences of the solution for infinitesimal disturbances are separable (Pellew and Southwell, 1940). For an initial condition corresponding to the static solution, the relative growth rate, σ , of the disturbances is uniquely determined as a function of the separation constant, a (wave number) and the system parameters R , P , N and $h(x)$ (for variable viscosity, including viscosity ratio number Γ). The (a, R) plane, with the other parameters being fixed, is divided by the marginal stability curve, where $\sigma = 0$. On the curve, a minimum value, $R = R_c$, is found corresponding to a_c . This is the critical point, where first order disturbances have the highest growth rate. Above this point, convective motion will set in and the solution to the equations will deviate from the static solution. Whether the resulting motion will be stationary or not, depends on the principle of exchange of stability. When the principle holds, no non-decaying disturbances show oscillatory behavior in time. In other words, for a general complex growth rate $\sigma = p + iq$, the principle means that $q \neq 0$ implies that $p < 0$. (Any oscillatory motion must necessarily decay.)

The principle always holds for a class of problems governed by self-adjoint differential systems, because the eigenvalues, σ , must be real. However, generally applicable conditions for the eigenvalues to be real are unknown. Sometimes, the principle can be proven to hold for a nonself-adjoint system (Davis, 1969). When the principle cannot be established, the possibility of imaginary growth rate, or oscillatory motion, cannot be ruled out. (See Chandrasekhar, p. 114.) For the system considered in the

previous section, the principle cannot be established, except for the case when the viscosity variation is a function of x only in the system of no internal heat source ($F = 0$). See Chapter VII. On the other hand, the experimental evidence indicates no oscillatory behavior at the onset of the roll motion. See Chapter V. Moreover, the observed instability makes it plausible to treat the problem in the transverse plane only. For these reasons, the principle of exchange of stability is assumed and analysis is restricted to the planform of roll cells in the transverse planes.

4.1.2 Onset Criterion for Longitudinal Roll Motion

In the case where motion is in the transverse (x - z) plane with no longitudinal (y) variation, the stream function concept is introduced

$$\bar{V}(x,z) \equiv -\nabla \times \Psi(x,z) \hat{j} \equiv -\nabla \times \bar{\Psi}$$

to combine the first two equations in (4.7) into

$$\sigma P^{-1} \nabla \times \bar{\Psi} = \nabla \Pi + R_S \theta \hat{i} + \nabla \cdot \left[\nu \{ \nabla \nabla \times \bar{\Psi} + (\nabla \nabla \times \bar{\Psi})^T \} \right]. \quad (4.10)$$

The pressure term is eliminated by operating $\hat{j} \cdot \text{curl}$ on it. The result can be put into a matrix operator form

$$\sigma \begin{bmatrix} \theta \\ P^{-1} \nabla^2 \Psi \end{bmatrix} = \begin{bmatrix} \nabla^2 & -h \partial_z \\ R_S \partial_z & \mathcal{L}_4 \end{bmatrix} \begin{bmatrix} \theta \\ \Psi \end{bmatrix}, \quad (4.11)$$

with the homogeneous boundary conditions:

$$\theta(0,z) = (\partial_x + N)\theta(1,z) = \Psi(0,z) = \Psi(1,z) = \partial_x \Psi(0,z) = \partial_x \Psi(1,z) = 0,$$

where $\mathcal{L}_4 \equiv -(\partial_z^2 - \partial_x^2) \{ \nu (\partial_z^2 - \partial_x^2) \} - 4\partial_{xz}^2 (\nu \partial_{xz}^2)$.

For roll cells, the functions Θ and Ψ are, respectively, even and odd periodic functions of z with wave number a (and wavelength, $\lambda \equiv \frac{2\pi}{a}$). Thus the equation (4.11) can be solved by separation of variables:

$$\begin{bmatrix} \Theta \\ \Psi \end{bmatrix} = \begin{bmatrix} \theta(x) \cos az \\ \phi(x) \sin az \end{bmatrix} .$$

Substitution into equation (4.11) yields

$$\sigma \begin{bmatrix} \theta \\ -P^{-1}(D^2 - a^2)\phi \end{bmatrix} = \begin{bmatrix} (D^2 - a^2) & -ah \\ aR_s & L_4 \end{bmatrix} \begin{bmatrix} \theta \\ \phi \end{bmatrix} \quad (4.12)$$

where $L_4 \equiv (D^2 + a^2)(\nu(D^2 + a^2)) - 4a^2\nu D$.

This is the eigenvalue problem which governs the growth rate σ as a function of R_s , P and $h(x)$ with the homogeneous boundary conditions:

$$\phi(0) = \phi(1) = D\phi(0) = D\phi(1) = 0 , \text{ and}$$

$$\theta(0) = (D + N)\theta(1) = 0 .$$

For non-oscillatory motion, the marginal stability curve is obtained by setting $\sigma = 0$. Note that the differential operator in equation (4.12) is nonself-adjoint with the given boundary conditions. The characteristic equations are readily solved using the Galerkin technique which is explained in the next section.

4.1.3 Galerkin Procedure

The function θ is expanded with a complete set of orthogonal functions,

$$\theta_k: \quad \theta = \sum_{k=1}^{\infty} A_k \theta_k$$

where a trial function θ_k is chosen to satisfy the equation

$$(D^2 - a^2)\theta_k = -\lambda_k^2\theta_k \quad (4.13)$$

with the boundary conditions $\theta_k(0) = (D + N)\theta_k(1) = 0$. Note that the equation utilizes one component of the original matrix operator. The solution is, of course, a sine series function:

$$\theta_k = \sin \beta_k \quad ,$$

where $N \tan \beta_k = -\beta_k$ and $\beta_k^2 = \lambda_k^2 - a^2$.

For each component of the trial functions, a corresponding second trial function ϕ_k is obtained by solving exactly one of the equations (4.12):

$$L_4\phi_k = \theta_k \quad , \quad (4.14)$$

which again satisfies the original boundary conditions:

$$\phi_k(0) = \phi_k(1) = D\phi_k(0) = D\phi_k(1) = 0 \quad .$$

It follows immediately that the second variable ϕ is in the form of

$$\phi = -aR \sum_{k=1}^{\infty} A_k \phi_k \quad (4.15)$$

because the operator L_4 is linear. ¶

Now, the series expansions for θ and ϕ are substituted into the unused equation of the original equations to yield

¶ At the marginal state, amplitude of θ was assumed infinitesimal. Then, the viscosity ν can be considered, to the first order, as a function of conduction temperature profile which, in turn, is a function of x only.

$$\sum_{k=1}^{\infty} A_k \lambda_k^2 \theta_k = a^2 R \sum_{k=1}^{\infty} A_k h \phi_k \quad (4.16)$$

Multiplying by θ_j and integrating over the range of x , an infinite set of linear homogeneous equations for A_k 's is obtained in a matrix form

$$\bar{E} \bar{A} = R \bar{G} \bar{A} \quad (4.17)$$

where

$$\bar{E} \equiv [E_{jk}] = \left[\frac{\lambda_j^2}{a^2} \int_0^1 \theta_j^2 dx \delta_{jk} \right]$$

$$\bar{G} \equiv [G_{jk}] = \left[\int_0^1 h \phi_k \theta_j dx \right] \quad j, k = 1 \rightarrow \infty$$

$$\bar{A} \equiv [A_k]$$

Since the matrix \bar{E} is diagonal, the matrix equation can be easily transformed into

$$\frac{1}{R} \bar{A} = \bar{E}^{-1} \bar{G} \bar{A} = \bar{G}' \bar{A} \quad (4.18)$$

Then the critical Rayleigh number is determined from the largest positive eigenvalue ($1/R$) for a given N , $h(x)$ and $v(x)$:

$$R_c = \min_a R \quad \text{when } R > 0$$

In practice, only a finite number of terms is used. When the original operator (coefficient matrix on the right hand side of equation (4.12)) is self-adjoint, all eigenvalues are positive and the standard power method can be effectively used (see Chapter VII). For internal heat source problems, the method cannot be used due to the nonself-adjointness of the coefficient matrix.

It should be pointed out that the choice of trial function based on a component of the original operator and the subsequent exact solution procedure for one of the equations make it possible to reduce the final matrix size by one-half. This is in contrast to the choice of polynomial type trial functions, as suggested by Finlayson (1970). This procedure was first used by Chandrasekhar (1961). Rintel (1967) studied the penetrative convection instability using the same procedure. Sani (1968) proved convergence of the procedure for determining the exact eigenvalues, when the trial function chosen is a complete set in a square integrable normed space.

4.1.4 Variational Principles Based on Adjoint Differential Systems

Roberts (1960) pointed out that the Galerkin procedure is equivalent to the variational methods based on adjoint differential systems. When the original and adjoint boundary conditions are the same, the eigenvalue is stationary. See Finlayson (1970). We will show that the above assertion is true, even if one of the boundary conditions is a mixed type and coefficient of differential operator is a function of independent variable.

An adjoint system to the original equation is best obtained by direct integration by parts. It is convenient to define an inner product of two functions:

$$\langle f, g \rangle \equiv \int_0^1 fg \, dx \quad .$$

The original and adjoint system can be written

$$\begin{aligned} (D^2 - a^2)\theta_m &= ah\phi_m & (D^2 - a^2)\theta_n^\dagger &= a\phi_n^\dagger \\ L_4 \phi_m &= -aR_m\theta_m & L_4 \phi_n^\dagger &= -aR_n h\theta_n^\dagger \end{aligned} \quad (4.19)$$

which satisfy the identical boundary conditions:

$$\phi(0) = \phi(1) = D\phi(0) = D\phi(1) = 0$$

$$\theta(0) = (D + N)\theta(1) = 0.$$

Note that the subscripts m and n are used to distinguish eigenfunctions corresponding to distinct eigenvalues. It can be shown, by direct integration by parts, that the following inner products are identical:

$$aR_m \langle \theta_m, \phi_n^\dagger \rangle = - \langle \phi_n^\dagger, L_4 \phi_m \rangle = - \langle \phi_m, L_4 \phi_n^\dagger \rangle = aR_n \langle \phi_m, \theta_n^\dagger \rangle = aR_m \langle \phi_m, \theta_n^\dagger \rangle \quad (4.20)$$

$$\text{i.e.} \quad a(R_m - R_n) \langle \phi_m, \theta_n^\dagger \rangle = 0 .$$

Hence, if R_m and R_n are unequal, the equations exhibit biorthogonal properties involving the eigenfunctions. A variational principle follows immediately when R_m and R_n are equal:

$$R = \frac{- \langle \theta, (D^2 - a^2) \theta^\dagger \rangle}{a \langle \phi, L_4 \phi^\dagger \rangle} \quad (4.21)$$

$$= \frac{\int_0^1 [D\theta \cdot D\theta^\dagger + a\theta \cdot \theta^\dagger + N\theta(1) \cdot \theta^\dagger(1)] dx}{a \int_0^1 [(D^2 + a^2) \phi \cdot (D^2 + a^2) \phi^\dagger + 4a^2 D\phi \cdot D\phi^\dagger] dx}$$

To prove that it is indeed a variational principle, consider R as a Lagrangian multiplier and seek the extremum of the integral with respect to arbitrary variations in θ and θ^\dagger , which satisfy

$$\delta\theta(0) = (D + N)\delta\theta(1) = 0 .$$

The variational form of the second equations in (4.19) will be the constraints with the boundary conditions. Then we obtain as the first variation

$$0 = \langle \delta\theta, (D^2 - a^2)\theta^\dagger - a\phi^\dagger \rangle + \langle \delta\theta^\dagger, (D^2 - a^2)\theta - ah\phi_m \rangle .$$

For the small variations in θ and θ^\dagger , the Euler equations in the integral restore the first equations in (4.19).

If we use the same expansion series as those in the Galerkin procedure, but with different expansion coefficients A_k and A_k^\dagger and minimize the variational formula with respect to its coefficients, the characteristic equation identical to the equation (4.17) will be restored. For the particular trial function chosen, note that $(D^2 - a^2)\theta = -\lambda^2\theta$. Therefore, the term $(D^2 - a^2)\theta$ in the numerator of the variational formulation is directly replaced by the term, $-\lambda^2\theta$, thus further simplifying the evaluation.

4.2 Finite Amplitude Convection

For a Rayleigh number just above the critical value, the convective motion generally becomes steady and finite instead of being exponentially dependent on time, as assumed in linear theory. The nonlinear interaction terms neglected in linear analysis become pronounced and the effects of the undisturbed motion less pronounced for bigger perturbations. Clearly, the effects of finite amplitude are the province of nonlinear stability theory. The theory provides a physical explanation for experimental observations such as cellular structure, amplitude of stationary velocity and temperature, cell size and heat transfer rates, etc. The theoretical approach

assumes a strong spatial connection between linear analysis and nonlinear theories; that is, the convection flow has approximately the cell size suggested by the linearized theory. In particular, for two dimensional rolls in Bénard convection, the wavelength, while not uniquely determined, is known for an infinite Prandtl number fluid to be in a narrow band near that predicted by the linear stability limit (Busse, 1967b).

The spatial connection assumption has been used frequently in numerical investigations of finite amplitude convection via finite difference techniques. Numerical solutions have been successful at predicting the heat transfer rate for moderately higher Rayleigh numbers, for which perturbation techniques cease to apply. However, numerical solutions near the critical conditions have seldom been reported in the literature. Probably, the large increase in the time required for convergence is the reason, as was pointed out by Liang, Vidal and Acrivos (1969). Another example (Torrance and Turcotte, 1971) showed that even for a Rayleigh number of six times the critical value, the final solution produces the static conduction field. The problem has been overlooked, because the problems analyzed already have handy solutions from the linear stability analysis.

To resolve the difficulties, a new method called the amplitude specification method has been developed. Its application will be presented in Chapter VII for the Rayleigh-Bénard problem with the large variation of temperature dependent viscosity. The problem is chosen because the numerical results would be checked against the well-known perturbation solution (Busse, 1967a).

4.2.1 Amplitude Specification Method

For two-dimensional roll cells, the governing equations for finite amplitude convective field are

$$\mathcal{E}\theta \equiv \nabla \cdot (\bar{V}\theta) - \nabla^2\theta = - \partial_z \psi$$

$$\mathcal{M}\psi \equiv P^{-1} \nabla \cdot (\bar{V}\nabla^2\psi) + \mathcal{L}_v\psi = - R\partial_z\theta$$

for any stationary solution. For the temperature dependent viscosity variation, the operator \mathcal{L}_v becomes a function of θ .

Suppose the equation is being solved by a finite difference technique for a specified set of boundary conditions (cell size being fixed as that predicted by linear analysis). The calculation procedure may be described in symbolic operator form

$$\bar{E}\bar{\theta} = - \Delta_z \bar{\psi}$$

$$\bar{M}\bar{\psi} = - R\Delta_z \bar{\theta}$$

where $\bar{\theta}$ and $\bar{\psi}$ are vectors representing values of θ and ψ at selected grid points and \bar{E} and \bar{M} are matrix operators corresponding to the finite difference form of the original differential equations. A normal calculational scheme might start from a random or guessed $\bar{\theta}$ and $\bar{\psi}$ with a supercritical Rayleigh number. The first equation is solved for $\bar{\theta}$ with the chosen $\bar{\psi}$. The resulting $\bar{\theta}$ is then introduced into the second equation to update $\bar{\psi}$. Through cyclic iteration, a final stationary solution is obtained when $\bar{\theta}$ and $\bar{\psi}$ no longer change their values between iterations. The complete

procedure of one iteration can be symbolically combined into a form

$$\frac{1}{R} \bar{\Psi} = \bar{B} \bar{\Psi} \quad ,$$

where $\bar{B} \equiv (\bar{M}^{-1} \Delta_z \cdot \bar{E}^{-1} \Delta_z)$. Since the operator \bar{B} involves nonlinear operations arising from the convective interaction terms, the above equation may be referred to as a characteristic equation for a "nonlinear eigenvalue problem". At the critical point, the nonlinear effects disappear and the linearized equations are reduced into a bona fide eigenvalue problem as discussed in the previous sections.

Just above the critical (that is, R is slightly greater than R_c , which is normally called as supercritical in the literature), the structure of Ψ is known to have a form similar to Ψ_c but with a fixed amplitude. Thus \bar{B} , a function of Ψ , must be disturbed only slightly from that of the linearized case. However, the presence of the nonlinear interaction terms plays a role in removing the indeterminacy of the eigensolution amplitudes. Also, a stationary solution requires that the amplitudes are steady and finite for a given Rayleigh number. This suggests a strategy which might yield an efficient solution procedure. By specifying a fixed amplitude, the Rayleigh number may be recovered along with the functional form.

For this purpose, the stream function is rescaled as

$$\Phi \equiv \frac{\Psi}{R} \quad . \quad (4.21)$$

By definition, velocity will become

$$\bar{V} = -R \|\Phi\| \nabla \times \left(\frac{\Phi}{\|\Phi\|} \hat{j} \right) \quad ,$$

where $\|\Phi\|$ denotes an appropriate norm of the rescaled stream function field (for example, a maximum value of Φ). Introducing an amplitude parameter, ϵ , such that

$$R \equiv \frac{\epsilon}{\|\Phi\|}, \quad (4.23)$$

the original equations are transformed into

$$\begin{bmatrix} \epsilon \cdot J(\Theta, \frac{\Phi}{\|\Phi\|}) \\ -P^{-1} \epsilon \cdot J(\nabla^2 \Phi, \frac{\Phi}{\|\Phi\|}) \end{bmatrix} = \begin{bmatrix} \nabla^2 & -\frac{\epsilon}{\|\Phi\|} \partial_z \\ \partial_z & \mathcal{L}_4 \end{bmatrix} \begin{bmatrix} \Theta \\ \Phi \end{bmatrix} \quad (4.24)$$

In practice, the calculation procedure will be exactly the same as before, except the normalization procedure. First, stream function field will be normalized with $\|\Phi\|$ and multiplied by ϵ to give a specified amplitude. Next, the energy equation will be solved for Θ . Then, the rescaled stream function field Φ will be obtained by solving the biharmonic equation. This sequence of steps will be iterated to obtain a final stationary solution.

The amplitude specification method is efficient near the critical point, because the variation of Rayleigh number with respect to the amplitude is extremely slow. Conversely, the amplitude may vary very strongly on R near R_c . For the similar reason, this method, though still valid, will be inefficient for high Rayleigh number range when the amplitude is only weakly dependent on R . One remarkable feature of the method lies in its capability to generate multiple stationary solutions, when the so-called hysteresis effect appears in a system. See Chapter VII. Finally, it should be pointed out that the method can be viewed as a numerical extension of

the modified perturbation technique employed by Schlüter et al. (1965). Their method is to expand dependent variables and Rayleigh number by a Taylor series with respect to ϵ , collect the coefficient equations for the same order and then solve the equations consecutively from the zeroth order (linear solution).

V. EXPERIMENTAL OBSERVATIONS OF CONVECTIVE INSTABILITY:
THE LONGITUDINAL ROLL MOTION

The purposes of the experimental work are to

- (i) provide a detailed exposition on the nature and development of the roll motion and
- (ii) collect quantitative data on that motion with which theoretical predictions can be compared.

An extensive investigation by Curlet (1976) on the three-dimensional nature of the convection currents eliminates the need to reexamine the structure of the overall convection motion.

A modification of Curlet's experimental equipment was made to obtain better temperature data for the roll motion. The original bank of transverse thermocouples was replaced by a new thermocouple net which can cover a pair of individual roll cells. Details of the net design are found in Section 5.3. It enables one to take detailed temperature data in the roll region. The experimental boundary conditions are chosen to preserve two-dimensionality in the overall circulation. A forced heat loss was provided at the bridgewall (end wall adjacent to the source). In this way, the secondary circulation cell, located in the bottom half of the enclosure, was stabilized and the heat leak from the top surface of heater did not affect the bridgewall boundary conditions. The experimental procedures are virtually identical to those described by Curlet.

5.1 Experimental Procedure and Operating Conditions

The key component of the experimental model is a multi-walled Plexiglas box, as schematically shown in Figure 5.1. The entire rectangular

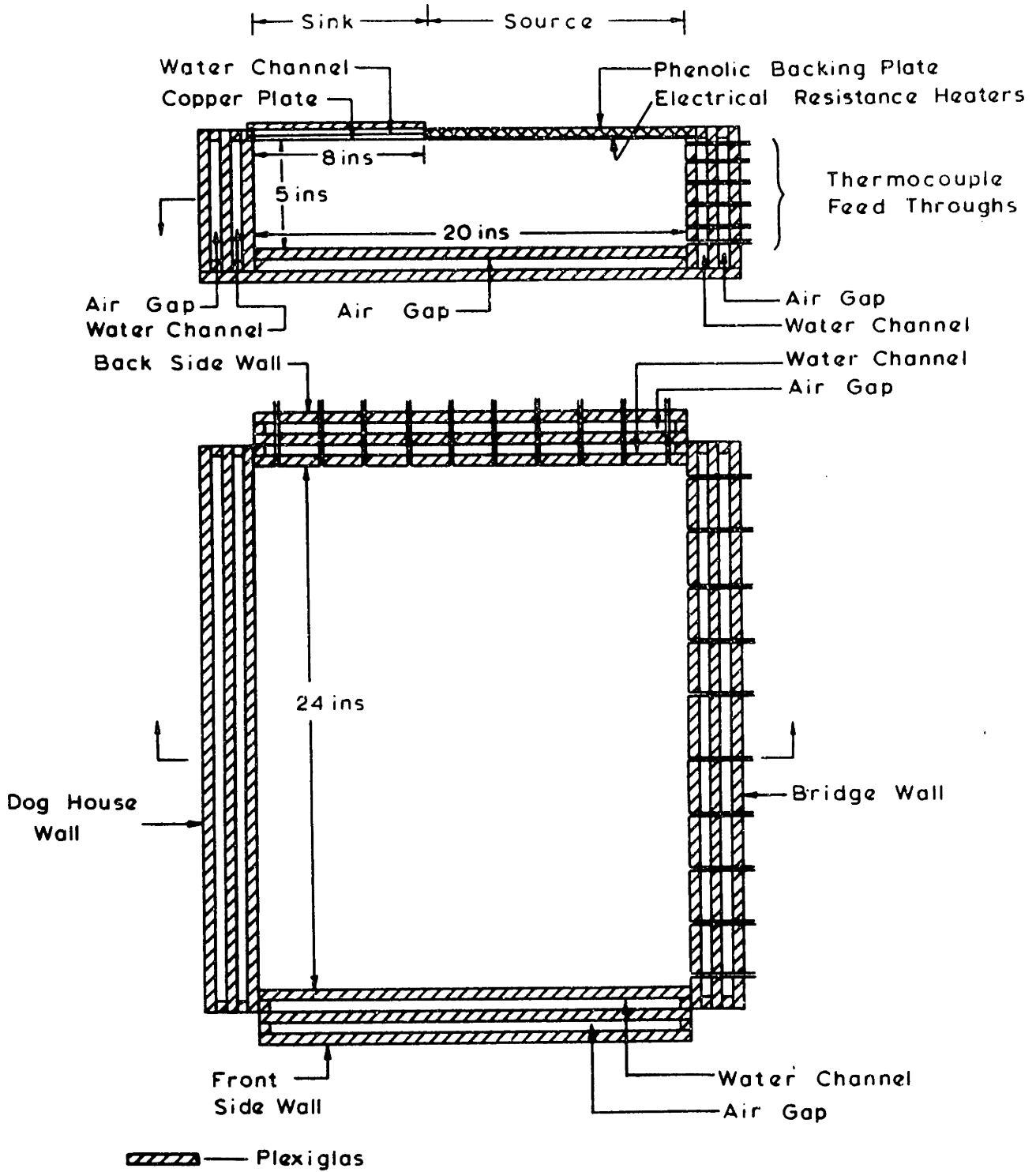


FIGURE 5.1

SCHEMATIC OF EXPERIMENTAL MODEL TANK

enclosure was filled with the modeling fluid, glycerine. Glycerine was selected, because it has a high Prandtl number and the temperature dependency of its viscosity can be made similar to that of glass melts.

Heat input to the top surface was provided by six electrical resistance heaters connected to a regulated D.C. power supply. The isothermal sink was simulated by a water-cooled, 6.35 mm ($\frac{1}{4}$ ") thick copper plate, located along the top surface adjacent to the heaters. The desired heat loss at the bridgewall was achieved by flowing water at a constant temperature through the inner gap of the wall. The apparatus arrangement is shown in Figure 5.2, where the cooling water circuits are also shown. Only the cold temperature tank (at 22°C) was used to provide cooling water to both the sink and the bridgewall.

Flow motion was visualized by mixing into glycerine approximately 2 grams of neutrally buoyant anthracene particles in the size range of 200 to 500 μ . These particles were illuminated using a planar (\sim 9.5 mm wide) light source. The scattered light from the slowly moving particles was recorded as streak photographs using a 35 mm single lens reflex camera (Minolta SR-T-101 with MC ROKKOR-PF 58 mm lens, f1.4) on Kodak TriX film (ASA 400). See Curlet (1976) for details.

Following Curlet's procedure, boundary temperatures, heater voltage drops and temperature increases in the cooling water channels were continuously scanned by a data acquisition system at intervals of 30 minutes. The glycerine temperatures were also monitored with the original longitudinal bank of thermocouples. The heat removal rates from the sink and the bridgewall were determined by measuring the flow rates of cooling water directly with both bucket-stopwatch technique and calibrated rotameters.

The operating conditions are summarized in Table 5.1. Since the duration of the experiment was almost one month (including the photographic session), it was necessary to sort out data which were taken at conditions deviating markedly from average conditions. The final results were based on an average of 700 scans. A measure of the data fluctuation is provided by the standard deviations reported for each parameter measured. As can be seen, the major fluctuations were in those temperatures most affected by abrupt weather changes and in the water flow rates. A relocation of the thermocouple net also disturbed the flow and temperature fields. However, the disturbances were easily eliminated by allowing sufficient time for return to steady, equilibrium state. The pertinent properties of glycerine are summarized in Table 5.2. These are evaluated at the temperature of batch sink. The glycerine concentration was determined by measurement of the viscosity and also used to ensure that no water absorption occurred during the experiment.

5.2 Two-Dimensional Nature of the Overall Circulation Pattern

As one of the basic features, the two-dimensional nature of the convection currents is caused by the specific arrangement of the top boundary conditions. The dominant motion in the enclosure forms a longitudinal circulation cell which is driven by the interaction of the heat source and the isothermal heat sink. Even though the small heat leaks through the side walls generate some secondary motion, the overall effect is negligibly small and the dominant two-dimensional motion is affected only in a region close to the side walls.

In this Section, the two-dimensional features of the flow are reexamined in relation to the roll motion. First, the possibility of true

TABLE 5.1

Experimental Operating Conditions

(1)	Heater Voltage	43.9 ± 0.065	V
	Overall Resistance	21.5	Ω
(2)	Temperature and Flow Rates of Cooling Water		
		Batch	Bridgeway
	Inlet Temperature (°C)	22.61 ± 0.049	22.79 ± 0.091
	Outlet Temperature (°C)	24.06 ± 0.054	23.21 ± 0.092
	Difference (°C)	1.45 ± 0.051	0.42 ± 0.082
	Flow Rate (cc/min)	741.6 ± 7.7	355.4 ± 4.5
	Flow Rate (m ³ /s)	1.236 × 10 ⁻⁵	5.923 × 10 ⁻⁶
(3)	Wall Temperature (°C)		
	Doghouse Wall	25.17 ± 0.21	
	Front Side Wall	25.53 ± 0.38	
	Back Side Wall	25.73 ± 0.30	
	Bridgeway	24.94 ± 0.25	
	Bottom	25.57 ± 0.32	
(4)	Ambient Temperature	24.98 ± 0.34	°C
	Water Supply Tank Temperature	22.07 ± 0.083	°C

Model Dimensions

Depth - Length - Width 0.127^m - 0.508^m - 0.6096^m (5" - 20" - 24")
 Sink Area .2032^m - .6096^m (8" - 24")

TABLE 5.2

Physical Properties of Glycerine

at Batch Temperature $T_s = 297.6$ K (535.7 R)

<u>Properties</u>			<u>SI Unit</u>	
Glycerine Concentration [¶]	99.7	wt %	99.7	wt %
Density, ρ_o	78.43	lb/ft ³	1256	kg/m ³
Heat Capacity, c_p	0.57	Btu/lb·R	2386	J/kg·K
Kinematic Viscosity, ν_o^*	28.66	ft ² /hr	7.396×10^{-4}	m ² /s
Thermal Diffusivity, α_o	$.3681 \times 10^{-2}$	ft ² /hr	9.499×10^{-7}	m ² /s
Thermal Conductivity, κ_o	.1645	Btu/hr·ft·R	0.2847	J/m·s·K
Coefficient of Volumetric Expansion, β	$.2698 \times 10^{-3}$	1/R	0.1499	1/K
Viscosity Exponential Constant, E	1.217×10^4	1/R	6.761×10^3	1/K

[¶] Estimated from viscosity measurement.

two-dimensional motion in the absence of roll motion is considered. Then, the two-dimensional motion obtained in the experiment will be briefly compared with the corresponding numerical solution.

5.2.1 The Two-Dimensional Circulation Pattern

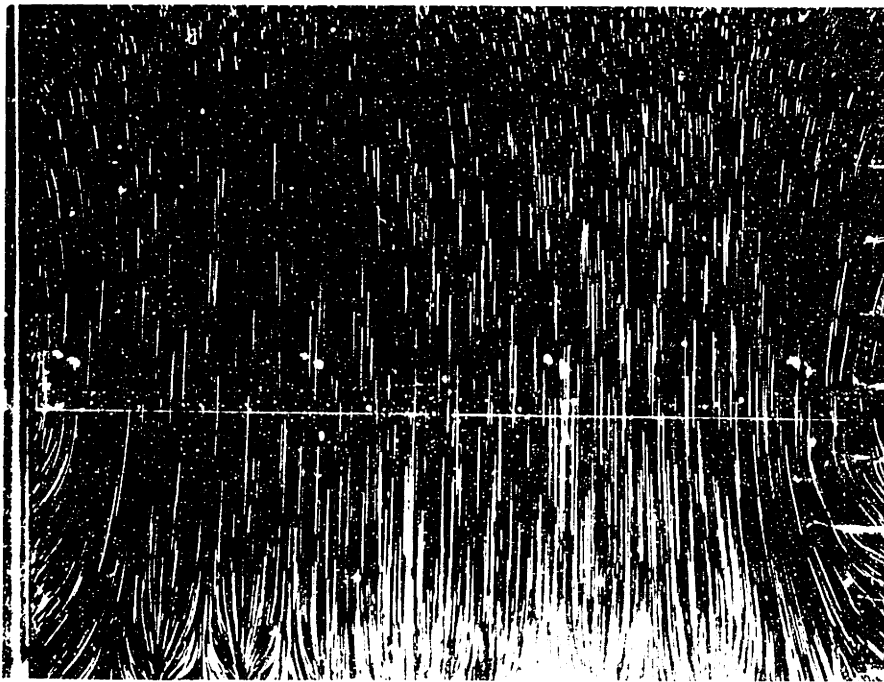
Curlet's thesis investigation was principally focused on the secondary motion generated by heat leaks through side walls. (We may call this transverse motion to distinguish it from roll motion.) The effect of various boundary conditions was well-documented. However, the effect of the top boundary condition (specifically, total heat input) was not investigated. The origin of roll motion is the instability due to the unstable temperature distribution which results when the hot longitudinal convection currents are cooled from above. If one could suppress the origin of the instability, then it should be possible to obtain true two-dimensional circulation current. This can perhaps be achieved by reducing the heat supply at the source to a value low enough so that critical conditions are not reached under the sink.

This hypothesis was confirmed by a simple, qualitative experiment in which heat input was reduced in a sequence of steps. Due to the difficulties encountered in controlling boundary conditions at low heating rates, only photographs were taken. The boundary conditions described earlier do not apply for this experiment. The heat inputs investigated were 10.5, 13.4, and 74.4 watts (corresponding to 15, 17, and 40 voltage drop across the heaters).

A streak photograph in Figure 5.3(a) shows the flow pattern at center longitudinal plane for the 15 volts condition. Since no crossing streaks appear in the upper left corner, the roll motion does not exist. Note that



(a) Longitudinal Motion at $z = 0$ (Exposure time 20 minutes)



(b) Horizontal Motion at $x \approx 0.1$ (Exposure time 10 minutes)

Figure 5.3

Experimental Flow Field without the Roll Motion (Heater Input 15 Volts)

the circulation center (eye) of the upper cell ($\sim 1\frac{1}{4}$ " from the top surface) is located closer to the heater side (the right top surface) than normal. The fluid in this eye is nearly stagnant. Also the overall cell is slightly slanted toward the heater side. In the upper part of the main circulation, the longitudinal current shows a sudden contraction. This contraction always appears at the boundary line between the heater and the sink surfaces. Upstream of this point, all the streamlines are essentially parallel to the top surface, while they diverge as the stream advances past this point. The contraction is purely due to the abrupt change in thermal boundary condition. Therefore, this point may be termed the "Thermal Vena Contracta".

The corresponding planform is shown in Figure 5.3(b). This photograph was taken through the bottom by illuminating the horizontal plane located at $x \cong 0.1$ ($\sim \frac{1}{2}$ inch below and parallel to the top surface). The parallel streaks indicate that the fluid motion is mainly in the longitudinal direction, thus confirming the two-dimensionality of the flow. The white perpendicular straight line in the middle of the photo is the edge of the sink in contact with the heater surface. In the middle of the sink region, streak lines move straight ahead toward the doghouse wall (bottom boundary in the photograph). The slight distortions in the streaks represent the downward motion of the flow close to the wall. No roll motion is noticeable. The longitudinal plane of photograph 5.3(a) corresponds to the center line orthogonal to the doghouse wall in this picture. Additional evidence for the two-dimensionality can be found by comparing the lengths of streaks. All streaks appear to have a constant length. Since the streak length is directly proportional to the stream velocity, each longitudinal plane motion may have a similar flow pattern.

Both photographs correspond to the same heater input condition of 15 volts drop across the heater. This condition is roughly $\frac{1}{9}$ of that corresponding to the experimental condition described in the earlier Section (45 volts). Due to the low rate of heat supply, the average glycerine temperature was only slightly higher than the ambient. Even the filtered light source can cause large disturbances in the flow.

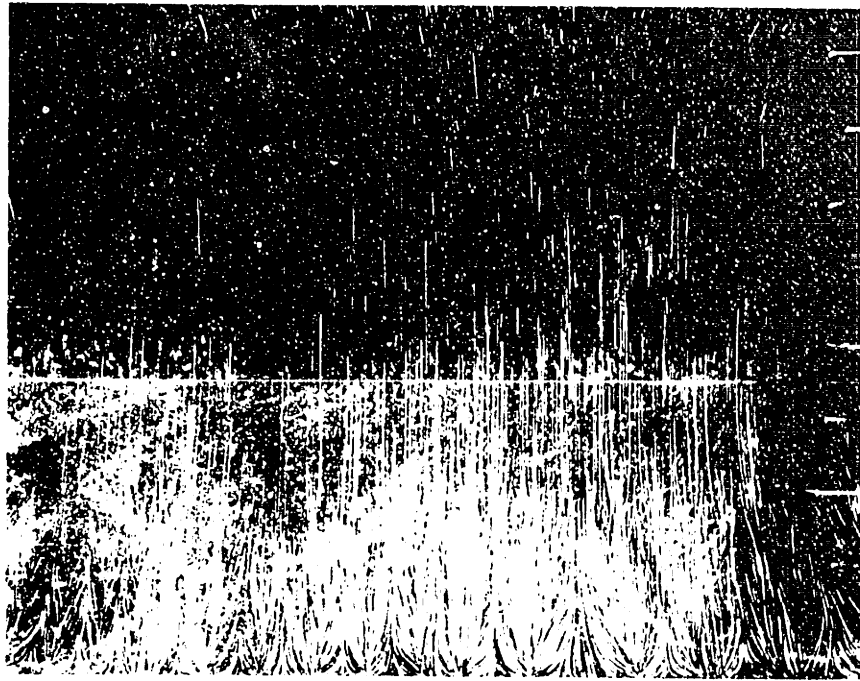
The two-dimensionality of the flow breaks down in the region close to both side walls. The slight curvature of streaks is indicative of transverse motion and is clearly a consequence of heat leaks through the walls. The similar structure of the streaks at both walls indicated that the heat leaks are symmetric. Notice that this disturbance is confined to only 10% of the whole transverse plane. In the left bottom corner, two pairs of rolls (4 individual cells) are still prevalent. Heating from the photo light beam may have caused this disturbance.

When the heat input increased to 17 volts, the longitudinal motion shows clear roll motion, as presented in Figure 5.4(a). Not only do the crossing streaks appear clearly in the upper left corner, but also a new circulation eye forms closer to the doghouse wall. The original eye is also moved toward the new eye. Thus the stagnant fluid area is broadened further.

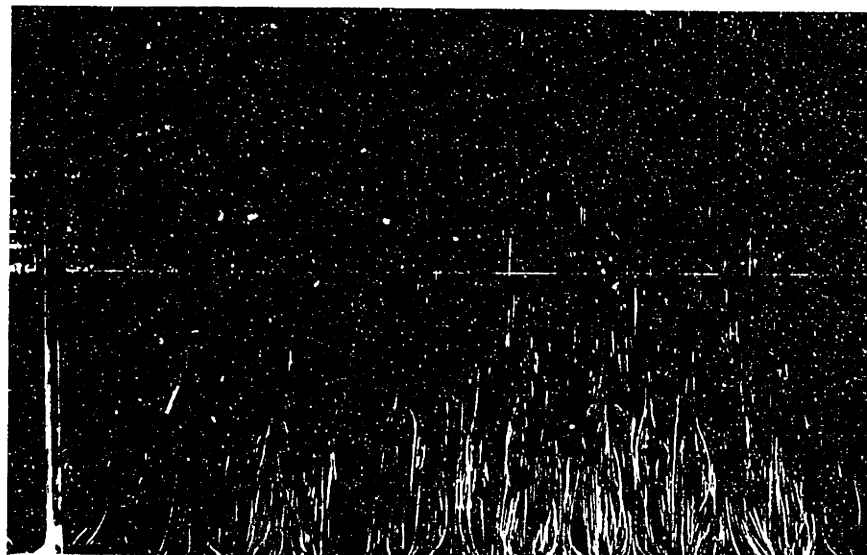
When the heater input further increased (to about a 40 voltage drop across the heater), the planform shows the frequency of roll cells in the transverse direction, as in Figure 5.4(b) and (c). The photograph (c) was taken at a planform slightly below that of (b), but still above the circulation eye level. In both cases, the heater input condition is the same. The regular structure shown in (b) contrasts with the somewhat



(a) Longitudinal Motion at $z = 0$ (17 Volts) (Exposure time 20 min.)



(b) Planform at $x = 0.1$ (40 Volts) (Exposure time 10 minutes)



(c) Planform at $x = 0.15$ (40 Volts) (Exposure time 8 minutes)

Fig. 5.4 Experimental Flow Fields with the Roll Motion

disorderly structure in (c), where curvature of streaks is more pronounced. This merely indicates the slow longitudinal velocity of the stream and the growing transverse disturbance velocity. In the middle part of the roll region, the wavelength appears constant in Figure (b), while, closer to the side walls, wavelength elongation is noted for this particular case. Again, most of the heater region and the entrance part of the sink region show clearly the two-dimensional nature of the flow.

5.2.2 Two-Dimensional Numerical Simulation for the Experiment

The above discussion points out that the two-dimensional nature of the overall convection still prevails, even in the presence of roll motion. This was the basis for the development of a heuristic method of obtaining three-dimensional flow by complementary two-dimensional solutions (Won, 1974). Specifically, the transverse motion was isolated from the longitudinal motion to obtain detailed distribution of flow and temperature. Interaction with the longitudinal planes was achieved by allowing heat source and sink distributions in the transverse plane. Physically, this source-sink distribution represents the loss or gain of enthalpy in convective longitudinal stream across the transverse plane. A conventional technique for treating similar problems by marching with an assumed longitudinal velocity field (Cheng et al., 1972) is not adequate due to the recirculating nature of the problem. Curlet extended the source-sink method to predict roll motions. He showed that the method reasonably predicts the number of roll cells and the amplitude of downflow velocity in the roll region.

The source-sink distribution technique will be used to analyze the onset condition for roll motion. As the first step, a two-dimensional

longitudinal numerical solution was obtained for the experimental conditions described earlier. The dimensionless variables are listed in Table 5.3. The computer program, originally written by Clomburg (1971), was revised to incorporate the source-sink method and the more exact treatment of viscosity variation (see Appendix E for the treatment of extra terms originally omitted).

The solution for the longitudinal flow field is directly compared with the experimental streak photograph in Figure 5.5. Since the relevant physics were reported by Curlet (1976), we only mention two points. The forced heat loss at bridgwall extends the lower circulation cell up to the doghouse wall. Roll motion is clear in the sink region. (The thermocouple net is also shown in the Figure.) The corresponding isotherm plot is shown in Figure 5.6. The boundary layer nature of the circulation current is clearly evident under the top surface.

A measure of the control achieved during the experiment is provided by the energy balance averaged over the duration of the experiment. This balance is presented in Table 5.4, in conjunction with the results of the numerical calculation. The energy removed through the sink and the bridge-wall was determined from the flow rates of water and the temperature rise of the cooling water. The heat input was determined from the measured voltage drop across and the overall resistances of the electrical strip heaters. Heat leaks out of the bottom and the side walls were estimated knowing the ambient temperature (see Table 5.1). Some of the heat generated by the heater was found to leak through the top insulation and, accordingly, this was estimated from the measured temperature difference across the insulation. Heat leakage to the bridgwall cooling water is due to the water

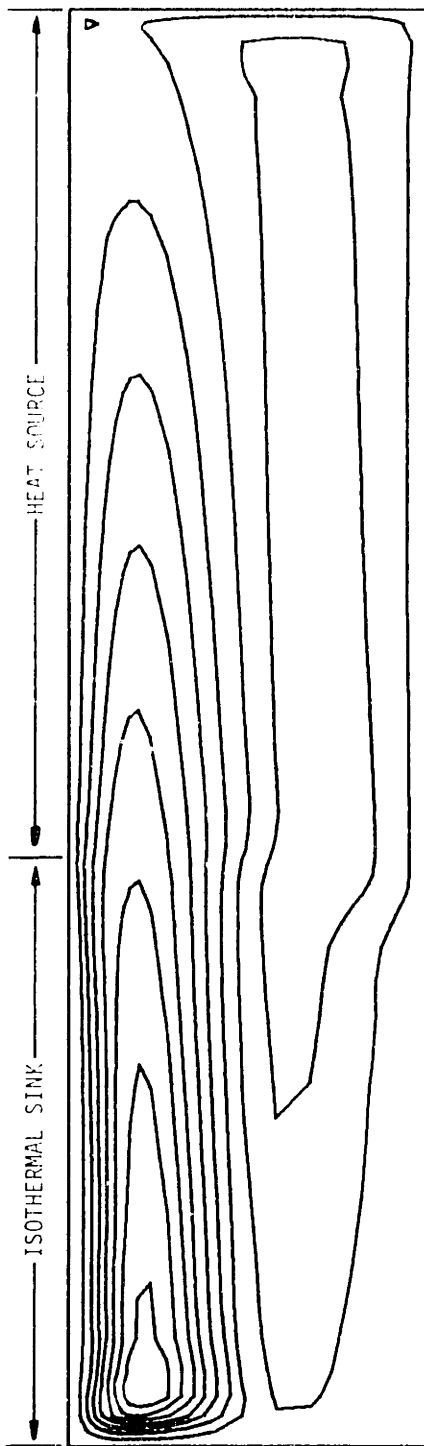
TABLE 5.3

Dimensionless Parameters for Two-dimensional Numerical Calculation

<u>Parameter</u>	<u>Definition</u>	
Rayleigh Number, R	$\frac{g\beta T_R^* H^3}{\nu_o^* \alpha_o}$	2.87x10 ⁷
Prandtl Number, P	ν_o^* / α_o	7.79x10 ⁴
Viscosity Number, γ	E / T_R^*	32.14
Longitudinal Aspect	L/H	4.0
Batch Coverage	L_B / L	0.4
<u>Boundary Condition</u>	<u>Definition</u>	
Batch Temperature, T_s	T_s^* / T_R^*	1.4147
Source Heat Flux, q_F	$q^* H / \kappa_o T_R^*$	1.0000
Bridgwall Temperature		1.4082
Bridgwall Biot Number, N	$U^* H / \kappa_o$	7.35
Doghouswall Temperature		1.4188
Doghouswall Biot Number [§]		0.6358
Bottom Temperature		1.4180
Bottom Biot Number [§]		0.8610
Side Wall Heat Loss, T		-7.546x10 ⁻³ ¶
Reference Temperature, $T_R^* \equiv q^* H / \kappa_o$	210.4 K	(378.7 R)
Heat Flux Density, q^*	471.6 J/m ² ·s	(149.5 Btu/ft ² ·hr)

¶ Uniform sink was assumed for the source-sink approximation method.

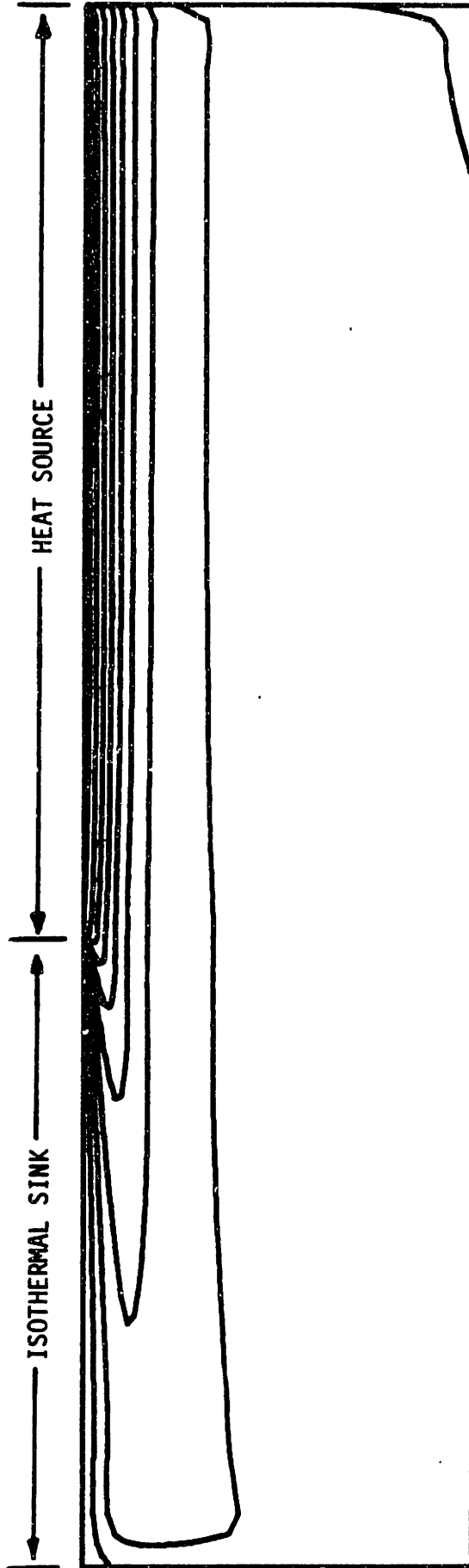
§ Estimated.



STREAM FUNCTION FIELD FOR RUN NUMBER 6019

PSI MAX = 54.05 PSI MIN = -15.32 DELTA PSI = 6.938

Figure 5.5 Experimental Streak Lines and Computed Streamlines for Longitudinal Plane ($z = 0$)
(Exposure time 20 minutes)



TEMPERATURE FIELD FOR RUN NUMBER 6019

THETA MAX = 1.5789 THETA MIN = 1.4147 DELTA THETA = 0.0164

FIGURE 5.6 COMPUTED ISOTHEM PLOT FOR LONGITUDINAL
PLANE (Z = 0)

TABLE 5.4

Comparison of Experimental and Numerical Energy Balance

	<u>Experimental</u>			<u>Numerical</u> [§]	
	Btu/hr	W	%	Dimensionless	%
INPUT					
Heater Input	305.9	89.65			
Leakage	(6.9)	(2.02)			
<u>Total Input</u>	<u>299.0</u>	<u>87.63</u>	<u>100.0</u>	<u>2.4000</u>	<u>100.0</u>
OUTPUT					
Batch	256.0	75.29	85.6	2.0278	84.5
Bridgwall	35.5	10.40			
Leakage	(1.3)	(0.38)			
	34.2	10.02	11.4	0.2721	11.3
Doghousewall	1.1	0.32	0.4	0.0116	0.5
Bottom	4.6	1.35	1.5	0.0493	2.1
Side Walls [§]	3.8	1.11	1.3	0.0302	1.3
<u>Total Output</u>	<u>299.7</u>	<u>87.83</u>	<u>100.2</u>	<u>2.3910</u>	<u>99.6</u>
DISCREPANCY					
Input - Output	-0.7	-0.31	-0.2	0.0090	0.4

[§] By the source-sink approximation method. (Heat losses at the side walls were assumed as uniform sink.)

being colder than the ambient temperature. Even if these leakages are not accounted for, the energy balance shows excellent agreement within the experimental error ranges.

5.3 The Thermocouple Net and Roll Cell Visualization

To obtain the temperature distributions in the roll cell region, a thermocouple net was constructed. The net is composed of sixty beads of thermocouple junctions arranged in six columns by ten rows in a 2.54 cm (1") square area. Figure 5.7 shows the net in the enclosure placed in the center of supporting frame. Notice that a pair of roll cells is still intact through the net. The downward streaks in the middle are due to the disturbance created as the fluid current crosses the net, where the sixty lines of copper wire are collected together.

A common base line of 0.127 mm (5 mil.) constantan wire was horizontally arranged in ten rows, with spacing of ~ 0.25 cm. Each row was firmly glued to the supporting frame of Plexiglas rod. (The distance between the vertical rods is 12.7 cm. The disturbance due to the frame does not affect the data collection area.) On each row, six copper thermocouple wires of 0.127 mm were welded and then soldered to form regularly spaced beads (~ 5.1 mm spacing). Sixty-one thermocouple lines (Isonel Enamel-coated) were collected through a hollow (~ 3.18 mm diameter) glass sheath which was attached to the middle of the bottom supporting rod. (Collected wires show a slight glare in the picture.) This glass sheath could slide in and out of the tank through one of the thermocouple feed ports in the bridge wall. The net was centered about 2.5 cm to the right of the center longitudinal plane and could only move in the longitudinal direction.

All the temperature measurements were taken without any interruption

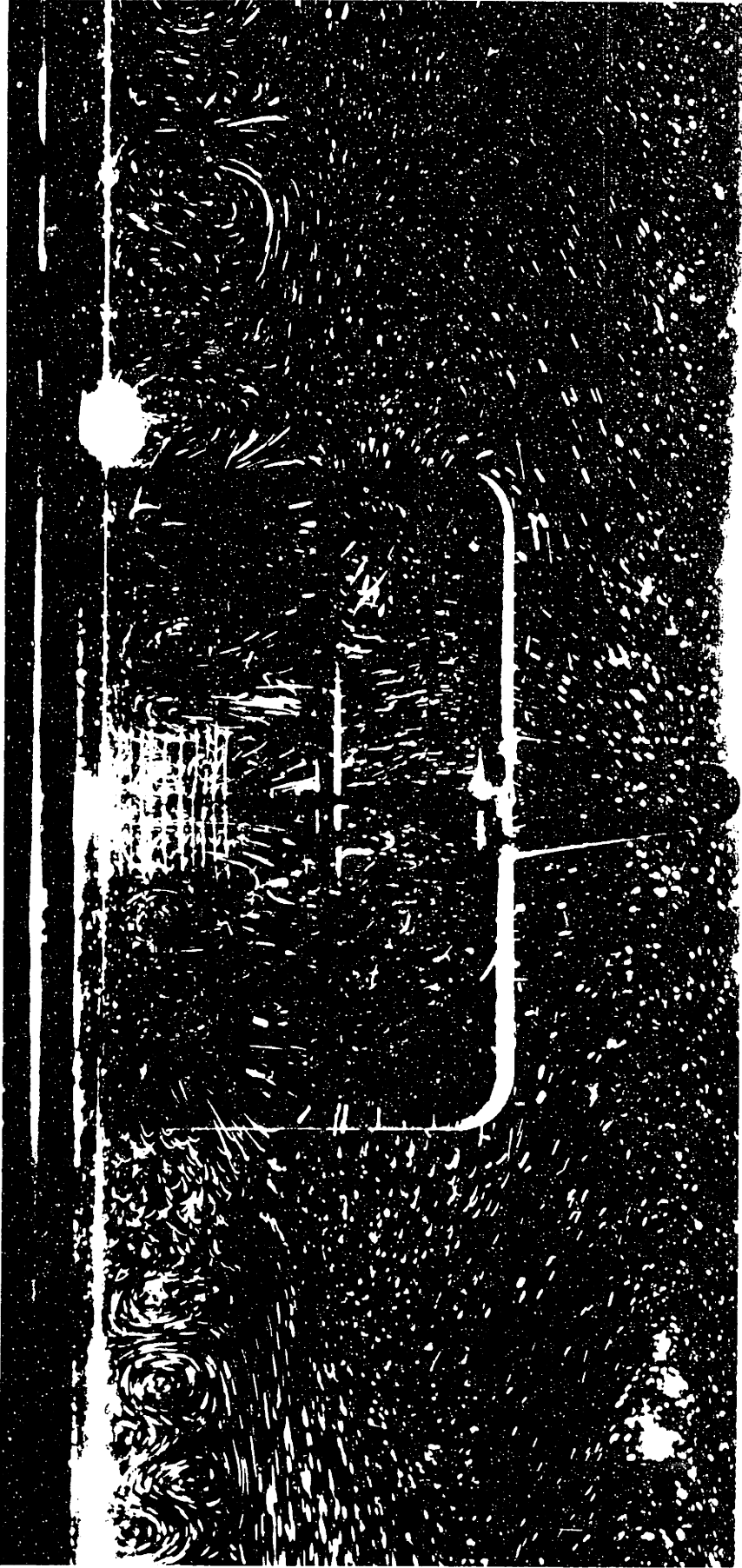


Figure 5.7 The Thermocouple Net in the Model Tank

of a photographic session. This was necessary to avoid heating effects associated with the photographic lighting system. The data collection was started from the 8" transverse plane. (Unless otherwise stated, the location reported for a transverse plane denotes the distance from the doghouse wall.) The net was moved every half inch toward the doghouse wall up to minimum 1.5" transverse plane. Then, the whole procedure was reversed to check the reproducibility of the data.

Once placed at a desired location, the net was allowed to sit several hours to ensure thermal equilibrium with the surrounding fluid and to restore a steady state to the disturbed flow field. Then the data acquisition system was activated to scan the temperature emf's at the beads row by row. Each row of six junction beads was scanned twice at 30 second intervals. It took ten days to collect the temperature data. This long period made the data susceptible to changes in the ambient conditions, in particular due to the abrupt weather changes. But the maximum change in room temperature was less than 2 K for a short period of time. The data obtained in this way are presented in Appendix B for selected transverse planes. The effect of viscous dissipation on the measured temperatures was estimated as negligible (see Appendix C). The consequence of the difference between the thermal conductivity of the thermocouple wire and the glycerine was also considered, but a noticeable effect was not found.

Isothermal contour plots are constructed based on the data. In actual construction, linear interpolation was used between adjacent data points to obtain points of constant contour value and then smooth curves were drawn. The interval between adjacent isotherms represents a 1 K difference ($\sim 41\mu\text{V}$ in emf). The data will be discussed in the next Section.

Before and after the data acquisition period, a sequence of streak photographs was taken for selected transverse planes (with about half-inch spacing) up to the 1.5" plane. The pictures not only provide a more graphical visualization of roll motions, but also form a basis for determining the wavelengths and the penetration depths of roll cells. For a chosen transverse plane, photographs of a complete plane and two close-up roll cells (one for the middle section and one for the side wall section) were taken. For a close-up photograph, a part of the half section, where the net has the least effect, was chosen (thus, the left half section of the transverse plane). A comparison of the longitudinal motions was made by taking pictures before and after the temperature measurements. In spite of the frequent relocations of the net, the overall flow pattern was well preserved. No attempts have been made to obtain multiple exposure photographs for determining the velocity components. The technique does not appear sensitive enough to resolve the early stage of roll development. However, the streak photographs themselves provide a qualitative measure of velocity. All the exposure times were set to 20 minutes for this purpose.

5.4 Physical Nature of Roll Motion

In this Section, the phenomenon of roll motion is isolated from the two-dimensional longitudinal motion. Extensive data obtained for various transverse planes are presented and critically examined. Special features of the development of roll motion are mentioned. Finally, data for a theoretical comparison will be presented.

5.4.1 Three Distinct Stages in the Development of Roll Motion

A close examination of the temperature data and photographs indicates that there are three distinct stages in the development of roll motion

under the sink: the unstably stratified stage followed by the onset of roll motion, the growth stage and the fully developed stage.

The Unstably Stratified Stage

As the longitudinal currents near the top surface move forward across the edge of the isothermal sink, the thermal Vena Contracta, the originally stable stratification in a fluid layer of the current, is suddenly converted into an unstable one. A fluid layer of maximum temperature starts to detach from the edge and progressively penetrate into the deeper level of the currents. Since the currents lose energy to the isothermal sink continuously, the maximum temperature in the currents continue to decrease. During this stage, the combination of these two competing factors for instability (increasing depth and decreasing ΔT) is not enough to generate roll motion. This stage covers roughly the first one inch (8" to 7" plane) from the sink edge in this experiment.

The stratified nature of the fluid stream is best shown in the isothermal plot, Run 611 of Figure 5.8. (From now on, the run number with plane position in parentheses will be used to designate the isotherm contour plots in transverse planes.) This corresponds to the temperature distribution at the 8" transverse plane (the sink edge). Isotherms are nearly horizontal. The maximum temperature layer is located below the top surface. The short distance to the top surface indicates steep gradient in this unstable layer. Since the top surface temperature is 24.4 °C, there are at least 16 isotherms between the top and the 41 °C isotherm. The 42 °C isotherm appearing in the upper left corner is superficial, resulting from the linear interpolation procedure with the limited data available. A close inspection shows that the recorded thermocouple data at the second

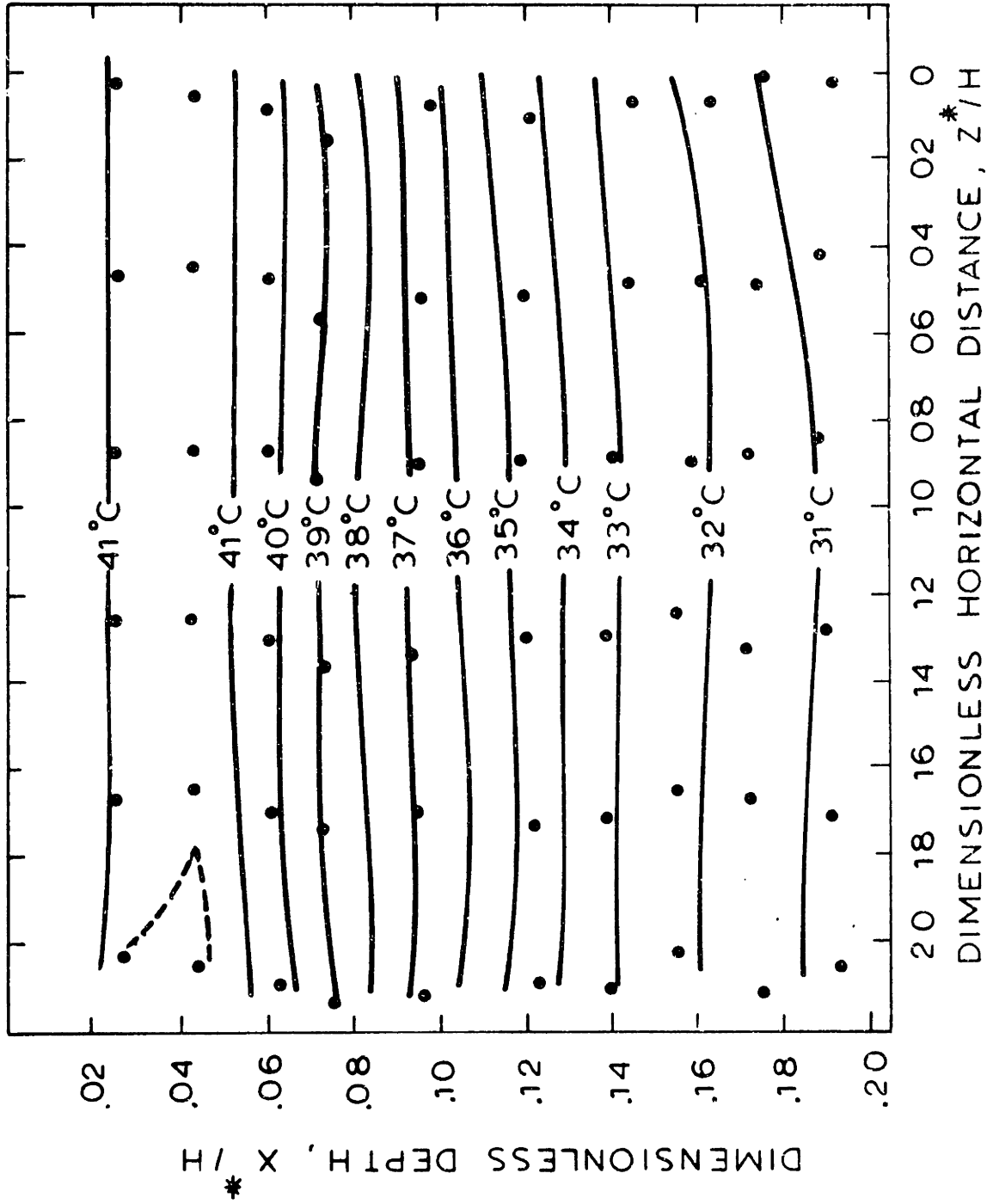


Figure 5.8 Experimental Isotherms at the 8" Transverse Plane ($Y=1.6$)(Run 611)

row of the net (located between the 41°C isotherms) exceed 41°C ($1653\ \mu\text{V}$) by more than $0.7\ \text{C}$ ($28\ \mu\text{V}$). An extrapolation of the steep temperature gradient near the top surface would easily result in the 42°C isotherm between the 41°C isotherms. Below the maximum temperature layer, fluid is in a state of stable stratification. The slightly wider interval of the isotherms near the bottom indicates the slower speed of currents and the influence of the upward turning flow of the return stream.

Onset of Roll Motion

Run 609 (7") shows that the maximum temperature layer moves further down and cools down rapidly. The regular pattern of sinusoidal isotherms is clearly evident in the upper unstable layer, although its amplitude is quite small. The linear stability analysis actually suggests the onset of roll motion around this location (see Chapter VI).

The corresponding streak photograph shown in Figure 5.10 does not reveal any disturbances over the top layer. It is emphasized that the isotherm plots only cover a pair of roll cells in the top $\frac{1}{5}$ of the total depth in this photograph. The point streaks over this top layer, as well as in the core region, indicate the two-dimensional nature of the longitudinal currents which move in the orthogonal direction to the photograph plane. The narrow band of streaks visible under the top unstable layer represents the upward motion of the turning flow in the longitudinal currents. In the corner regions, weak circulation cells are easily detectable. This is a secondary motion termed earlier as the transverse motion. It is caused by the heat leaks through the side walls. The relatively short streaks indicate the weak strength of the circulations. This motion is confined to a small area close to the side walls. It should

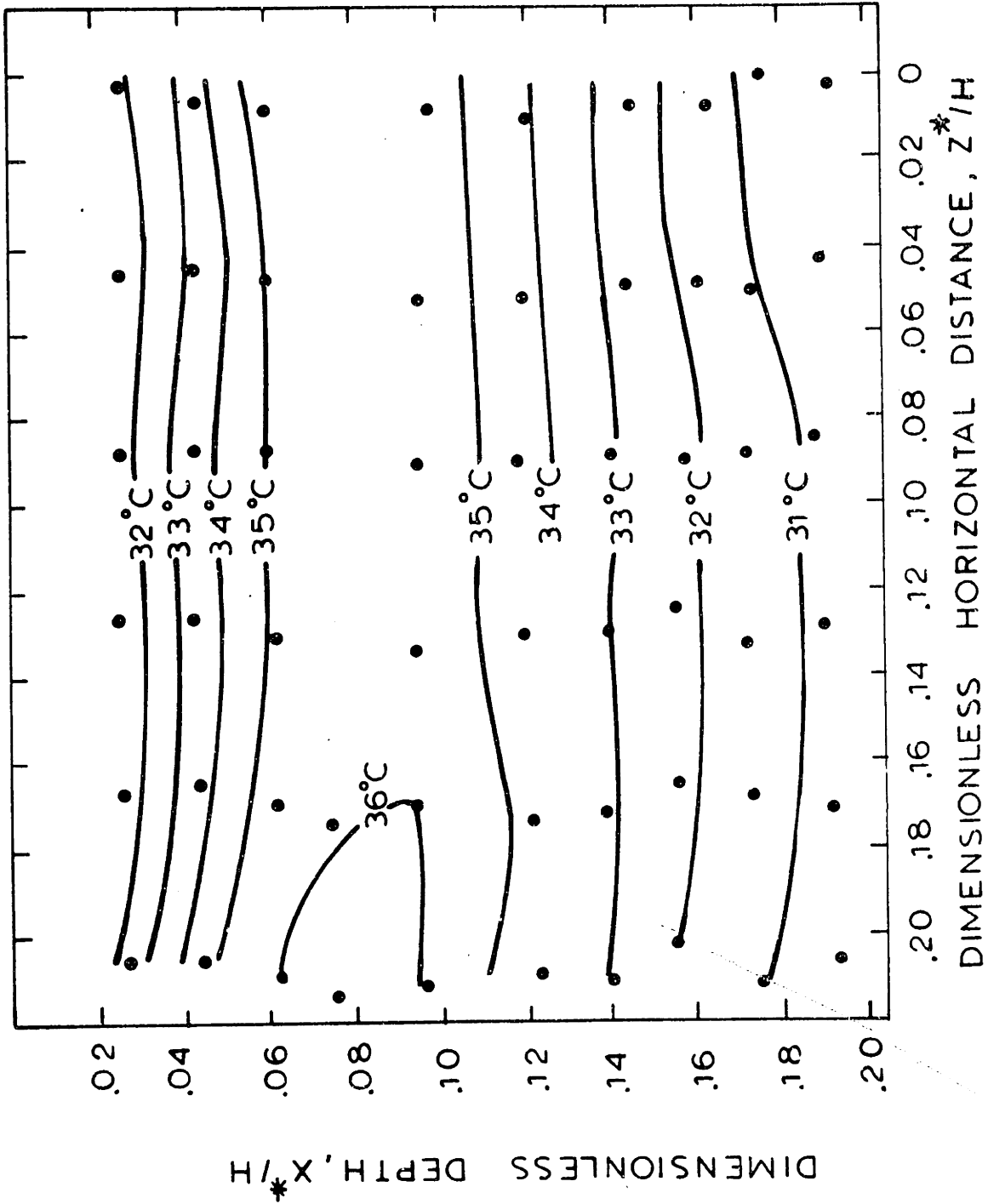


Figure 5.9 Experimental Isotherms in the Roll Cells at the 7" Transverse Plane (Y=1.4). (Run 609)



Figure 5.10 Experimental Streak Lines for the 7" Transverse Plane ($y=1.4$)
(Exposure time 20 minutes)

be noted that the two cells in the upper corners appear only under the sink.

As implied in the above discussion, it is very difficult to pinpoint experimentally the onset of roll motion. At the onset point, all disturbances are supposed to be infinitesimal. Once they occur, the disturbances are convected along by the relatively fast longitudinal currents. Nevertheless, it appears that the onset point occurs somewhere near the 7" transverse planes.

Figure 5.11, a close-up of the 6" transverse plane, is the first photograph taken downstream of the onset. In the middle of the top layer a glimpse of a few pairs of roll cells are clearly detectable. However, stronger evidence of the onset is found in the orientation of the streaks in the layer, which shows both vertical and horizontal inclination at regular intervals. This is in contrast to the streaks in the core region and in the turning flow region. The slight upward motion of the return stream in the core region makes the streaks appear vertical.[§] While the horizontal streaks exhibit the occurrence of disturbances in the currents, the vertical streaks evidently break up the layer into rolls: In each roll, the trace of two vortex eyes are arranged in staggered positions. These roll cells do not appear to contact the turning flow.

Further to the right, the layer does not seem to have developed roll motions. Examination of subsequent photographs shows that this is the case. Incidentally, this region is close to the longitudinal plane to which

[§] Curvature, appearing close to the sides, is due to lens aberration which is further pronounced by the use of a close-up lens at short distance.



Figure 5.11 Experimental Streak Lines of the Roll Motion at the 6" Transverse Plane
($y = 1.2$) (Exposure time 20 minutes)

the vertical rod of the net frame belongs.

It is interesting to estimate the order of magnitude of the disturbance velocities. A comparison of the streaks in the roll region to the band streaks shows that the ratio of lengths is at least $\frac{1}{10}$. Since the band streaks of the turning flow may both start and end up out of the transverse plane, this estimation should be an upper bound. In the longitudinal photograph (Figure 5.5), the ratio of the velocity of the turning flow to the horizontal velocity of longitudinal flow is approximately the same as the ratio of the depth of the circulation eye to the distance between the eye and the bridgewall. This ratio is about $\frac{1}{20}$. In both pictures, the exposure times are identical (20 minutes). We can conclude that the disturbances near the onset of roll motion are at least two orders of magnitude less than the average velocity of the longitudinal currents.

The isotherm plot (Run 607) corresponding to the same plane shows similar behavior. The layer of maximum temperature moves further down and has a slow vertical temperature gradient. Now, the wavy nature of isotherms is pronounced both above and below the layer of maximum temperature. The overall temperature data up to this plane indicate an absolute stability in that the thermocouple readings show no detectable fluctuations at all (loosely defined as greater than $0.1^{\circ}\text{C} \approx 4 \mu\text{V}$).

The Growth Stage

Once the roll motion sets in, the cells grow in depth as they are convected. The growth stops when the roll cells finally penetrate up to the stagnant areas of circulation eye (the elongated ellipsoidal region). In this experiment, the growth stage persists up to the $3\frac{1}{2}$ " transverse plane.

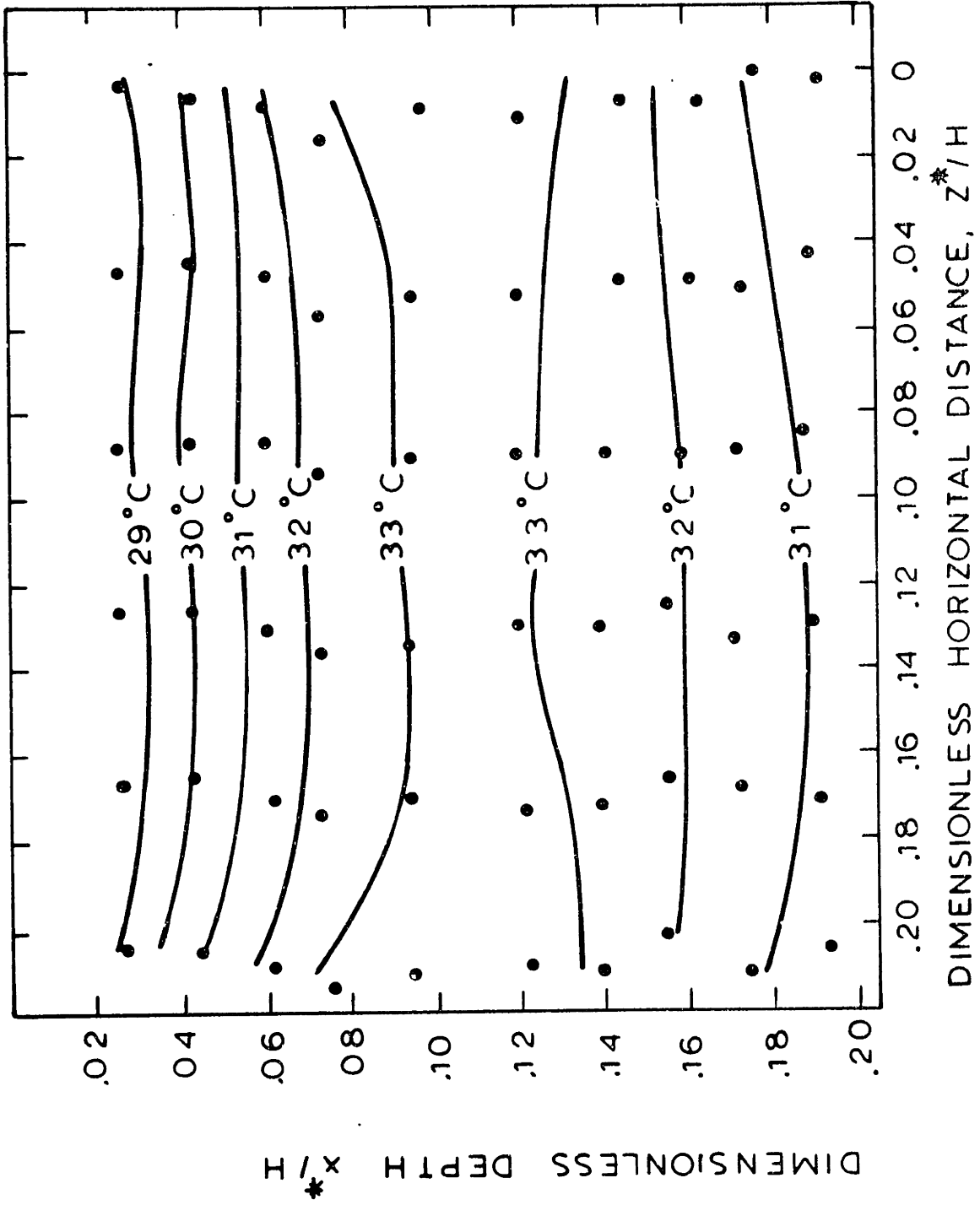


Figure 5.12 Experimental Isotherms in the Roll Cells at the 6" Transverse Plane ($Y=1.2$), (Run 607)

This stage can be characterized by the following features:

- (a) Constant wavelength cells
- (b) Generally staggered positions for vortex eyes
- (c) Penetrative nature
- (d) Small fluctuations of transient type.

Of these, the last two features appear unique in this stage and seem to be closely associated with the influence of the turning flow. These features will be examined along with the development of roll motion.

The roll wavelengths in the experiment which were determined from streak photographs at six different transverse planes are listed in Table 5.5. The wavelength has a physical significance only relative to the depth of fluid layer occupied by the roll motion. It is this ratio that the linear stability analysis can predict at the onset condition. There are two individual cells in one wavelength span. In the Rayleigh-Bénard problem, it is known that the liquid ascends at the cell centers and descends at the cell boundaries (Stuart, 1963). In this experiment, however, the ascending streams seem to be the more convenient choice for cell boundaries. The data clearly indicate that the absolute wavelength is maintained for each of the roll cells. Column 4 shows that a smaller roll continues to remain smaller during the entire development of roll motion. The other interesting point is that the aspect ratio (wavelength/depth) is well preserved in any transverse planes. Even though the dimensions vary roll by roll, the structure remains intact in most of the roll cells and the roll cells grow only in depth.

Figure 5.13 and 5.14 represent structures of roll cells in the growth stage (5" and 4" transverse planes). The vortex centers of roll cells are

TABLE 5.5

Observed Wavelength (W) and Depth (D) of the Roll Motion
(unit in inch)

Plane Location	roll 1		roll 2		roll 3 [†]		roll 4		$\lambda \equiv \frac{W}{D}$	$a \equiv \frac{2\pi}{\lambda}$
	W	D	W	D	W	D	W	D		
6 "	0.90	0.42	0.89	0.43	0.88	0.42	-	-	2.10	2.99
5½"	-	-	0.92	0.50	0.90	0.49	0.86	0.48	1.82	3.45
5 "	0.90	0.61	0.91	0.60	0.88	0.61	0.83	0.56	1.48	4.25
4½"	-	-	0.94	0.84	0.91	0.82	0.86	0.74	1.13	5.56
4 "	0.95	0.97	0.94	0.94	0.91	0.94	0.84	0.87	0.98	6.38
3 "	0.93	1.23	0.93	1.27	0.90	1.17	0.85	1.03	0.77	8.16
2 "	0.93	1.22	0.91	1.29	0.92	1.24	0.85	1.14	0.74	8.49
Average	0.92		0.92		0.90		0.85			

† Wavelength of the roll 3 is marked in photographs.

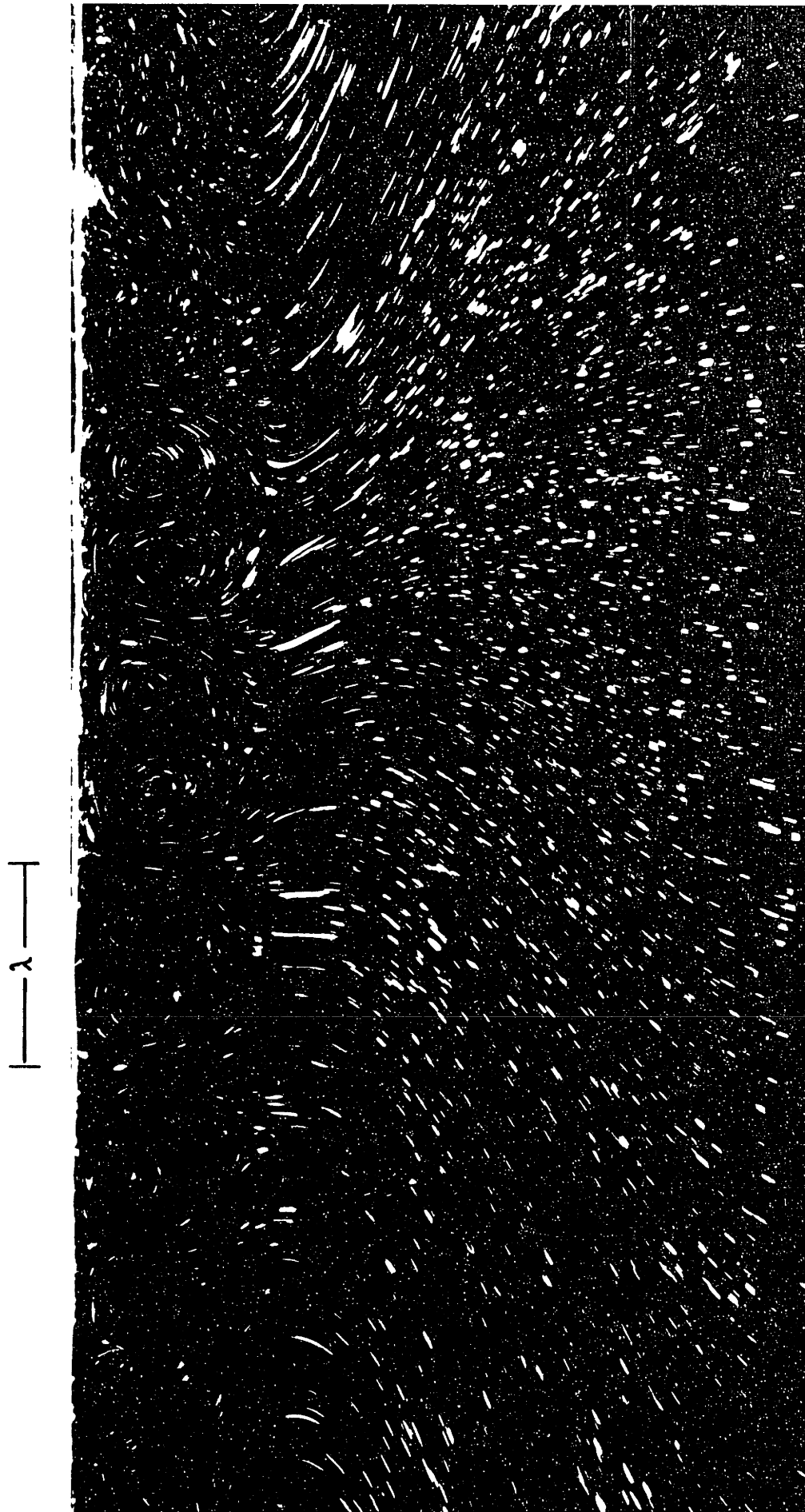


Figure 5.13 Experimental Streak Lines of the Roll Motion at the 5" Transverse Plane
($y = 1.0$) (Exposure time 20 minutes)

|— λ —|

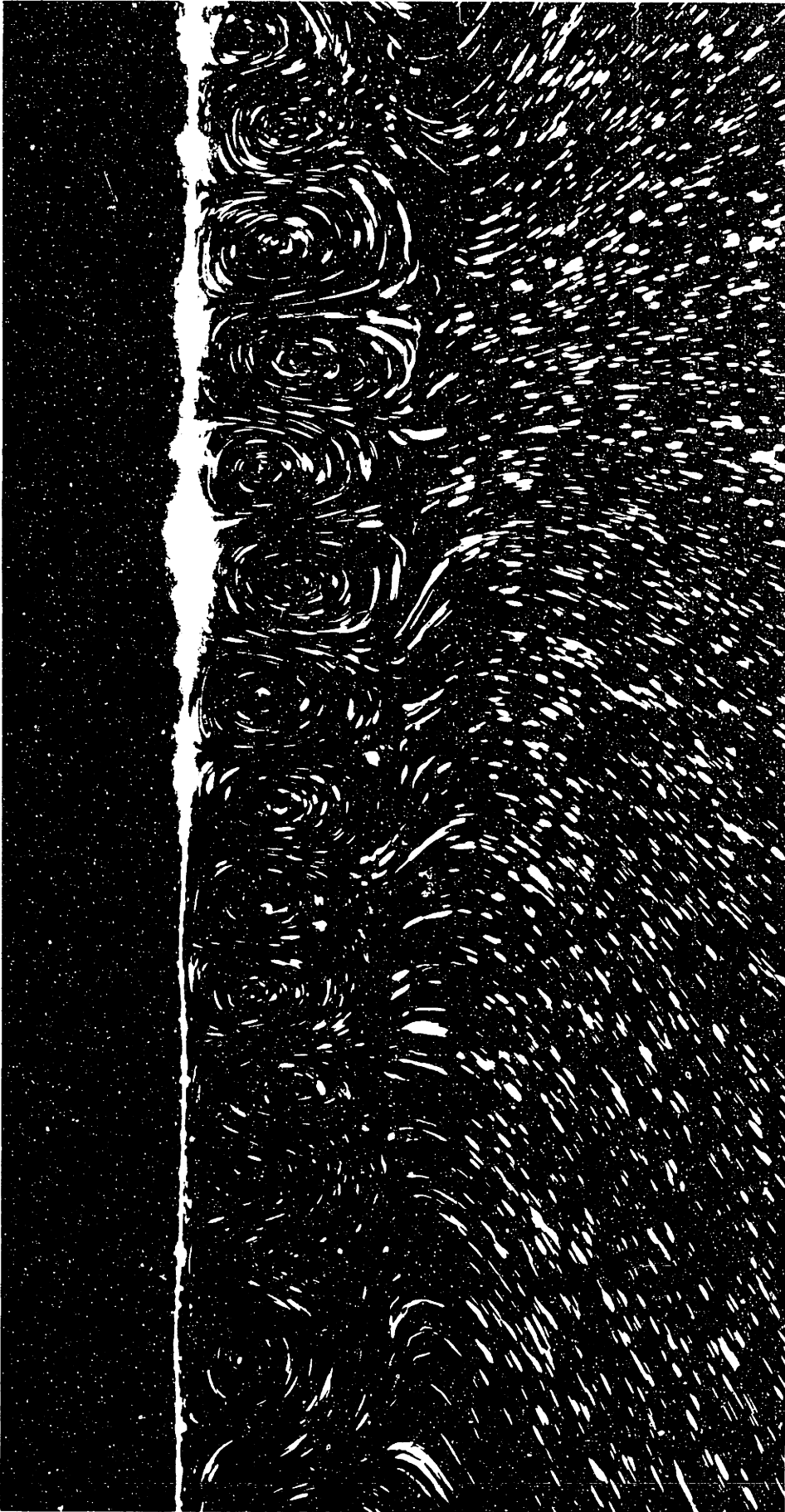


Figure 5.14 Experimental Streak Lines of the Roll Motion at the 4" Transverse Plane
($y = 0.8$) (Exposure time 20 minutes)

arranged in a staggered fashion. The roll cells marked in Figure 5.14 show an exceptional case, where the roll cell structures have a symmetric arrangement with the cell eyes being placed at the same horizontal level.

Associated with the growth stage is the upward turning flow of the return circulation currents. As previously discussed, these appear as a narrow band of streaks under the roll cells. The turning flow always appears to converge into the ascending interface of the roll boundaries. The turning flow velocity is noticeably higher than that of the roll disturbance in the earlier stage, but becomes comparable as the rolls penetrate deeper into the longitudinal currents. The temperature of the ascending fluid is higher than that of the descending fluid at the same transverse level. Since the refractive index of glycerine decreases with higher temperature, the scattered light from the ascending fluid is always less refracted than that from the colder fluid. This is responsible for the clear curvature appearing at the top surface line. The points where the ascending streams meet the top surface are clearly lower than those corresponding to the descending fluid. Also notice that the descending fluid, plunging down along the cell interfaces, is decelerated and spreads laterally at the level of the turning flow. The separation points of the descending fluid indicate behavior similar to that of a jet impinging against a plate.

The above discussion points out the influence of the turning flow. Nevertheless, this influence does not undermine the degree of freedom which the roll motion can find in the stratified layer. That is, the roll cells grow by penetrating into the stably stratified region below the adverse temperature gradients without changing their wavelength. It should again be

emphasized that the longitudinal currents have a much higher velocity component relative to any of these flow streams.

The local influence of the turning flow can be understood by examining the corresponding isotherm plots, Runn 622 and Run 616. Compare the relative positions of the isotherm envelope of 32°C. Since the longitudinal currents always lose energy to the top surface (as well as through the stably stratified layer), the upward displacement of the hot fluid envelope seems physically improbable. However, the continuous influx of the turning flow into the upper longitudinal currents can provide an upward inertial momentum to the diverging stream from the thermal Vena Contracta. Since the turning flow interacts through the ascending fluid in roll motion, only the hot envelope of fluid is displaced. As the roll disturbances grow stronger, this influence diminishes.

The influence of the turning flow is also associated with the fluctuation observed in the thermocouple readings. This fluctuation is observed only in the growth stage. The strong influence of the turning flow in the earlier stage (Run 622) makes this fluctuation appear in the ascending fluid. As the influence diminishes, the fluctuation occurs in the descending stream. Even though the maximum fluctuation is quite small (about 20 μ V or 0.5°C, see the data in Appendix B), the reproducibility check indicates its real existence (Section 5.4.2). This slightly transient nature may be responsible for the staggered eye positions and the unbalanced growth of cells which results in some eventual cell destruction. (This appears in the next stage.) Unfortunately, the quantitative influence of this on roll motion (relative to the pure unstable stratification) cannot be determined in this experiment.

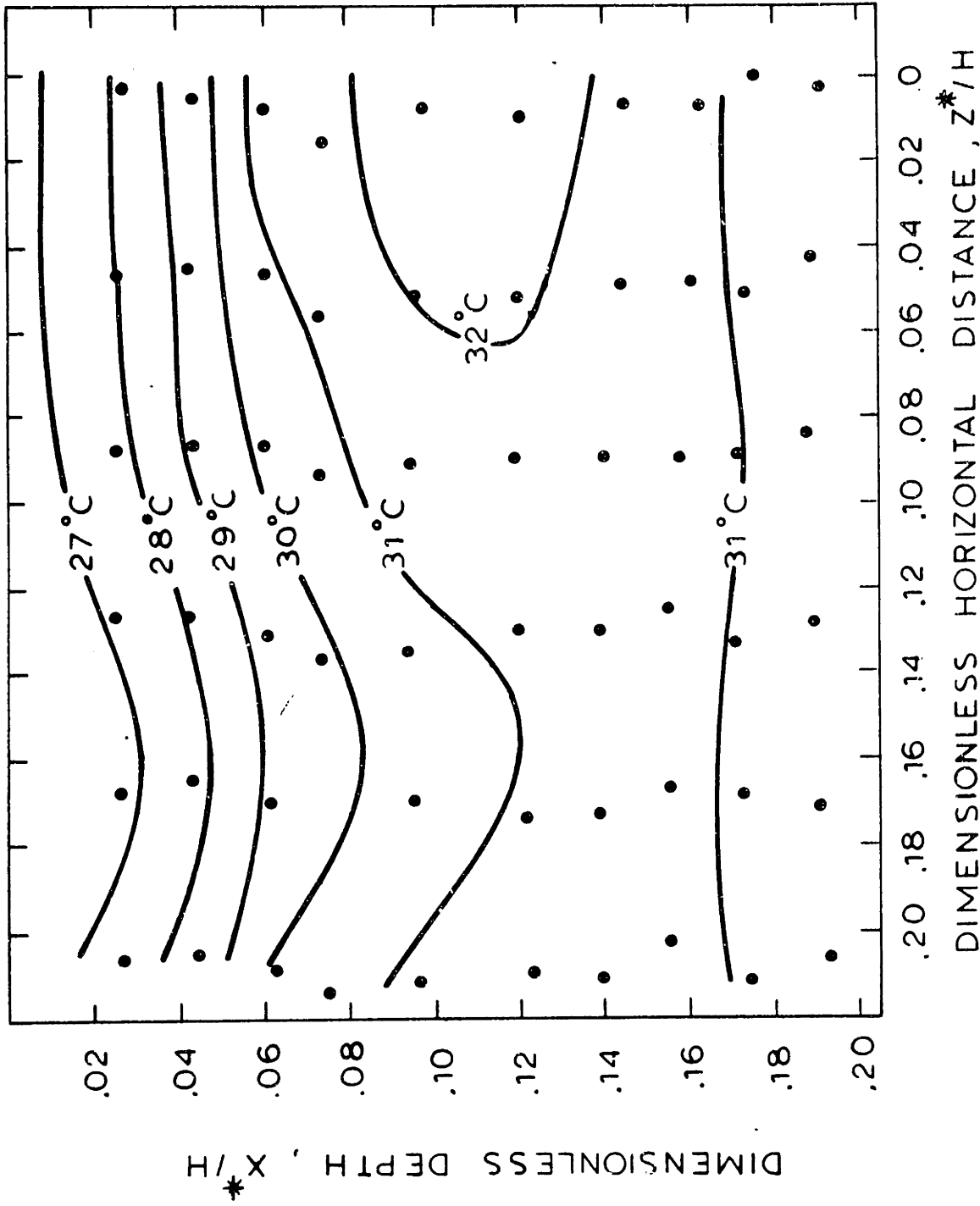


Figure 5.15 Experimental Isotherms in the Roll Cells at the 5" Transverse Plane ($Y=1.0$). (Run 622)

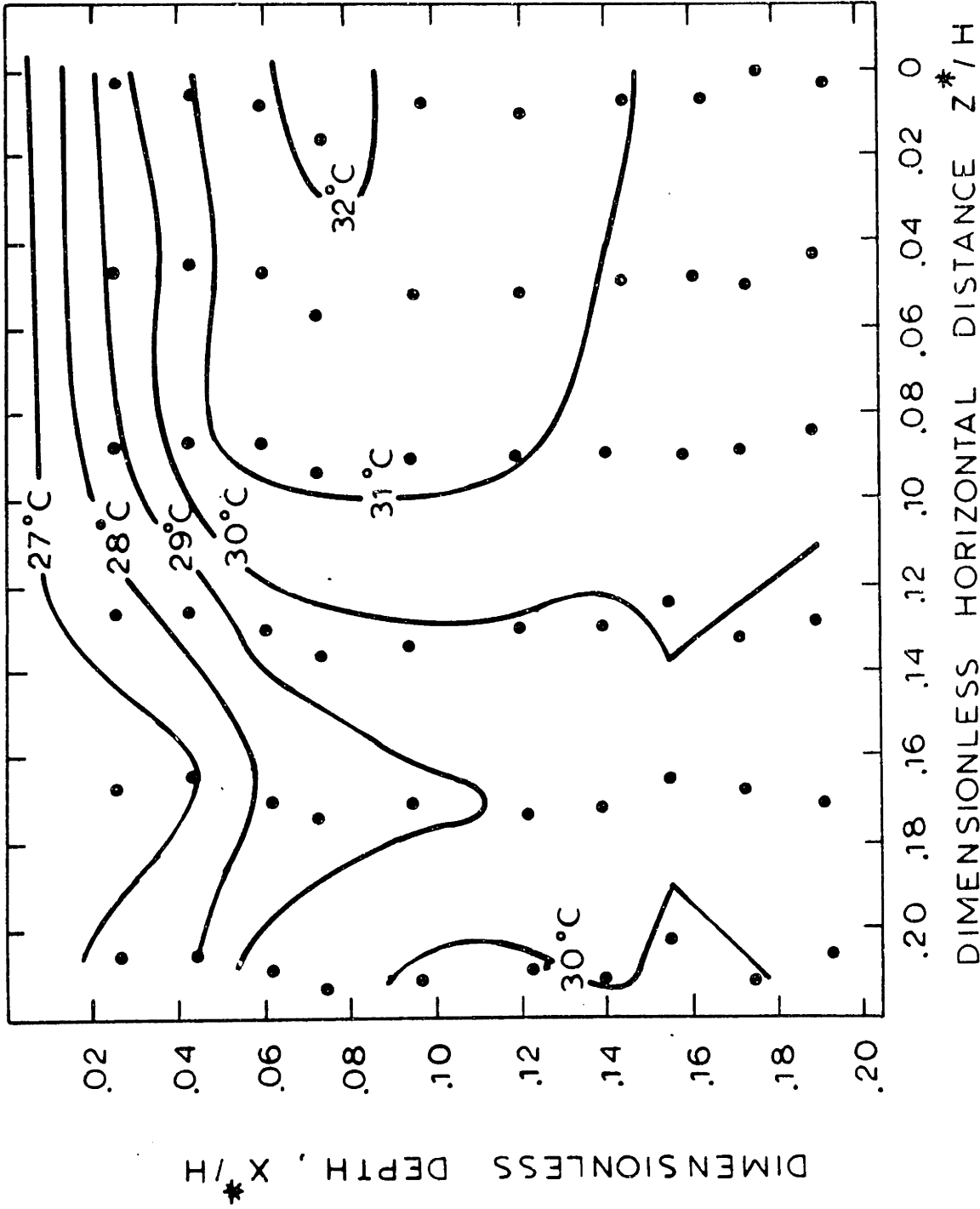


Figure 5.16 Experimental Isotherms in the Roll Cells at the 4" Transverse Plane ($Y=0.8$). (Run 616)

On the other hand, all the isotherm plots clearly show that the ascending flow is heated in a broader lateral region, while the descending flow plunges down in a narrow area. Also, the temperature gradients in the ascending flow are steeper than those in descending flow. This behavior is particularly pronounced in Run 616, where the disturbance velocities are comparable to the turning flow velocity. The narrow band of the descending flow and the weak conduction isotherms point to a stronger downward convective mode. The disturbed state in a transverse plane motion is somewhat analogous to a convection in a stagnant fluid with an internal heat source. It is this analogy that is exploited in the linear analysis in conjunction with the source-sink approximation method.

The Fully Developed Stage

Once roll motion extends down to the level of the longitudinal circulation eye (elongated ellipsoidal region), the growth stage ceases to exist and makes a transition to a fully developed stage. This stage is not influenced by the dynamics of the turning flow, since the roll motion encounters almost stagnant longitudinal flow when it reaches the bottom of the roll cells. This allows the fluid to flow freely in the lateral direction.

The flow patterns exhibiting this behavior are shown in Figures 5.17 and 5.18. While it is difficult to locate the exact transition point, the temperature data and the photographic evidence indicate that this stage develops between the 4" and 3" transverse planes. Notice that the band streaks of the turning flow have completely disappeared. Streaks at the bottom of roll cells become longer. The roll cells still manage to grow, because the elongated cell eye is slightly slanted. Most of the roll cells



Figure 5.17 Experimental Streak Lines of the Roll Motion at the 3" Transverse Plane
($y = 0.6$) (Exposure time 20 minutes)



Figure 5.18 Experimental Streak Lines of the Roll Motion at the 2" Transverse Plane
($y = 0.4$) (Exposure time 20 minutes)

are still intact in their structure.

A few cells begin to disarray and finally coalesce, as shown in the left side of the photographs. However, these cells have already shown irregularities in the earlier stage. Moreover, the disintegration is not due to the influence of the heat leaks at the side wall. Figure 5.19 shows the roll cell region close to the side wall at the 3" transverse plane. The cells in disarray at the upper left corner are the identical cells that appeared at the right upper corner in Figure 5.17. Two pairs of rolls are still intact in the middle, but their wavelengths are longer (~ 1.09" and 1.20") than those reported in Table 5.5. (The distance between two thermocouples at the side wall is one inch.) The corner cell has also grown larger and penetrates deeper. Similar pictures taken at other planes show the same behavior.

The corresponding isotherm plots are shown in Figure 5.20 and 5.21. The data show that fluctuations in temperature have completely disappeared. Colder fluid which originates from the unstable layer plunges down and finds its same temperature level in the stably stratified layer. Also note that the hot fluid envelope continues to cool down without its upward displacement. The broader ascending flow is similar to the previous stage.

This stage finally ends when the longitudinal currents move downward along the doghouse wall. This downward flow eventually destroys the roll cell structure and forms a return flow as a countercurrent stream below the circulation cell eye. The two-dimensionality of the flow is restored, as shown in Figure 5.22.

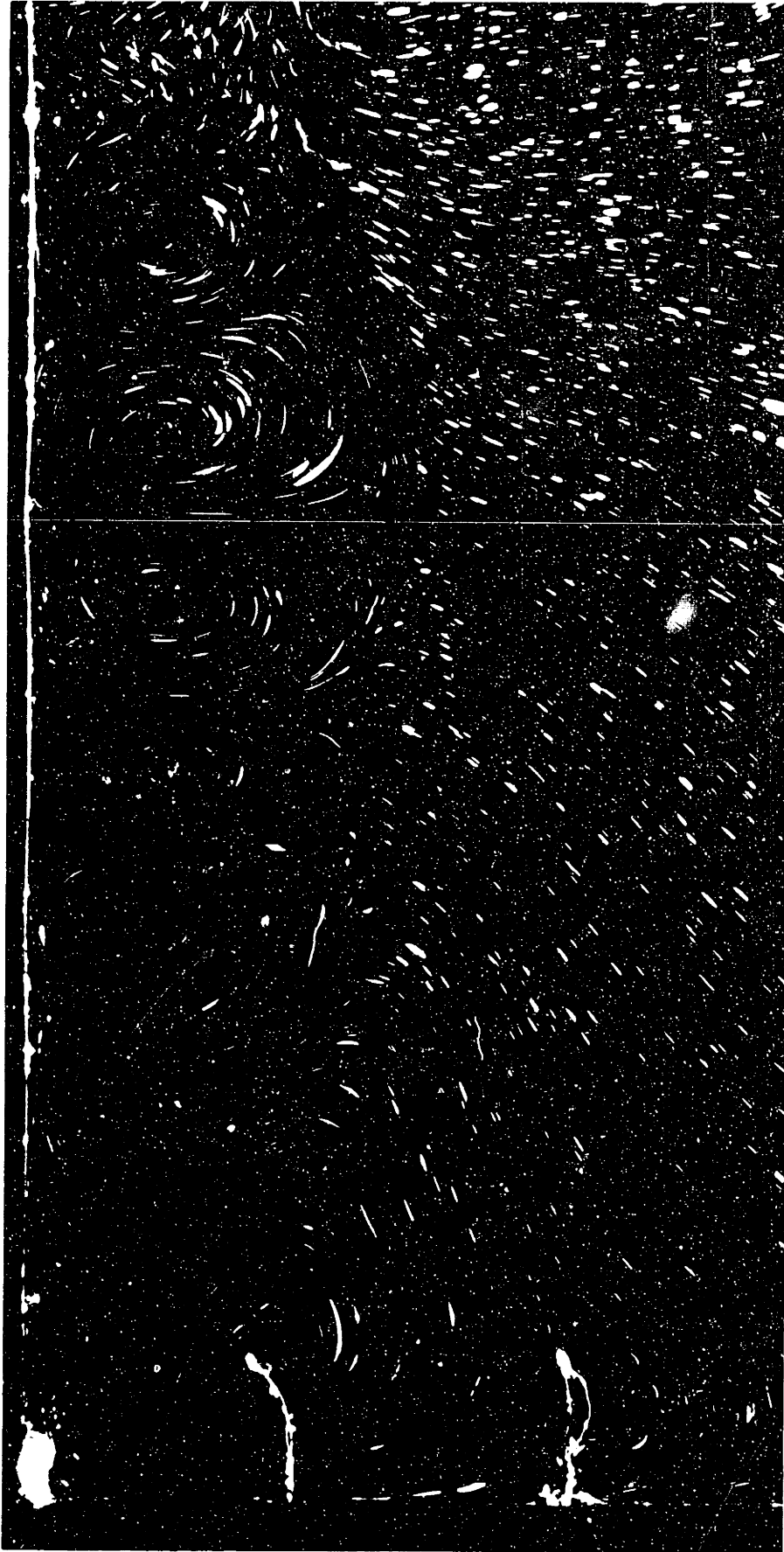


Figure 5.19 Experimental Streak Lines for the 3" Transverse Plane ($y = 0.6$) showing Roll Cells close to the Side Wall (Exposure time 20 minutes)

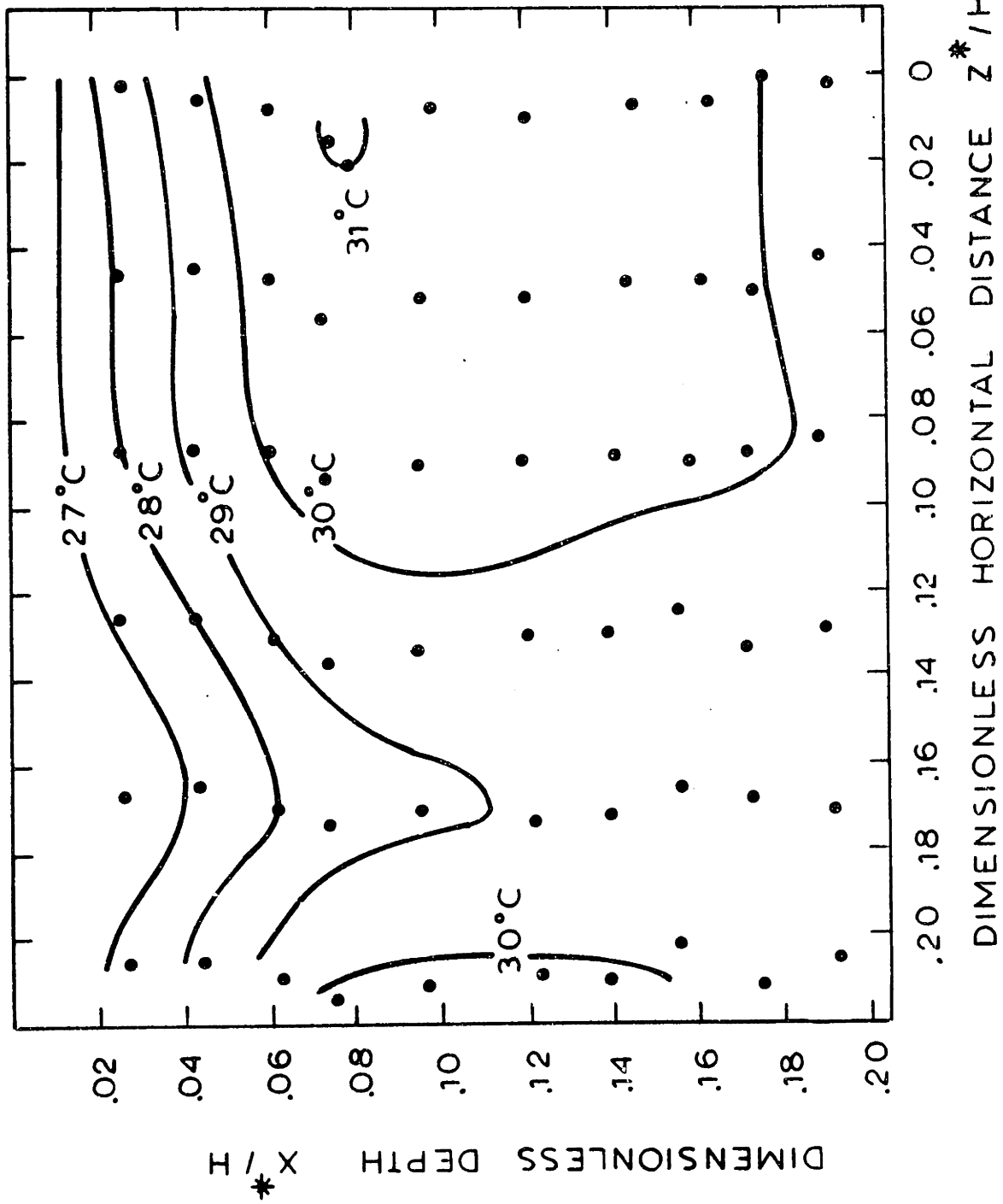


Figure 5.20 Experimental Isotherms in the Rolls at the 3" Transverse Plane (Y=0.6).(Run 618)

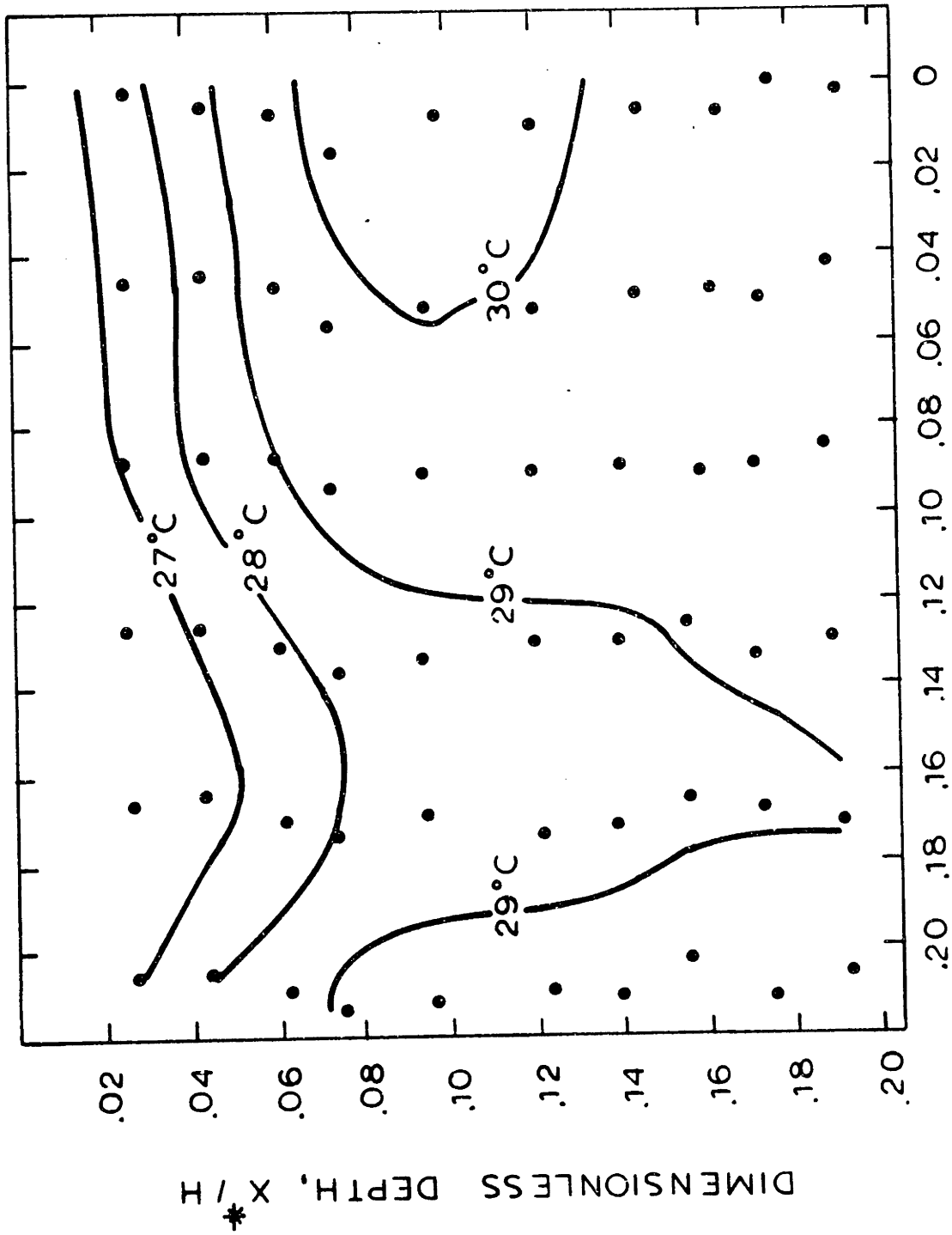


Figure 5 21 Experimental Isotherms in the Roll Cells at the 2" Transverse Plane ($Y=0.4$), (Run 620)

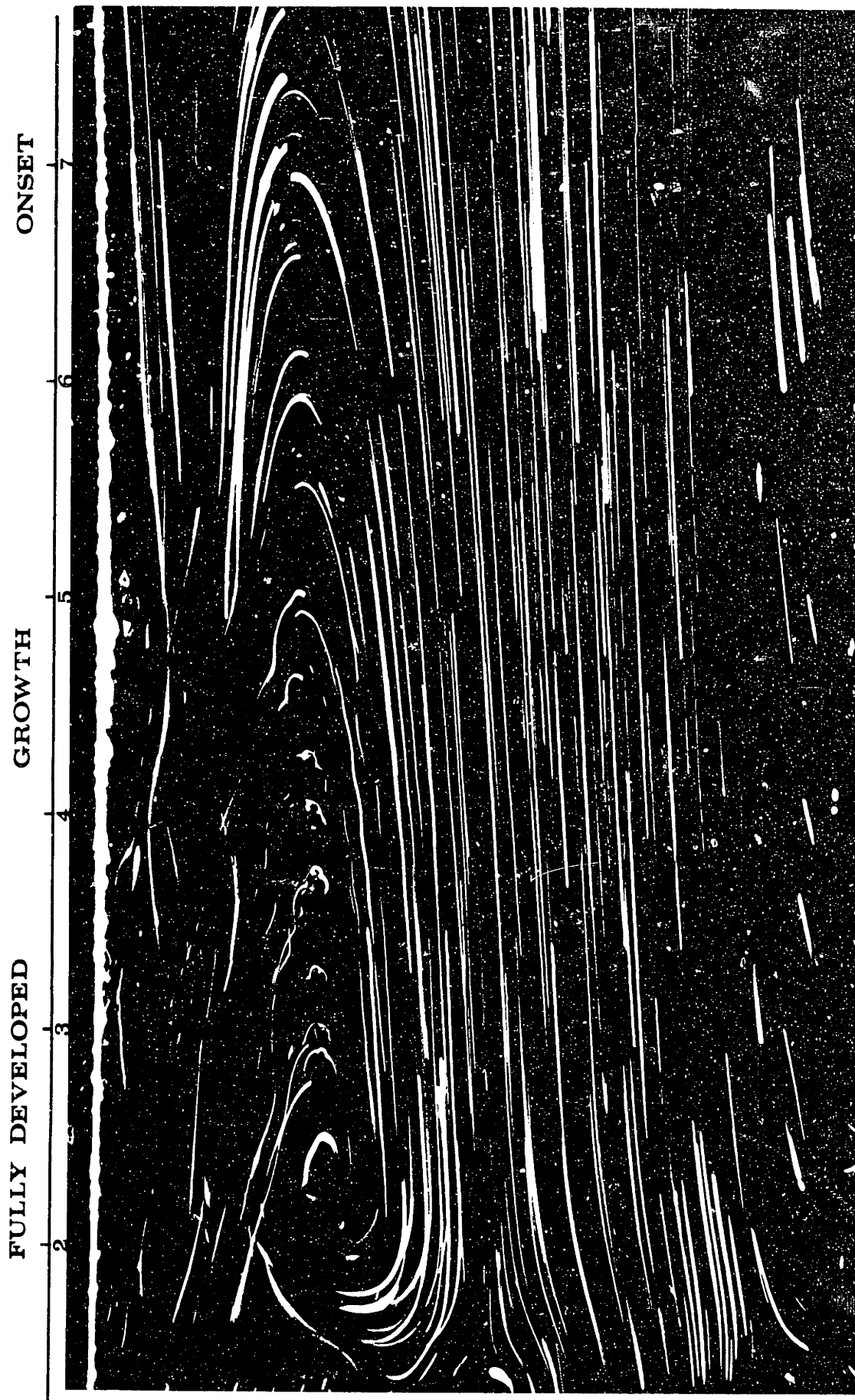


Figure 5.22 Experimental Streak Lines in the Roll Motion Region for the Longitudinal Plane ($z = 0$) (Exposure Time 20 minutes)

Recapitulation

We described how roll motion develops after the longitudinal currents cross the edge of the sink. The three distinct stages, identified during the course of roll development, are summarized in a close-up photograph, Figure 5.22. It is clearly evident that disturbances in the growth stage are penetrating in depth within the longitudinal currents. Only when the rolls are fully developed, does the return flow limit the growth.

5.4.2 Reproducibility of Temperature Data

One might question whether the long duration of the experiment and the frequent relocation of the net affected the reproducibility of the data. Also, we are concerned about the validity of small fluctuations of a transient nature which were observed at a specific area in the growth stage of the roll motion. To answer these questions, the temperature data were taken at least twice for every transverse plane.

Figure 5.23 shows two sets of data taken at the 5.5" transverse plane. Six and one-half days passed between the time when the solid and dashed line data were taken. During the time interval, more than a dozen relocations of the thermocouple net were made. The solid isotherms were taken at noon and the dashed ones at midnight. The two sets of isotherms show excellent agreement in overall shape. There appears to be no sign of translational (lateral) movement by the roll. In spite of the net relocations, the wavelength of the roll cells remains constant and the roll cells appear locked in the position. The maximum temperature difference between the two sets of data is less than $\frac{1}{2}^{\circ}\text{C}$ ($21\ \mu\text{V}$) and it occurs around the place where the fluctuations are significant, namely, the ascending flow regime at both upper vertical sides. This is the place

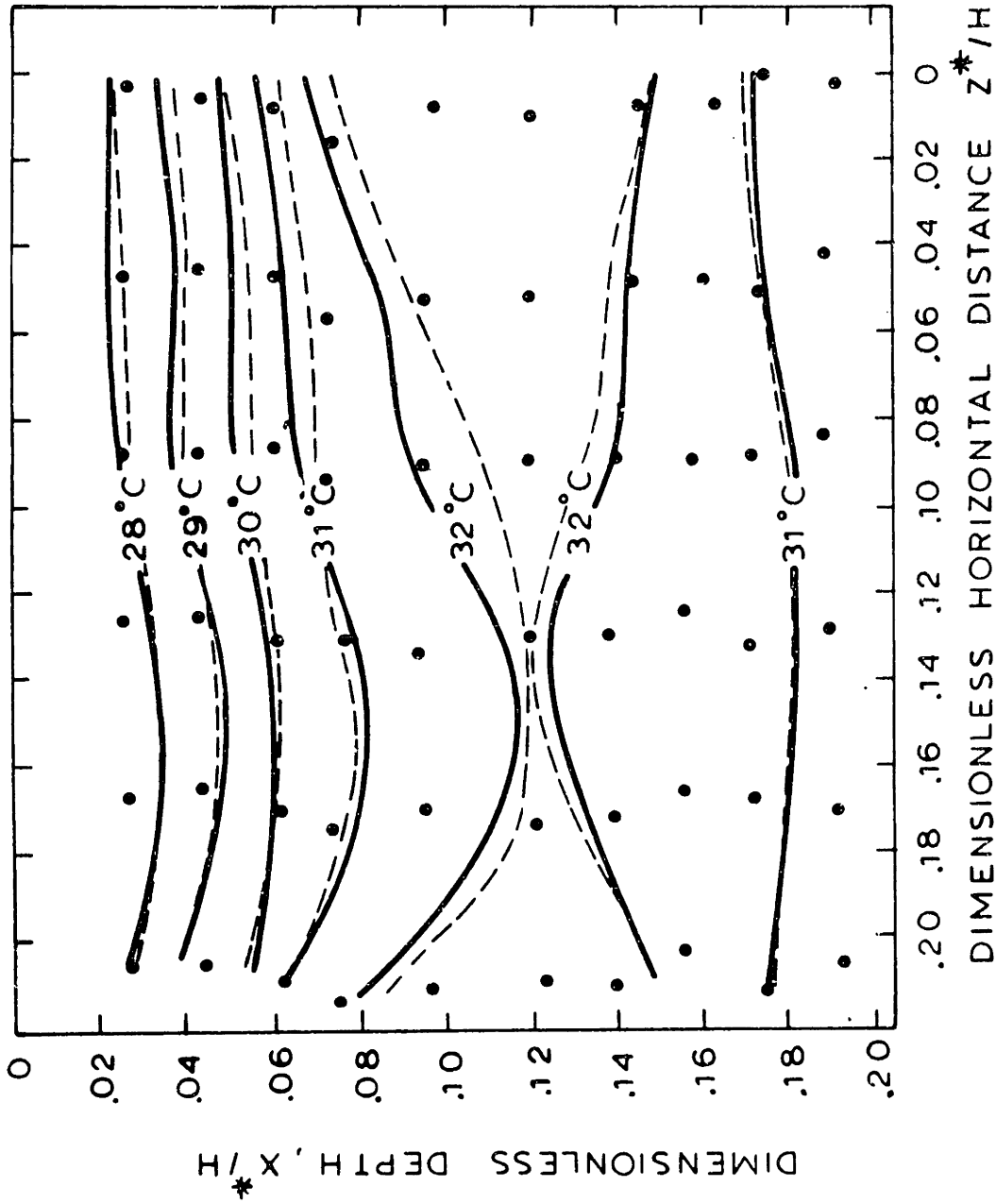


Figure 5.23 Reproducibility Test for Experimental Temperature in the Roll Cell at the $5\frac{1}{2}$ Transverse Plane ($Y=1.1$)

Run 606 - Solid Line Taken at 12.15. 1977

Run 623 - Dotted Line Taken at 12.21. 1977

where the turning flow affects the cell boundaries. In the solid isotherms, the fluctuations are about $0.25\text{ }^{\circ}\text{C}$ ($10\text{ }\mu\text{V}$) and occur at somewhat lower locations. This is in contrast to the data at the bottom layer, where fluctuations are at most a few microvolts.

The apparent relocation of the $32\text{ }^{\circ}\text{C}$ isotherm is somewhat deceptive, because the temperature gradients are low in this region. The most significant departures occur for the isotherms of 30 and $31\text{ }^{\circ}\text{C}$ and are comparable in magnitude to the fluctuations observed.

The data at the stratified stage and the fully developed stage do not show any comparable fluctuations, while the data at the growth stage always show fluctuations in the ascending flow and descending flow. These observations suggest that the fluctuations are real.

It has already been mentioned that the cause of these fluctuations is probably associated with the turning flow. In this regard, it is worthwhile to consider short-period temperature fluctuations in Bénard convection observed by Willis and Deardorff (1967). They observed the sudden appearance of a well-defined period in the temporal temperature fluctuations at a single thermocouple located at a mid plane. The fluctuations occurred intermittently, however, only if the Rayleigh number exceeded a value well above the critical one. This number increases with Prandtl number. The fluctuations discussed above, however, occurred near the onset point. Hence, one might disregard any analogy between these fluctuations.

However, in the same paper, it was reported that the fluctuations seem to occur in a region where the temperature is near an extremum and where vertical convection from the boundary regions would be expected. Since our lower boundary is flexible and not well-defined and disturbances

caused by the turning flow can be considered as a sort of finite amplitude disturbance, it is possible for the fluctuations to occur earlier than in better controlled experiments. If this is the case, then the fluctuations originate locally in the turning flow and are convected in the longitudinal currents to the descending flow area. Thus, they could appear only on the vertical cell interfaces. Since the fluctuations were ascertained from only two data points taken at 30 second intervals, more data would be required before the complete nature of the phenomenon can be ascertained.

5.5 Comparison of Experimental Temperature Data and Two-Dimensional Numerical Solutions

It is now evident that the existence of roll motion in the sink region not only alters the structures of the flow, but also has a significant influence on overall temperature distribution in the enclosure. The energy required to convert the longitudinal currents into roll motions comes from within the fluid (even though it originated at the heater surface). The motion thus generated will clearly contribute towards equilibrating temperature differences and result in the heat transfer enhancement in the region where it exists. It is manifested in a lower average temperature in the enclosure than that predicted using the two-dimensional assumption. These conclusions were made by Curlet, using limited data obtained from his experiment. Interested readers should refer to his thesis. In this Section, the intent is merely to indicate the limitations of the two-dimensional numerical solution through a discussion of the more detailed data available from this thesis.

For this purpose, the temperature fields presented in Section 5.2.2 will be directly compared to the experimental data in Figure 5.24. Note

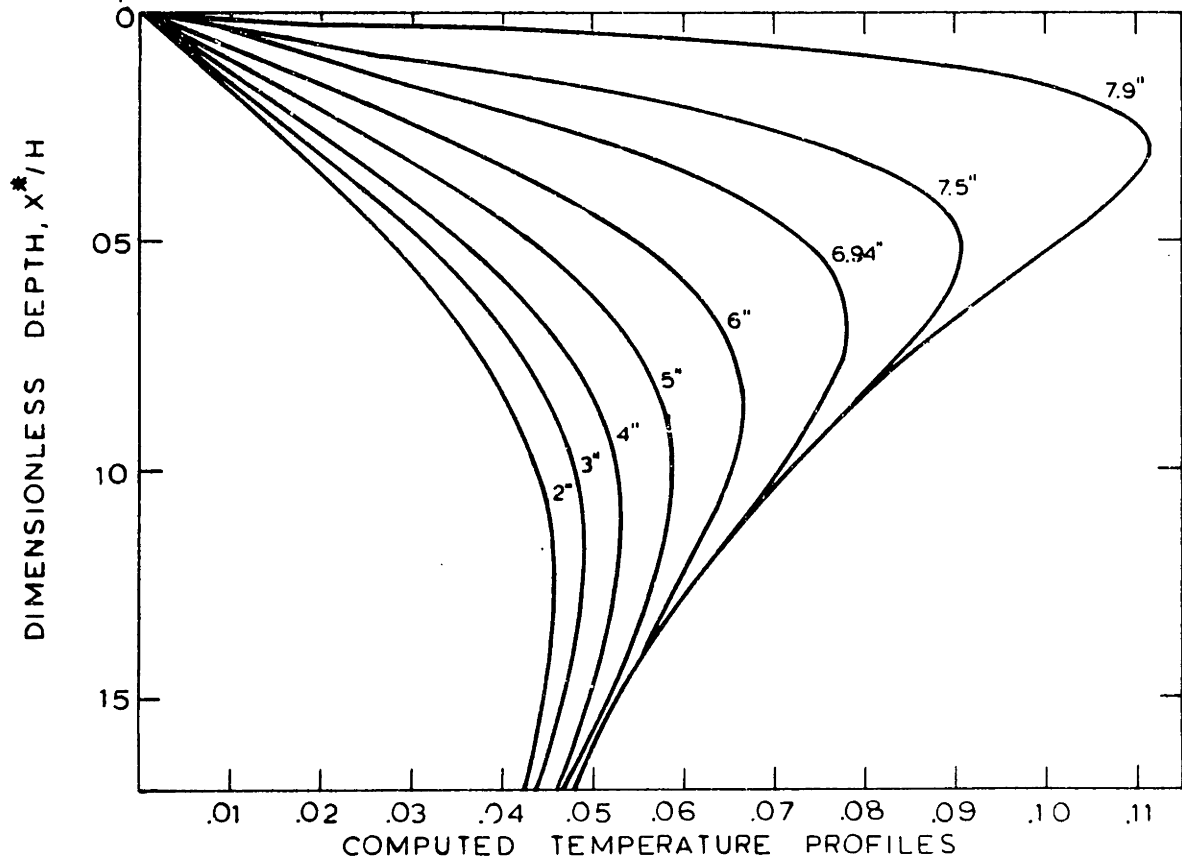
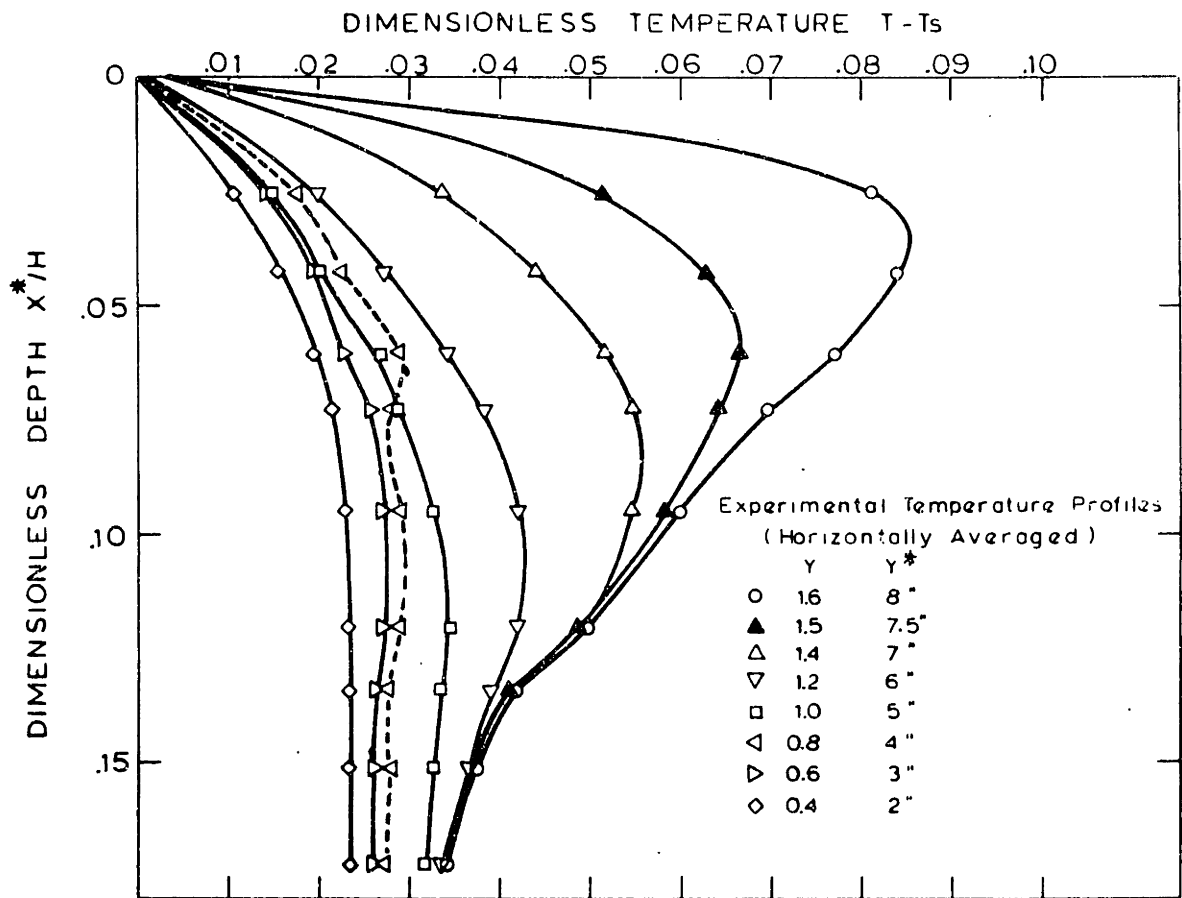


Figure 5.24 Comparison of Experimental and Computed Temperature Profiles in the Roll Region

that the excess temperatures from the isothermal sink temperatures are plotted, i.e. $T - T_s$. Each of the experimental temperature profiles was obtained by taking the horizontal averages of the data over one cell. The dimensionless scale of 0.01 is equivalent to an actual temperature difference of about 2.1 °C.

Several differences are evident. First, the experimental temperatures are consistently lower than those predicted numerically. The difference diminishes from the sink edge ($\sim 5^\circ\text{C}$) to the 2" plane ($\sim 4^\circ\text{C}$). In the core region, say $x > 0.17$, the trend is reversed. The absolute value of the deviation increases from 3°C to 4°C .

Second, the positions of maximum temperature indicate additional complexities. In general, more penetration is achieved in the experiment. This particularly true after the roll motion has started. However, even the profiles of the average temperatures are not continuously cooled down, as discussed in the growth stage (Section 5.4.1). Once roll cells start to grow, particularly under the influence of the turning flow, the overall temperatures close to the top surface appear to warm slightly with downstream distance. This is shown as a dotted line. Below the level of this abnormal heating, the temperature profiles are nearly flat (constant). These observations are due to the true three-dimensional nature of the flow. The fluid, which originated at the hotter part (bottom of the unstable gradient) of the earlier stage, starts to diverge at the edge of the sink. As the disturbances grow, the fluid parcels follow a spiral path within a cell. When the original fluid in a spiral advancement reaches to the top, the maximum heating effect would appear in that region. The heat transfer enhancement is evident from the steeper (compared with the two-dimensional

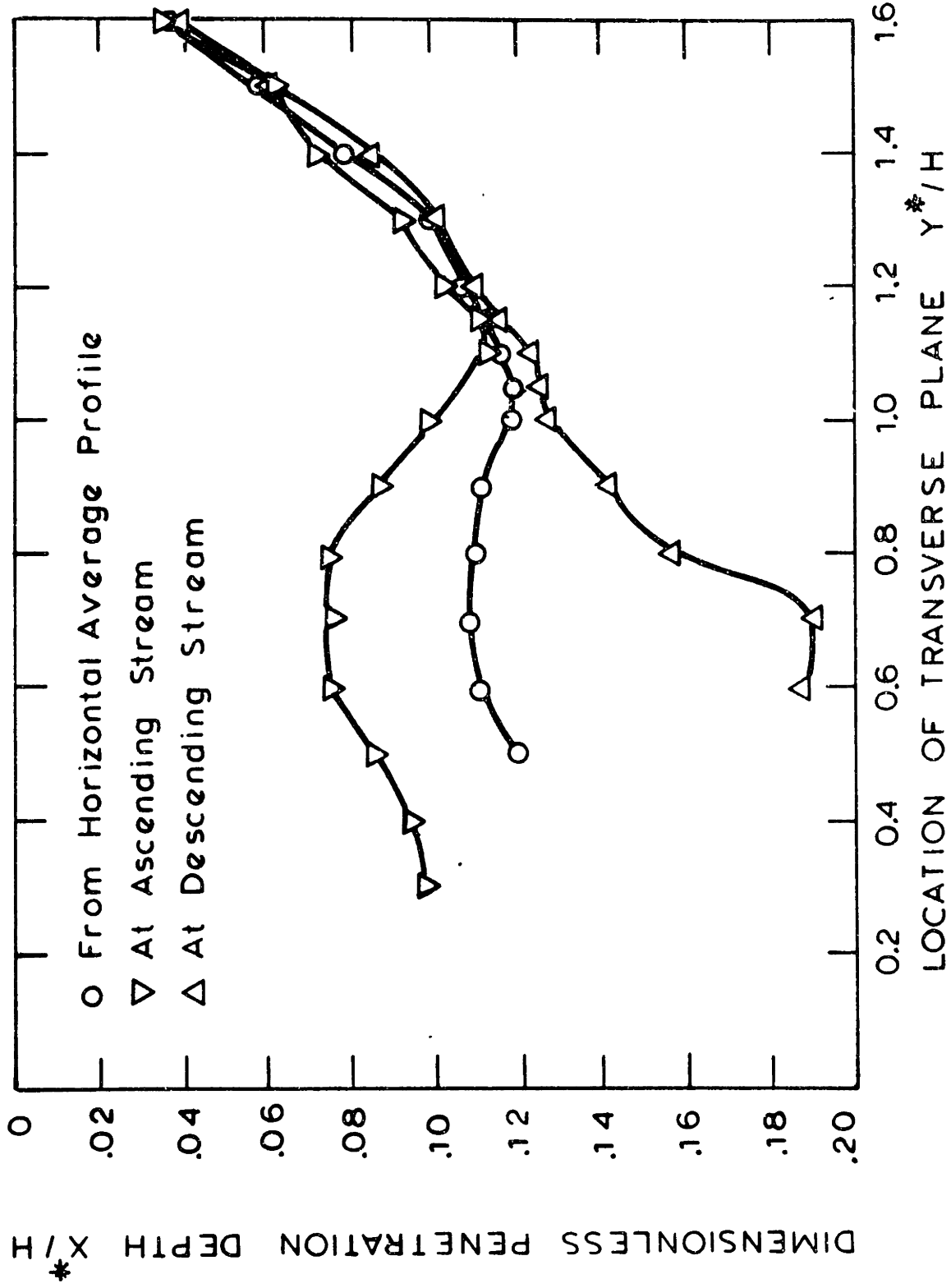


Figure 5.25 Experimental Penetration Depth of Maximum Temperature Layer in the Roll Region

solution) gradients when this turnover has occurred. In Figure 5.25, the maximum temperature position is plotted against the plane position. Circled data represent the positions obtained from Figure 5.24. Also included are the positions of the maximum temperature at the cell center and boundary. Notice that maximum penetration in both flows occur roughly at the same place (around 3.5" plane). This may be best understood as a complete turnover of the originally unstable fluid. Finally, the data points begin to deviate from each other around the 7.5" transverse plane, indicating the onset of roll motion.

VI. THE ONSET CRITERIA OF THE ROLL MOTION

In this chapter, the onset condition for the roll motion will be determined from the linear stability analysis. The result will be compared with the experimental data presented in the previous chapter.

6.1 Basic Assumptions in Linear Stability Analysis

A theoretical framework of linear analysis has been presented in Chapter IV for a fluid layer heated internally. In this Section, a specific distribution function of heat source will be chosen, based on phenomenological evidence gathered in the experiment and simplifying features of the problem. The principal assumptions can be summarized in the two statements:

- (i) the basic circulation (longitudinal) currents are strictly two-dimensional and perturbed only in transverse direction;
- (ii) an appropriate heat source distribution can be used as an instability agent to reflect the contribution of the longitudinal currents toward orthogonal (transverse) plane motion.

The first assumption is merely the restatement of experimental observations. It allows one to analyze the problem as a longitudinal roll motion. The regular vortex structure over most of the roll cell region is not significantly altered by the side wall effects. The existence of 25 pairs of such roll cells is enough to support this claim. As discussed in Chapter III, the theoretical results for stratified shear flows can also be construed to support this assumption in a more general sense.

The second assumption is necessary because of the recirculating nature of the longitudinal motion. Previous approaches to similar problems chose to suppress the effect of recirculating flow. For example, in his study of

Hadley circulation, Hart (1972) invoked the assumption of extreme enclosure aspect ratio to ignore the effect of return flow. A similar treatment is also found in Weber (1973, 1978). In this limit, a basic analytic solution exists which is, of course, important for deciding the preferred mode of the instability. Here we take a different approach; that is, we determine critical conditions based on the experimental evidence of roll preference. The results of both investigators, however, may have some bearing on our problem. In Section 5.2.1, a transition was observed to the pure two-dimensional motion. This motion is clearly in a state of finite amplitude convection which might be grown out of transverse mode instability (i.e., z-independent mode) in the limiting state of basic flow. The complexity of the problem is compounded by the facts that instability occurs only in part of the recirculating flow, and that the peculiar top boundary conditions are intractable to analytic treatment.

6.2 Nonlinear Source Distribution under the Batch Sink

Since we do not attempt to explain why the longitudinal roll motion is preferred, only the stability of flow in a transverse plane is examined. It was pointed out that finite amplitude motion in the plane can be well represented by using heat source-sink distributions imbedded in the plane. These distributions must reflect energy transfer from the longitudinal currents to fluid in transverse motion. The source-sink approximation method provides for the required distributions (Won, 1974). It has been extended successfully to predict both wavelength and amplitude of the roll motion (Curlet, 1976). Therefore, it seems reasonable to employ the same method for predicting the onset condition of the roll motion.

The source-sink functions are computed as

$$S(x) \equiv SI_T = - \partial_x^2 T - T \Big|_{y=y_T} \quad (6.1)$$

where $T(x,y)$ is the longitudinal plane solution for which side wall heat losses were allowed as a uniform sink, T . The computed $S(x)$ for any transverse plane (indicated by y_T) is assumed uniform in transverse (z) direction. This function is equivalent to

$$\partial_y^2 T - v(\partial_y T) - u(\partial_x T) \Big|_{y=y_T}.$$

The first two terms are conductive and convective energy contribution of the longitudinal flow to the chosen transverse plane y_T . The third term arises from the fact that the vertical motion of the longitudinal flow tends to redistribute energy within the transverse plane. In the roll region, the second term is the largest because of the fast longitudinal velocity and the steep horizontal gradient over the region. The functions obtained for a particular transverse plane are only a function of x , but these change shape for different transverse sections.

Figure 6.1 shows the distribution curves for the source-sink functions obtained from the solution for the experimental conditions as presented in Chapter V. Each function is normalized based on its maximum source strength (S_m) and the corresponding position, which are summarized in Table 6.1. Notice that the source depth is twice the distance to the position of maximum source strength. Each symbol represents the curve for a different transverse plane. (A total of 14 curves are plotted.) All of the functions are well represented by a single parabolic profile. In the deeper part

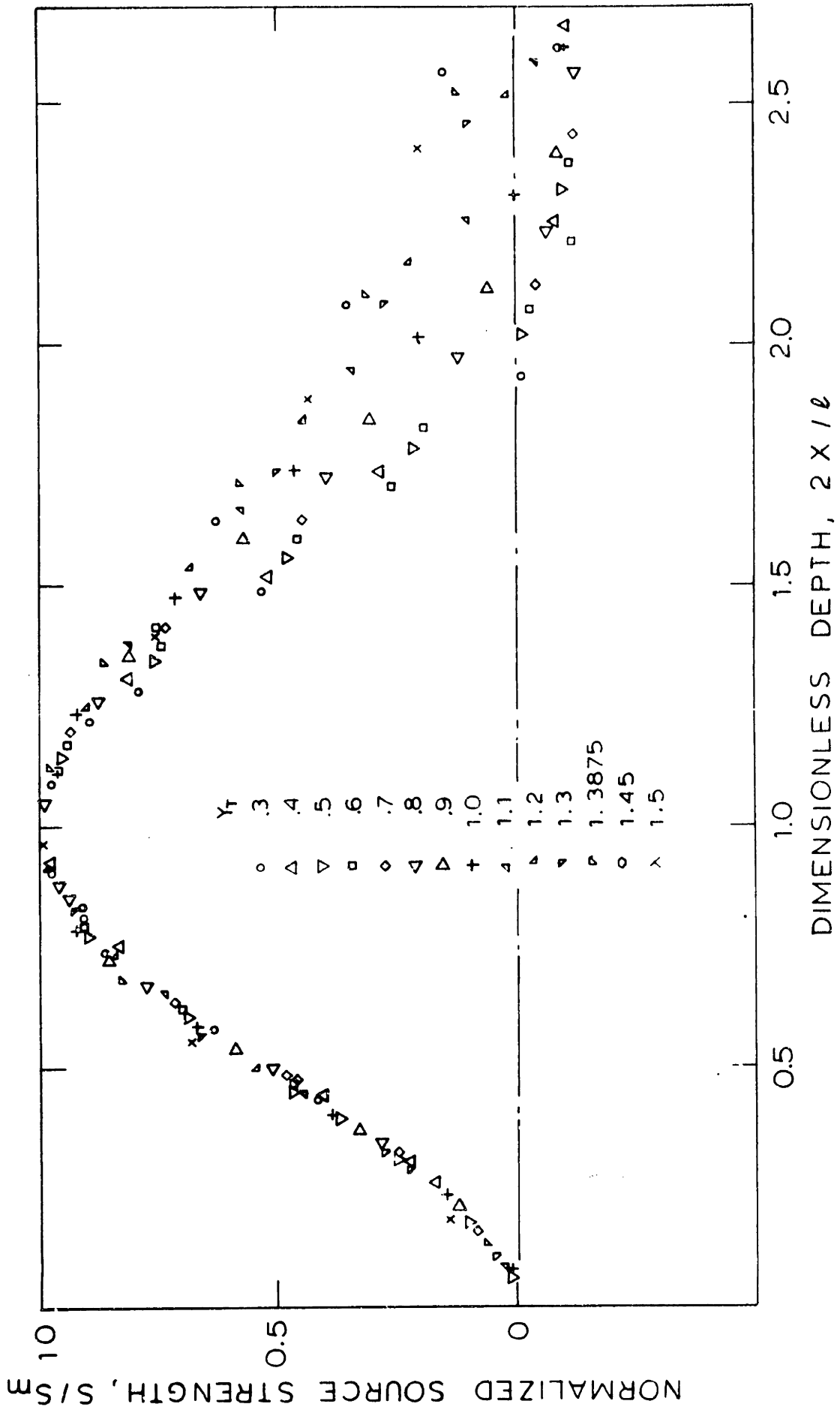


Figure 61 Similarity Curve for Source - Sink Functions

-164-
TABLE 6.1

Maximum Source Strength and Source Depth from the Numerical Solution

Plane Location (y)	Maximum Source Strength (S_m)	Source Depth (λ)	Temperature Gradient Parameter (η_s)
0.3	7.02	0.176	0.06677
0.4	7.17	0.173	0.07135
0.5	8.00	0.168	0.08265
0.6	8.67	0.164	0.08475
0.7	9.37	0.160	0.09205
0.8	10.52	0.156	0.09506
0.9	12.08	0.142	0.10056
1.0	14.29	0.130	0.10908
1.1	17.78	0.118	0.11004
1.2	22.31	0.104	0.11658
1.3	30.40	0.092	0.11030
1.3875	43.12	0.076	0.11429
1.45	66.20	0.062	0.10780
1.5	92.50	0.054	0.09844

beyond the parabolic profile, the source function is set to zero. Deviations occurring in the lower part of the layer (including the bottom part of parabolic profile) will be compensated for by using heat flux (mixed type) condition at the bottom boundary. This point will be further discussed in the results section.

For a definite treatment, the equations presented in Chapter IV are supplemented with the internal heat source distribution curve

$$F(x) = \frac{4x}{\ell^2} (\ell - x) H(\ell-x) , \quad (6.2)$$

where ℓ is defined[†] as twice the depth to the location of maximum source strength and the Heaviside step function $H(x)$ is used with an understanding of an x range of 0 to 1. Then, the static temperature gradient, $h(x)$, have the form of

$$h(x) = -\frac{N}{N+1} \left(\Delta T + \frac{\ell^2}{3} \right) + \frac{1}{3\ell^2} (4x^3 - 6\ell x^2 - 2\ell^3) H(\ell-x) \quad (6.3)$$

where ΔT denotes the temperature difference, $T_s - T_A$. The static conduction profile corresponding to equation (4.6) becomes

$$T - T_s = -\frac{N}{N+1} \left(\Delta T + \frac{\ell^2}{3} \right) x + \frac{1}{3\ell^2} (x^4 - 2\ell x^3 - 2\ell^3 x) H(\ell-x) + \frac{\ell^2}{3} H(x-\ell) . \quad (6.4)$$

The maximum temperature difference in the layer is found

$$T_m \equiv T_m - T_s = \frac{\ell_t^3}{\ell^2} \left(\frac{4}{3} \ell - \ell_t \right) , \quad (6.5)$$

where ℓ_t denotes the depth to the location of maximum temperature, T_m , and

[†] The dimensionless source depth, ℓ , is defined as ℓ_s^*/H , which should not be confused as the reference length scale, ℓ^* .

can be obtained from $h(\ell_t) = 0$. Since the source distributions cannot be measured directly, it is convenient to relate parameters in terms of temperature. Thus, the temperature Rayleigh number is defined as

$$R_T = \frac{g\beta\Delta T_m^* H^{*3}}{\nu_o^* \alpha_o^*} \quad (6.6)$$

which is related to the source Rayleigh number

$$\frac{R_T}{R_S} = \left(\frac{\ell_t^3}{\ell} \right)^2 \left(\frac{4}{3}\ell - \ell_t \right). \quad (6.7)$$

When the source depth ℓ is quite small, it could be an appropriate length scale. Then, the two Rayleigh numbers can be modified:

$$R_{S,\ell} \equiv R_S \cdot \ell^5 \quad (6.8)$$

$$R_{T,\ell} \equiv R_T \cdot \ell_t^3 .$$

The temperature gradient in the stably stratified layer under the source region turns out to be a very important parameter:

$$\eta \equiv -DT = \frac{N}{N+1} \left(\Delta T + \frac{\ell^2}{3} \right) \quad \text{for } \ell < x < 1 , \quad (6.9)$$

along with $\eta_s = \frac{\eta}{\ell}$ and $\eta_t = \frac{\eta}{\ell_t}$.

Fluid viscosity is assumed to be constant, because the maximum variation of viscosity in the experiment is only a fourfold change and this small change has a negligible effect on the results. The effect of

viscosity variation will be treated in the next chapter. The assumption of constant viscosity simplifies the differential operator L_4 to the form

$$L_4\phi \equiv (D^2 - a^2)^2\phi \quad (6.10)$$

and make it possible to obtain each ϕ analytically. The final equation corresponding to equation (4.17) is in the form:

$$A_j \frac{\lambda_j^2}{2a^2} \left\{ 1 - \frac{\sin 2\beta_j}{2\beta_j} \right\} = R \sum_{k=1}^m A_k \int_0^1 h(x)\phi_k\theta_j dx \quad , \quad (6.11)$$

where $\theta_j = \sin \beta_j x$, and

$$\phi_k = \frac{-1}{\lambda_k^4} \left\{ c_1 x \cosh ax + c_2 x \sinh ax + c_3 \sinh ax - \sin \beta_k x \right\} .$$

The coefficients, c_1 , c_2 and c_3 , are functions of a , β and N , and can be easily obtained by solving equation (4.14) with boundary conditions.

6.3 Results of the Linear Stability Analysis

Numerical calculations were performed for a limited range of parameters, N and λ . The parameter, ΔT , was set to zero in most cases, because the sink temperature is close to the ambient temperature in the experiment. Moreover, there is a strong indication that combined form of these parameters is only important, as will be discussed in the next Section. The results are summarized in Table 6.2 for the critical conditions only. The wave numbers are correct up to the digits shown and all calculations were performed in a double precision arithmetic.

The numerical procedure itself deserves some comment. All the eigenvalues are found to be real for each characteristic equation. Since

TABLE 6.2

Critical Parameters for Internal Source Problem

<u>N</u>	<u>ℓ</u>	<u>R</u>	<u>a</u>	<u>ΔT_m</u>	<u>ℓ_t</u>	<u>R_{s,ℓ}</u>	<u>a_s ≡ a · ℓ</u>
0.0	0.1	45780220.	4.210	0.0033333	0.1	457.80	0.421
	0.2	1852635.	3.667	0.0133333	0.2	592.84	0.733
	0.3	311655.5	3.355	0.03	0.3	757.32	1.006
	0.4	94028.27	3.148	0.0533333	0.4	962.85	1.259
	0.5	39159.35	3.002	0.0833333	0.5	1223.73	1.501
	0.6	20043.66	2.89	0.12	0.6	1558.60	1.740
	0.7	11851.12	2.81	0.1633333	0.7	1991.82	1.967
	0.8	7796.72	2.75	0.2133333	0.8	2554.83	2.2
	0.9	5566.62	2.70	0.27	0.9	3287.03	2.43
	1.0	4235.70	2.665	0.3333333	1.0	4235.70	2.665
0.5	0.1	119721700.	13.68	0.0032279	0.0923487	1197.22	1.368
	0.2	4923869.	8.036	0.0125087	0.178104	1575.64	1.607
	0.3	793927.7	5.926	0.0272673	0.259395	1929.24	1.778
	0.4	222945.9	4.785	0.0469583	0.336969	2282.97	1.914
	0.5	84243.48	4.015	0.0710604	0.411250	2632.61	2.007
	0.6	38814.62	3.492	0.0990740	0.482520	3018.23	2.095
	0.7	21036.93	3.18	0.130519	0.550979	3535.68	2.226
	0.8	13035.11	3.002	0.164935	0.616779	4271.34	2.402
	0.9	8969.60	2.90	0.201877	0.680038	5296.46	2.610
	1.0	6689.06	2.835	0.240917	0.740851	6689.06	2.835
1.0	0.1	139374200.	15.01	0.00317706	0.0905701	1393.74	1.501
	0.2	6024634.	8.871	0.0121188	0.172930	1927.88	1.774
	0.3	1012737.	6.565	0.0259954	0.249668	2460.95	1.969
	0.4	296272.8	5.344	0.0440329	0.321680	3033.83	2.138
	0.5	117061.8	4.556	0.0655040	0.389469	3658.17	2.278
	0.6	55549.23	3.965	0.0897229	0.453359	4319.51	2.379
	0.7	30072.36	3.520	0.116043	0.513576	5054.26	2.464
	0.8	18289.29	3.225	0.143852	0.570287	5993.04	2.580
	0.9	12358.31	3.060	0.172574	0.623614	7297.46	2.754
	1.0	9115.45	2.962	0.201668	0.673648	9115.45	2.962
1.5	0.1	150470900.	15.65	0.00314702	0.0896355	1504.71	1.565
	0.2	6682910.	9.291	0.0118901	0.170197	2138.53	1.858
	0.3	1150384.	6.895	0.0252542	0.244504	2795.43	2.069
	0.4	344135.5	5.620	0.0423393	0.313526	3523.95	2.248
	0.5	139443.9	4.827	0.0623076	0.377799	4357.62	2.413
	0.6	68067.69	4.240	0.0843779	0.437662	5292.94	2.544
	0.7	37649.8	3.77	0.107821	0.493349	6327.78	2.64
	0.8	23045.53	3.42	0.131958	0.545021	7551.56	2.74
	0.9	15526.03	3.19	0.156157	0.592793	9167.97	2.87
	1.0	11414.16	3.066	0.179833	0.636743	11414.16	3.066

TABLE 6.2 (CONT.)

<u>N</u>	<u>ℓ</u>	<u>R</u>	<u>a</u>	<u>ΔT_m</u>	<u>ℓ_t</u>	<u>R_{s,ℓ}</u>	<u>a_s ≡ a · ℓ</u>
2.0	0.1	157704200.	16.07	0.00312717	0.0890520	1577.04	1.607
	0.2	7126549.	9.544	0.0117396	0.168484	2280.50	1.909
	0.3	1245983.	7.095	0.0247685	0.241260	3027.74	2.128
	0.4	378292.4	5.791	0.0412337	0.308389	3873.71	2.316
	0.5	155746.7	4.989	0.0602293	0.370425	4867.08	2.494
	0.6	77499.61	4.41	0.0809166	0.427716	6026.37	2.65
	0.7	43720.23	3.945	0.102519	0.480402	7348.06	2.761
	0.8	27126.46	3.57	0.124322	0.528907	8888.80	2.86
	0.9	18372.0	3.31	0.145665	0.573068	10848.49	2.98
	1.0	13531.83	3.15	0.165948	0.613037	13531.83	3.15

some of them are negative, the well-known power method is no longer applicable. The critical conditions must be determined as the smallest positive eigenvalue (R_c) among all the eigenvalues. The QR algorithm was used for the purpose (for program list, see Appendix F). The smallest negative eigenvalue (in absolute value) would correspond to an uninteresting, internal sink (opposed to source) distribution. First, the Rayleigh numbers are unusually large when the sources exist in a narrow top layer. This fact simply reflects the stabilizing effect of the stably stratified layer. It is further pronounced when the downward heat flux ($N > 0$) induces a stably stratified region. Closer inspection indicates that increase in Rayleigh number is generally accomplished with the smaller convection cell sizes. More importantly, this is not dependent on the choice of reference scales, provided a consistent system is used (for example, $R_{T,\ell}$ with a_T).

Whitehead and Chen (1970) investigated the stability of a fluid layer with internal sources of the exponential decay type. Our results are consistent with their general discussion. They also found that the temperature gradient of the stable bottom layer, η , is an important parameter for the deep layer. (Actually, their parameter S is equivalent to our $R_{T,\ell} \cdot \eta_t$).

Even though a direct comparison with previous results is not possible, some indication of the validity of our calculational procedure could be found. The critical condition is known as $R_c = 2772.27$ and $a_c = 2.63$ for the uniform internal source problem with an insulated bottom boundary. This result was obtained by Roberts (1967) and, independently, by Tveitereid and Palm (1976). Since the parabolic source profile can provide the same total heat generation with its maximum strength being 1.5 times the uniform

source, this condition is equivalent to

$$R_c = 4158.4$$

$$a_c = 2.63$$

which is in excellent agreement with the results for $N = 0$ and $\lambda = 1.0$:

$$R_T = R_S = 4235.7$$

$$a_c = 2.665 .$$

Another cross-check is possible. For the case $\lambda = 1.0$ and $N = 2.0$, the critical condition in this thesis becomes

$$R_{T,\lambda} = 517.35$$

$$a_T = 1.931 .$$

This condition appears to be a minimum Rayleigh number for a fixed $\lambda = 1.0$ and is not sensitive to the variation of N . The conduction temperature profiles tend to approach a parabolic shape, as N increases. Veronis (1963), in his study of penetrative convection of density inversion of water at 4°C , calculated the critical condition for the parabolic "temperature" profile:

$$R_c = 583.77$$

$$a_c = 2.0$$

while Whitehead and Chen (1970) obtained

$$R_c = 589.44$$

$$a_c = 2.03$$

for the same profile, but as an asymptotic profile for the exponential type heat source in the limit of infinite S . However, this latter comparison should be construed as a qualitative similarity in the physical mechanism because of the different temperature condition at the bottom boundary.

Next, the number of expansion terms (A_k 's) required for convergent solutions varies with the depth of source, ℓ . For $\ell = 0.1, 0.2, 0.3, 0.4, 0.5$ or up, the required number was 25, 20, 20, 15 and 10, respectively. Thus, the trial functions chosen for the Galerkin procedure are not efficient for the problem. This inefficiency is reflected in the expansion coefficients obtained for the critical conditions which are shown in Figure 6.2. The ratio of adjacent coefficients are plotted against the reciprocals of term number for $N = 1.0$ case. Notice that coefficients of the first few modes tend to increase for the small depth of source. This contrasts with the normal case of fast convergence. (For example, see Appendix D in which only four terms are enough to obtain accurate final results for the Rayleigh-Bénard problem.)

Close inspection indicates that the mode corresponding to the maximum coefficient (for example, the sixth mode for $\ell = 0.1$) is always associated with a trial function of which the first cycle (remember the trial functions are sine series, $\sin \beta_k x$) renders a best fit to the top portion of the characteristic functions. Figure 6.3 shows the characteristic

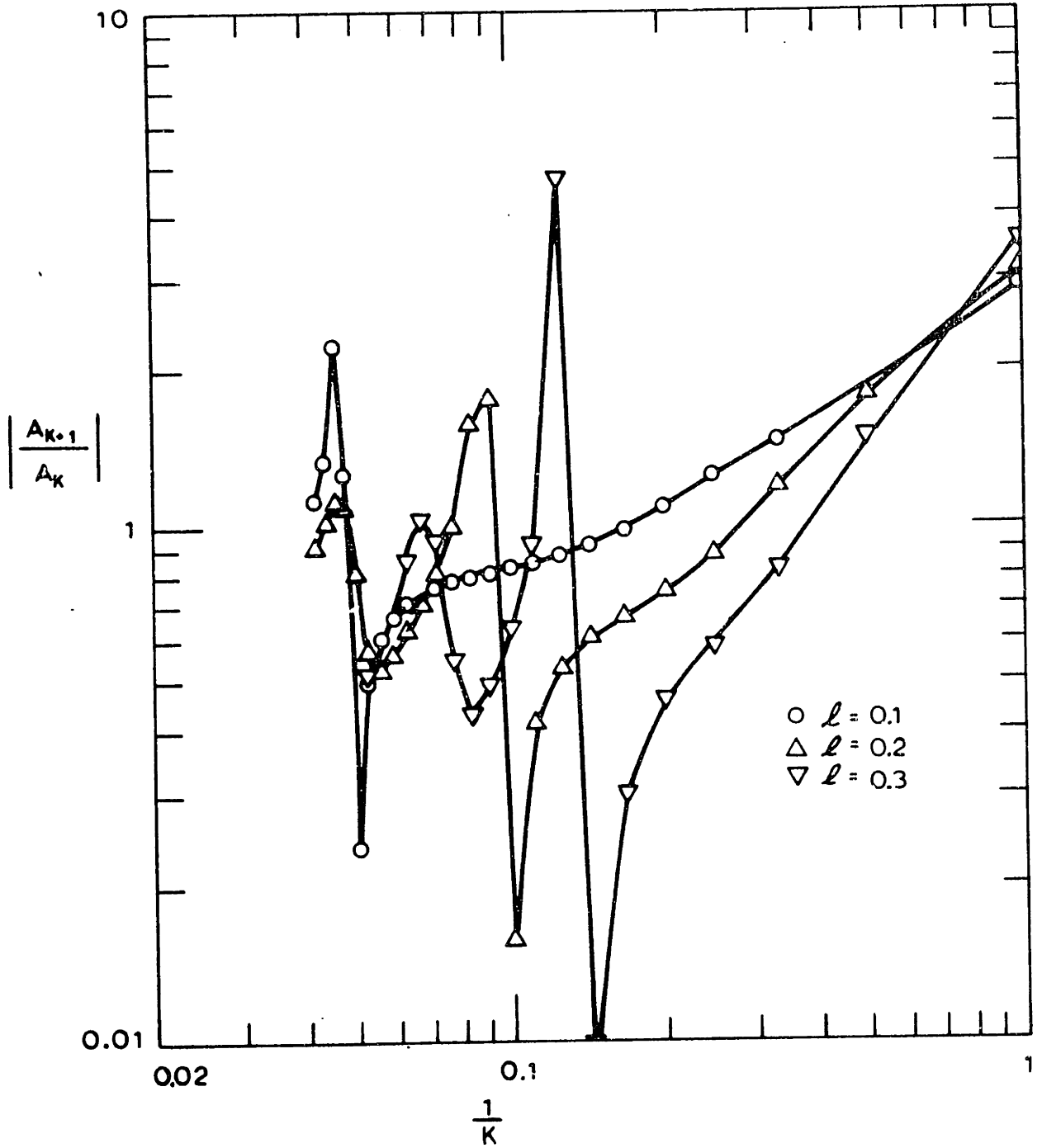
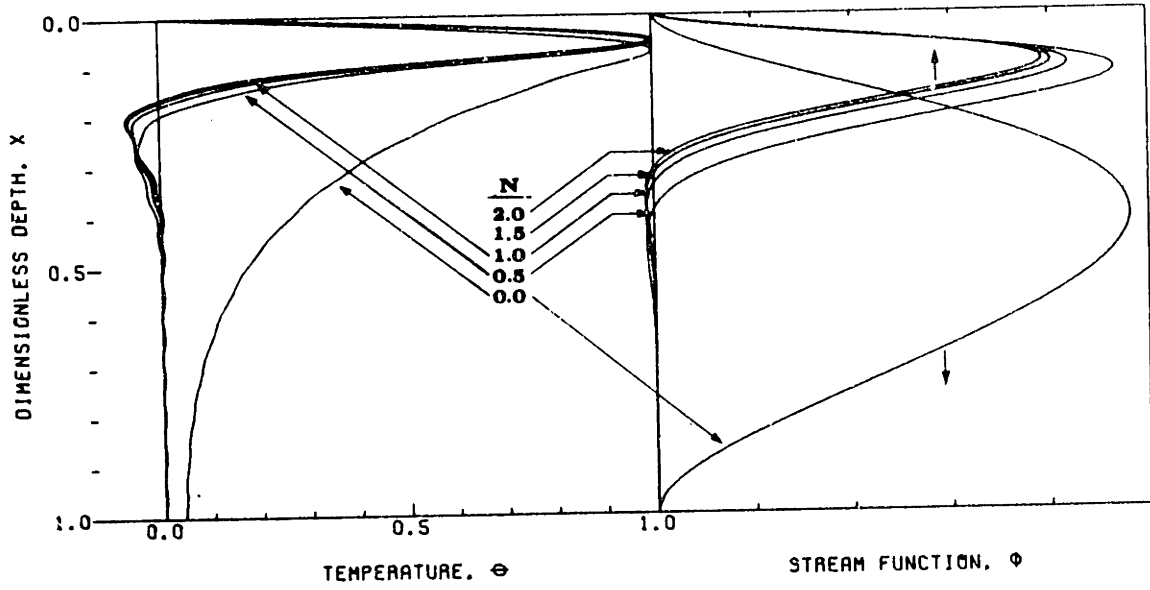


Figure 62 Expansion Coefficients of Characteristic Functions, $N = 1.0$

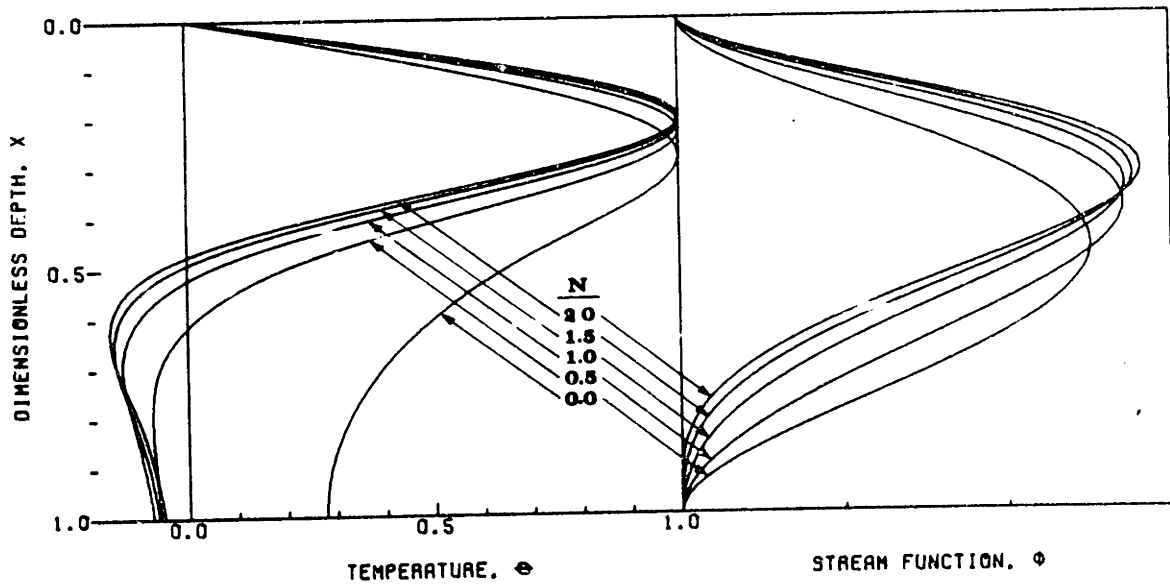
functions for $\lambda = 0.1$ and 0.5 . Clearly, the disturbances are largely confined to the top layer. Since the trial functions are sine series and the first few modes necessary to fit the top portion of profile always leave large, unwanted amplitudes in the rest of the layer, a large number of terms are required to negate these unwanted components of amplitude. As the depth of the source (λ) increases, the number of terms required is reduced. For $\lambda = 0.5$, the first two modes of trial functions turns out to have similar shapes to the characteristic functions. Therefore, a smaller number of expansion terms is required. If one wants to improve convergence of the solution, the trial functions must be chosen to have shapes similar to those of characteristic functions.

All the characteristic profiles are normalized with $\theta_{\max} = 1$, since the linear stability analysis cannot predict the amplitudes of disturbances. For the experimental comparison, the results for the smaller depth of source are of great interest. This is because the longitudinal currents, which are the origin of the source and the resulting roll motion, are confined only to the top portion of the layer. Some interesting observations can be drawn from these profiles.

(1) The fluid layer with insulated bottom boundary ($N = 0$) behaves quite differently from the case where the bottom boundary is cooled ($N > 0$). Regardless of the depth of source, the entire layer becomes unstable. The rate of work done by the buoyancy force is represented by the net convective heat transfer $\overline{w\theta} \propto \overline{\phi\theta}$. (Bar denotes horizontal average.) The fact that this term has the same sign over the entire layer indicates no stabilizing effect.



THE CHARACTERISTIC FUNCTIONS FOR SOURCE DEPTH 0.1



THE CHARACTERISTIC FUNCTIONS FOR SOURCE DEPTH 0.5

FIGURE 6.3 CHARACTERISTIC FUNCTIONS FOR SOURCE DEPTH 0.1 AND 0.5

(2) When the bottom is not insulated, the fluid layer instability tends to penetrate beyond the stably stratified region. This fact is manifest in sign change of $\overline{\theta\phi}$ term, which means the energy pumped into the stable region.

(3) For the small depth of source, the bottom layer of fluid is hardly disturbed beyond a certain penetration depth. As the depth of source increases, the penetration of instability reaches to the bottom. This occurs roughly when $\ell = 0.5$.

The last point is of special interest. It implies that the bottom boundary conditions are irrelevant for the prediction of the critical conditions. The profiles for $\ell = 0.1$ clearly show that any of the following boundary conditions could be imposed at the bottom, or any part of the unperturbed region, without altering the final results.

$$\begin{aligned} D\theta + N\theta &\cong D\theta \cong \theta = 0 \\ \phi &= D\phi = D^2\phi = 0. \end{aligned} \tag{6.12}$$

However, we must be cautious in preserving the original conduction state. Even though the parameter N is no longer important in the boundary conditions, it still exerts an influence through the static temperature profile.

This can be best understood if the depth of source is chosen as the reference length scale and the original systems of equations is transformed accordingly:

$$\begin{aligned} x' &= x/\ell \\ a' &= a \cdot \ell \\ R_{s,\ell} &= R_s \cdot \ell^5 \end{aligned} \tag{6.13}$$

$$\theta' = \theta/\ell^2$$

$$\phi' = \phi$$

$$h'(x) = \frac{h}{\ell}$$

The transformation merely provides a stretched coordinate system. Thus, the boundary conditions described above are applied at $x' \rightarrow \infty$ (any position in the unperturbed layer). Then, we have

$$h'(x) = -\frac{\eta}{\ell} + \frac{4}{3} (x'^3 - 1.5x'^2 + 0.5) H(1-x) \quad (6.14)$$

Now all the physical parameters are combined into a single parameter

$$\eta_s = \frac{\eta}{\ell} = \frac{1}{\ell} \frac{N}{N+1} \left(\Delta T + \frac{\ell^2}{3} \right) \quad (6.15)$$

while the second term in $h'(x)$ involves no physical parameters. Note that η_s is not a temperature gradient at the stable fluid layer, but its ratio to the depth of the source. Thus it follows

$$R_{S,\ell} = R_{S,\ell}(\eta_s) \quad (6.16)$$

Physically, the deeper the source depth is, the steeper stable gradients must be in order to achieve the identical stability condition. The importance of this parameter will be made clearer in the next Section.

Similarly, the critical conditions based on the maximum temperature position, ℓ_t , can be expressed in the form of

$$R_{T,\ell} = R_{T,\ell} \left(\eta_t, \frac{\ell}{\ell_t} \right) \quad (6.17)$$

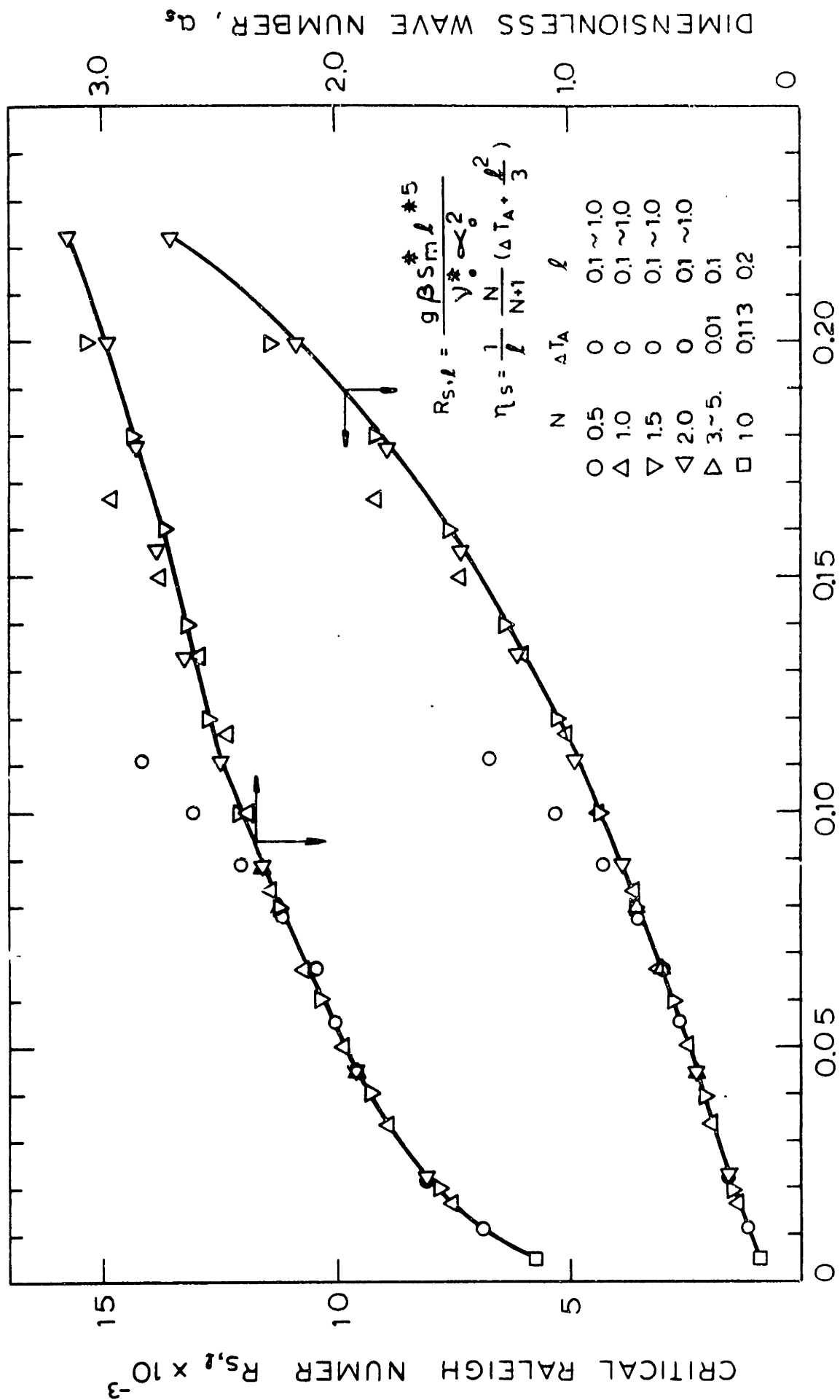


Figure 6.4 Critical Conditions for the Onset of Roll Motion $R_{s,1}$ vs η_s

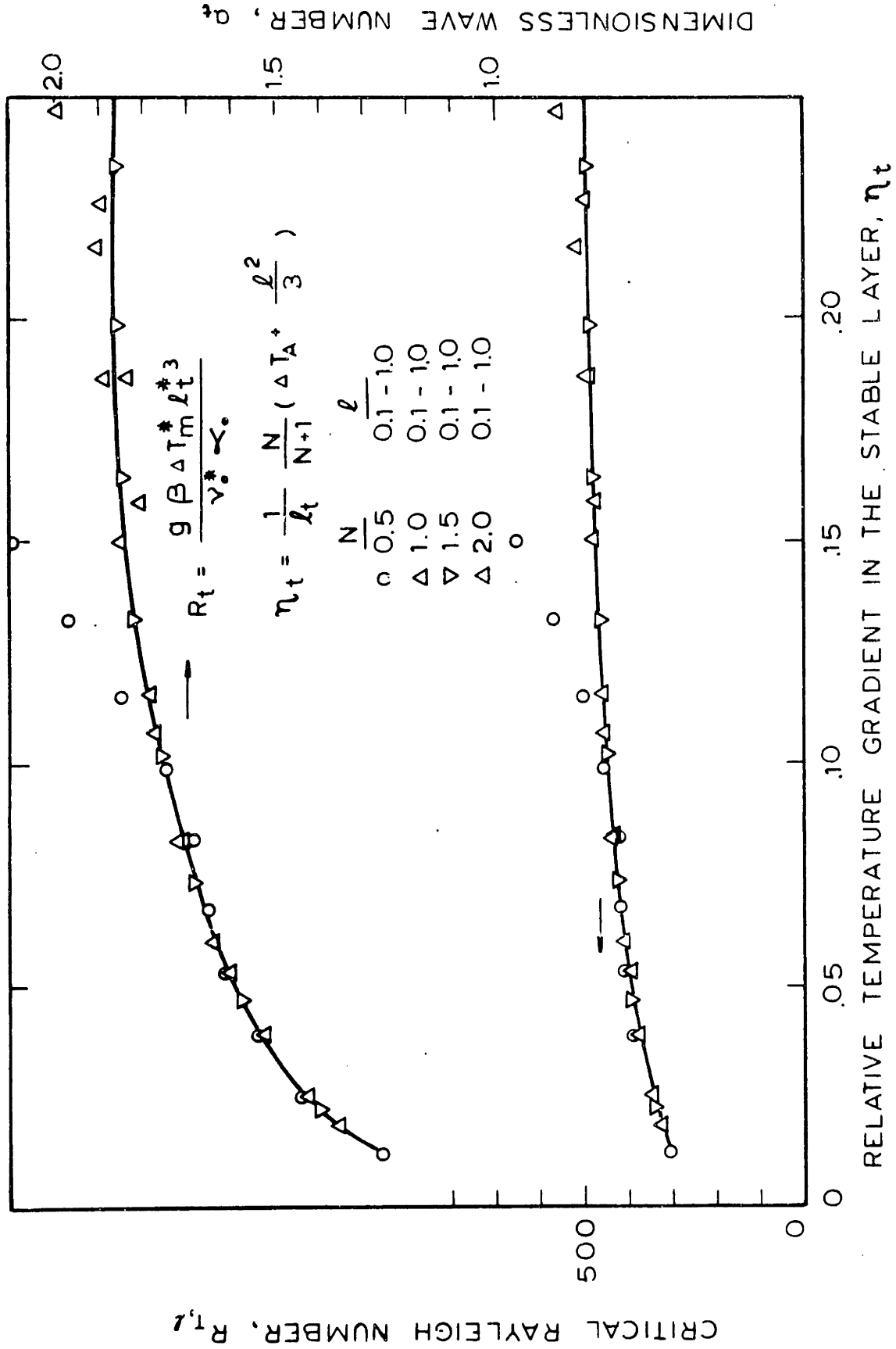


Figure 6.5 Critical Conditions for the Onset of Roll Motion: $R_{T,l}$ vs η_t

This form is particularly useful for the experimental comparison. Note that an extra parameter (ℓ/ℓ_t) is involved.

Figure 6.4 shows a plot of modified Rayleigh number $R_{S,\ell}$ and wave number a_s ($\equiv a \cdot \ell$) vs η_s . According to the discussion in the previous section, all the data points should fall on a single curve. This curve is indicated by the solid line. When the depth of source is greater than 0.5, the data points deviate from the generalized curve. The deviation is due to the influence of the bottom hydrodynamic boundary conditions. Since viscous dissipation stabilizes the fluid motion, Rayleigh number increases with the increasing depth of source.

Figure 6.5 is a plot of $R_{T,\ell}$ vs η_t . Notice that $R_{T,\ell}$ is nearly constant for a wide range of η_t values. For η_t greater than 0.1, the general criterion for the onset condition is:

$$R_{T,\ell} \cong 500 \quad \text{and} \quad a_c \cong 1.88 \quad .$$

It is a striking result, because the stability criterion is only dependent on the Rayleigh number as long as η_t is greater than 0.1. Therefore, this criterion can be directly used for comparison with experimental data.

6.4 Comparison of Theoretical and Experimental Onset Condition for Roll Motion

In Figure 6.6, the Rayleigh number $R_{T,\ell}$ from the experimental temperature data is compared to the generalized criterion. The circled data points were obtained from the horizontal average temperature profiles in Figure 5.24. Two additional profiles (at the ascending flow and the descending flow area of the roll cells) are also used to indicate horizontal variation of the Rayleigh number.

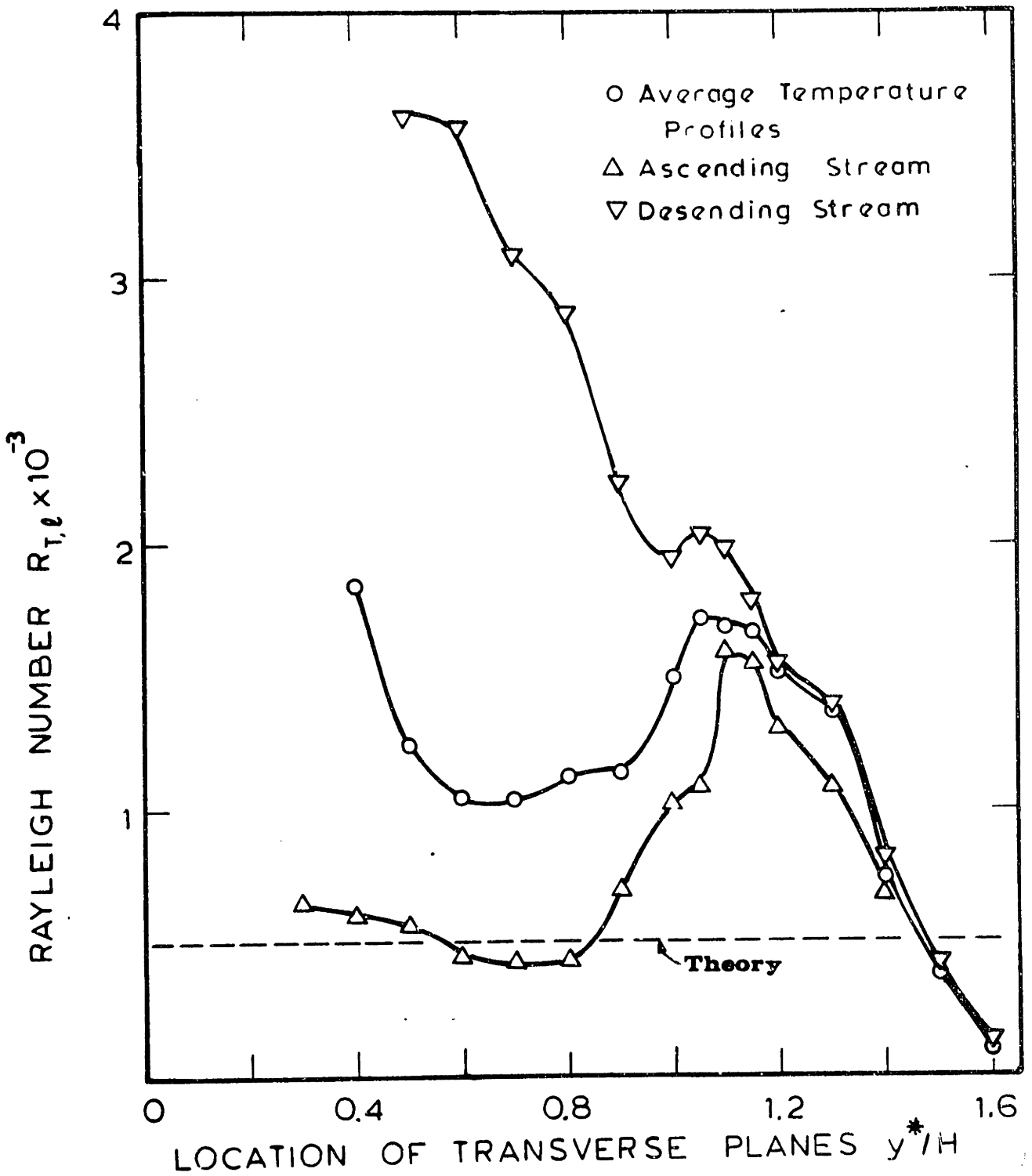


Figure 6.6 Comparison of Theoretical and Experimental Onset Condition for the Roll Motion

This figure clearly indicates that the roll motions should set in at 7.3" transverse positions. In Chapter V, the contour temperature plot at the 7" plane showed a wavy nature in the isotherm plot. The theoretical prediction is in excellent agreement with the observations. This figure itself provides an indication of the onset of roll motion around the 7" plane. The three different curves appear to diverge at this position. A marked departure of these, however, was recorded around the 5.5" plane. Interestingly enough, this is the location where the growth stage first appeared. The decrease in Rayleigh numbers beyond this point is largely due to the fact that fluid turnover results from the spiral advance of the longitudinal currents and the resulting maximum temperature position is accordingly raised closer to the top surface. The first photographic evidence of roll motion was at the 6" plane. But disturbances at this plane are in the state of finite amplitude convection.

As gratifying as the agreement between the theoretical prediction and the present data might be, there still remains the problem of including the effect of stable layer temperature gradients. The origin of this difficulty lies in the fact that source strength is not experimentally obtainable. In this sense, it is really fortunate to have the general criteria for the onset point. Linkage between the temperature data and the source distribution is only provided by the source-sink approximation method. Since the solution obtained by the method was found to represent the experimental conditions reasonably well, we can apply the theoretical results to determine the onset of roll motion directly from the two-dimensional numerical solution.

Figure 6.7 shows the temperature profiles of the two-dimensional numerical solution at various transverse planes. The profiles are normalized with the maximum source strengths listed in Table 6.1. It clearly indicates the increasing potential energy as the longitudinal currents advance toward the doghouse wall. Notice that the profiles show the opposite trend to those shown in Figure 5.24. The source depth is also indicated on each profile as a circled data point. Each profile shows changing temperature gradients in the core region, say, below the source depth. On the other hand, linear analysis has assumed one constant temperature gradient in the stably stratified region. To resolve this problem, the gradient parameter will be chosen as the value just underneath the unstable layer. In other words, it is assumed that the deeper portion of the layer does not contribute to the criterion of the onset of roll motion.

With this choice, the critical Rayleigh number $R_{s,\ell}$ of each profile can be determined from the generalized curve of the critical conditions by the value of η_s which is directly obtained from Figure 6.7. The source strength and its depth listed in Table 6.1 enables one to evaluate Rayleigh number corresponding to each profile. These are plotted in Figure 6.8. The two Rayleigh numbers will be identical only when the chosen profile is in the critical condition. The figure shows that the onset of roll motion should occur near the 6-3/4" plane. This location differs slightly from that suggested by the temperature data. Considering the various assumptions introduced, the agreement is remarkable.

Finally, the observed wavelength data will be compared with the theory. Direct comparison is impossible, because the data were determined from the

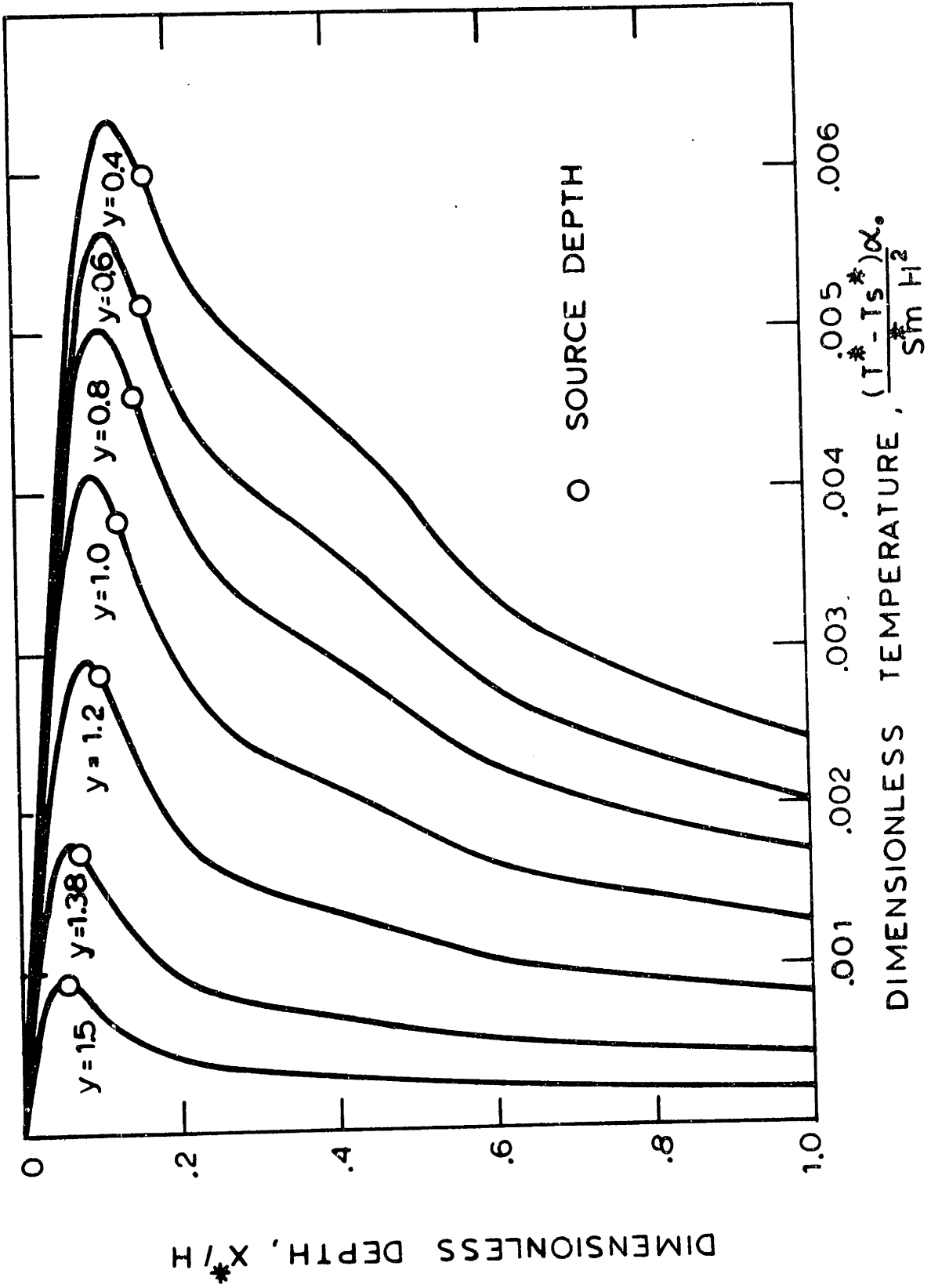


Figure 6.7 Temperature Profiles Normalized with Source Strength
(from Numerical Solution)

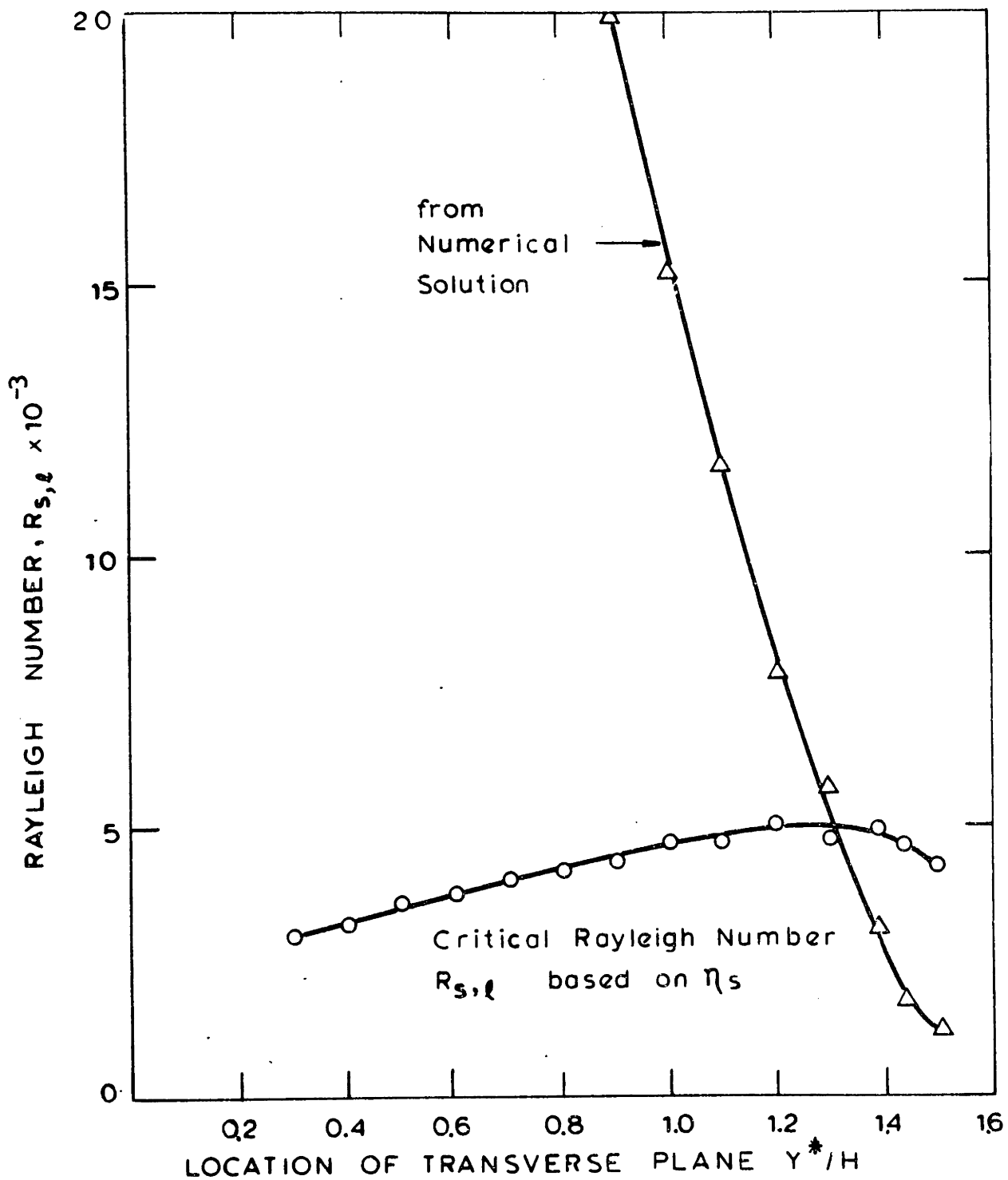


Figure 6.8 Prediction of the Onset of Roll Motion from Numerical Solution Two - Dimensional

photographs which cannot pinpoint the onset of roll motion. Nevertheless, the data indicate a certain trend in relation to the location of the transverse plane. The trend might be extrapolated to the onset point of roll motion and compared with the theoretical results. Since the theory assumes the importance of η_s that the conditions of the deeper layer are irrelevant to the critical condition, the absolute value of wavelength based on the total depth of layer cannot be directly compared with the experimental conditions. Instead, it should be compared with the wavelength in relation to the source depth. This comparison is shown in Figure 6.9. The observed data are shown with circled symbols (taken from Table 5.5). An extrapolation of these data suggests that the critical condition would set in near the 7" plane, when compared to the triangle data points. The triangle data were obtained from the generalized curve (Figure 6.4) by the values of η_s determined for each profile in Figure 6.7. There is another way to obtain wave number. As discussed above, Rayleigh number can be evaluated for each transverse plane using the data in Table 6.1. Using the generalized curve, the corresponding critical wave number could be determined, if these Rayleigh numbers would represent the critical state. These are shown as square symbols. The predicted critical wave number is valid only when the temperature profile is in the critical state. Therefore, the intersection of square and triangle data curve represents the onset condition of roll motion. This condition is around the 6½" plane and appears to be consistent with the previous comparisons for the onset. Furthermore, the observed photographic data could be well extrapolated to this intersection point. The penetrative behavior in the roll motion makes the observed wave number increase with the development of roll motion.

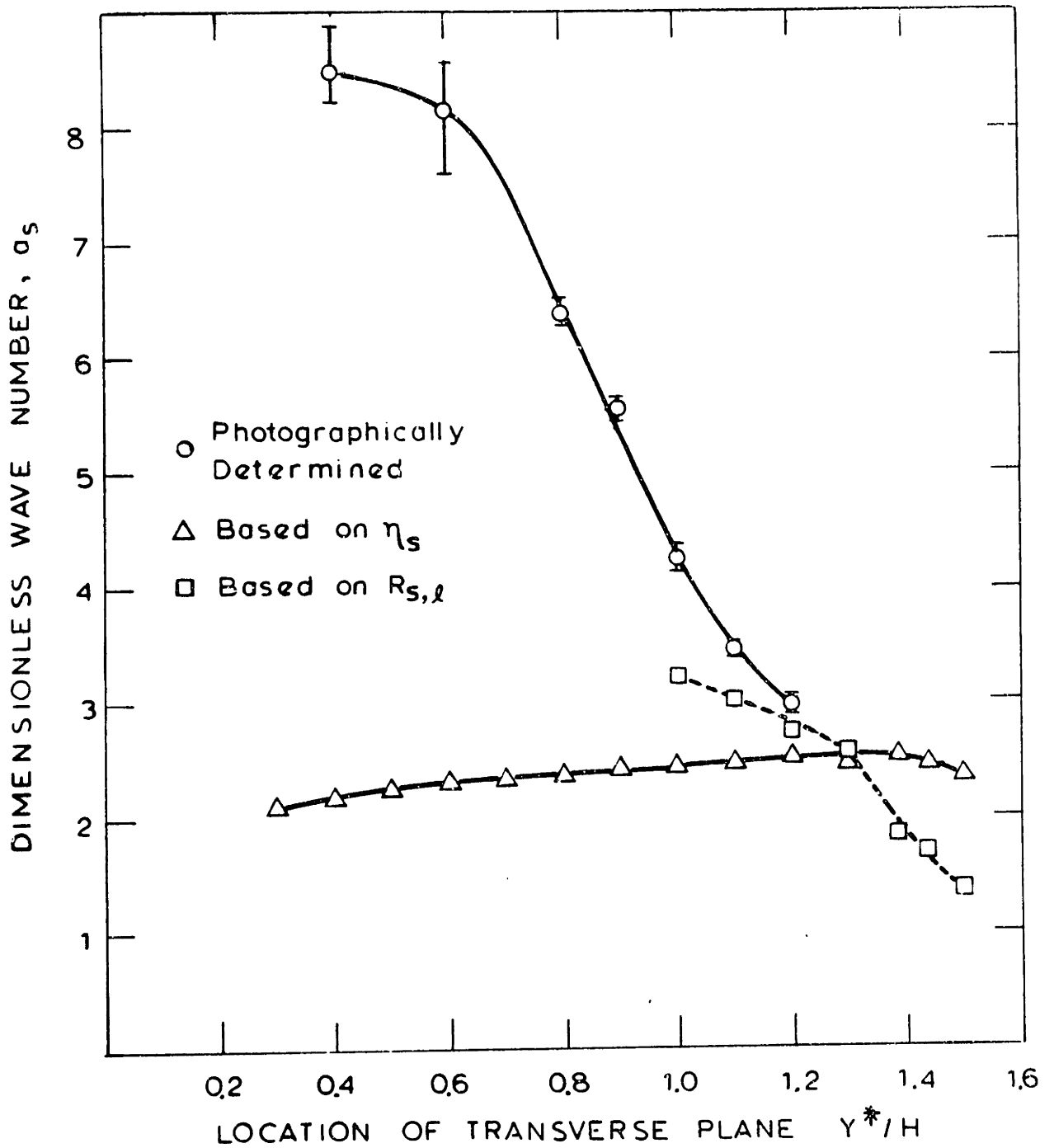


Figure 6.9 Observed Wave Number and Prediction of Critical Wave Number for the Onset of Roll Motion

However, it must be emphasized that the observed data represent the finite amplitude states.

This analysis shows the ability of linear analysis to predict the correct wave number. However, the increasing wave number beyond the onset point is clearly out of the domain of linear stability analysis. This finite amplitude behavior is certainly associated with the degree of freedom provided by the unconstrained fluid layer below the roll motions and shows marked difference from the ordinary Bénard problem. Particularly, the narrow band width of the wave number predicted by Busse (1967b) is no longer valid for this problem.

In summary, reasonable agreement between the experimental data and the theoretical prediction has been demonstrated for the onset condition of roll motion. Thus, the utility of the source-sink approximation method has been further extended to include critical, as well as finite amplitude calculations.

VII THE RAYLEIGH-BÉNARD PROBLEM

WITH LARGE TEMPERATURE-DEPENDENT VISCOSITY VARIATION

During the process of glass making the viscosity of the melt undergoes a several order of magnitude variation before being formed into a final product. Cooling in the melting and refining regions of the glass melt is mostly accomplished from the above. Therefore, it is possible to induce a gravitational instability in the glass melt layer through rapid cooling. If this results in cellular motion in the region where the melt is being removed from the furnace, the final product may possess an unwanted inhomogeneous structure. On the other hand, the same type of instability should be promoted under the batch blanket to enhance heat and mass transfer. In addition, the instability phenomenon is of considerable interest in the studies of the geophysics of the earth's mantle and the nonlinear behavior of equations in the field of applied mathematics, as discussed earlier in Chapter II. For these reasons, the effect of viscosity variation on cellular motion warrants a close examination.

7.1. Introduction

The physical problem treated in this chapter is concerned with cellular motion in a fluid later heated from below, that is, the well-known Rayleigh-Bénard problem. However, the fluid viscosity is supposed to be dependent on the temperature. Both horizontal boundaries are maintained at constant temperature, while no slip (rigid) top and free bottom boundary conditions are specified. In finite amplitude computations only, an infinite Prandtl number is assumed. The static conduction solution to the problem is, of course, a simple linear temperature profile. Since the temperature gradient

function, $h(x)$, is unity, the perturbation equation corresponding to equation (4.7) satisfies

$$\begin{aligned} \nabla \cdot \bar{V} &= 0 \\ P^{-1}(\sigma \bar{V} + \bar{V} \cdot \nabla \bar{V}) &= -\nabla \Pi - R_X \theta \hat{i} + \nabla \cdot 2\nu \bar{D} \\ \sigma \theta + \bar{V} \cdot \nabla \theta &= \nabla^2 \theta - \bar{V} \cdot \hat{i} \end{aligned} \quad (7.1)$$

with the boundary conditions

$$\begin{aligned} \bar{V} = \theta = 0 & \quad \text{at } x = 0 \\ (u, \partial_x v, \partial_x w) = \theta = 0 & \quad \text{at } x = 1 \end{aligned}$$

where the exponential growth rate, σ , of the disturbances has been already substituted for the transient terms, and u , v and w represent the velocity components of \bar{V} . Fluid temperature is defined as:

$$T = 1 + x + \theta \quad (7.2)$$

The specific viscosity-temperature relationship of interest is that empirically found to describe many liquids:

$$\nu = \nu_X \text{EXP}\left\{\gamma \left(\frac{1}{T} - \frac{1}{T_X}\right)\right\} \quad (7.3)$$

From a physical point of view, the problem contains three independent dimensionless parameters: the Rayleigh number, the Prandtl number and the viscosity ratio number;

$$R_X \equiv \frac{g \cdot \beta \cdot (T_h^* - T_c^*) \cdot H^3}{\alpha_o \cdot \nu_X^*}$$

$$P \equiv \frac{v_{\chi}^*}{\alpha_0}$$

$$\Gamma \equiv \frac{v_c^*}{v_h^*}$$

where H is the total depth of the fluid layer and the subscripts h and c denote the hot (bottom) and cold (top) boundaries. As defined, the viscosity ratio number, Γ , is the ratio of the maximum fluid viscosity to the minimum one. Note that the choice of reference temperature, T_{χ}^* , for evaluating v_{χ}^* also fixes the parameter, T_{χ} , as well as the Rayleigh number. The dummy subscript, χ , stands for either θ (denoting that the arithmetic mean of boundary temperatures is used for reference viscosity), or M (denoting the geometric mean of boundary viscosity values).

The objective of this study is both to understand the effect of large viscosity variation on the cellular motion and also to clarify some difficulties associated with the finite difference technique. Contrary to general belief, numerical solutions to problems with parameter sets near those that correspond to critical conditions converges very slowly, when conventional finite difference technique is applied. Even though analytic solutions exist for a few cases, direct comparison with numerical solutions has been seldom reported in the literature. The amplitude specification method, outlined in Chapter IV, was devised and successfully applied to resolve this convergence problem.

The critical wavelength for each chosen viscosity ratio number is determined by a linear analysis to fix the cell size for the numerical computation. For the constant viscosity case, the results of the amplitude specification method is directly compared to the results of the analytic

perturbation solution of Busse (1967a) to assess the validity of the method. A novel feature of the amplitude specification method is its capability of predicting even the unstable solution associated with the hysteresis effect, which appears when the viscosity ratio number exceeds 100.

7.2 The Principle of Exchange of Stability

In the limit of infinitesimal disturbances, the viscosity variation must be only a function of the conduction temperature profile. Therefore, viscosity will be dependent only on the vertical coordinate x . Also, in this limit, the nonlinear terms in equation (7.1) vanish because they are the second order. In this case, the principle of exchange of stability can be proven to hold, as follows.

If the momentum equation is multiplied (inner product) by \bar{V}^+ (complex conjugate of \bar{V}) and integrated over the entire fluid layer, one readily finds, on taking account of the boundary conditions and the requirements of horizontal periodicity:

$$\sigma P^{-1}(\bar{V} \cdot \bar{V}^+)_m = -R (\Theta \bar{V}^+ \cdot \hat{i})_m - 2(\nu \bar{D} : \bar{D}^+)_m \quad (7.4)$$

where $(\quad)_m$ denotes the average over the fluid layer and the J. Willard Gibbs' convention is understood for the dyadic multiplication[¶]. This equation represents an overall kinetic energy balance for the fluid layer.

[¶] By definition, $\bar{A} \bar{B} : \bar{C} \bar{D} \equiv (\bar{A} \cdot \bar{C}) (\bar{B} \cdot \bar{D})$.

Useful formulas for derivation are:

$$\nabla \cdot (\bar{K} \cdot \bar{V}) \equiv \bar{V} \cdot (\nabla \cdot \bar{K}) + \bar{K} : \nabla \bar{V}$$

$$\bar{V} \cdot \nabla^2 \bar{V} \equiv \nabla^2 \left(\frac{1}{2} \bar{V} \cdot \bar{V} \right) - \nabla \bar{V} : \nabla \bar{V}$$

where single and double overbars denote vectors and dyads, respectively.

At steady state, it reduces to a balance between the rate of generation of energy by motion in the presence of buoyancy force field and the rate of dissipation of energy by viscosity. It is called the "power Integral" by Howard (1963). If the energy equation is multiplied by $R\theta^+$ and integrated over the layer, one obtains:

$$\sigma R (\theta^+ \theta)_m = -R (\nabla\theta^+ \cdot \nabla\theta)_m - R (\bar{V} \cdot \hat{i}\theta^+)_m . \quad (7.5)$$

The two equations may be combined:

$$\begin{aligned} \sigma \{ P^{-1}(\bar{V}^+ \cdot \bar{V}^+)_m + R(\theta^+ \theta)_m \} &= -R(\nabla\theta^+ \cdot \nabla\theta)_m - R(\bar{V}^+ \cdot \hat{i}\theta + \bar{V} \cdot \hat{i}\theta^+)_m \\ &\quad - 2(\nu \bar{D} : \bar{D}^+)_m \end{aligned} \quad (7.6)$$

All of the terms in the equation are real, because the product of complex conjugate is positive real and the sum of complex conjugate is also real. In terms of the velocity components, the dyadic multiplication for the viscous term is:

$$\begin{aligned} 2 \bar{D} : \bar{D}^+ &\equiv \frac{1}{2} (\nabla \bar{V} + \nabla \bar{V}^+) : (\nabla \bar{V}^+ + \nabla \bar{V}^{++}) \\ &= |\partial_x u|^2 + |\partial_x v + \partial_y u|^2 + |\partial_y v|^2 \\ &\quad + |\partial_y v|^2 + |\partial_y w + \partial_z v|^2 + |\partial_z w|^2 \\ &\quad + |\partial_z w|^2 + |\partial_z u + \partial_x w|^2 + |\partial_x u|^2 \end{aligned} \quad (7.7)$$

where $|\partial_x u|^2 \equiv (\partial_x u)(\partial_x u^+)$, etc.

Since ν is always positive, the integrand for the viscous term must yield a positive result. It follows that σ and, hence, all the perturbation variables must be real. Therefore, the principle of exchange of stability

holds, as indicated by Tveitereid and Palm (1976). It is emphasized again that the conclusion is strictly true when the viscosity is only a function of the vertical coordinate x .

7.3 Linear Stability Analysis

A linear stability analysis is performed to suggest a specific wavelength for the numerical computation of the finite amplitude convection. The planform of the cellular motion of interest is chosen as longitudinal roll cells.

Method of Solution

Following the procedure outlined in Chapter IV, the critical Rayleigh number was determined as the minimum eigenvalue of the linear system:

$$\begin{vmatrix} (D^2 - a^2) & -a \\ aR_\theta & L_4 \end{vmatrix} \begin{vmatrix} \theta \\ \phi \end{vmatrix} = \begin{vmatrix} 0 \\ 0 \end{vmatrix} \quad (7.8)$$

where $L_4 \equiv (D^2 + a^2)\{\nu(D^2 + a^2)\} - 4a^2D(\nu D)$.

Either ϕ or θ may be eliminated to obtain:

$$\{L_4(D^2 - a^2) + a^2R_\theta\} \theta = 0 \quad ; \quad \{(D^2 - a^2)L_4 + a^2R_\theta\} \phi = 0 \quad (7.9)$$

where θ or ϕ must satisfy the boundary conditions:

$$\begin{aligned} \theta(0) = D^2\theta(0) = D(D^2 - a^2)\theta(0) = 0 \quad ; \quad \phi(0) = D\phi(0) = L_4\phi(0) = 0 \\ \theta(1) = D^2\theta(1) = D^4(1) = 0 \quad ; \quad \phi(1) = D^2\phi(1) = L_4\phi(1) = 0 . \end{aligned}$$

Note that Rayleigh number R_θ , based on the viscosity at arithmetic mean boundary temperature, is used. The self-adjointness of the operator in equation (7.8) leads to two different variational formulations for the

critical Rayleigh number R_c :

$$R_c = \min_{(a,Q)} \frac{\frac{1}{a^2} \int_0^1 [(DQ)^2 + a^2 Q^2] dx}{\int_0^1 \nu [\{ (D^2 + a^2)\phi \}^2 + 4a^2 (D\phi)^2] dx} \quad (7.10)$$

with the constraints on Q and ϕ ,

$$L_4 \phi = Q \quad \text{and} \quad Q(0) = Q(1) = \phi(0) = \phi(1) = D\phi(0) = D^2\phi(1) \quad ;$$

and, alternatively,

$$R_c = \min_{(a,W)} \frac{\int_0^1 \nu [\{ (D^2 + a^2)\phi \}^2 + 4a^2 (D\phi)^2] dx}{a^2 \int_0^1 [(DW)^2 + a^2 W^2] dx} \quad (7.11)$$

with the constraints on W and ϕ ,

$$(D^2 - a^2)W = \phi \quad \text{and} \quad W(0) = W(1) = \phi(0) = \phi(1) = D\phi(0) = D^2\phi(1).$$

These formulations reduce to the forms used in Pellew and Southwell (1940) and Chandrasekhar (1961), respectively, for a constant viscosity fluid.

For the actual calculation, the first variational principle, equation (7.10), was used. The trial functions, satisfying equation (4.13) with the boundary conditions $\theta(0) = \theta(1) = 0$, are Fourier sine series:

$$Q = \sum_{k=1}^{\infty} A_k \sin(k\pi x) \quad .$$

The variational formula reduces the problem to an eigenvalue problem:

$$\bar{E}^{-1} \bar{G} \bar{A} = \frac{1}{R_c} \bar{A} \quad (7.12)$$

where $\bar{E} = [E_{kj}] = \left[\delta_{kj} \frac{1}{2} \left\{ 1 + \left(\frac{\pi k}{a} \right)^2 \right\} \right]$

$$\bar{G} = [G_{kj}] = \left[\int_0^1 v \{ (D^2+a^2)\phi_k \cdot (D^2+a^2)\phi_j + 4a^2(D\phi_k)(D\phi_j) \} dx \right]$$

$$\bar{A} = [A_k]$$

The power method can be used for this problem because all eigenvalues are real positive. Thus,

$$\left[\frac{1}{R_c} \right] = \max_a \lim_{i \rightarrow \infty} \frac{[(\bar{E}^{-1}\bar{G}) \bar{A}^i]}{[\bar{A}^i]} \quad (7.13)$$

where

$$[\bar{A}^i] = \frac{[(\bar{E}^{-1}\bar{G}) \bar{A}^{i-1}]}{[\bar{A}^{i-1}]}$$

The index i denotes the iteration number and the initial vector chosen is

$$[\bar{A}^0] = [1, 0, 0, 0, \dots]$$

For the constant viscosity case, an analytic solution is possible. (See Appendix D.) The analytic results were used to check the accuracy of the finite difference solution technique. The comparison suggested that an accurate value of R_c can be obtained with a four term expansion of Q . For variable viscosity cases, the ϕ_k functions were computed by finite difference technique using a uniform grid of 50 and 100 zones. The G_{kj} integrals were performed assuming that $(D^2 + a^2)\phi_k$, $D\phi_k$ and v are each piecewise linear within each grid interval. The two different uniform grid systems were employed to extrapolate the final values of R_c , assuming that the G_{kj} 's are second order accurate with grid size. The extrapolation technique only

affected the fifth significant digit for the highest viscosity ratio number ($\Gamma = 10^4$). All the computations were performed using double precision arithmetic on an IBM 370/168 system.

Results and Discussion

Before commenting on the results, the Rayleigh numbers must be specifically defined by the selection of a suitable mean viscosity. Various choices have been advanced by past investigators. Busse - for small viscosity variation (1967a) - defined the reference temperature in such a way that the resulting critical Rayleigh number did not depend on viscosity variations to the first order. For large viscosity variation, the arithmetic mean boundary temperature is usually adopted to calculate a reference viscosity (denoted as ν_{θ}^* and employed in the numerical computations). In this thesis, a geometric mean viscosity will be chosen as a reference viscosity:

$$\nu_M^* \equiv \sqrt{(\nu_h^* \cdot \nu_c^*)} \quad . \quad (7.14)$$

For the viscosity law of equation (7.3), the two Rayleigh numbers are related by

$$R_M = \Gamma^{-\frac{1}{6}} R_{\theta} \quad . \quad (7.15)$$

Note that the subscripts θ and M will distinguish the two different Rayleigh numbers for an identical problem. The distinction is important for discussion purposes, because the critical Rayleigh number is either an increasing (for R_{θ}) or a decreasing (for R_M) function of the viscosity ratio number, Γ , depending on the choice. The results will be discussed using both definitions.

The marginal stability diagram is shown in Figure 7.1. This is the plot of R_M versus a (wave number) at each chosen Γ . The critical Rayleigh number is the minimum value of R_M on each curve and decreases with increasing Γ . Palm (1960) also obtained the similar results for a small viscosity variation case. If the R_θ curve, rather than R_M , has been plotted, the stability curves would cross one another in the higher wave number range. A cross plot of the critical Rayleigh number is shown in Figure 7.2. Note that the R_θ curve attains a maximum around the viscosity ratio of 2000, as mentioned earlier. Both curves converge to the critical Rayleigh number for the constant viscosity case, which is 1100.67.

By choosing the reference viscosity to be a function of Γ , one can force the critical Rayleigh numbers to be independent of Γ . This has a disadvantage because choice of the reference viscosity is not simple. Alternatively, one can choose a reference viscosity to yield the same critical Rayleigh number (i.e. 1100.67) for a small values of Γ . When this is done (viscosity was chosen at the temperature corresponding $x = 0.374$) the resulting curve is shown as a dotted line. This is the choice suggested by Busse. Now, it renders the Rayleigh number constant up to $\Gamma = 20$.

The critical wave number increases with the value of Γ . For example, the critical wave number at $\Gamma = 100$, corresponds to a 10% decrease in wavelength compared with the constant viscosity case. Booker (1976) observed increasing wavelength in his experiment with the rigid bottom boundary. His number of roll cells was only about 10. It has been mentioned earlier in Chapter II that this is an area of controversy between experiment and theory.

The linear stability theory does not predict the limiting amplitude of

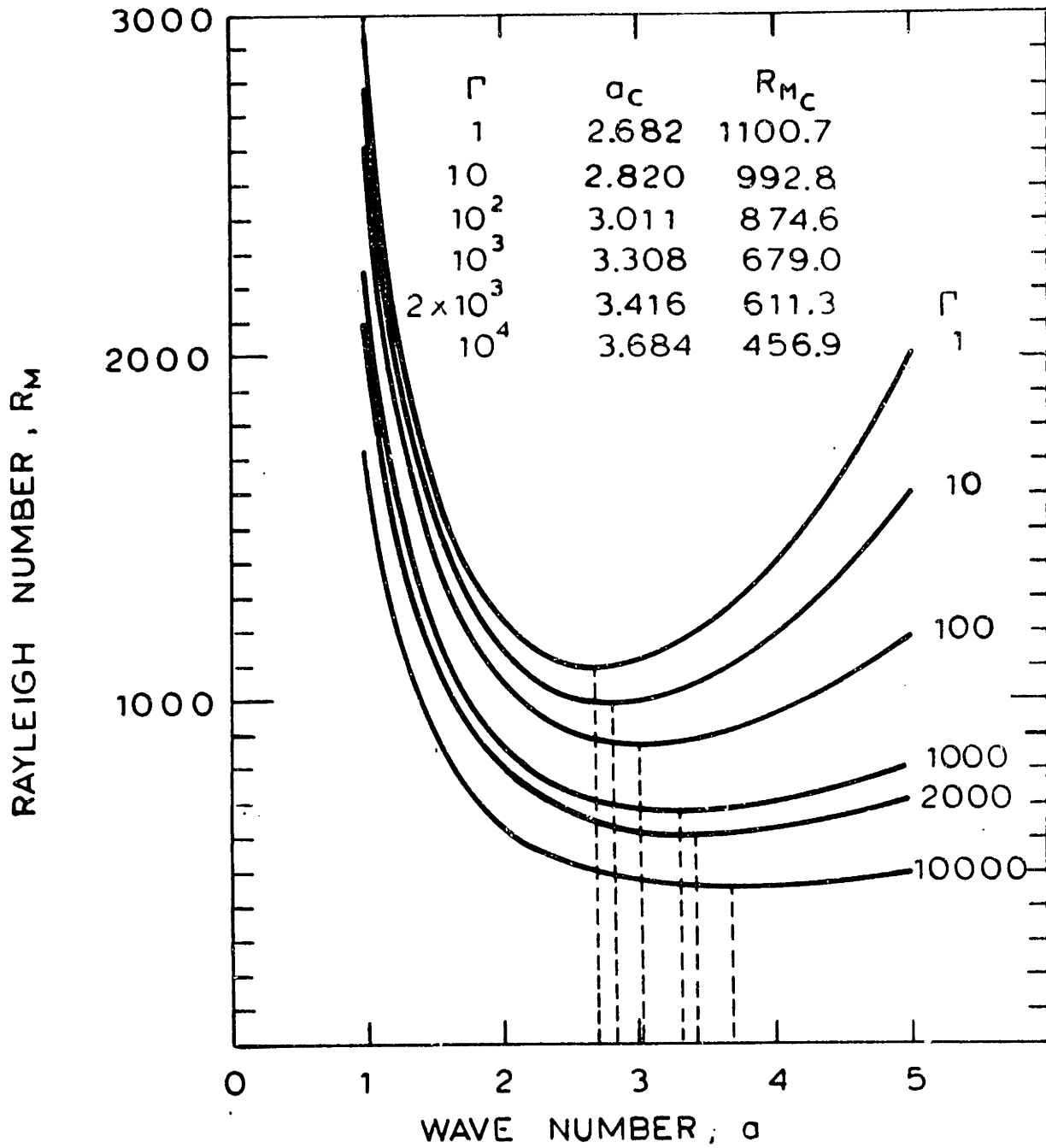


Figure 7.1 Stability Diagram - R_M vs Wave Number at Fixed Viscosity Ratio Number

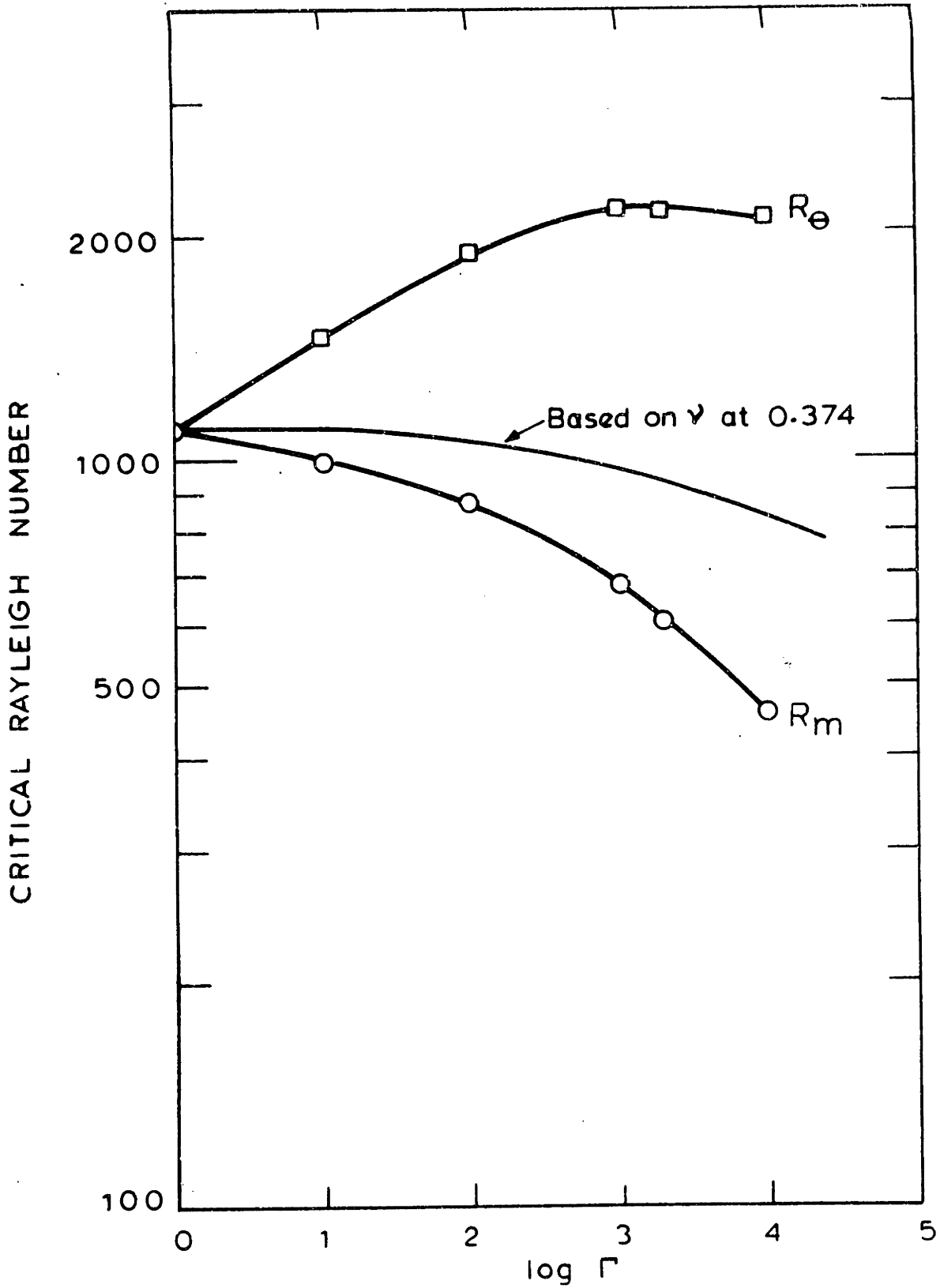


Figure 7.2 Critical Rayleigh Number vs Viscosity Ratio Number

the convection field, but does provide the functional shape of the eigen-solution for the critical states. These eigensolutions θ and ϕ are plotted in Figure 7.3, where the θ functions are normalized with their maximum and the ϕ functions have the proper magnitude relative to the θ solutions. As the Γ values increase, the positions of maximum perturbations in temperature and stream function tend to displace towards the hot bottom boundary. Also the ϕ functions increase their maximum values. The circled points for $\Gamma = 1000$ represent the result obtained by the amplitude specification method, as the disturbance amplitude ε goes to near zero (see Section 7.4). The remarkable agreement serves to validate the results of both computational methods.

7.4 Finite Amplitude Convection

The amplitude specification method, outlined in Chapter IV, was applied to obtain the finite amplitude convection fields for this problem. The results of the linear stability analysis now provide the wavelength to fix the cell size for the vertical boundary conditions:

$$\partial_z \theta = \phi = \partial_z^2 \phi = 0 \quad \text{at } z = \text{both } 0 \text{ and } \frac{\lambda_c}{2} .$$

With these, equation (4.24) was solved numerically using a finite difference technique for a restricted range of parameter values. The focus of the study was to examine the behavior of highly viscous fluids (for an assumed infinite Prandtl number), near the critical conditions for various Γ .

Finite Difference Formulation

Finite difference formula obtained by sectioning the region of interest into non-uniformly sized rectangular grids and integrating both equations in (4.24) over each of the rectangular grid, viz.,

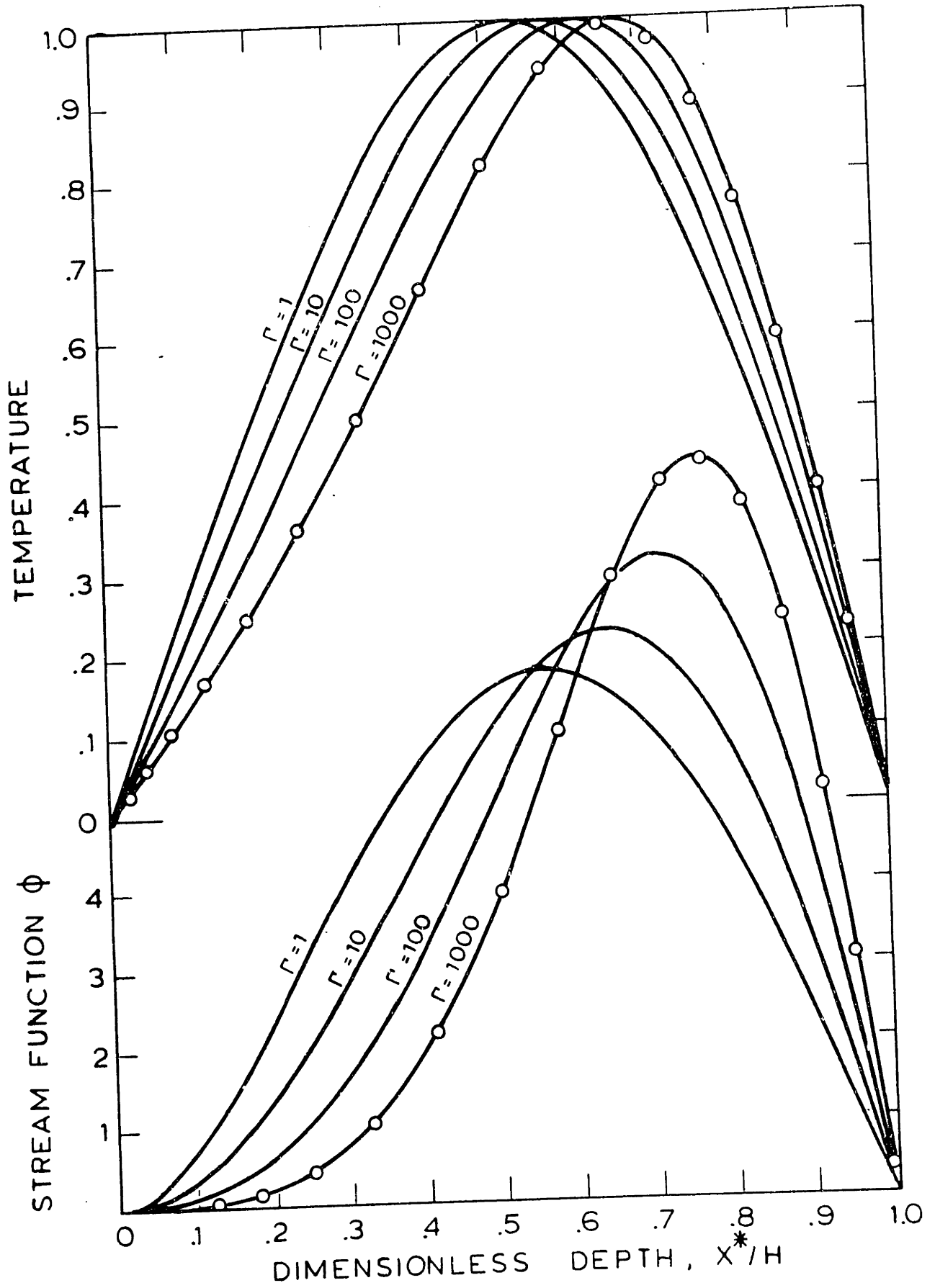


Figure 7.3 Profiles of Characteristic Functions

$$0 = \frac{1}{s} \oint_{\bar{l}} \nabla \Theta \cdot d\bar{l} - \frac{1}{s} \oint_{\bar{l}} (1 + x + \Theta) \bar{V} \cdot d\bar{l} \quad (7.16)$$

$$0 = \frac{1}{P} \frac{1}{s} \oint_{\bar{l}} (-\nabla^2 \Phi) \bar{V} \cdot d\bar{l} - \iint_s \partial_z \Theta \, ds$$

$$+ \frac{1}{s} \oint_{\bar{l}} d\bar{l} \cdot \left[\hat{i} \{ v \partial_x (\nabla^2 \Phi) + 2(\partial_z v)(\partial_{xz}^2 \Phi) + (\partial_x v)(\partial_x^2 \Phi - \partial_z^2 \Phi) \} \right.$$

$$\left. + \hat{j} \{ v \partial_z (\nabla^2 \Phi) + 2(\partial_x v)(\partial_{xz}^2 \Phi) - (\partial_z v)(\partial_x^2 \Phi - \partial_z^2 \Phi) \} \right]$$

where \bar{l} and s denote the directed boundary length (vector) and the area of rectangular grids, respectively. The velocity \bar{V} should be normalized according to equation (4.22). A set of conservative formulations were obtained by replacing the above expressions with suitable difference forms, which are presented in Appendix E.

The set of difference equations were solved by an alternately direct implicit line overrelaxation scheme. (See Clomburg (1971) for details). A cyclic advance of the energy and biharmonic equations was followed by a normalization process for the amplitude, ϵ , of the velocity. At each cycle, a number of inner iterations were performed for each of energy and biharmonic equations to obtain internally consistent results. This appears to facilitate the overall convergence rate. In general, a total of 100 to 150 iteration cycles (15 cycle by 10 inner iteration) were enough to obtain convergent solutions. This requires about 0.6 CPU minute on an IBM 370/168 system. Non-uniform grid of 15 by 15 to 20 by 20 were used.

Convergence was ascertained by examining the residuals of each of the equations and computing an overall energy balance, and, in addition, determining the horizontal average heat fluxes. The net convective Nusselt

number was obtained from:

$$\begin{aligned} \text{Nu} - 1 &= \partial_x \bar{\theta} - \bar{u\theta} \\ &= (-u\theta)_m \end{aligned} \tag{7.17}$$

where overbars denotes horizontal average. A further check was provided by examining the variation of the Rayleigh number calculated in each iteration and also comparing the relative magnitude of stream function values at the two arbitrarily chosen grid points. When convergence was achieved, these values were constant within the relative error less than 0.1%.

Numerical Results and Discussions

The parameter values for the finite amplitude cases are listed in Table 7.1. Shown in the table are the predicted Rayleigh numbers and net convective Nusselt numbers for the specified amplitudes and viscosity ratio numbers. The predicted critical Rayleigh number for the constant viscosity case agrees within 1% to the linear stability result. A coarse grid employed for this case (15 by 15 nonuniform grid) is responsible for this small error. Some additional information are presented in Figure 7.4 as contour plots of ϕ and θ for the selected viscosity ratio numbers ($\Gamma = 1, 10, 10^2, 10^3$) at a fixed amplitude $\varepsilon = 5$. Nine contour lines are spaced at a constant interval and each plot is drawn with its relative cell size predicted by the linear stability analysis. Notice that each case corresponds to a different Rayleigh number ratio (defined as R/R_c , which is 2.195, 1.977, 1.637, 1.319 in that order from the top). As viscosity ratio number increases, motion is constrained to the lower reaches of the cell where the viscosity is lowest. In this region, convection is dominant, while in the upper region conduction

TABLE 7.1
 Numerical Results for Finite Amplitude Convection

Amplitude (ϵ)	$\Gamma = 10^0$		$\Gamma = 10^1$		$\Gamma = 10^2$		$\Gamma = 10^3$	
	R_θ	Nu - 1	R_θ	Nu - 1	R_θ	Nu - 1	R_θ	Nu - 1
0.001	1112.85	8.717(-8) [¶]	1461.9	8.775(-8)	1890.16	7.475(-8)	2148.05	5.590(-8)
0.01	1112.85	8.717(-6)	-	-	-	-	2148.05	5.588(-6)
0.05	1113.0	2.179(-4)	-	-	-	-	2147.7	1.395(-4)
0.1	1113.43	8.713(-4)	-	-	-	-	2147.1	5.571(-4)
0.2	1115.16	3.480(-3)	-	-	-	-	2144.6	2.223(-3)
0.5	1127.3	2.152(-2)	-	-	-	-	2129.0	1.375(-2)
1.0	-	-	1531.2	8.802(-2)	1909.37	6.495(-2)	-	-
1.005	-	-	-	-	-	-	2092.0	5.411(-2)
1.554	-	-	-	-	-	-	2074.0	1.183(-1)
2.0	-	-	1699.9	2.632(-1)	2023.0	2.219(-1)	-	-
2.5	1464.34	4.172(-1)	-	-	-	-	-	-
2.56	-	-	-	-	-	-	2150.0	2.732(-1)
3.82	-	-	-	-	-	-	2432.0	4.768(-1)
5.0	2442.80	1.0283	2889.5	9.078(-1)	3095.0	7.747(-1)	2834.0	6.463(-1)
10.0	5988.3	1.876	6720.0	1.618	6630.0	1.356	-	-
15.0	-	-	-	-	11993.0	1.765	10357.0	1.405

[¶] Numbers in parentheses denote the power of 10.

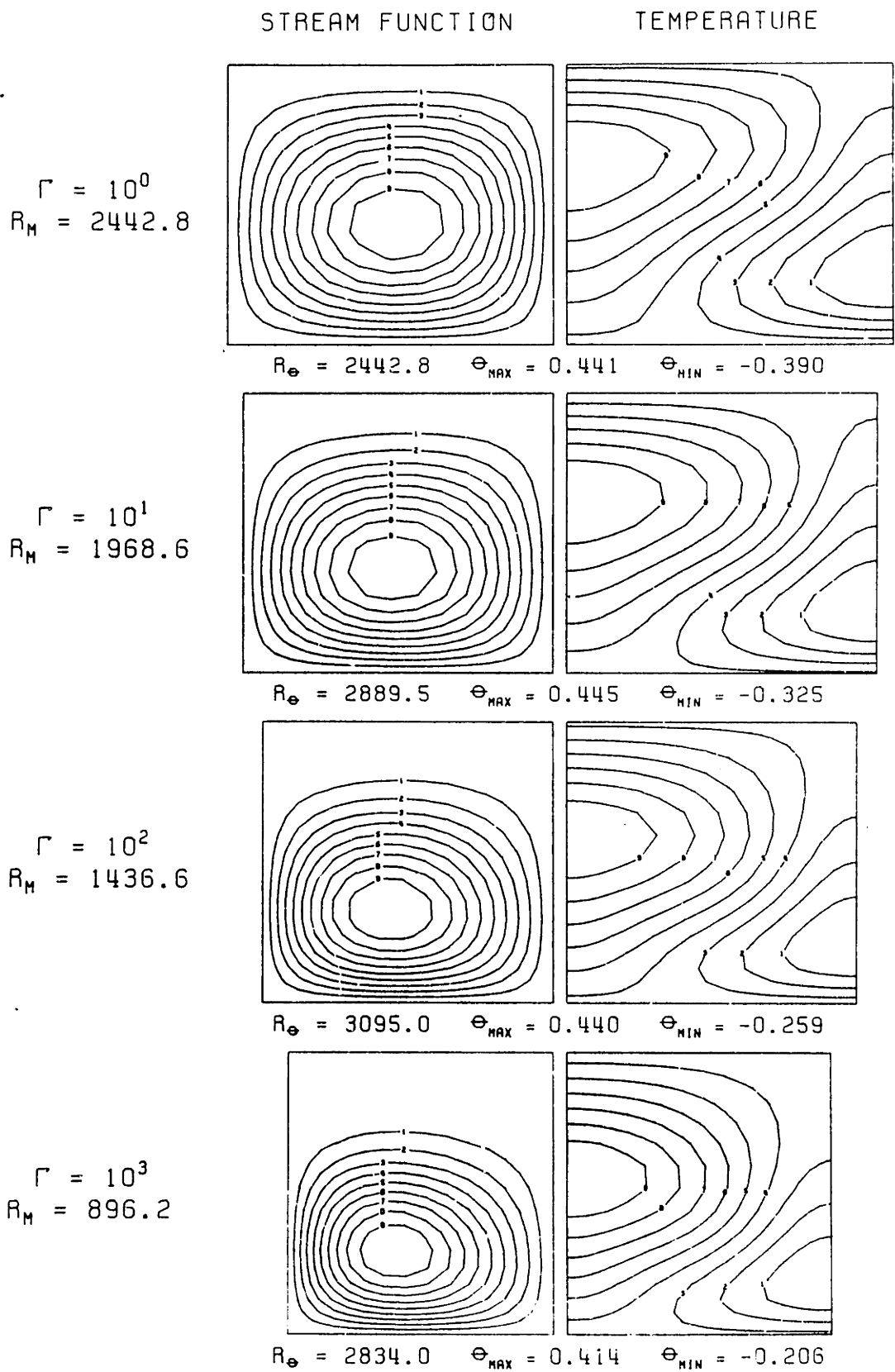


FIGURE 7.4 FLOW AND TEMPERATURE CONTOUR PLOTS AT CONSTANT AMPLITUDE, $\epsilon = 5.0$

is responsible for most of the energy transfer. Notice that the corresponding Rayleigh number R_θ exhibits a maximum around the viscosity ratio number of 100, which is similar to the behavior observed by Torrance and Turcotte (1971) for the free-free boundary conditions. (Actually, a maximum stream function value at constant R_θ was reported.) A judicious definition of the Rayleigh number, i.e. R_M , makes this behavior disappear.

Figure 7.5 shows Nusselt number and maximum stream function versus Rayleigh number at various viscosity ratios. Above the Rayleigh number ratio of 1.3, an increasing viscosity ratio has the effect of upward displacement of both parameters. Near the critical point, the results for a large viscosity variation shows an interesting behavior: the hysteresis effect. (The transition appears to occur just above the viscosity ratio number of 100.) The case of the viscosity ratio number of 1000 shows that, when the Rayleigh number increases slowly, the convection starts to grow directly to a finite amplitude state at the critical Rayleigh number. The total circulation suddenly jumps to 2.5. When the Rayleigh number decreases, however, convection motion is sustained even below the critical Rayleigh number and decays to the motionless conduction state only if the Rayleigh number is reduced to a value less than $0.965 R_C$. Whether this behavior occurs or not physically is not certain, since this analysis is based on the roll cell motion, while other forms of cellular motion may have a more stable behavior. However, as far as the calculation is concerned, the result is valid. To show this, a plot of $(R-R_C)/R_C$ versus $(Nu-1)R/R_C$ is prepared in Figure 7.6. According to the modified perturbation method by Busse (1967a), the proportionality constant of the relationship is 1.628 for the mixed boundary conditions. This result is plotted as a dotted line.

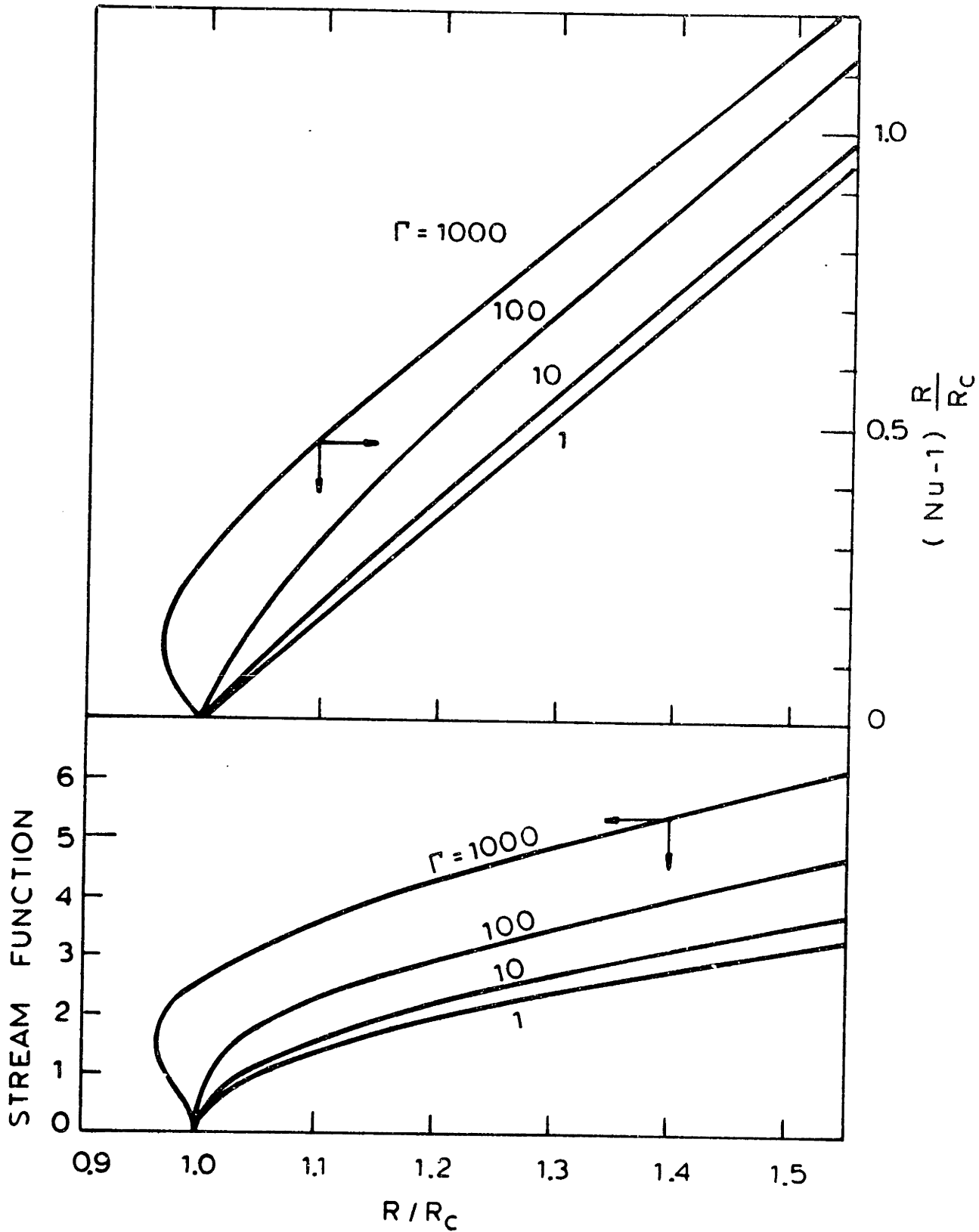


Figure 7.5 Finite Amplitude Behavior of Nusselt Number and Stream Function

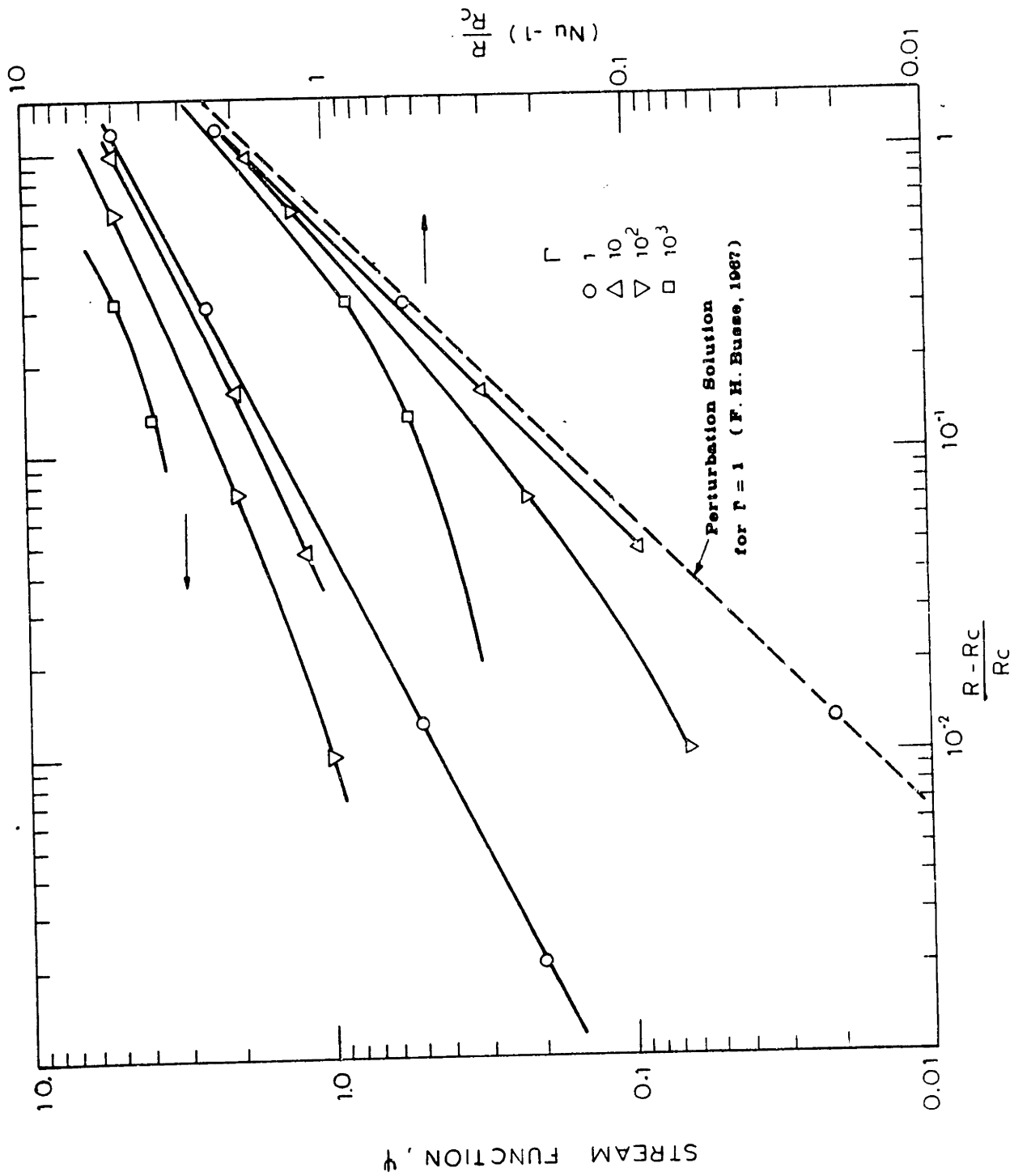


Figure 7.6 Asymptotic Behavior of Nusselt Number and Stream Function

Clearly, present result obtained by the amplitude specification method shows the same relationship up to $1.5 R_c$. Beyond this point, it starts to deviate slightly from the perturbation result. The slope of the maximum stream function values indicates that the amplitude, ϵ , is proportional to $(R-R_c)^{\frac{1}{2}}$, up to this point.

The compatibility of the method with the linear stability analysis is shown in Figure 7.7. The temperature profile from the linear analysis is directly compared to the limiting solution of the finite amplitude convection solution (circles) for a viscosity ratio number of 1000. For the comparison, the maximum value for the linear solution was fixed at the same value as that of the finite amplitude calculation. Not only does the maximum position coincide, but also the functional shape of the two solutions are in perfect agreement. The curve plotted with the square symbols show the stable solution of finite amplitude convection at the same critical Rayleigh number due to the hysteresis behavior. It shows completely different functional shape from the critical state solutions. If a conventional procedure were adopted (that is, solving the equation with a specified Rayleigh number via finite difference technique), numerical procedure would clearly suffer a difficulty to choose one of the two stable stationary solution (if possible at all). This may be shown in Figure 7.8, where the convergence behaviors are plotted in terms of the maximum stream function values for the case of $\Gamma = 100$. Supercritical and subcritical cases converge quickly to final stable solution. However, near the critical point (denoted by triangle symbols), the use of more than ten times of the normal number of iterations does not produce the final stable solution.

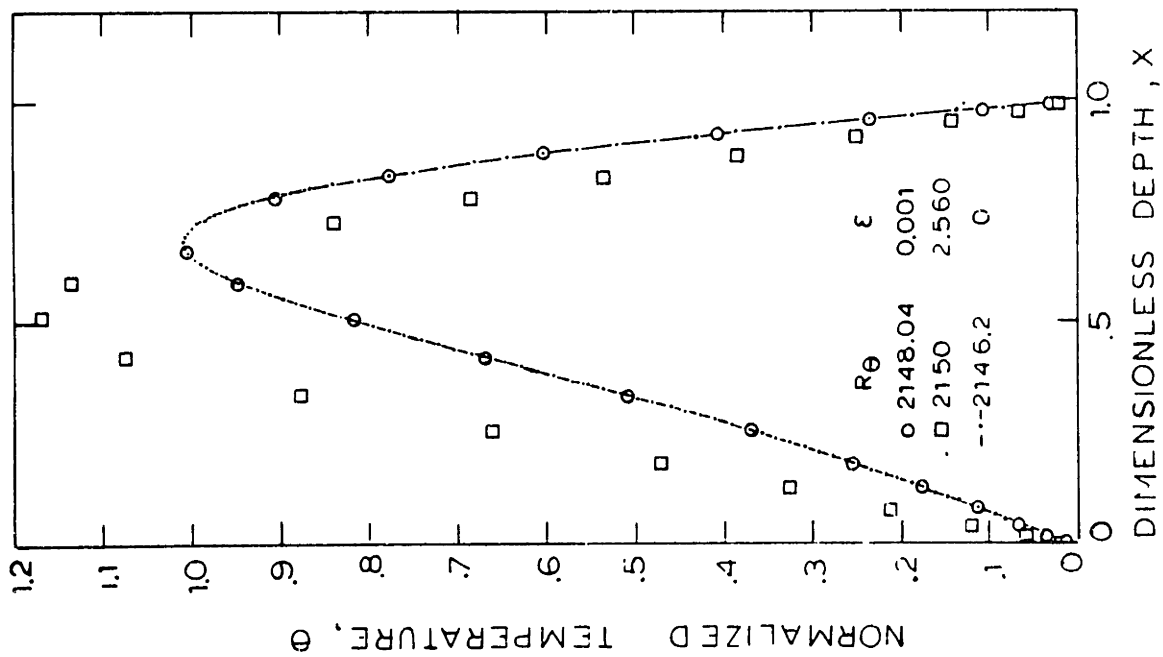
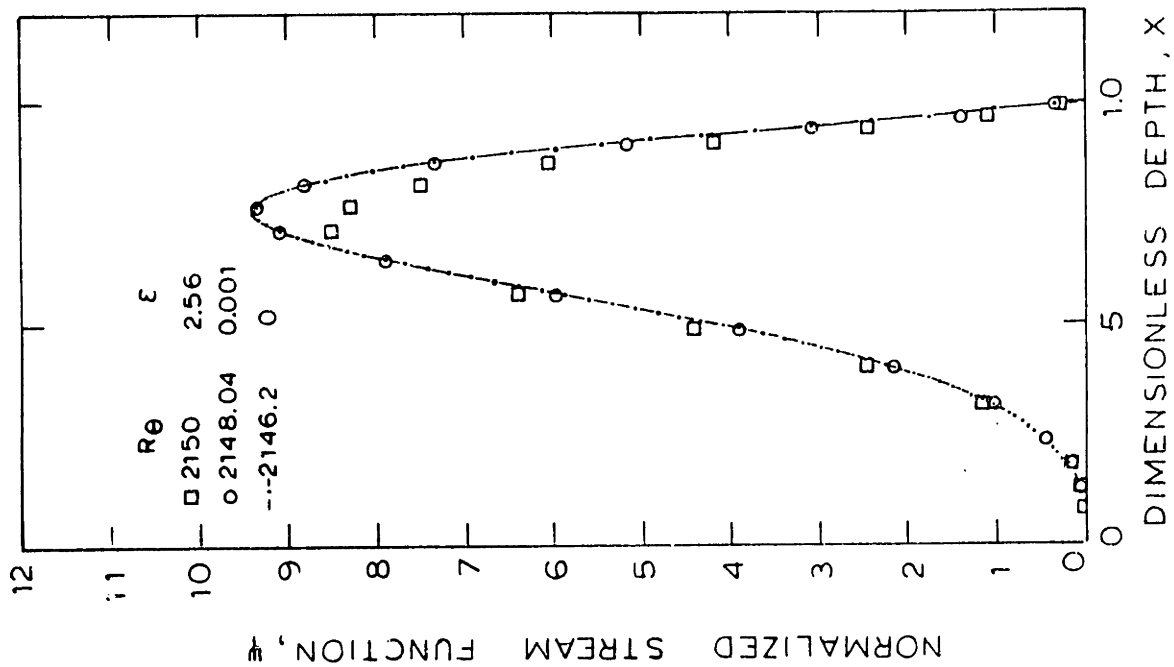


Figure 7.7 Two Distinct Finite Amplitude Solutions near Critical Rayleigh Number ($\Gamma = 10^3$)

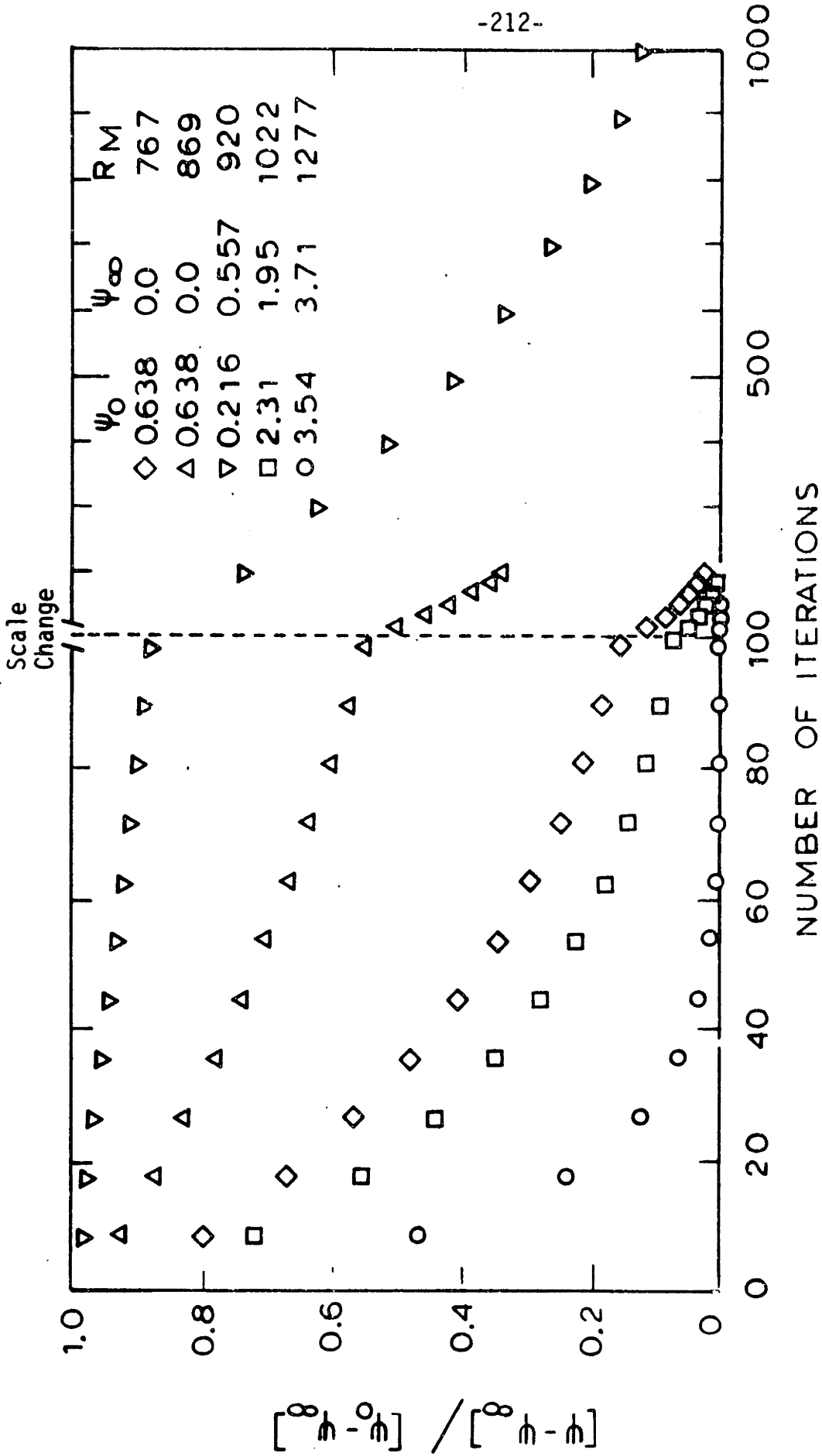


Figure 7.8 Convergence Behavior of the Conventional Numerical Technique $R_c = 874.6$ $\Gamma = 100$

7.5 Summary

The stability of the roll cell planform of the Rayleigh-Bénard problem was investigated with large temperature dependent viscosity. The critical conditions were obtained through the linear theory for a chosen viscosity law. The amplitude specification method was devised to avoid convergence problem near the critical state.

The results shows that the critical condition is strongly dependent on the viscosity variation number and the choice of reference viscosity is important for determining numerical values of the critical Rayleigh number. One of the suprising results is that the hysteresis behavior occurs when the viscosity ratio number exceeds 100. It was possible to obtain this result only because the amplitude specification method is capable of predicting multiple stationary solutions, which are not obtainable via conventional procedures (specifying Rayleigh numbers to find the corresponding convective fields).

Finally, the results obtained in this chapter imply that the viscosity variation would not have any significant impact on the roll motion observed in the experimental run, largely due to the small viscosity variation over the roll region (at most, a four fold change). However, it is not necessarily the case for the melter section of real glass furnace. The extremely low temperature observed within the batch raw material in real glass furnace (Jebsen-Marwedel, 1937) is suggestive of many order of magnitude variation in viscosity of melts under the batch blanket, where the roll motion is supposed to exist.

VIII CONCLUDING REMARKS

A general onset criterion was established through the use of linear stability analysis for the roll motion which occurs locally within the longitudinal circulation current of a simulated glass melt flow. The critical condition is determined from the maximum temperature difference, ΔT_m^* , in the unstable fluid layer and its depth, ℓ_t^* ,

$$R_C \equiv \frac{g \cdot \beta \cdot \Delta T_m^* \cdot \ell_t^{*3}}{\nu_o^* \cdot \alpha_o} \approx 500$$

$$a_C \equiv 1.88 \text{ (based on the } \ell_t^* \text{)}.$$

This onset criterion has been experimentally verified with a physical model of a glass furnace using glycerine as a working fluid. Temperature measurements obtained from the roll cell region agreed quite well with the theoretical prediction of the onset of roll motion.

The linear stability analysis was applied to study the disturbances confined to the transverse plane, which is orthogonal to the plane of the basic (longitudinal) motion. Energy transfer was allowed to the transverse planes from the circulation currents, as these pass through the plane. This energy transfer was evaluated using the source-sink approximation method. In the region of roll motion, a parabolic profile of internal heat source was found to effectively represent this energy transfer. In the analysis, the ratio of temperature gradient in the stable fluid layer (under the source region) to the depth of the source region was identified as a principal parameter for the roll instability. Since this parameter is directly reflected in the values of ΔT_m^* and ℓ_t^* , the general criterion

presented above was found nearly independent of the parameter, η_t .

The utility of the source-sink approximation method previously reported (Curlet, 1976) has been extended in its capability for predicting the onset condition. The predicted location of onset of roll motion agrees satisfactorily with the experimental observation. The observed wave number (decided from the streak photographs) also agrees well with the prediction.

A numerical investigation, independent of the experiment, has been performed to assess the effect of large viscosity variations on the roll motion in the Rayleigh-Bénard problem. When the maximum viscosity ratio within the fluid exceeds 100, a hysteresis effect in heat transfer as well as a marked contraction in cell sizes are observed. The numerical results, which required stationary solutions (stable or unstable) near the critical conditions, were made possible only through the use of a new technique, named the amplitude specification method. The method was devised to resolve convergence problems encountered in the conventional approach of the finite difference technique, and even provided multiple solutions for a range of subcritical Rayleigh numbers.

Even though the roll motion has not been reported from a direct observation of operating furnaces, its influence has probably been accounted for through the empirical approaches prevailing in the industry. The methodology developed in this thesis can be extended to allow a quantitative treatment of the heat transfer mechanism and the homogenization process under the batch blanket in a glass furnace tank. Specifically, the heat transfer enhancement and the mixing power by the finite amplitude roll motion can be quantitatively investigated with the use of the amplitude specification method.

The results in this thesis also suggest that any attempts at the development of a numerical program for three dimensional glass melt calculations should be approached with caution. Unless more powerful techniques are devised, such efforts would be futile in understanding operation. The spatial resolution required to predict the roll motion - rigorous results require at least 15 grid points within each cell - would be too expensive to implement even with the most advanced computer. The source-sink approximation method might be useful as an interim measure.

APPENDIX A

INTERFACE HEAT TRANSFER OF BATCH MELTING PROCESS

Most of the complex reactions of glass formation and the melting process occur within the batch blanket. Since the pioneering work of Preston and Turner (1940), an enormous bank of knowledge has been accumulated on the chemical reaction sequence of batch material mainly through crucible melting experiments (Cable, 1968). Recently, progress has also been made on numerical modeling for predicting circulation currents of melt in glass furnace. Even a few attempts have been made to couple the convective heat transfer in melt with the combustion radiation transfer (Mase and Sasagawa, 1973; Clomburg et al., 1975). However, these modeling studies suffer a drawback because of the present lack of a theoretical understanding of batch melting and its interaction with the glass melt and with the combustion flame in real glass furnace. In this appendix, modeling of the batch melting process is attempted in relation to the heat transfer mechanisms at batch interfaces.

Chemical Reaction Sequence of Batch Material

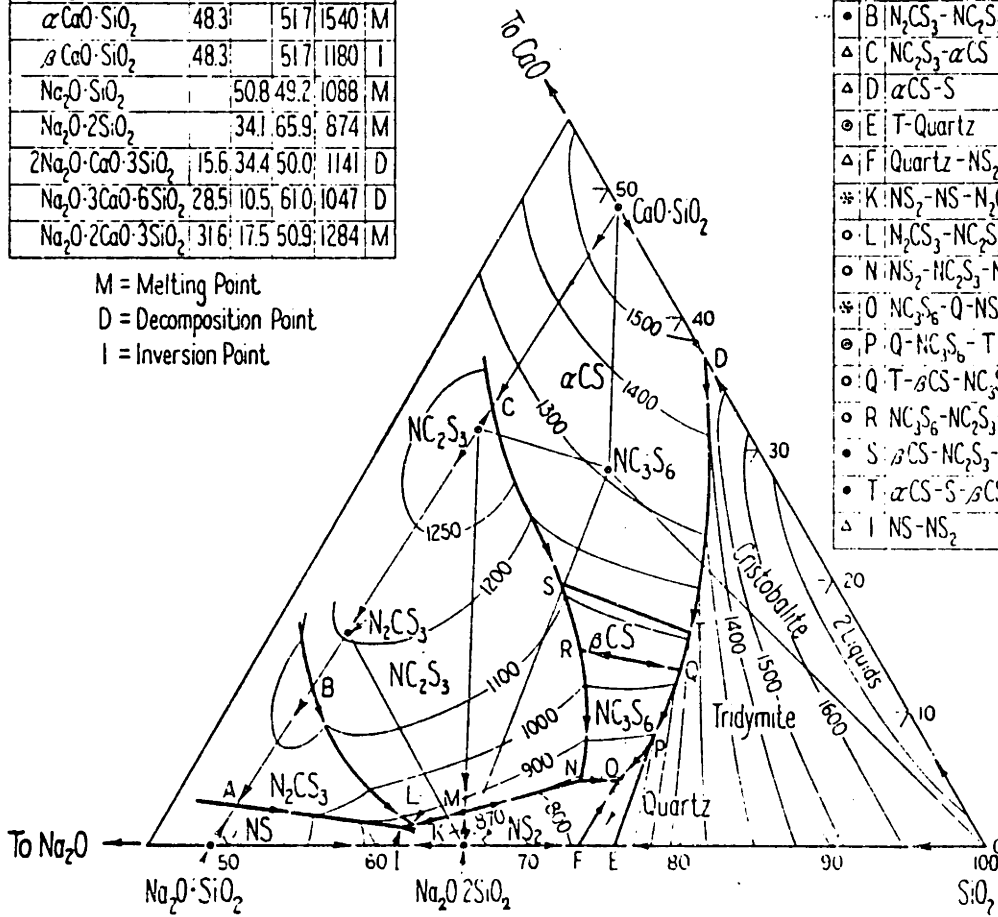
In a mixture of soda-lime-silica, liquid phase does not exist below 998 K, as shown in the phase diagram of Figure A.1. This is the ternary eutectic temperature of the mixture. Below this temperature, reactions proceed in a subliquidus state to form metasilicates (Harrington et al. 1962). This reaction continues to proceed until binary eutectic point between metasilicates and disilicates at 1113 K is attained. This polymorphic transition in soda and quartz compounds results in shrinkage of batch material.

Compounds	CaO	Na ₂ O	SiO ₂	Temp.
SiO ₂			100.0	1710 M
α CaO · SiO ₂	48.3		51.7	1540 M
β CaO · SiO ₂	48.3		51.7	1180 I
Na ₂ O · SiO ₂		50.8	49.2	1088 M
Na ₂ O · 2SiO ₂		34.1	65.9	874 M
2Na ₂ O · CaO · 3SiO ₂	15.6	34.4	50.0	1141 D
Na ₂ O · 3CaO · 6SiO ₂	28.5	10.5	61.0	1047 D
Na ₂ O · 2CaO · 3SiO ₂	31.6	17.5	50.9	1284 M

M = Melting Point
 D = Decomposition Point
 I = Inversion Point

Point	Crystal Phases	CaO	Na ₂ O	SiO ₂	Temp.
△ A	NS - N ₂ CS ₃	3.0			1060
• B	N ₂ CS ₃ - NC ₂ S ₃	11.5			1141
△ C	NC ₂ S ₃ - αCS	33.0			1280
△ D	αCS - S	37.0		63.0	1436
⊙ E	T-Quartz	24.3	75.7		870
△ F	Quartz - NS ₂	26.4	73.6		790
* K	NS ₂ - NS - N ₂ CS ₃	18	37.5	60.7	821
⊙ L	N ₂ CS ₃ - NC ₂ S ₃ - NS ₂	2.0	36.6	61.4	827
⊙ N	NS ₂ - NC ₂ S ₃ - NC ₃ S ₆	5.2	24.1	70.7	740
* O	NC ₃ S ₆ - Q - NS ₂	5.2	21.3	73.5	725
⊙ P	Q - NC ₃ S ₆ - T	7.0	18.7	74.3	870
⊙ Q	T - βCS - NC ₃ S ₆	12.9	13.7	73.4	1035
⊙ R	NC ₃ S ₆ - NC ₂ S ₃ - αCS	14.5	19.0	66.5	1030
⊙ S	βCS - NC ₂ S ₃ - αCS	19.5	17.7	62.8	1110
⊙ T	αCS - S - βCS	15.6	11.4	73.0	1110
△ I	NS - NS ₂	38.0			840

△ Binary Eutectic
 * Ternary Eutectic
 • Decomposition Point
 ⊙ Reaction Point
 ⊙ Inversion Point
 C = CaO N = Na₂O
 S = SiO₂ Q = Quartz
 T = Tridymite



G. W. Morey and N. L. Bowen, *J. Soc. Glass Technol.*, 9, pp. 232, 233 (1925).

Figure A.1 Phase Diagram for Soda-Lime-Silica Glass

The first major changes in batch appearance occur at the melting point of sodium carbonate around 1124 K. Violent reaction takes place with rapid decomposition of sodium carbonate and liquid phase is dominant. This change is called the primary melt stage. Because of a low surface tension of low silica content melts, the primary melts completely wet the remaining silica grains. Thus, sand grains have a wet appearance. Around the limestone decomposition temperature of 1173 K, CO₂ gas begins to evolve vigorously. The CO₂ gas continues to disengage from the melts until the entire silica residues are completely dissolved (Kröger, 1952). At slow heating rates, the CO₂ evolution is completed before permanent liquid metasilicates form. This early CO₂ evolution prevents the decomposition of metasilicate into sodium carbonate at higher temperatures than 1480 K. The presence of metasilicate facilitates further silicate formation. In contrast, high heating rates result in a formation of silica scum on the melt surface (Manning et al., 1964). The silica scum has low density (specific gravity of 2.38) and tends to float on melts (specific gravity of 2.45-2.55) in the form of cristobalite clusters. Once formed, scums usually dissolve at an extremely slow rate during the final melting stage, while most of the silica grains are rapidly consumed in the primary melt stage.

Alkali carbonates are readily dissolved in the liquid phase at temperatures of 1260-1310 K and react with the silica residues underneath the metasilicate crust. Vigorous bubble formation persists through the temperature range of 1250 to 1300 K. The dissolution of the remaining silica continues to proceed at higher temperatures until it is completely dissolved.

This three-stage reaction sequence, namely the subliquidus reaction stage, the primary melt stage and the residual silica dissolution, will undoubtedly occur at the batch blanket in glass furnace. According to crucible experiments, chemical reactions demand only 10% of the total batch free time, while the dissolution of residual silica consumes the rest of the time. Recent observation appeared to support these results in real furnace (Zhuza et al., 1973). The total melting time of the batch was reported less than 1 hour at 1773 K or above.

Physical Process of Batch Melting

Direct observation in tank furnace indicated that the interior temperature of a batch blanket was only a little over 373 K after remaining 30 minutes in furnace, although the melted crust of the batch surface had already reached 1573 K at the same time. Furthermore, the temperatures of melts just underneath the batch blanket are only 50 K lower than that of top surface melt (Jebsen-Marwedel, 1937). Therefore, there exist steep temperature gradients in the fused layers covering the interior batch material. This is due to the extremely low thermal conductivity (0.28-0.35 J/m·s·K) of batch material at low temperature.

The melting of top batch surface by flame radiation takes place instantaneously to form a fused crust, even at temperatures as low as 1073 K (Jack and Jacquest, 1958). Once the fused layer forms, its effective thermal conductivity will increase dramatically because of the contribution of diffusive radiation effect at high temperature. The presence of liquid phase also changes dramatically the chemical reaction rate (Kröger, 1957). Thus silicate formation proceeds rapidly with residual silica in the layer. On the other hand, the top fused layer

tends to shield radiation of the combustion flame from the interior batch. Since heat penetration into the interior batch is obstructed by its low thermal conductivity, chemical reactions for the primary melt must proceed in a virtually thin interface of the unmelted batch (Pugh, 1968). Consequently, heat transfer within the fused layer takes place by conduction. Under the layer, the batch materials remain cold in solid state. These observations were realized in a laboratory furnace experiment of Daniels (1973).

Unlike the top fused layer, the bottom of the batch blanket is in direct contact with the hot glass melts, which are in convective motion. Even though direct observations in this region are difficult, there are no doubts that a steep temperature gradient exists between the solid interior batch and the melt in convective motion. However, melting process in this region is much more complicated due to the interaction with gas evolution and convective motion in melts.

The gas evolution brings out stirring motion in the batch blanket, which provides direct contact of solid batch with fused melt through percolation. The volume of gas evolved is enormous, as much as 100 times the volume of the final glass product. Most of these gases are formed in the early reaction stages, although gas formation continues until all the residual silica is consumed. A continuous burst and new formation of gas bubbles on the top surface of batch has been directly observed in the furnace. The gas release at the top surface occurs rapidly due to its low partial pressure of CO_2 , which is maintained by the continuous gas stream over the surface. Bubbles trapped in top fused layer rapidly build up its pressure due to high temperature and easily erupt. On the other hand,

gases which evolve under the solid batch can hardly escape, because they are effectively sealed by the solid batch and the top fused layer. No reactions are expected to occur in the solid interior. If it occurs, partial pressure of CO_2 builds up in the batch and the reaction will be suppressed accordingly. Moreover, endothermic reactions in this low temperature make the solid batch remain cold. Gas bubbles trapped in the bottom of batch build up pressure, being subject to continuous heat flux from the melt below. Occasional eruptions through the solid batch provide the opportunity for the top fused layer to flow down to the bottom. This stirring motion is clearly an important factor for batch melting.

The convective motion of melt in the furnace tank also contributes significantly to batch melting. Primary circulation pattern generates a steep velocity gradient at the interface with the fused batch layer. The abrasive effect will help to wash away freshly formed melt from the fused layer as soon as its viscosity becomes low enough to flow freely.[§] An unstable temperature gradient exists in the melt, because the energy required for batch melting comes from the melt below. As shown in this thesis, this unstable temperature gradient causes an instability in fluid motion. If it occurs in a real furnace, it may profoundly influence the heat and mass transfer rates under the batch. The enhanced local heat transfer would promote more batch melting. The roll motion itself would provide extra mixing for the freshly formed melt joining the melt in tank.

§ Lillie (1952) defined flow point of glass as the temperature at which glass has a viscosity of 10^5 poise ($10^4 \text{ N}\cdot\text{s}/\text{m}^2$). Viscosity of melt in tank is in the range of 10^2 - 10^3 poises.

Gamm (1975) conjectured that melting from the bottom of the batch would be more than 50% of the total melting. It is in contrast with the earlier estimation of 10% (Kitaigorodski, 1959).

Heat Transfer Modeling at the Interfaces of Batch Blanket

The entire batch blanket may be considered to consist of the cold interior batch in solid state and the top and bottom fused layers covering the solid batch. See Figure A.2. Further, it is assumed that raw materials are introduced continuously with a constant thickness at the doghouse, and batch blanket moves with a constant velocity toward the far end (the bridge-wall). In particular, a steady state is assumed for the overall process of batch melting. Floating on the glass melt, the batch blanket receives energy required for its melting at both surfaces. Intensive radiation flux from the combustion gas flames is responsible for the formation of top fused layer and heat transfer from the glass melt in convective motion promotes formation of bottom fused layer. These fused layers are characterized by a high content of residual silica grains, compared to the glass melt in furnace tank, and fresh melts in both fused layers are too viscous to flow away freely from the solid batch. Due to the constant movement of the batch blanket, the thickness of the fused layers continues to grow until all the batch materials are completely melted down.

Whatever definition of interface is adopted to define surfaces between the interior solid batch and the fused layers, certain criticisms may be brought against it. But the least susceptible to criticisms appears to designate as interface condition the temperature of the ternary eutectic point (998 K). The percolation effect of fused melt is not considered in the modeling.

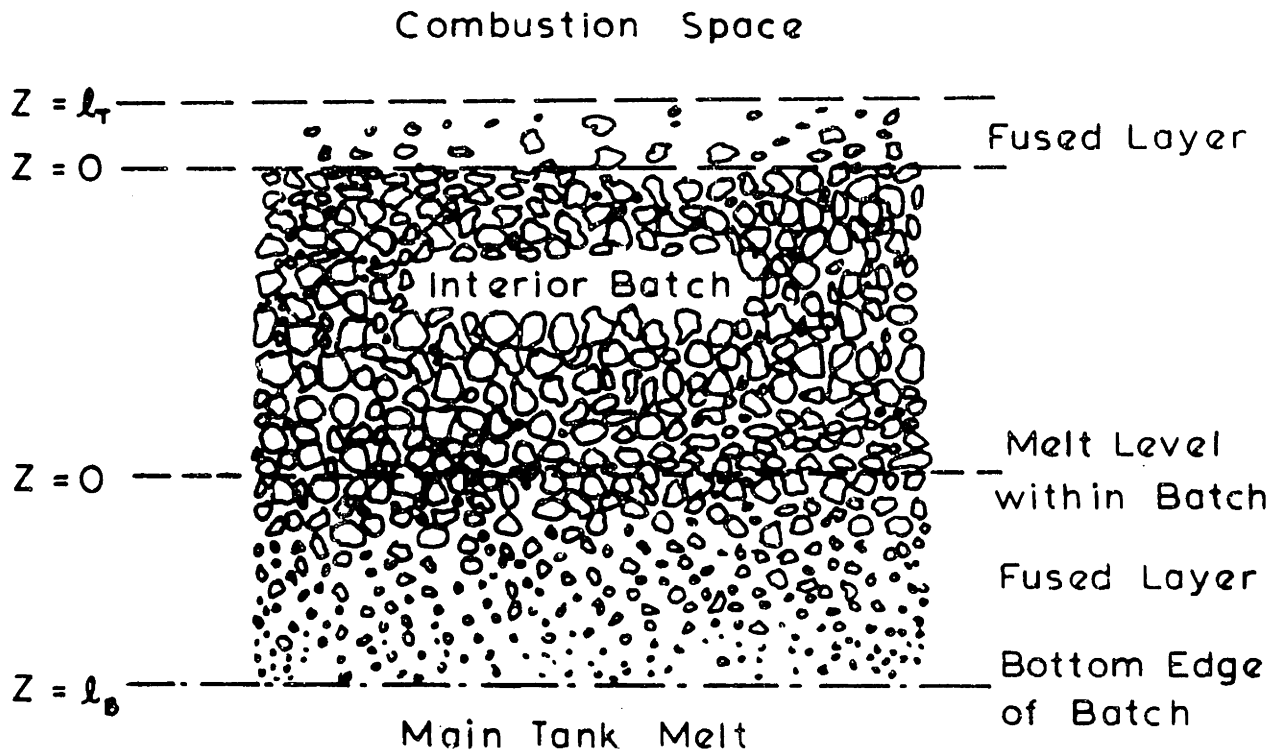


Figure A.2 Modeling of Batch Melting Process

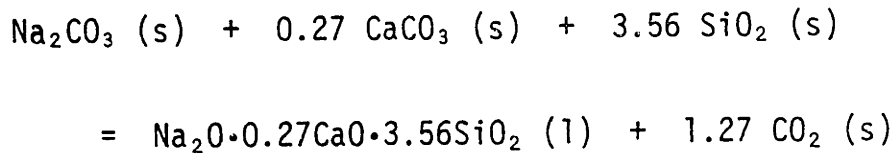
The Lower Fused Layer Model

Since the batch effective thermal conductivity is extremely low in a solid state, the heat flux density, q , is essentially zero at the lower interface of the interior batch layer, $z = 0$. At the bottom interface of the lower fused layer, $z = \ell_B$, fused melt is joining to the underlying natural convection currents. At this bottom interface, a constant temperature is assigned:

$$T = T_2 \quad \text{at } z = \ell_B \quad (\text{A.1})$$

which will be determined later according to the interaction with the heat transfer from the main tank melt.

Near the interface $z = 0$, the batch raw materials are rapidly heated to the eutectic temperature, T_e , from the batch feed temperature, T_0 , and the following reaction occurs:



with the heat of formation, $\Delta H_1 = 98.0 \text{ Kcal/gmole}$ ($4.10 \times 10^5 \text{ J/gmole}$).

As a result of the reaction, the fused melt passes through the interface at the rate of \dot{m} g glass/m \cdot s with gas bubbles and residual batch components being included. If all of the Na_2CO_3 grains are dissolved and reacted here, then, the heat flux density at the interface will be

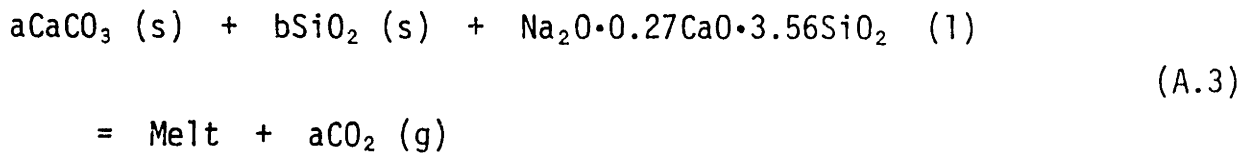
$$k \left. \frac{dT}{dz} \right|_{z=0} = \dot{m} * (C_p(T_e - T_0) + \Delta H_1) \quad (\text{A.2})$$

and

$$T = T_e = 998 \text{ K at } z = 0$$

where ΔH_1 is the heat of formation for the melting reaction based on the unit gram of glass being formed.

Between the interface $z = 0$ and the bottom edge of batch $z = \ell_B$, the remaining batch grains dissolve and react according to:



with the heat formation, $\Delta H_2 = (49.9a + 2.1b) \text{ Kcal/gmole}$ (for cullet, $12.2a + 2.1b$). The final melt will have a glass composition of $\text{Na}_2\text{O}\cdot (a+0.27)\text{CaO}\cdot (b+3.56)\text{SiO}_2$. The residual batch components are further dissolved within the layer. The dissolution rate of these residuals is strongly dependent on the surrounding temperature, or the position within the layer (z), and it must be determined from the consideration of mass transfer aspects of the residual dissolution. For simplicity, we assign a simple functional form, $f(z)$, which represents the fraction of the residual grains being dissolved in a unit depth at the position z . Then, the energy balance in the layer, $0 \leq z \leq \ell_B$, can be expressed as:

$$0 = \frac{d}{dz} \left(\kappa \frac{dT}{dz} \right) - \dot{m} \left(c_p \frac{dT}{dz} \right) + f(z) \cdot \Delta H_2 \quad (\text{A.4})$$

where ΔH_2 is based on the gram of glass being formed.

The equation (A.4) can be integrated with the boundary conditions (A.1) and (A.2) to obtain the heat flux density at the bottom edge of the

fused layer, q_2 , as function of any specific temperature, T_2 ,

$$q_2 = \kappa \frac{dT}{dz} \Big|_{z=l_B} = \dot{m} \left[c_p(T_2 - T_0) + \Delta H_1 + \Delta H_2 \right] \quad (A.5)$$

Since the form, $f(z)$, is unknown, a certain assumption is necessary to estimate and bracket the value of heat flux density, q_2 . For example, if all of the melting reactions are assumed to occur at the interface, $z=0$, then, the calculated q_2 will represent minimum heat flux requirements for the entire melting process. Conversely, a maximum value for q_2 will be realized if the residual dissolution reaction (A.3) occurs at the bottom edge only ($z=l_B$). Between these extreme cases, we may postulate a linear variation of $f(z)$ with respect to the position, z . Using Dirac delta function, these conditions are written:

$$f(z) = \left\{ \frac{\delta(0)}{l_B}, \frac{\delta(l_B)}{l_B}, \frac{2z}{l_B^2} \right\}. \quad (A.6)$$

Introducing the dimensionless variables:

$$Z = \frac{z}{l_B}, \quad \theta = \frac{T - T_0}{T_e - T_0}, \quad K = \frac{\kappa}{\kappa_e}, \quad \beta = \frac{\dot{m} c_p l_B}{\kappa_e} \quad (A.7)$$

$$\gamma_1 = \frac{\Delta H_1}{c_p(T_e - T_0)}, \quad \gamma_2 = \frac{\Delta H_2}{c_p(T_e - T_0)},$$

the normalized equation for the energy balance will be

$$\frac{d}{dZ} \left(K \frac{d\theta}{dZ} \right) - \beta \frac{d\theta}{dZ} = \beta \gamma_2 \cdot \{ \delta(0), \delta(1), 2Z \} \quad (A.8)$$

with the boundary conditions,

$$\begin{aligned} \theta &= 1 \quad \text{and} \quad \frac{d\theta}{dZ} = \beta(1 + \gamma_1) \quad \text{at } Z = 0 \\ \theta &= \theta_2 \quad \text{at } Z = 1 \end{aligned} \quad (\text{A.9})$$

Integration yields

$$\theta_2 = e^{\beta \int_0^1 \frac{dZ}{K}} \left\{ 1 + \int_0^1 \beta e^{-\beta \int_0^Z \frac{dZ}{K}} (\gamma_1 + \gamma_2 \begin{pmatrix} 1 \\ 0 \\ Z^2 \end{pmatrix}) dZ \right\} \quad (\text{A.10})$$

For a constant thermal conductivity, the solution is obtained:

$$\theta_2 = 1 + (1 + \gamma_1)(e^\beta - 1) + \frac{\gamma_2}{\beta^2} \begin{pmatrix} \beta^2(e^\beta - 1) \\ 0 \\ 2(e^\beta - 1 - \beta - \frac{\beta^2}{2}) \end{pmatrix} \quad (\text{A.11})$$

Notice that the thermal conductivity used in the above expressions should be a thermal conductivity excluding the contribution from the heat of reactions. Finally, the normalized heat flux density will be

$$q^* = \frac{q_2 l_B}{\kappa_e (T_e - T_0)} = \beta (\theta_2 + \gamma_1 + \gamma_2) \quad (\text{A.12})$$

To illustrate the result, the above equations are applied on the glass composition of 1:1:5 in mole and the batch is assumed to contains 25% cullets. The result is plotted in the temperature range of practical interest, $1200 \text{ K} \leq T_2 \leq 1630 \text{ K}$ ($1.3 \leq \theta_2 \leq 1.9$), which is shown in Figure A.3. Inspection shows that the heat flux is almost linear with respect to the temperature and the best fit equation for the linear dissolution case can

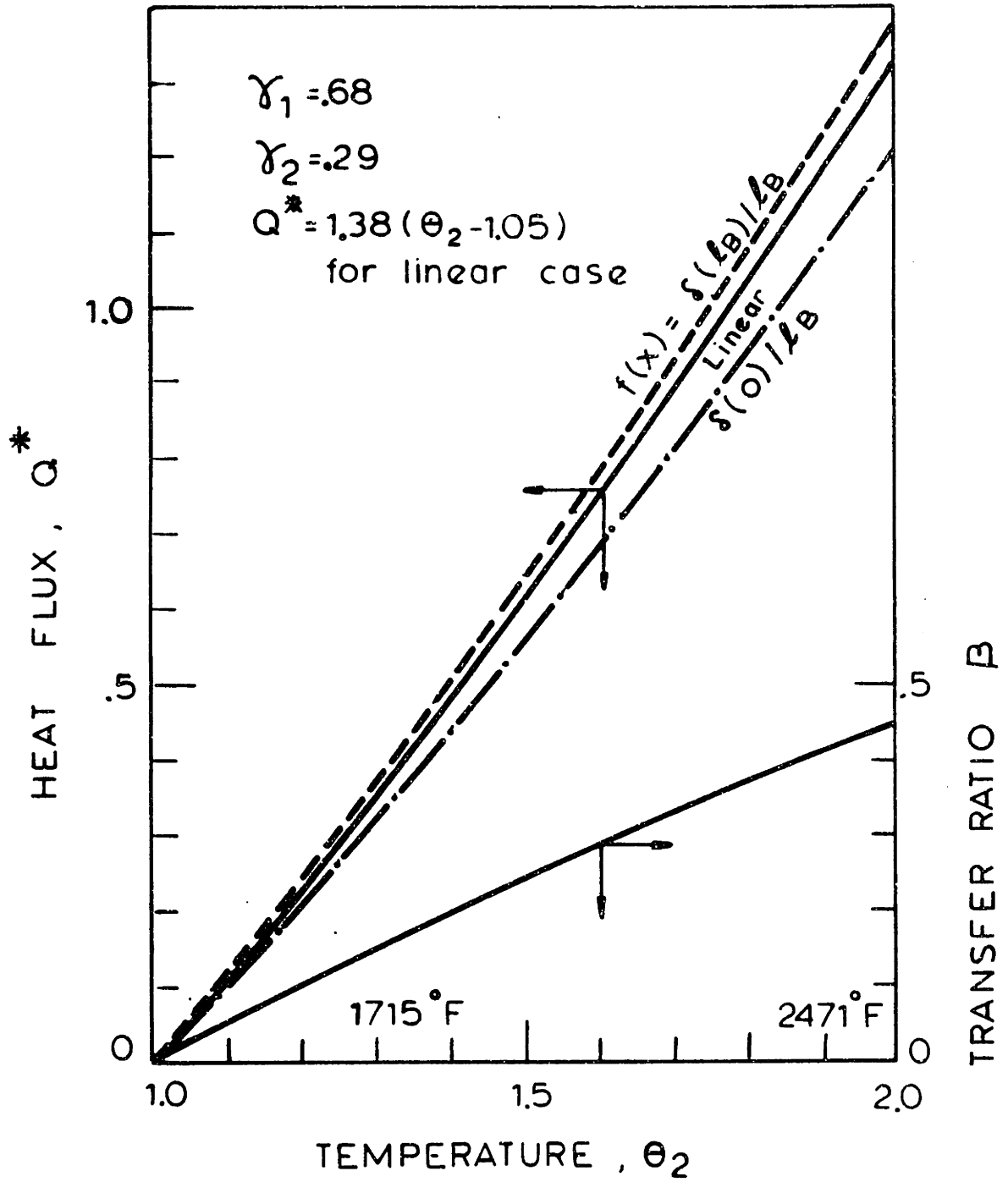


Figure A.3 Batch-Melt Heat Transfer

be written

$$q^* = 1.38 (\theta_2 - 1.05) \quad (A.13)$$

or

$$q_2 = 1.38 \frac{k}{\lambda_B} (T_2 - 1400), T_2 \text{ in } ^\circ\text{F}. \quad (A.14)$$

When the thermal conductivity is not constant, a good assumption is to take a log-mean value of the thermal conductivity values at both interfaces. As an illustration, the bottom temperature T_2 is taken (1589 K), at which glass melts are known to have sufficient fluidity ($\sim 10^3$ poise). Then thermal conductivity value is calculated 8.1 J/m·s·K (4.7 Btu/hr-ft-°F). For a fused layer of 0.102m (4") thick, calculated heat flux becomes 63,100 J/m²·s (20,000 Btu/hr-ft²). This is in the same order of magnitude as the value estimated from the melt side numerical model based on the same effective batch temperature.

The Upper Fused Layer Model

As already discussed, the upper fused layer is instantaneously formed, when receiving intensive radiation fluxes. This fused layer moves away from the doghouse as new batch materials are continuously discharged into the furnace. As time progresses ($t = y/v_{\text{Batch}}$), liquid film builds up on the top surface of the batch. When gas bubbles erupt through this layer, it may drain through the cold batch material and tends to resolidify as direct contact makes its temperature lower. Then, the liquid film will remain near the top surface and its thickness will increase gradually until it merges into the main body of glass melt, probably at the end zone of the batch blanket.

At time t , the top portion of the fused layer will consist of a slurry of unmelted silica in fresh, inhomogeneous melt. Energy added to the top surface ($z = \ell_T$) by flame radiation will be conducted through the film to the interface of solid batch. Reaction will proceed at this interface and more batch materials will be melted away. If we assume that all of the silica in this layer has been melted for heat transfer purposes, we have

$$\int_0^t q|_{x=\ell_T} dt = \rho(\ell_T(\Delta H_1 + \Delta H_2) + \int_0^{\ell_T} C_p(T - T_0) dz). \quad (A.15)$$

The temperature distribution may be nearly linear between T_1 and T_T (top surface temperature)

$$\int_0^{\ell_T} C_p(T - T_0) dz \cong \frac{C_p}{2} (T_T + T_1 - 2T_0)\ell_T. \quad (A.16)$$

At the top surface, the radiation heat fluxes will balance the conduction profile in the layer

$$q_z \cong \ell_T \cong \frac{k(T_T - T_1)}{\ell_T} = h(T_g - T_T). \quad (A.17)$$

Rearranging

$$\frac{T_T - T_1}{T_g - T_1} = \frac{N}{N+1} \quad \text{where } N = \frac{h\ell_T}{k} \quad (A.18)$$

Substituting into (A.18)

$$\int_0^t \frac{k}{\ell_T} \frac{N}{N+1} (T_g - T_1) dt = \rho\ell_T(\Delta H_1 + \Delta H_2 + C_p(T_1 - T_0) + \frac{C_p}{2} \frac{N}{N+1} (T_g - T_1)) \quad (A.19)$$

Define dimensionless variables as

$$\gamma_3 = 2 \left(\frac{T_1 - T_0}{T_g - T_1} \right) (1 + \gamma_1 + \gamma_2)$$

$$\tau = \frac{2h^2t}{\kappa\rho c_p} .$$

Equation (A.19) becomes

$$\int_0^\tau \frac{d\tau}{1 + N} = N \left(\gamma_3 + \frac{N}{1 + N} \right) . \quad (A.20)$$

Ideally, this equation should be solved with the radiation heat flux model in combustion space (such as suggested by Clomburg et al., 1974).

To illustrate the result, thickness of the fused layer will be estimated for a typical furnace condition. If γ_3 is assumed constant, equation (A.20) can be directly integrated

$$\tau = (1 + \gamma_3) \left(N + \frac{N^2}{2} \right) - \ln(1 + N) . \quad (A.21)$$

The heat flux density to the top surface is taken 63,000 J/m²·s (20,000 Btu/hr·ft²). Then, from the combustion calculation result (Clomburg et al., 1974), the effective heat transfer coefficient can be read 96 J/m²·s·K (17 Btu/m·ft²·R) for the surface temperature of 1700 K (2600 F) and the corresponding combustion gas temperature is found 1890 K (2940 F). Thus,

$$\gamma_3 = 2 \times \frac{700}{890} (1 + .68 + .29) = 3.10$$

$$\tau = \frac{(2)(17^2) \cdot t}{(4.7)(140)(0.39)} = 2.25 \cdot t \text{ (t in hours).}$$

For an hour of residence time in furnace, the equation (A.21) is solved to give

$$N = 0.517$$

The thickness of the top fused layer is 0.043m (1.7"). This estimation is an upper limit, because of the assumed linear temperature profile. (Since the effective thermal conductivity increases exponentially with temperature, a steep temperature gradient is expected only near the top surface of the layer.) These results indicate a relatively small contribution of the top layer to the overall melting rate.

APPENDIX B

THE TEMPERATURE DATA FOR TRANSVERSE PLANES

All the temperature data obtained from the thermocouple net were recorded in microvolt units by the data acquisition system. The voltage can be converted into temperature using the formula

$$T = aE + bE^2 + cE^3$$

where $a = 2.586017984 \times 10^{-2}$
 $b = -6.764148405 \times 10^{-7}$
 $c = 2.057786340 \times 10^{-11}$
T in °C
E in μ V.

This formula was obtained by the least square method for the temperature - emf data of copper-constantan thermocouples in the range of 20 °C to 60 °C. Conversion error is less than ± 0.013 °C.

Associated with the temperature data are the positions of sixty thermocouple beads in the net. These data were determined using photographs of the beads. Also a cathetometer was used to measure the vertical positions. Average values of these measurements are listed in Table B.1. The first coordinate denotes the horizontal position of the beads in cm unit and the second denotes the depth from the top surface. For convenience, the thermocouple columns are designated with numerals and the rows by alphabet. This designation is consistently used for the temperature data.

In Table B.2, all the temperature data of transverse planes are listed in μ V unit. The locations of the transverse planes are specified in the

second column in 100th inch units. For example, 550 in the first row indicates the $5\frac{1}{2}$ " transverse plane from the doghouse wall. Part of these data was presented in Chapter V as contour isotherm plots.

B.1 COORDINATES OF THE THERMOCOUPLE NET POSITIONS (UNIT IN CM)

	COL. 1	COL. 2	COL. 3	COL. 4	COL. 5	COL. 6	
A	(0.03,0.33)	(0.59,0.32)	(1.11,0.32)	(1.60,0.32)	(2.12,0.33)	(2.61,0.34)	A
B	(0.07,0.55)	(0.57,0.54)	(1.10,0.54)	(1.60,0.54)	(2.09,0.55)	(2.61,0.56)	B
C	(0.10,0.76)	(0.60,0.76)	(1.10,0.76)	(1.66,0.77)	(2.16,0.78)	(2.66,0.79)	C
D	(0.20,0.94)	(0.72,0.92)	(1.19,0.92)	(1.73,0.93)	(2.21,0.93)	(2.72,0.95)	D
E	(0.10,1.23)	(0.66,1.21)	(1.15,1.20)	(1.70,1.19)	(2.16,1.20)	(2.69,1.22)	E
F	(0.13,1.53)	(0.64,1.52)	(1.14,1.51)	(1.65,1.52)	(2.20,1.54)	(2.66,1.56)	F
G	(0.09,1.84)	(0.62,1.83)	(1.13,1.78)	(1.65,1.76)	(2.18,1.76)	(2.68,1.77)	G
H	(0.09,2.07)	(0.61,2.04)	(1.14,2.01)	(1.58,1.97)	(2.10,1.97)	(2.57,1.97)	H
I	(0.0,2.23)	(0.64,2.20)	(1.12,2.18)	(1.68,2.17)	(2.13,2.19)	(2.69,2.22)	I
J	(0.03,2.43)	(0.54,2.40)	(1.07,2.39)	(1.63,2.41)	(2.17,2.43)	(2.61,2.45)	G

B.2 THERMOCOUPLE EMF DATA

- 1) UNIT IN MICRO-VOLT
- 2) PL. DENOTES THE LOCATION OF TRANSVERSE PLANE IN 100TH INCH.

RUN	PL.	THERMOCOUPLE COLUMN NUMBER												
		1	2	3	4	5	6							
606	550	1133	1119	1118	1097	1088	1113	1119	1118	1097	1087	1118	A	
606	550	1176	1168	1174	1144	1140	1173	1172	1164	1173	1143	1139	1171	B
606	550	1246	1230	1220	1200	1199	1234	1253	1235	1224	1202	1201	1236	C
606	550	1284	1263	1259	1234	1227	1274	1275	1256	1253	1228	1225	1267	D
606	550	1308	1292	1281	1263	1259	1299	1313	1296	1284	1268	1260	1302	E
606	550	1314	1304	1293	1282	1287	1306	1315	1304	1295	1282	1286	1303	F
606	550	1284	1278	1279	1270	1276	1287	1283	1276	1279	1270	1274	1287	G
606	550	1251	1258	1265	1267	1267	1270	1251	1258	1265	1267	1268	1273	H
606	550	1229	1239	1250	1249	1250	1237	1229	1238	1250	1249	1246	1238	I
606	550	1204	1217	1228	1228	1221	1214	1202	1218	1228	1230	1221	1216	J
607	600	1146	1134	1142	1132	1132	1162	1145	1133	1142	1133	1131	1162	A
607	600	1202	1192	1209	1192	1199	1232	1201	1192	1208	1191	1198	1232	B
607	600	1275	1258	1258	1253	1263	1297	1275	1259	1259	1253	1263	1296	C

RUN	PL.	1	2	3	4	5	6	1	2	3	4	5	6
607	600	1312	1292	1299	1289	1294	1332	1311	1292	1298	1290	1294	1331
607	600	1345	1328	1326	1321	1324	1356	1345	1328	1326	1320	1324	1355
607	600	1337	1329	1327	1325	1335	1341	1336	1329	1327	1323	1335	1341
607	600	1298	1294	1304	1300	1308	1310	1298	1294	1303	1299	1307	1309
607	600	1257	1269	1280	1285	1285	1282	1258	1269	1280	1285	1285	1281
607	600	1233	1246	1260	1260	1257	1242	1232	1245	1260	1260	1256	1242
607	600	1206	1220	1233	1234	1227	1216	1207	1219	1232	1234	1227	1214
608	650	1176	1167	1183	1176	1184	1223	1178	1167	1183	1176	1183	1228
608	650	1244	1233	1259	1245	1261	1308	1244	1233	1259	1246	1260	1307
608	650	1323	1306	1312	1311	1327	1369	1324	1305	1312	1312	1328	1369
608	650	1362	1343	1351	1347	1357	1398	1361	1342	1352	1347	1356	1398
608	650	1385	1371	1371	1370	1378	1401	1385	1370	1371	1371	1378	1400
608	650	1358	1356	1358	1357	1366	1361	1358	1354	1359	1358	1365	1361
608	650	1303	1302	1317	1316	1320	1314	1304	1303	1317	1315	1319	1313
608	650	1257	1271	1284	1292	1288	1283	1257	1271	1285	1290	1287	1283
608	650	1233	1245	1262	1262	1255	1241	1234	1245	1263	1261	1255	1240
608	650	1209	1217	1232	1232	1222	1216	1209	1217	1233	1231	1225	1216
609	700	1269	1246	1259	1248	1255	1294	1269	1247	1261	1249	1256	1295
609	700	1346	1327	1351	1335	1353	1391	1345	1326	1351	1335	1355	1391
609	700	1422	1402	1405	1406	1423	1454	1422	1402	1406	1405	1423	1453
609	700	1446	1429	1432	1430	1440	1469	1446	1428	1433	1429	1439	1469
609	700	1428	1428	1430	1431	1444	1442	1425	1428	1430	1431	1444	1441
609	700	1366	1375	1385	1383	1392	1373	1366	1375	1384	1384	1392	1372
609	700	1298	1304	1325	1323	1330	1316	1298	1303	1323	1321	1329	1315
609	700	1252	1267	1285	1289	1290	1281	1251	1267	1284	1290	1290	1281
609	700	1227	1239	1258	1257	1255	1233	1226	1241	1259	1258	1256	1240
609	700	1203	1214	1228	1228	1224	1214	1203	1215	1229	1229	1223	1214
610	750	1425	1398	1409	1400	1416	1470	1425	1399	1409	1401	1414	1470
610	750	1507	1489	1510	1497	1516	1554	1507	1489	1511	1497	1517	1555
610	750	1553	1537	1534	1530	1539	1560	1551	1536	1535	1530	1539	1561
610	750	1531	1524	1513	1510	1512	1530	1531	1524	1513	1510	1514	1530
610	750	1448	1463	1464	1465	1469	1453	1447	1464	1463	1464	1472	1452
610	750	1366	1378	1389	1386	1384	1366	1365	1378	1388	1386	1385	1365
610	750	1298	1301	1320	1320	1318	1310	1298	1302	1321	1320	1320	1310
610	750	1252	1267	1279	1285	1280	1279	1254	1267	1280	1285	1279	1279

RUN	PL.	1	2	3	4	5	6	1	2	3	4	5	6	I	J	A	B	C	D	E	F	G	H	I	J	A	B	C	D	E	F	G	H	I	J	A	B	C				
610	750	1231	1241	1256	1256	1250	1239	1230	1241	1257	1256	1248	1239	1239	I	J	A	B	C	D	E	F	G	H	I	J	A	B	C	D	E	F	G	H	I	J	A	B	C			
610	750	1206	1216	1228	1227	1220	1214	1207	1216	1227	1226	1223	1213	1214	J	A	B	C	D	E	F	G	H	I	J	A	B	C	D	E	F	G	H	I	J	A	B	C				
611	800	1674	1664	1667	1655	1602	1698	1674	1664	1666	1655	1660	1698	1674	A	B	C	D	E	F	G	H	I	J	A	B	C	D	E	F	G	H	I	J	A	B	C					
611	800	1683	1681	1691	1685	1690	1706	1684	1681	1691	1685	1690	1706	1684	B	C	D	E	F	G	H	I	J	A	B	C	D	E	F	G	H	I	J	A	B	C	D	E	F	G		
611	800	1633	1635	1631	1621	1623	1632	1633	1634	1631	1621	1623	1632	1633	C	D	E	F	G	H	I	J	A	B	C	D	E	F	G	H	I	J	A	B	C	D	E	F	G			
611	800	1567	1574	1556	1557	1560	1570	1567	1575	1557	1558	1562	1572	1567	D	E	F	G	H	I	J	A	B	C	D	E	F	G	H	I	J	A	B	C	D	E	F	G				
611	800	1453	1475	1477	1481	1490	1468	1453	1475	1477	1482	1489	1469	1453	E	F	G	H	I	J	A	B	C	D	E	F	G	H	I	J	A	B	C	D	E	F	G					
611	800	1369	1382	1395	1393	1392	1375	1370	1383	1394	1393	1392	1377	1370	F	G	H	I	J	A	B	C	D	E	F	G	H	I	J	A	B	C	D	E	F	G	H	I	J			
611	800	1304	1307	1325	1326	1327	1321	1304	1307	1327	1327	1327	1322	1304	G	H	I	J	A	B	C	D	E	F	G	H	I	J	A	B	C	D	E	F	G	H	I	J				
611	800	1260	1273	1286	1293	1289	1288	1260	1271	1286	1292	1286	1290	1260	H	I	J	A	B	C	D	E	F	G	H	I	J	A	B	C	D	E	F	G	H	I	J	A	B	C		
611	800	1235	1246	1262	1263	1255	1250	1236	1246	1263	1263	1257	1249	1236	I	J	A	B	C	D	E	F	G	H	I	J	A	B	C	D	E	F	G	H	I	J	A	B	C			
611	800	1212	1222	1234	1234	1227	1225	1212	1224	1234	1234	1227	1225	1212	J	A	B	C	D	E	F	G	H	I	J	A	B	C	D	E	F	G	H	I	J	A	B	C				
613	550	1134	1115	1102	1083	1085	1116	1139	1117	1104	1085	1087	1116	1139	A	B	C	D	E	F	G	H	I	J	A	B	C	D	E	F	G	H	I	J	A	B	C	D	E	F	G	
613	550	1188	1169	1160	1132	1141	1177	1180	1164	1156	1129	1140	1174	1180	B	C	D	E	F	G	H	I	J	A	B	C	D	E	F	G	H	I	J	A	B	C	D	E	F	G		
613	550	1250	1225	1199	1184	1198	1236	1258	1230	1205	1187	1199	1240	1258	C	D	E	F	G	H	I	J	A	B	C	D	E	F	G	H	I	J	A	B	C	D	E	F	G			
613	550	1291	1256	1240	1225	1231	1276	1285	1252	1237	1222	1228	1271	1285	D	E	F	G	H	I	J	A	B	C	D	E	F	G	H	I	J	A	B	C	D	E	F	G				
613	550	1313	1287	1266	1251	1257	1301	1315	1287	1268	1253	1259	1302	1315	E	F	G	H	I	J	A	B	C	D	E	F	G	H	I	J	A	B	C	D	E	F	G	H	I	J		
613	550	1314	1296	1281	1271	1284	1304	1314	1298	1281	1272	1285	1305	1314	F	G	H	I	J	A	B	C	D	E	F	G	H	I	J	A	B	C	D	E	F	G	H	I	J			
613	550	1282	1272	1271	1264	1272	1285	1282	1272	1271	1263	1271	1288	1282	G	H	I	J	A	B	C	D	E	F	G	H	I	J	A	B	C	D	E	F	G	H	I	J	A	B	C	
613	550	1249	1255	1259	1260	1263	1272	1250	1255	1260	1261	1262	1271	1249	H	I	J	A	B	C	D	E	F	G	H	I	J	A	B	C	D	E	F	G	H	I	J	A	B	C		
613	550	1229	1239	1248	1247	1246	1240	1229	1238	1248	1246	1244	1239	1229	I	J	A	B	C	D	E	F	G	H	I	J	A	B	C	D	E	F	G	H	I	J	A	B	C			
613	550	1201	1216	1227	1226	1220	1214	1203	1217	1228	1228	1221	1215	1203	J	A	B	C	D	E	F	G	H	I	J	A	B	C	D	E	F	G	H	I	J	A	B	C				
616	400	1180	1163	1152	1098	1041	1097	1181	1162	1150	1095	1036	1078	1180	A	B	C	D	E	F	G	H	I	J	A	B	C	D	E	F	G	H	I	J	A	B	C	D	E	F	G	
616	400	1235	1218	1210	1131	1068	1105	1236	1218	1210	1130	1074	1121	1235	B	C	D	E	F	G	H	I	J	A	B	C	D	E	F	G	H	I	J	A	B	C	D	E	F	G		
616	400	1277	1262	1238	1168	1121	1180	1277	1263	1239	1172	1123	1182	1277	C	D	E	F	G	H	I	J	A	B	C	D	E	F	G	H	I	J	A	B	C	D	E	F	G			
616	400	1284	1269	1246	1170	1133	1188	1283	1268	1244	1164	1123	1170	1284	D	E	F	G	H	I	J	A	B	C	D	E	F	G	H	I	J	A	B	C	D	E	F	G	H	I	J	
616	400	1274	1265	1250	1188	1141	1194	1274	1270	1250	1191	1154	1213	1274	E	F	G	H	I	J	A	B	C	D	E	F	G	H	I	J	A	B	C	D	E	F	G	H	I	J		
616	400	1260	1257	1242	1194	1167	1209	1260	1256	1241	1190	1150	1191	1260	F	G	H	I	J	A	B	C	D	E	F	G	H	I	J	A	B	C	D	E	F	G	H	I	J			
616	400	1237	1233	1225	1188	1160	1190	1238	1232	1226	1189	1163	1191	1237	G	H	I	J	A	B	C	D	E	F	G	H	I	J	A	B	C	D	E	F	G	H	I	J	A	B	C	
616	400	1220	1220	1217	1201	1181	1198	1219	1220	1218	1202	1184	1205	1220	H	I	J	A	B	C	D	E	F	G	H	I	J	A	B	C	D	E	F	G	H	I	J	A	B	C		
616	400	1213	1215	1216	1193	1181	1201	1213	1215	1215	1189	1173	1195	1213	I	J	A	B	C	D	E	F	G	H	I	J	A	B	C	D	E	F	G	H	I	J	A	B	C			
616	400	1198	1204	1206	1188	1175	1184	1198	1202	1206	1190	1178	1185	1198	J	A	B	C	D	E	F	G	H	I	J	A	B	C	D	E	F	G	H	I	J	A	B	C	D	E	F	G
617	350	1153	1138	1135	1102	1048	1071	1150	1135	1132	1098	1043	1055	1153	A	B	C	D	E	F	G	H	I	J	A	B	C	D	E	F	G	H	I	J	A	B	C	D	E	F	G	
617	350	1202	1189	1192	1141	1063	1085	1204	1190	1194	1145	1087	1098	1202	B	C	D	E	F	G	H	I	J	A	B	C	D	E	F	G	H	I	J	A	B	C	D	E	F	G		
617	350	1248	1236	1225	1185	1129	1154	1247	1236	1225	1184	1125	1140	1248	C	D	E	F	G	H	I	J	A	B	C	D	E	F	G	H	I	J	A	B	C	D	E	F	G			

RUN	PL.	1	2	3	4	5	b	1	2	3	4	5	6
617	350	1256	1245	1237	1184	1131	1155	1255	1246	1237	1184	1132	1156
617	350	1251	1248	1243	1210	1161	1188	1252	1249	1243	1210	1161	1194
617	350	1240	1239	1235	1204	1162	1182	1239	1239	1234	1202	1157	1172
617	350	1224	1222	1222	1200	1176	1187	1224	1221	1222	1202	1183	1198
617	350	1211	1212	1215	1205	1186	1196	1210	1213	1214	1204	1180	1187
617	350	1206	1207	1212	1157	1181	1190	1206	1207	1211	1199	1186	1191
617	350	1194	1198	1205	1198	1189	1191	1194	1199	1205	1198	1188	1192
618	300	1134	1117	1114	1078	1036	1078	1135	1116	1114	1078	1036	1081
618	300	1182	1167	1170	1117	1075	1128	1183	1166	1170	1117	1074	1125
618	300	1227	1214	1201	1152	1112	1169	1227	1213	1201	1153	1116	1175
618	300	1237	1225	1215	1160	1142	1205	1238	1225	1215	1160	1140	1200
618	300	1235	1231	1222	1179	1143	1204	1234	1230	1223	1179	1144	1206
618	300	1226	1223	1217	1181	1161	1200	1226	1224	1217	1183	1160	1201
618	300	1210	1207	1206	1180	1167	1199	1210	1207	1206	1180	1165	1199
618	300	1199	1199	1200	1185	1167	1192	1198	1200	1201	1184	1169	1193
618	300	1196	1197	1199	1179	1171	1192	1196	1197	1199	1179	1172	1193
618	300	1187	1191	1194	1179	1170	1184	1187	1191	1194	1179	1171	1184
619	250	1107	1093	1093	1067	1026	1044	1108	1094	1094	1068	1026	1046
619	250	1155	1142	1149	1109	1067	1091	1155	1142	1149	1108	1065	1089
619	250	1202	1189	1180	1144	1095	1120	1202	1189	1180	1144	1097	1124
619	250	1215	1203	1198	1152	1115	1158	1216	1203	1197	1152	1115	1159
619	250	1218	1213	1207	1170	1123	1161	1217	1213	1206	1169	1123	1160
619	250	1212	1209	1203	1174	1141	1165	1212	1209	1203	1174	1142	1168
619	250	1201	1197	1195	1172	1149	1170	1200	1197	1195	1171	1148	1169
619	250	1191	1191	1191	1178	1156	1169	1191	1191	1190	1178	1157	1171
619	250	1190	1190	1191	1174	1160	1170	1189	1190	1190	1173	1158	1175
619	250	1182	1185	1188	1174	1160	1169	1181	1186	1187	1175	1161	1171
620	200	1057	1080	1075	1045	1023	1067	1098	1079	1074	1044	1023	1066
620	200	1142	1126	1125	1078	1056	1110	1143	1126	1125	1078	1057	1109
620	200	1188	1172	1155	1111	1092	1144	1188	1172	1155	1111	1093	1146
620	200	1202	1185	1171	1119	1114	1171	1201	1184	1170	1119	1115	1172
620	200	1206	1198	1183	1139	1122	1177	1205	1197	1183	1140	1123	1179
620	200	1201	1195	1183	1147	1135	1172	1201	1195	1183	1146	1135	1171
620	200	1191	1184	1178	1150	1143	1174	1190	1185	1177	1150	1144	1174
620	200	1184	1180	1175	1158	1147	1171	1183	1180	1175	1158	1146	1171

RUN	PL.	1	2	3	4	5	6	1	2	3	4	5	6
625	525	1255	1244	1231	1199	1194	1236	1255	1242	1231	1200	1197	1243
625	525	1297	1286	1269	1247	1241	1281	1310	1296	1279	1256	1248	1285
625	525	1304	1296	1281	1264	1264	1284	1295	1289	1273	1253	1251	1273
625	525	1274	1268	1265	1251	1254	1269	1275	1268	1265	1254	1257	1272
625	525	1248	1254	1258	1256	1257	1263	1246	1253	1257	1256	1256	1262
625	525	1226	1237	1244	1242	1241	1234	1230	1238	1247	1243	1242	1236
625	525	1205	1220	1230	1228	1224	1215	1206	1221	1229	1229	1223	1216
626	000	993	1157	1137	1113	1086	1062	993	1155	1137	1112	1086	1061
626	000	1273	1227	1128	1102	1076	1064	1272	1229	1128	1102	1075	1064
626	000	1071	1299	1135	1092	1075	1062	1071	1296	1135	1092	1075	1064
626	000	1497	1230	1133	1097	1075	1064	1497	1283	1132	1098	1074	1062
626	000	2129	1284	1140	1093	1071	1061	2129	1281	1140	1093	1071	1061
626	000	1824	1236	1122	1092	1069	1055	1824	1237	1122	1092	1069	1056
626	000	1926	1304	1128	1092	1067	1050	1926	1307	1126	1091	1066	1051
626	000	1783	1293	1123	1089	1062	1044	1783	1291	1123	1090	1062	1046
626	000	2078	1298	1120	1090	1055	1036	2079	1296	1121	1090	1056	1038
626	000	2083	1294	1117	1088	1062	1018	2083	1250	1117	1087	1062	1018
627	000	993	1155	1137	1109	1081	1052	992	1155	1137	1109	1081	1052
627	000	1274	1232	1126	1099	1068	1058	1274	1226	1126	1098	1070	1055
627	000	1067	1299	1132	1087	1069	1058	1067	1295	1133	1088	1069	1055
627	000	1496	1232	1130	1093	1069	1057	1496	1236	1130	1092	1068	1059
627	000	2127	1285	1137	1088	1065	1057	2128	1281	1138	1089	1066	1055
627	000	1332	1237	1120	1087	1065	1052	1333	1232	1120	1087	1064	1049
627	000	1926	1305	1125	1086	1061	1048	1929	1303	1125	1036	1060	1049
627	000	1783	1291	1121	1084	1056	1043	1783	1292	1121	1085	1056	1043
627	000	2079	1293	1118	1085	1051	1032	2079	1295	1119	1085	1051	1036
627	000	2082	1249	1115	1092	1056	1020	2081	1244	1114	1082	1058	1016

NOTE: RUN 626 & 627 FOR THE LONGITUDINAL CENTER PLANE

APPENDIX C

ESTIMATION OF TEMPERATURE INCREASE IN THERMOCOUPLE LINES
DUE TO FLUID MOTION

When the thermocouples are immersed in a fluid in motion, the fluid brought to rest at the surface of the thermocouples is heated by internal friction. It makes thermocouple readings somewhat higher than the fluid temperature, even though the fluid itself is in a thermal equilibrium. A rough estimation of this temperature increase is made to indicate the reliability of the collected thermocouple data for transverse planes.

The solution of the general problem is given by solving the energy equation with internal friction term (ϕ_v) and the flow equation for a steady state incompressible flow

$$\bar{V} \cdot \nabla T = \alpha \nabla^2 T + \frac{\nu}{C_p} \phi_v$$

$$\bar{V} \cdot \nabla \bar{V} = -\nabla \frac{P}{\rho} + \nu \nabla^2 \bar{V}$$

$$\nabla \cdot \bar{V} = 0 \tag{C.1}$$

with appropriate boundary conditions. Ideally, this may be supplemented by the equation of thermal conduction in the thermocouple body. Complexities associated with roll cell motion make the problem intractable. Therefore, some simplifications are required.

In the experiment, Reynolds number is very small, an order of 10^{-5} . Peclet number is also small, even though Prandtl number is large, as shown in Table C.1.

TABLE C. 1Representative Physical Properties and Experimental ConditionsProperty of Glycerine at 303.16 K

Heat Capacity, c_p	0.584 Btu/lb·°F	2445.1 J/Kg·K
Thermal Diffusivity, α	3.6×10^{-3} ft ² /hr	9.29×10^{-8} m ² /s
Kinematic Viscosity, ν	~ 20 ft ² /hr	$\sim 5.16 \times 10^{-4}$ m ² /s
Thermal Conductivity, κ	0.165 Btu/hr·ft·°F	0.286 J/m·s·K
κ_{copper}	223.0 Btu/hr·ft·°F	386.0 J/m·s·K
$\kappa_{\text{constantan}}$	13.1 Btu/hr·ft·°F	22.7 J/m·s·K

Experimental Conditions

Maximum Velocity, U	~ 3 ft/hr	$\sim 2.54 \times 10^{-4}$ m/s
Wire Radius, a	0.0025 inch	0.635×10^{-4} m

Dimensionless Parameters

Prandtl Number, $P \equiv \nu/\alpha$	~ 5600
Reynolds Number, $Re \equiv U \cdot a/\nu$	$\sim 3.1 \times 10^{-5}$
Peclet Number, $Pe \equiv P \cdot Re$	~ 0.17

In this case, the convective terms $\bar{V} \cdot \nabla T$ and $\bar{V} \cdot \nabla \bar{V}$ are small compared with $|\alpha \nabla^2 T|$ and $|\nu \nabla^2 T|$, respectively, so that the equations become

$$\begin{aligned} \nabla^2 T &= -\frac{P}{C_p} \phi_V \\ \nabla \frac{\Pi}{\rho} &= \nu \nabla^2 \bar{V} \\ \nabla \cdot \bar{V} &= 0. \end{aligned} \tag{C.2}$$

For simplicity, cylindrical planar motion of uniform velocity is assumed for a flow field far away from the thermocouples. Then, we can take the well-known Oseen approximation form as our flow field (Batchelor, 1967)

$$\begin{aligned} \psi &= KUr \sin \theta \left(\ln \frac{r}{a} - \frac{1}{2} + \frac{1}{2} \frac{a^2}{r^2} \right) \\ K &= \left(\frac{1}{2} - \gamma + \ln \frac{4}{Re} \right)^{-1} \quad \gamma = 0.57721 = \text{Euler's constant} \end{aligned} \tag{C.3}$$

We note that, with this value of K, Oseen's solution is valid when $KRe \frac{r}{a} \ln \frac{r}{a} \ll 1$ (Van Dyke, 1964).

The equation satisfied by the temperature becomes

$$\left(\frac{1}{r} \frac{\partial}{\partial r} r \frac{\partial}{\partial r} + \frac{1}{r^2} \frac{\partial^2}{\partial \theta^2} \right) T = -A \frac{4}{r^2} \left\{ \frac{a^4}{r^4} + \cos^2 \theta \left(1 - 2 \frac{a^2}{r^2} \right) \right\} \tag{C.4}$$

$$\text{with} \quad A = P \left(\frac{U^2}{C_p} \right) K^2$$

with the boundary conditions

$$(i) \quad T = \text{constant} \quad \text{at} \quad r = a$$

$$(ii) \quad kf \frac{\partial T}{\partial r} r d\theta = 0 \quad \text{at } r = a \quad (C.5)$$

$$(iii) \quad T \rightarrow T_0 \quad \text{as } r \rightarrow \infty \quad \text{when } KRe \frac{r}{a} \ln \frac{r}{a} \gg 1.$$

The first boundary condition represents the high thermal conductivity of the thermocouples (see table); the second indicates the condition of thermal equilibrium of the thermocouple. Although the heat flux will not in general vanish over the entire surface, the total heat flux through the surface should be zero to maintain a steady state within the thermocouple. The third condition merely indicates an unperturbed uniform temperature of fluid far away from the thermocouple. Because of the singular nature of Oseen's solution at infinity, the temperature distribution obtained by solving equation (C.4) may not satisfy this boundary condition at all. The solution is assumed to be valid when $KRe \frac{r}{a} \ln \frac{r}{a} \ll 1$ for any fixed r .

The equation with these boundary conditions clearly has a particular solution in the form (Landau and Lifshitz, 1959)

$$T(r, \theta) = f(r) \cos^2 \theta + g(r). \quad (C.6)$$

Substituting for T in (C.5) and separating the part which depends on θ , the equations for $f(r)$ and $g(r)$ satisfy

$$r^2 f'' + r f' - 4f = -4A \left(1 - 2 \frac{a^2}{r^2}\right)$$

$$r^2 g'' + r g' = -4A \frac{a^4}{r^4} - 2f \quad (C.7)$$

Also, the first two boundary conditions reduce to $f(a) = 0$ and $\frac{1}{2}f'(a) + g'(a) = 0$, respectively. The temperature distribution is then

$$T(r, \theta) = A \left\{ \left(1 - \frac{a^2}{r^2} + 2 \frac{a^2}{r^2} \ln \frac{a}{r} \right) \cos^2 \theta + \frac{a^2}{r^2} \left(\frac{3}{2} - \ln \frac{a}{r} \right) - \frac{1}{4} \frac{a^4}{r^4} - \ln \frac{a}{r} - \left(\ln \frac{a}{r} \right)^2 \right\} + C_0 \quad (C.8)$$

where the term r^2 arising in $f(r)$ is omitted, since it does not vanish at infinity. When the third boundary condition is directly applied to (C.8), C_0 cannot be determined due to the divergent behavior of the bracket term

$$\begin{aligned} & \text{const} * K^2 [\cos^2 \theta - \ln \frac{a}{r} - (\ln \frac{a}{r})^2] \quad (C.9) \\ & \cong \text{const} * \left[\frac{K \text{Re} \frac{r}{a} \ln \frac{a}{r}}{\text{Re} \frac{r}{a}} \right]^2 \end{aligned}$$

Since the Oseen approximation is only valid when $K \text{Re} \frac{r}{a} \ln \frac{a}{r}$ is less than the order of unity for fixed $\text{Re} \frac{r}{a}$ (i.e. lengths are scaled to viscous dimension $\frac{\nu}{U}$), this term should vanish or does not contribute any when fluid is far away. With this understanding, we choose

$$C_0 = T_\infty$$

Now the desired temperature difference between the thermocouple and the surrounding fluid becomes

$$\begin{aligned} T_s - T_\infty &= \frac{5}{4} \left(\ln \frac{3.703}{\text{Re}} \right)^{-2} \frac{U^2}{C_p} \quad (C.10) \\ &= \frac{5}{4} \left(\ln \frac{3.703}{3.1 \times 10^{-5}} \right)^{-2} * \frac{3^2 (5.6 * 10^3)}{(0.584)(2.504 \times 10^4)(3600)} \\ &= 1.4 * 10^{-5} \text{ } ^\circ\text{F.} \end{aligned}$$

The thermocouples are not heated due to the internal friction of fluid.

APPENDIX D

ANALYTIC GALERKIN SOLUTION OF LINEAR STABILITY EQUATION
FOR A CONSTANT VISCOSITY CASE

In this case, the linear stability equation is simplified

$$\begin{bmatrix} D^2 - a^2 & -a \\ -aR & -(D^2 - a^2)^2 \end{bmatrix} \begin{bmatrix} \theta \\ \phi \end{bmatrix} = \begin{bmatrix} 0 \\ 0 \end{bmatrix} \quad (D.1)$$

with the boundary conditions:

$$\theta(0) = \theta(1) = \phi(0) = \phi(1) = \phi''(0) = \phi'(1) = 0. \quad (D.2)$$

(Note that the boundary conditions at 0 and 1 have been inverted to simplify the analytic form of the solution.) The exact solution, obtained by Reid and Harris (1958), will be compared to a solution obtained by the Galerkin procedure.

The first variational principle of equation (7.8) is employed using the Galerkin procedure with trial functions,

$$Q = \sum_{k=1}^{\infty} A_k \sin k\pi x \quad (D.3)$$

which satisfy the first two boundary conditions of equation (D.2). Then, the analytic solution for ϕ function is

$$\phi = \sum_{k=1}^{\infty} \frac{A_k}{(k^2\pi^2+a^2)} \left[(-1)^{k+1} \frac{k\pi a \sinh a}{(\frac{1}{2} \sinh 2a - a)} \sinh ax - \sin k\pi x \right]. \quad (D.4)$$

A minimum R with respect to the expansion coefficients $A_j (j = 1, \infty)$ can be found, at a fixed wave number a , as the largest eigenvalue ($\lambda = \frac{1}{R}$) of the matrix equation

$$\lambda \bar{A} = \bar{E}^{-1} \bar{G} \bar{A}$$

where

$$\bar{E} = [E_{kj}] = [\delta_{kj} \{ (\frac{j\pi}{a})^2 + 1 \}]$$

$$\bar{G} = [G_{kj}] = \frac{1}{a^2 E_{kk}^2} \left[\delta_{kj} - (-1)^{k+j} \frac{kj}{E_{jj}^2} \frac{4\pi^2 \sinh^2 a}{(\frac{1}{2} \sinh 2a - a)a^3} \right]$$

The critical pair, R_c and a_c , is determined from minimum of R with respect to wave number a . Then, the expansion coefficients are calculated as a ratio

$$\frac{A_k}{A_1} = k (-1)^{k+1} \frac{E_{11}^3 - \frac{R_c}{a_c^4}}{E_{kk}^3 - \frac{R_c}{a_c^4}} \quad (k = 2, \infty)$$

In practice, only the first N terms in series (D.3) are retained. Numerical results obtained in this way are given in Table D.1. This result should be compared with the exact solution $R_c = 1100.65$ at $a_c = 2.682_5$ by Reid and Harris. The comparison shows that a four term expansion is adequate.

TABLE D.1

The Critical Rayleigh Number Derived by the Variational Method

N	a_c	R_c	A_k ($k = 2, N$, with $A_1 = 1$)
1	2.6824	1112.703	
2	2.6819	1101.359	-6.5729710(-2)
3	2.6823	1100.740	-6.2943164(-2), -1.0088438(-2)
4	2.6823	1100.668	-6.2931685(-2), -1.0086648(-2), -2.6262841(-3)

APPENDIX E

THE FINITE DIFFERENCE FORMULATION OF CONVECTION EQUATIONS

Numerical calculations required for the two-dimensional convection problems in this thesis have been performed by using the finite difference algorithm which was originally developed and written by Clomburg (1971). In his computer program, terms associated with viscosity variation was not rigorously treated, because its effect is usually negligible when the temperature variation is small compared to the absolute average temperature. However, the large viscosity variation problem (Chapter VII) necessitates an exact treatment of these terms. In addition, a refinement has been introduced to handle the energy equation more accurately. Since Clomburg's basic algorithm has been employed in its original form, only the finite difference representation will be presented and the way to incorporate the changes into the program will be briefly explained.

In Chapter VII, a conservative formulation for convection equations was written in the form:

$$\begin{aligned} & \frac{1}{s} \oint_{\bar{\ell}} \nabla \Theta \cdot d\bar{\ell} - \frac{1}{s} \oint_{\bar{\ell}} \bar{V} \Theta \cdot d\bar{\ell} - \frac{1}{s} \oint_{\bar{\ell}} \bar{V} (1 + x) \cdot d\bar{\ell} = 0 \\ & p^{-1} \frac{1}{s} \oint_{\bar{\ell}} \bar{V} (-\nabla^2 \Psi) \cdot d\bar{\ell} - R \frac{1}{s} \iint_s (\partial_y T) ds \\ & + \frac{1}{s} \oint_{\bar{\ell}} \left[\hat{i} \left\{ \nu \partial_x (\nabla^2 \Psi) + \frac{2(\partial_y \nu)(\partial_{xy}^2 \Psi) + (\partial_x \nu)(\partial_x^2 \Psi - \partial_y^2 \Psi)}{\text{-----}} \right\} \right. \\ & \quad \left. + \hat{j} \left\{ \nu \partial_y (\nabla^2 \Psi) + \frac{2(\partial_x \nu)(\partial_{xy}^2 \Psi) - (\partial_y \nu)(\partial_x^2 \Psi - \partial_y^2 \Psi)}{\text{-----}} \right\} \right] \cdot d\bar{\ell} = 0. \end{aligned}$$

Note that perturbation temperature is used in energy equation, but T will be employed for finite difference representation. The terms underlined in the second equation were neglected in the original program by Clomburg. When applied to a chosen grid (i,j) in the nonuniform, staggered grid system (Figure D.1), these equations can be converted into the finite difference form. It is understood that each of the grid sizes (δ_i 's and δ_j 's) can be assigned independently ($\delta_i \neq \delta_j$ even if $i=j$. δ_i stands for ΔX_i). In Figure D.1, index ranges for various variables are indicated as a reminder of the M x N grid system used by Clomburg.

It is convenient to define the following abbreviation:

$$\frac{1}{\delta P_i} = \frac{1}{2}(\delta_i + \delta_{i-1}) \quad ; \quad \frac{1}{\delta P_j} = \frac{1}{2}(\delta_j + \delta_{j-1})$$

$$D_i = (8/\delta_{i-1} - \delta P_i - \delta P_{i-1}) \quad ; \quad D_j = (8/\delta_{j-1} - \delta P_j - \delta P_{j-1})$$

$$\Delta_x T_{i,j} = T_{i+1,j} - T_{i,j} \quad ; \quad \Delta_y T_{i,j} = T_{i,j+1} - T_{i,j}$$

$$U^N = \frac{1}{2}(|U_{i-1,j-1}| + U_{i-1,j-1}) \quad ; \quad U^S = \frac{1}{2}(|U_{i,j-1}| - U_{i,j-1})$$

$$V^W = \frac{1}{2}(|V_{i-1,j-1}| + V_{i-1,j-1}) \quad ; \quad V^E = \frac{1}{2}(|V_{i-1,j}| - V_{i,j-1})$$

where U and V are the vector components of velocity \bar{V} and the superscripts denote four boundaries for each grid zone.

Parameters	Index	Range
	i	j
δ	M	N
δ_P	$M+1$	$N+1$
θ, T, ψ	$M+2$	$N+2$
U, γ^S	$M+1$	N
V, γ^E	M	$N+1$

* all indices start from 1

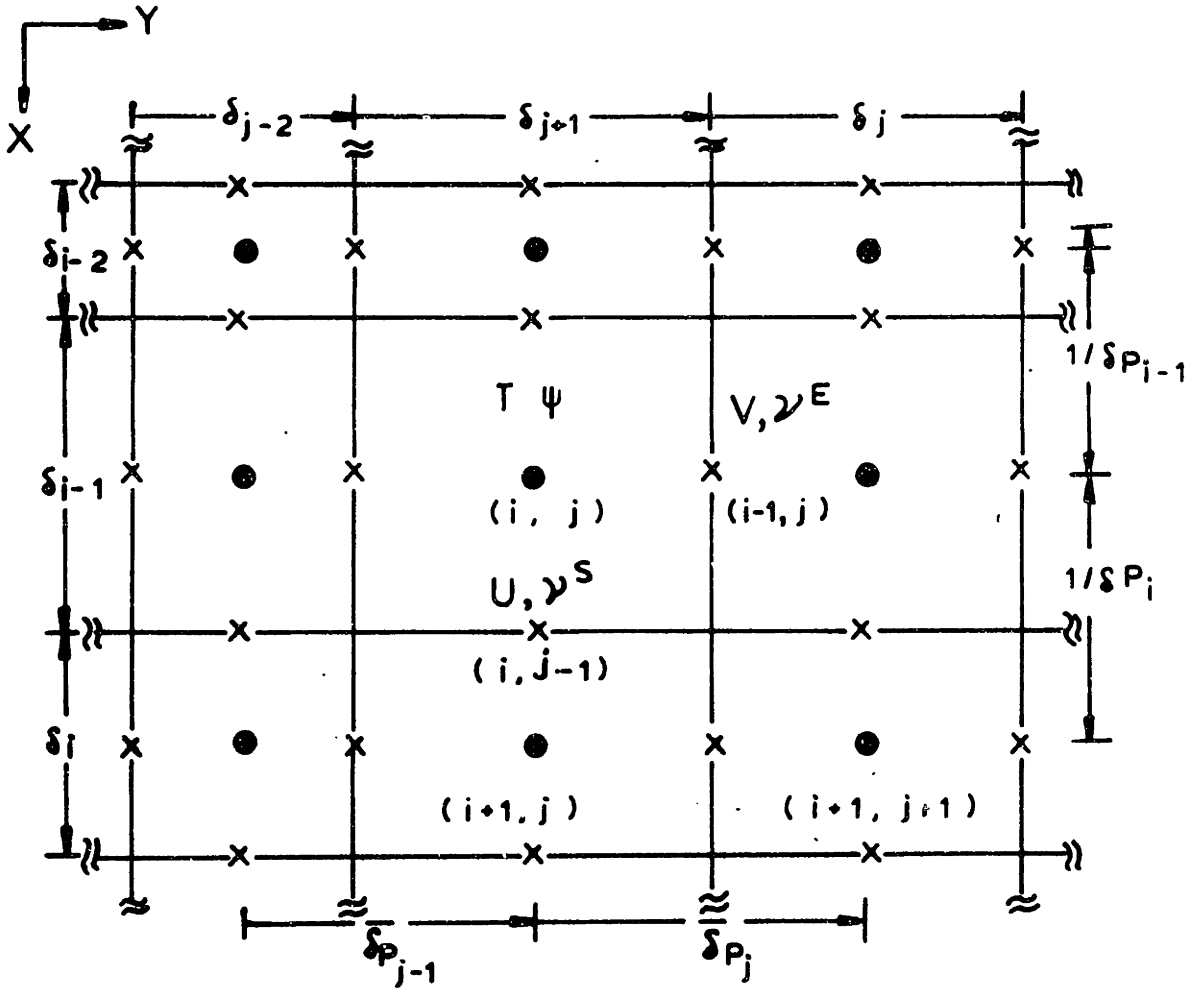


Figure E.1 Non - Uniform , Staggered Grid System

Energy Equation

Clomburg solved the following finite difference form of the energy equation:

$$\begin{aligned}
 & (\Delta_x T_{i,j} \cdot \delta P_i - \Delta_x T_{i-1,j} \delta P_{i-1}) / \delta_{i-1} + (\Delta_y T_{i,j} \cdot \delta P_j - \Delta_y T_{i,j-1} \cdot \delta P_{j-1}) / \delta_{j-1} \\
 & + (U^S \cdot \Delta_x T_{i,j} - U^N \Delta_x T_{i-1,j}) / \delta_{i-1} + (V^E \cdot \Delta_y T_{i,j} - V^W \cdot \Delta_y T_{i,j-1}) / \delta_{j-1} \\
 & + (U^S \cdot \delta P_i - U^N \cdot \delta P_{i-1}) / \delta_{i-1} = 0
 \end{aligned}$$

Notice that the contribution of convective term is accounted for, only if the fluid flows into the grid zone. This treatment is referred to as the "upwind differencing" scheme in the literature. Physically, it assumes that fluid in the grid zone is well mixed with the temperature, $T_{i,j}$. On the other hand, the conductive contributions are evaluated based on the temperatures defined at the node points of grid zones. The essence of the scheme is to conserve energy transfer in each grid zone. Under the alternate direction implicit method, a tridiagonal matrix is being solved.

A different conservative formulation is possible, if temperature can be defined at the same point where the velocity is defined. For the purpose, temperature is assumed to have bilinear variations in a rectangle made of four node points surrounding any corner of the grid zone. A simple linear interpolated temperature can be defined at the mid-points of grid boundaries

$$T_{i,j}^S = \frac{1}{2} \delta P_i (T_{i+1,j} \delta_{i-1} + T_{i,j} \delta_i)$$

$$T_{i,j}^E = \frac{1}{2} \delta P_j (T_{i,j+1} \delta_{j-1} + T_{i,j} \delta_j)$$

Temperatures at the boundary mid-points, however, should be defined using the above interpolated temperature. Then, the energy equation is represented in the form

$$\begin{aligned}
 & \frac{1}{8} \frac{\delta_{j-1}}{\delta_{i-1}} \left(\delta P_i * (\Delta_x T_{i,j+1} \delta P_j + \Delta_x T_{i,j} * D_j + \Delta_x T_{i,j-1} \delta P_{j-1}) \right. \\
 & \quad \left. - \delta P_{i-1} * (\Delta_x T_{i-1,j+1} \delta P_j + \Delta_x T_{i-1,j} * D_j + \Delta_x T_{i-1,j-1} \delta P_{j-1}) \right) \\
 & + \frac{1}{8} \frac{\delta_{i-1}}{\delta_{j-1}} \left(\delta P_j * (\Delta_y T_{i+1,j} \delta P_i + \Delta_y T_{i,j} * D_i + \Delta_y T_{i-1,j} \delta P_{i-1}) \right. \\
 & \quad \left. - \delta P_{j-1} * (\Delta_y T_{i+1,j-1} \delta P_i + \Delta_y T_{i,j-1} * D_i + \Delta_y T_{i-1,j-1} \delta P_{i-1}) \right) \\
 & - \frac{1}{8} \frac{\delta_{j-1}}{\delta_{i-1}} \left(U_{i,j-1} (T_{i,j+1}^S \delta P_j + T_{i,j}^S D_j + T_{i,j-1}^S \delta P_{j-1}) \right. \\
 & \quad \left. - U_{i-1,j-1} (T_{i-1,j+1}^S \delta P_j + T_{i-1,j}^S D_j + T_{i-1,j-1}^S \delta P_{j-1}) \right) \\
 & - \frac{1}{8} \frac{\delta_{i-1}}{\delta_{j-1}} \left(V_{i-1,j} (T_{i+1,j}^E \delta P_i + T_{i,j}^E D_i + T_{i-1,j}^E \delta P_{i-1}) \right. \\
 & \quad \left. - V_{i-1,j-1} (T_{i+1,j-1}^E \delta P_i + T_{i,j-1}^E D_i + T_{i-1,j-1}^E \delta P_{i-1}) \right) \\
 & - \frac{1}{2} (U_{i,j-1} + U_{i-1,j-1}) = 0 .
 \end{aligned}$$

Unfortunately, the resulting matrix from this difference form cannot be reduced to the tridiagonal system under the ADI scheme. Moreover, diagonal dominance is no longer guaranteed, which is necessary for the stable solution. For this reason, the tridiagonal system resulting from

the equation (2) has been solved, under the ADI scheme, but the difference between equations (2) and (3) has been introduced as an explicit correction. (Mechanically, this difference can be included in the term $S_{i,j}$, defined as source term in Clomburg's thesis.)

Biharmonic Equation

To be consistent with the bilinear assumption in temperature, the generation term in vorticity was casted in the form

$$\frac{R}{s} \iint_S \partial_y T ds = R \frac{\delta_{i-1}}{4} \left(\delta P_{j-1} * (\Delta_y T_{i+1,j-1} \delta P_i + \Delta_y T_{i,j-1} \cdot D_i + \Delta_y T_{i-1,j-1} \cdot \delta P_{i-1}) \right. \\ \left. + \delta P_j * (\Delta_y T_{i+1,j} \delta P_i + \Delta_y T_{i,j} \cdot D_i + \Delta_y T_{i-1,j} \cdot \delta P_{i-1}) \right).$$

It is derived by dividing the grid zone into the four quadrants, in which the values of $\partial_y T$ are assumed constant and evaluated at the four one-quarter points of the vertical boundary. The above equation results in taking an average of the four gradients.

The temperature dependency of the viscosity can be factored out

$$\partial_T \nu = - \frac{\nu}{T} \nu.$$

It may be a good approximation to consider this term to be independent of spatial variation along the identical boundaries of the grid zone. Then, the extra terms can be written

$$\frac{1}{s} \oint_{\bar{\ell}} \left((\partial_T \nu)_x \{ (\partial_x T) \cdot (\partial_x^2 \Psi - \partial_y^2 \Psi) + 2(\partial_y T) \cdot (\partial_{xy}^2 \Psi) \} \hat{i} \right. \\ \left. + (\partial_T \nu)_y \{ -(\partial_y T) (\partial_x^2 \Psi - \partial_y^2 \Psi) + 2(\partial_x T) \cdot (\partial_{xy}^2 \Psi) \} \hat{j} \right) \cdot d\bar{\ell}.$$

The corresponding difference form follows easily.

$$\frac{\gamma}{2\delta_{i-1}} * v_{i,j-1}^S \frac{\delta P_i}{(T_{i+1,j} \cdot T_{i,j})} \cdot \{ \Delta_x T_{i,j} \cdot \delta P_i * ((\psi_{xx} - \psi_{yy})_{i+1,j} \delta_{i-1} + (\psi_{xx} - \psi_{yy})_{i,j} \delta_i) \\ + \delta P_{j-1} (\Delta_y T_{i+1,j-1} \cdot \delta_{i-1} + \Delta_y T_{i,j-1} \cdot \delta_i) (\psi_{xy})_{i,j-1} \\ + \delta P_j (\Delta_y T_{i+1,j} \cdot \delta_{i-1} + \Delta_y T_{i,j} \cdot \delta_i) (\psi_{xy})_{i,j} \}$$

- terms obtained by changing index i into i-1

$$+ \frac{\gamma}{2\delta_{i-1}} * \frac{v_{i-1,j}^E \cdot \delta P_j}{T_{i,j+1} \cdot T_{i,j}} * \{ - \Delta_y T_{i,j} \cdot \delta P_j * ((\psi_{xx} - \psi_{yy})_{i,j+1} \cdot \delta_{j-1} + (\psi_{xx} - \psi_{yy})_{i,j} \delta_j) \\ + \delta P_{i-1} * (\Delta_y T_{i-1,j+1} \cdot \delta_{j-1} + \Delta_x T_{i-1,j} \cdot \delta_j) * (\psi_{xy})_{i-1,j} \\ + \delta P_i * (\Delta_x T_{i,j+1} \delta_{j-1} + \Delta_x T_{i,j} \delta_j) * (\psi_{xy})_{i,j} \}$$

- terms obtained by changing index j into j-1

where

$$(\partial_x^2 \psi - \partial_y^2 \psi)_{i,j} = \{ \delta P_i * (\psi_{i+1,j} - \psi_{i,j}) - \delta P_{i-1} * (\psi_{i,j} - \psi_{i-1,j}) \} / \delta_{i-1} \\ - \{ \delta P_j * (\psi_{i,j+1} - \psi_{i,j}) - \delta P_{j-1} * (\psi_{i,j} - \psi_{i,j-1}) \} / \delta_{j-1}$$

and

$$(\partial_{xy}^2 \psi)_{i,j} = (\psi_{i+1,j+1} - \psi_{i+1,j} - \psi_{i,j+1} + \psi_{i,j}) * \delta P_i * \delta P_j.$$

The term $(\partial_{xy}^2 \psi)_{i,j}$ is defined at a corner point of the grid zone. These extra terms are added to the explicit operator \mathcal{L}_{xy} in the program.

APPENDIX F

PROGRAM LISTING FOR LINEAR STABILITY ANALYSIS

The FORTRAN program listed in this appendix was written to determine eigenvalues of the linear stability equation (6.11) for the internal heat source problem. When stability parameters, ℓ , N and $\Delta T (= T_S - T_A)$ are specified, the program determines the smallest positive eigenvalue R (the largest of $1/R$ in calculation) for each of given wave numbers. The critical Rayleigh number for the specified parameters are found as the minimum value of the smallest Rayleigh numbers with respect to wave number. These are listed in Table 6.2. The input variables for the program are;

<u>Variable Name</u>	<u>Definition</u>
JOB	Number of jobs to be processed
NWAVE	Number of wave numbers (Maximum 50 for each job)
N	Number of expansion coefficients (A_k 's)
EL	Source depth (ℓ)
HT	Biot number at the bottom boundary (N in the text)
TS	Temperature difference, $T_S - T_A$
W(I)	Wave numbers specified for each job with $I = 1$ to NWAVE
IPARA	= 0 (Logical parameter controlling evaluation of trial function parameter β_k)
IPRINT	Logical parameter controlling printed output = 0 : print the Rayleigh number only; = 1 : print eigen solutions.
IPUNCH	Logical parameter controlling punched output = 0 : no punch; = 1 : punch eigen solutions with relevant parameters.

In each job, stability parameters (EL, HT and TS) are fixed.

```

//STEP1 EXEC FORHCGO,LIBRARY='SYS5.EISPACK.LOAD'
//C.SYSIN DD *,DCB=BLKSIZE=2000
C LINEAR STABILITY ANALYSIS FOR INTERNAL HEAT SOURCE PROBLEM
IMPLICIT REAL*8(A-H,O-Z)
DIMENSION A(50),B(50),C(50),W(50),E(50),F(50,50),R(50,4),ZP(50,50)
1 ,X(202),T(202),P(202)
PHI= 3.14159265358979D 00
LPS= 1.0D-12
TMAX= 1.0
XMAX= 0.0
READ (5,200) JOB,NWAVE,IPARA,IPRINT,IPUNCH
DO 1000 KKK= 1, JOB
READ (5,220) NWAVE,N,EL,HT,TS
READ (5,210) (W(I),I=1,NWAVE)
IF (IPUNCH .NE. 0) READ (5,210) XMAX
IF (IPRINT .NE. 0) WRITE (6,300) EL
E2= EL*EL
E3= E2*EL
GT= -HT*(E2/3.0+TS)/(HT+1.0)
C DEPTH FOR MAXIMUM TEMPERATURE
C2= 0.5
C1= 0.5 + 0.75*GT/EL
DO 10 K=1,20
10 C2= C2-(C2*C2*(C2-1.5)+C1)/(3.0*C2*(C2-1.0))
ELT= EL*C2
TMX= ELT**3/E2*(4.0/3.0*EL-ELT)
C EXPANSION PARAMETER
CALL EXPAN (HT,EL,IPARA,N,B)
C MAIN CALCULATION
DO 500 I=1,NWAVE
AL= W(I)
AA= AL*AL
A1= DSINH(AL)
A2= DCOSH(AL)
AE= AL*EL
A3= DSINH(AE)

```

MAIN0001
 MAIN0002
 MAIN0003
 MAIN0004
 MAIN0005
 MAIN0006
 MAIN0007
 MAIN0008
 MAIN0009
 MAIN0010
 MAIN0011
 MAIN0012
 MAIN0013
 MAIN0014
 MAIN0015
 MAIN0016
 MAIN0017
 MAIN0018
 MAIN0019
 MAIN0020
 MAIN0021
 MAIN0022
 MAIN0023
 MAIN0024
 MAIN0025
 MAIN0026
 MAIN0027
 MAIN0028
 MAIN0029
 MAIN0030
 MAIN0031
 MAIN0032
 MAIN0033
 MAIN0034
 MAIN0035
 MAIN0036

MAIN0037
 MAIN0038
 MAIN0039
 MAIN0040
 MAIN0041
 MAIN0042
 MAIN0043
 MAIN0044
 MAIN0045
 MAIN0046
 MAIN0047
 MAIN0048
 MAIN0049
 MAIN0050
 MAIN0051
 MAIN0052
 MAIN0053
 MAIN0054
 MAIN0055
 MAIN0056
 MAIN0057
 MAIN0058
 MAIN0059
 MAIN0060
 MAIN0061
 MAIN0062
 MAIN0063
 MAIN0064
 MAIN0065
 MAIN0066
 MAIN0067
 MAIN0068
 MAIN0069
 MAIN0070
 MAIN0071
 MAIN0072

A4= DCCSH(AE)
 AF= AL-AE
 A5= DSINH(AF)
 A6= DCOSH(AF)
 DL= AL*AI-AA
 DG 20 K=1,N
 DG 20 J=1,N
 20 F(K,J)= 0.0
 DC 40 K=1,N
 BK= B(K)
 B2= BK*BK
 B3= DSIN(BK)
 B4= DSIN(2.0*BK)
 B5= B3*(AL*A2 + (HT+1.0)*AI)
 BP= (BK*AI*AI - AL*B5)/CL
 CC= (B5 - AL*BK)/CL
 DC= (B3*(AI*(AA-HT) + AL*HT*A2) - BK*(AI*A2-AL))/DL
 AP= AL*BK
 XX= (-BK*AI*A6+AL*B3*(AL*A5+HT*A6)-(AL*A3+HT*A4)*AI*B3+AB*A4)/DL
 YY= (RK*AI*A5-AL*B3*(AL*A6+HT*A5)-(AL*A4+HT*A3)*AI*B3+AB*A3)/DL
 BE= BK*EL
 B6= DSIN(BE)
 B7= DCOS(BE)
 K=J ONLY
 E(K)= (AA+B2)*(2.0-B4/BK)/AA/4.0
 F(K,K)= GT*(B4/BK/4.0-0.5)-E2/6.0+(2.0*C*B6*B6-BE*DSIN(2.0*BE))/
 1 (4.0*B2*B2*E2)
 DC 40 J=1,N
 BJ= R(J)
 DE= BJ*EL
 D2= RJ*BJ
 D1= AA+D2
 D3= DSIN(DE)
 D4= DCCS(DE)
 D5= D1*D1
 D6= D5*D1

C

MAIN0073
 MAIN0074
 MAIN0075
 MAIN0076
 MAIN0077
 MAIN0078
 MAIN0079
 MAIN0080
 MAIN0081
 MAIN0082
 MAIN0083
 MAIN0084
 MAIN0085
 MAIN0086
 MAIN0087
 MAIN0088
 MAIN0089
 MAIN0090
 MAIN0091
 MAIN0092
 MAIN0093
 MAIN0094
 MAIN0095
 MAIN0096
 MAIN0097
 MAIN0098
 MAIN0099
 MAIN0100
 MAIN0101
 MAIN0102
 MAIN0103
 MAIN0104
 MAIN0105
 MAIN0106
 MAIN0107
 MAIN0108

```

D7= D6*D1
D8= D7*D1
COMMON TERMS
C1= (AL*(HT*HT-AA)*B3 + BK*(A1*(AA-HT)+AL*HT*A2) -(A2*(AA+HT*HT) +
1 2.0*AL*HT*A1)*A1*B3)/D1
F(K,J)= F(K,J) - 2.0D OC*AL/D5*( GT*(DSIN(BJ))*C1 + BJ*CD) +
1 2.0/3.C*DE*DD)
C1= 32.0/E2*( AL*D3*((AA-5.0*D2)**2-20.0*D2*D2)*XX-BJ*D4*((D2-5.0*
1 AA)**2-20.0*AA*AA)*YY+8J*((D2-5.0*AA)**2-20.0*AA*AA)*BB)/D8
C2= 4.0/E2*( D3*(8.0*AA*D2-D5)*(5.0*EL*YY+2.0*A3*CC)+4.0*AL*BJ*(AA
1 -D2)*D4*(5.0*EL*XX+2.0*CC*A4)+4.0*AL*BJ*(AA-D2)*(3.0*EL*DD-2.0*
2 CC))/D7
C3= 4.0/EL*( AL*D3*(AA-3.C*D2)*(EL*XX+A4*CC)+BJ*D4*(D2-3.C*AA)*
1 (EL*YY+A3*CC))/D6
F(K,J)= F(K,J)+C1+C2+C3
K .NE. J ONLY
IF (J .EQ. K) GO TO 30
C4= .B2+D2
C5= B2-D2
C6= C5*C5*C5
F(K,J)= F(K,J) + 4.0*( 2.0*((C4*C4+4.0*B2*D2)*B6*D3 + 4.0*BJ*BK*
1 C4*(B7*D4-1.0))/C5 -BE*(B2+3.0*D2)*B7*D3+DE*(3.0*R2+D2)*B6*D4)/
2 (E2*C6)
30 F(K,J)= -F(K,J)/(AA+B2)**2
4C CONTINUE
C INTERCHANGE ROW AND COLUMN
DC 50 J=1,N
C1= E(J)
F(J,J)= F(J,J)/C1
IF (J .EQ. N) GO TO 55
J1= J+1
DC 50 K=J1,N
TEMP= F(K,J)/C1
F(K,J)= F(J,K)/E(K)
50 F(J,K)= TEMP
55 CONTINUE
  
```

```

IF (IPRINT .EQ. 0) GO TC 60
WRITE (6,310)
WRITE (6,320) (E(K),K=1,N)
WRITE (6,330)
CALL ARRAY (50,50,N,N,F)
60 CONTINUE
CALL EISPAC(50,N,MATRIX('REAL',F),VALUES(A,C),VECTOR(ZP),
1 METHOD('ORTHOGNAL'),ERRCR(IERROR))
C1= A(1)
IF (C1 .EQ. 0.0) C1= 1.0D 00
C2= C1
INDEX= 1
IF (N .EQ. 1) GO TO 75
DC 70 K=2,N
C3= A(K)
IF (C3 .LE. C2) GO TO 65
C2= C3
INDEX= K
GC TO 70
65 IF (C3 .LT. C1) C1= C3
70 CONTINUE
75 CONTINUE
IF (C2 .LT. 0.0) C2= 1.0
R(I,1)= 1.0D 00/C2
R(I,2)= R(I,1)*E3*E2
R(I,3)= R(I,1)*ELT**6/E2*(4.0/3.0*EL-ELT)
R(I,4)= 1.0D 00/C1
IF (C1 .GT. 0.0) R(I,4)= C.0
IF (IPRINT .EQ. 0) GO TC 500
WRITE (6,340)
WRITE (6,320) (A(K),K=1,N)
WRITE (6,350)
WRITE (6,320) (C(K),K=1,N)
AK1= ZP(1,INDEX)
KDEX= 1
DC 80 K=2,N

```

MAIN0109
MAIN0110
MAIN0111
MAIN0112
MAIN0113
MAIN0114
MAIN0115
MAIN0116
MAIN0117
MAIN0118
MAIN0119
MAIN0120
MAIN0121
MAIN0122
MAIN0123
MAIN0124
MAIN0125
MAIN0126
MAIN0127
MAIN0128
MAIN0129
MAIN0130
MAIN0131
MAIN0132
MAIN0133
MAIN0134
MAIN0135
MAIN0136
MAIN0137
MAIN0138
MAIN0139
MAIN0140
MAIN0141
MAIN0142
MAIN0143
MAIN0144


```

C1= ZP(K,INDEX)
IF (DABS(C1/AK1) .LT. 1.0D 00) GO TO 80
AK1= C1
KDX= K
80 CONTINUE
WRITE (6,360) IERROR,INDEX,KDEX
CALL ARRAY(50,50,N,N,ZP)
WRITE (6,370)
X1= XMAX
J= 0
81 F1= 0.0
F2= 0.0
J= J+1
DO 82 K=1,N
AK= ZP(K,INDEX)/AK1
BK= B(K)
C1= BK*X1
C2= AK*BK
F1= F1+C2*DCOS(C1)
F2= F2+C2*BK*DSIN(C1)
X1= X1+F1/F2
IF (DABS(F1/F2) .GT. 1.0D-10 .OR. J .LT. 50) GO TO 81
XMAX= X1
TMAX= 0.0D 00
DO 83 K=1,N
TMAX= TMAX + DSIN(B(K)*X1)*ZP(K,INDEX)/AK1
C2= (HT+1.0)*A1 + A1*A2
DO 85 J=1,201
C1= 0.005D 00*(J-1)
X(J)= C1
AE= AL*C1
A3= DSINH(AE)
A4= DCOSH(AE)
AF= AL-AE
A5= DSINH(AF)
A6= DCOSH(AF)

```

```

MAIN0145
MAIN0146
MAIN0147
MAIN0148
MAIN0149
MAIN0150
MAIN0151
MAIN0152
MAIN0153
MAIN0154
MAIN0155
MAIN0156
MAIN0157
MAIN0158
MAIN0159
MAIN0160
MAIN0161
MAIN0162
MAIN0163
MAIN0164
MAIN0165
MAIN0166
MAIN0167
MAIN0168
MAIN0169
MAIN0170
MAIN0171
MAIN0172
MAIN0173
MAIN0174
MAIN0175
MAIN0176
MAIN0177
MAIN0178
MAIN0179
MAIN0180

```

```

TEMP= 0.0
STR= 0.0
DO 84 K=1,N
BK= B(K)
C3= BK*C1
C4= DSIN(C3)
AK= ZP(K,INDEX)/AK1
TEMP= TEMP+AK*C4
STR= STR + AK/(AA+BK*BK)**2*(( C3*A1*A5-DSIN(BK) *(AE*(HT*A5+AL*A6)
1 + C1*A1*(AL*A4+HT*A3)-C2*A3) -BK*AF*A3)/DL-C4)
84 CONTINUE
T(J)= TEMP/TMAX
85 P(J)= -AL*R(I,1)*STR/TMAX
WRITE (6,380) (X(J),T(J),P(J),J=1,201,4)
WRITE (6,390) R(I,1),W(I)
500 CONTINUE
WRITE (6,510) EL,HT,TS,TMX,ELT,TMAX,XMAX,N,IPARA
WRITE (6,320) (B(K),K=1,N)
WRITE (6,530)
DO 700 I=1,NWAVE
C1= W(I)
C2= C1*EL
C3= C1*EIT
WRITE (6,540) C1,R(I,1),C2,R(I,2),C3,R(I,3),R(I,4)
700 CONTINUE
IF (IPUNCH .EQ. 0) GO TO 900
WRITE (7,710) EL, HT, ELT, TMX
WRITE (7, 710) W(1),R(1,1),TMAX
WRITE (7,720) (T(J), J=1,201)
WRITE (7,720) (P(J), J=1,201)
900 CONTINUE
1000 CONTINUE
200 FORMAT (5I5)
210 FORMAT (5D15.5)
220 FORMAT (2I5,4D15.5)
300 FORMAT (1H1,20X,'SOURCE DEPTH',D15.5)

```

MAIN0181
 MAIN0182
 MAIN0183
 MAIN0184
 MAIN0185
 MAIN0186
 MAIN0187
 MAIN0188
 MAIN0189
 MAIN0190
 MAIN0191
 MAIN0192
 MAIN0193
 MAIN0194
 MAIN0195
 MAIN0196
 MAIN0197
 MAIN0198
 MAIN0199
 MAIN0200
 MAIN0201
 MAIN0202
 MAIN0203
 MAIN0204
 MAIN0205
 MAIN0206
 MAIN0207
 MAIN0208
 MAIN0209
 MAIN0210
 MAIN0211
 MAIN0212
 MAIN0213
 MAIN0214
 MAIN0215
 MAIN0216

```

310 FORMAT (1H0, 10X, 'E ELEMENTS')
320 FORMAT (1X, 1P10D13.6)
330 FORMAT (1H, 10X, 'F/E MATRIX')
340 FORMAT (1H, 10X, 'EIGENVALUES, REAL PARTS')
350 FORMAT (1H, 10X, 'EIGENVALUES, IMAGINARY PARTS')
360 FORMAT (1H, 10X, 'EIGENVECTORS', 5X, '(ERROR =', I5, 5X, 'INDEX =', I3,
1 5X, 'KDEX =', I3, ')')
370 FORMAT (1H, 10X, 'EIGEN FUNCTIONS', /, 6X, 'X', 11X, 'TEMPERATURE', 7X,
1 'STREAM FUNCTION')
380 FORMAT (F9.3, 2D20.5)
390 FORMAT (1H0, '***** RAYLEIGH NUMBER IS', 1PD13.5, ' FOR WAVE NUMBE'
1 'R', 1PD13.5, ' *****')
510 FORMAT (1H1, 'COMMON PARAMETER FOR INTERNAL HEAT SOURCE PROBLEM',
1 /, 6X, 'SOURCE DEPTH =', F7.4, 5X, 'NUSSULT NUMBER =', D13.5, 5X,
2 'TOP TEMPERATURE =', D13.5, /, 6X, 'MAX. TEMP. =', D15.6, 2X, 'AT',
3 'D15.6, 10X, 'MAX. PERT. TEMP. =', D15.6, 2X, 'AT', D15.7, /, I7, ' EXP',
4 'ANSION PARAMETERS (IPARA =', I3, ') :')
530 FORMAT (1H, 'WAVE NUMBER', 6X, 'R(SOURCE)', 17X, 'W(EL)', 11X, 'R(EL)',
1 18X, 'W(ELT)', 10X, 'R(ELT)', 17X, 'R(SINK)', /)
540 FORMAT (1X, F8.3, D20.7, F20.3, D20.7, F20.3, D20.7, D22.6)
710 FORMAT (1P4D15.6)
720 FORMAT (1P8D10.3)
STOP
END

```

```

MAIN0217
MAIN0218
MAIN0219
MAIN0220
MAIN0221
MAIN0222
MAIN0223
MAIN0224
MAIN0225
MAIN0226
MAIN0227
MAIN0228
MAIN0229
MAIN0230
MAIN0231
MAIN0232
MAIN0233
MAIN0234
MAIN0235
MAIN0236
MAIN0237
MAIN0238
MAIN0239
MAIN0240

```

```

SUBROUTINE EXPAN (HT,EL,IPARA,N,B)
REAL*8 HT,EL,PHI,BN,BC,B(50),C1,C2,C3
LOGICAL LCGIC
EXPANSION PARAMETERS: HT = 0.0 INSULATED BOTTOM
PHI= 3.14159265358979D 0
LCGIC= IPARA .GT. 0
LMODE= 0.50001/EL
IF (LMODE .EQ. 0) LMODE= 1
C1= 0.0
IF (HT .GT. 0.0) C1= -1.0/HT
B0= PHI/(1.0-C1)
IF (HT .LE. 1.0) B0= PHI*C.67
IF (LOGIC) B0= B0+(LMODE-1)*PHI
DO 10 K=1,N
KMODE= 1
IF (LOGIC) KMODE= LMODE
J= K*KMODE
IF (IPARA .LT. 0 .AND. K .GT. LMODE) J=(K-LMODE+1)*LMODE
IF (HT .GT. 0.0) GO TC 2
BN= PHI*(J-0.5D 00)
IF (HT .LT. 0.0) BN= J*PHI
GO TO 6
2 DO 4 I=1,40
C2= C1*BC
BN= DATAN(C2) + J*PHI
C3= DABS ((BN-B0)/BN)
IF (C3 .LT. 1.0D-12) GO TC 6
4 B0= BN
6 B(K)= BN
10 BC= BN+PHI*J
RETURN
END

```

XSPAN0001
XSPAN0002
XSPAN0003
XSPAN0004
XSPAN0005
XSPAN0006
XSPAN0007
XSPAN0008
XSPAN0009
XSPAN0010
XSPAN0011
XSPAN0012
XSPAN0013
XSPAN0014
XSPAN0015
XSPAN0016
XSPAN0017
XSPAN0018
XSPAN0019
XSPAN0020
XSPAN0021
XSPAN0022
XSPAN0023
XSPAN0024
XSPAN0025
XSPAN0026
XSPAN0027
XSPAN0028
XSPAN0029
XSPAN0030
XSPAN0031
XSPAN0032

```

SUBROUTINE ARRAY (MDIM,NDIM,M,N,X)
REAL*8 X
DIMENSION X(MDIM,NDIM)
NTEN= (N-1)/10 + 1
DO 55 K=1,NTEN
JSTAR= (K-1)*10 +1
IF (10*K .GE. N) GO TO 25
JEND= 10*K
GC TO 30
25 JEND= N
30 WRITE (6,100)
DC 55 I=1,M
WRITE (6,101) (X(I,J), J=JSTAR, JEND)
55 CONTINUE
100 FCRMAT (IH )
101 FCRMAT (IX ,1P10D13.6)
RETURN
END

```

```

ARRY0001
ARRYC002
ARRYC0C3
ARRY0004
ARRYC0C5
ARRYC0C6
ARRY0007
ARRYC0C8
ARRYC0C9
ARRY0010
ARRYC011
ARRY0012
ARRY0013
ARRY0014
ARRY0015
ARRY0016
ARRY0017
ARRY0018

```

DATA0001
DATA0002
DATA0003
DATA0004
DATA0005
DATA0006
DATA0007
DATA0008
DATA0009

```
//G.EISPACLB DD DSN=SYS5.EISPACK.LOAD, DISP=SHR
//G.SYSIN DD *,DCB=BLKSIZE=2000
2 1 0 1 1
1 25 0.10000D 00 0.00000D 00 0.00000D 00
4-21000D 00
0.08000D 00
1 25 0.10000D 00 0.50000D 00 0.00000D 00
1.36800D 01
0.06000D 00
```

NOMENCLATURE

<u>SYMBOLS</u>	<u>DEFINITION</u>	<u>PAGE</u> [¶] <u>(EQUATION)</u> <u>NUMBER</u>
a	Wave number	94
a_s, a_t	Wave numbers in the internal source problem	180
\bar{A}	Vector for expansion coefficients	96
c_p	Heat capacity	75
D	Penetration depth of the roll cells	137
\bar{D}	Deformation (Rate of strain) tensor	(3.5)
E	Dimensional exponent for viscosity law	(3.2)
$\bar{E}, \bar{G}, \bar{G}'$	Matrices arising from Galerkin procedure	96
F	Normalized source distribution curve	(4.3)
g, \bar{g}	Acceleration due to gravity, and its vector	75
$h(x)$	Temperature gradient function for static solution	(4.9)
H	Depth of the experimental enclosure model	90
$\hat{i}, \hat{j}, \hat{k}$	Unit vectors for Cartesian coordinate	89
l^*	Reference scale for length (See Table 3.1)	79
l, l_s^*	Source depth occupying the upper part of a fluid layer	165
l_t	Depth to the maximum temperature location in a fluid layer with heat source distribution	165
\bar{l}	Directed length vector tangential to the grid boundaries	203
L	Length of the experimental enclosure model	119

[¶] Numbers (in parentheses) after definition refer to page (equation) numbers in which symbols are first used or thoroughly defined, except in Chapter I. Symbols used in Appendices are not listed.

<u>SYMBOLS</u>	<u>DEFINITION</u>	<u>PAGE</u> <u>(EQUATION)</u> <u>NUMBER</u>
\bar{n}	Unit vector (inward) normal to the enclosure surfaces or two-dimensional planes	80, 81
N	Biot number	80
Nu	Nusselt number	204
p^*	Pressure	77
p	Real part of the growth rate	92
P	Prandtl number	78
q	Imaginary part of the growth rate	92
q^*, q_F	Heat flux density	80
$Q^*(x)$	Internal heating rate	89
Q	Functional in the first variational principle	195
R	Rayleigh number; See Table 3.1 for specific choice of reference scales.	78
R_c	Critical Rayleigh number (subscripts suppressed)	96
s	Area of rectangular grid	203
$S^*(x), S(x)$	Adiabatic heating rate	89
S_m^*	Maximum source strength	90
SI_L, SI_T	Source-sink distribution functions; $S(x) \equiv SI_T$	85
t	Time; also temperature as a subscript	75
T	Temperature	75
T_R	Reference scale for temperature	77
u, v, w	Components of velocity vector \bar{V}	190
U^*	Heat transfer coefficient at boundaries	80
\bar{V}	Velocity vector (= $u\hat{i} + v\hat{j} + w\hat{k}$)	75
W	Wavelength of the roll cells	137

<u>SYMBOLS</u>	<u>DEFINITION</u>	<u>PAGE</u> <u>(EQUATION)</u> <u>NUMBER</u>
W	Functional in the second variational principle	195
\bar{x}^*	Distance vector (= $x\hat{i} + y\hat{j} + z\hat{k}$)	77
x, y, z	Cartesian coordinates:	
	x in the direction of gravity	77
	y in the longitudinal direction	93
	z in the transverse direction	93
 <u>GREEK SYMBOLS</u>		
α	Thermal diffusivity	78
β	Coefficient of volumetric expansion	76
β_k	Parameter associated with trial function	95
γ	Dimensionless exponent in viscosity law	80
Γ	Viscosity ratio number	191
δ	Small variation	98
Δ	Temperature difference, as in ΔT , ΔT_m	165
ϵ	Amplitude parameter in finite amplitude convection	103
ν	Kinematic viscosity	(3.6)
π	= 3.1426	
Π, Π^*	Dynamic Pressure	77
ρ	Density	76
σ	Relative growth rate for disturbances, $\sigma = p + iq$	91
Σ	Enclosure surfaces	80
η	Temperature gradient parameter in the stably stratified layer under the roll cell region	166
θ_k	Trial function for temperature	95

<u>GREEK SYMBOLS</u>	<u>DEFINITION</u>	<u>PAGE (EQUATION) NUMBER</u>
θ, θ	Perturbation temperature, and its normal mode amplitude	91, 94
$\kappa, (\kappa_e)$	(Effective) thermal conductivity	76
λ	Wavelength	94
λ_k	Parameter associated with trial function	95
μ	Viscosity	(3.2)
χ	Dummy index (for θ or M) for reference viscosity designation	191
ϕ_k	Trial function for stream function	95
Φ	Rescaled stream function	102
Ψ, ϕ	Stream function and its normal mode amplitude	(3.8), 94
T	Uniform sink for heat losses at side walls	162
ω	Vorticity	(3.9)

SUBSCRIPTS

o	Properties evaluated at T_o ; $T_o = T_s$	78
s	Batch sink (T_s); or, Internal heat source, as in R_s, a_s	80, 89
ss	Static state	(4.5)
A	Ambient (T_A)	81
c	Critical condition, as in R_c, a_c , etc.	96
c	Cold (top) boundary in the variable viscosity problem	191
h	Hot (bottom) boundary in the variable viscosity problem	191
l	Parameters related to the internal heat source problem, as in $R_{s,l}$ and $R_{T,l}$	166

<u>SUBSCRIPTS</u>	<u>DEFINITION</u>	<u>PAGE</u> <u>(EQUATION)</u> <u>NUMBER</u>
m	Melt surface, or Maximum temperature	80, 165
M	Reference viscosity based on a geometric mean viscosity value of boundary viscosity values	197
t	Temperature related in the internal source problem, as is a_t, η_t	166
θ	Reference viscosity based on an arithmetic mean boundary temperature, as in R_θ	191

SUPERSCRIPTS

*	Dimensional quantity	77
'	Transformed variables	(6.13)
†	Adjoint system	97
+	Complex conjugate	192
T	Transpose of tensor or dyad	75
i	Iteration number for the power method	196

OVERLINES

—	Vector; or, Horizontal average in a fluid layer	78, 174
=	Tensor, dyad or matrix	
~	Variables in the transverse (x-z) plane	86

MATHEMATICAL OPERATORS AND SYMBOLS

.	Single dot multiplication, or Scalar multiplication	75
:	Double dot multiplication of dyads	192
∇	Gradient operator on vectors or scalars	

<u>MATHEMATICAL OPERATORS AND SYMBOLS</u>	<u>DEFINITION</u>	<u>PAGE</u> <u>(EQUATION)</u> <u>NUMBER</u>
$\nabla \cdot$	Divergence operator	
$\nabla \times$	Curl operator	
∇^2	Laplacian operator	86
∇^4	Biharmonic operator	
\mathcal{L}_4	Biharmonic operator with variable viscosity	93
L_4	Ordinary differential operator for \mathcal{L}_4	94
D	Ordinary differentiation with respect to x	91
∂_x , etc.	Partial differentiation with respect to x , etc.	
Δ_z	Finite difference operator for ∂_z	101
δ_{jk} (δ_{ij})	Kronecker delta(tensor)	76
$H(x)$	Heaviside step function ($= 1$ if $x > 0$; $= 0$ if $x < 0$)	165
J	Jacobian operator: $J_k(f,g) \equiv \partial_x f \cdot \partial_y g - \partial_y f \cdot \partial_x g$	85
$\ \ $	Matrix norm (maximum norm used in calculation)	103
$()_m$	Average over the entire fluid layer	192
\langle , \rangle	Inner product of two functions	97
$\mathcal{E}, \bar{\mathcal{E}}$	Operator associated with Energy equation	101
$\mathcal{M}, \bar{\mathcal{M}}$	Operator associated with Momentum equation	101
$\bar{\mathcal{B}}$	Symbolic nonlinear operator for stream function field	102

BIBLIOGRAPHY

- Batchelor, G. K. (1967) An Introduction to Fluid Dynamics, Cambridge University Press, Chapter 3.
- Bénard, H. (1901) Les tourbillons cellulaires dans une nappe liquide transportant de la chaleur par convection en régime permanent, Ann. Chim. Phys. 23, 62
- Booker, J. R. (1976) Thermal convection with Strongly Temperature-Dependent Viscosity, J. Fluid Mech. 76, 4, 741
- Booker, J. R. and Stengel, K. C. (1978) Further Thoughts on Convective Heat Transport in a Variable-Viscosity Fluid, J. Fluid Mech. 86, 2, 289
- Busse, F. H. (1967a) The Stability of Finite Amplitude Cellular Convection and its Relation to an Extremum Principle, J. Fluid Mech. 30, 4, 625
- Busse, F. H. (1967b) On the Stability of Two-Dimensional Convection in a Layer Heated from Below, J. Math. Phys. 46,2,140
- Chandrasekhar, S. (1961) Hydrodynamic and Hydromagnetic Instability, Clarendon Press, Oxford
- Cheng, K. C., Hong, S. W. and Hwang, G. J. (1972) Buoyancy Effects on Laminar Heat Transfer in the Thermal Entrance Region of Horizontal Rectangular Channels with Uniform Wall Heat Flux for Large Prandtl Number Fluid, Int. J. Heat Mass Transfer 15, 1819
- Clomburg, L. A. Jr. (1971) Mathematical and Experimental Modeling of the Circulation Patterns in Glass Melts, Sc.D. Thesis, Department of Chemical Engineering, Massachusetts Institute of Technology, Cambridge
- Clomburg, L. A. Jr. (1976) Convection in an Enclosure - Source and Sink Located along a Single Horizontal Boundary, ASME Publication 76-HT-22
- Clomburg, L. A. Jr., Curlet, N. W. E. and Won, K. J. (1975) Modeling the Effect of Flame Heat Transfer on Batch Extent in Glass Melting Furnaces, presented at IEEE IAS Meeting, Atlanta
- Curlet, N. W. E. (1976) Experimental and Numerical Modeling of Three Dimensional Natural Convection in an Enclosure, Sc.D. Thesis, Department of Chemical Engineering, Massachusetts Institute of Technology, Cambridge
- Daniels, M. (1973) Einschmelzverhalten von Glasgemengen, Glastech. Ber. 46, 3, 40
- Davis, S. H. (1969) On the Principle of Exchange of Stabilities, Proc. Roy. Soc. A.310, 341

- Deardroff J. W. (1965) Gravitational Instability between Horizontal Plates with Shear, Phys. Fluid 8, 6, 1027
- Denn, M. M. (1975) Stability of Reaction and Transport Process, Prentice-Hall Inc., New Jersey
- Ellingsen, T. and Palm, E. (1975) Stability of Linear Flow, Phy. Fluids 18, 4, 487
- Finlayson, B. A. (1972) The Method of Weighted Residuals and Variational Principles, Academic Press
- Foster, T. D. (1969) Convection in a Variable Viscosity Fluid Heated from within, J. Geophys. Res. 74, 2, 685
- Gage, K. S. and Reid, W. H. (1968) The Stability of Thermally Stratified Plane Poiseuille Flow, J. Fluid Mech. 33, 1, 21
- Gallagher, A. P. and Mercer A. McD. (1965) On the Behavior of Small Disturbances in Plane Couette Flow with a Temperature Gradient, Proc. Roy. Soc. A.286, 119
- Gamm, H. D. (1975) Mass Transfer Problems in Glass Furnace Simulation, Sc.D. Thesis, Department of Chemical Engineering, Massachusetts Institute of Technology, Cambridge .
- Günther, R. (1958) Glass-Melting Tank Furnaces, Soc. Glass Tech., Sheffield, England
- Harrington, R. V. and Hutchins, J. R. III. and Sherman, J. D. (1962) The Kinetics and Mechanisms of Subliquidus Alkali Carbonate-Silica Reactions, Adv. in Glass Tech. 29
- Hart, J. E. (1972) Stability of Thin Non-Rotating Hadley Circulations, J. Atmos. Sci. 29, 687
- Hottle, H. C. and Sarofim, A. F. (1967) Radiative Transfer, McGraw-Hill, New York .
- Howard, L. N. (1963) Heat Transport by Turbulent Convection, J. Fluid Mech. 17, 405
- Jack, H. R. S. and Jacquest, J. A. T. (1958) Heat Transfer in Glass-Batch Material, Symposium sur la fusion du verre, Bruxelles, Comptu rendu Charleroi, Union Scientifique du Verre, 339
- Jebsen-Marwedel, H. (1937) Temperature Changes in Melting Piles of Batch, Glass Ind. 18, 276
- Jebsen-Marwedel, H. (1959) Glastechnische Fabrikationsfehler, Second Edition, Section IV, p113, Springer-Verlag

- Joseph, D. D. (1966) Nonlinear Stability of Boussinesq Equations by the Method of Energy, Arch. Pat. Mech. Anal. 2, 163
- Joseph, D. D. (1976) Stability of Fluid Motions II, Springer Tracts in Natural Philosophy, Vol. 28, Springer-Verlag
- Kitaigorodski, I. I. (1959) Technologie des Glases, p306, VEB Verlag Technik
- Kröger, C. (1952) Gemengereaktionen und Glasschmelze, Glastechn. Ber. 25, 10, 307
- Kröger, C. (1957) Über die Geschwindigkeit, den Mechanismus und die Phasenbildung bei den unter Schmelzbildung ablaufenden Festkörpereaktionen, Glastechn. Ber. 30, 2, 42
- Koschmieder, E. L. (1974) Bénard Convection, Adv. in Chem. Phys. Vol. 26 177
- Krishnamurti, R. (1968) Finite Amplitude Convection with Oscillating Mean Temperature, Part I - Theory, Part II - An Experimental Test of the Theory, J. Fluid Mech. 33, 3, 445
- Kuo, H. L. (1963) Perturbations of Plane Couette Flow in Stratified Fluid and Origin of Cloud Streets, Phys. Fluid 6, 2, 195
- Landau, L. D. and Lifshitz, E. M. (1959) Fluid Mechanics, Pergamon Press
- Liang, S. F., Vidal, A. and Acrivos, A. (1969) Buoyancy-Driven Convection in Cylindrical Geometries, J. Fluid Mech. 36, 2, 239
- Lillie, H. R. (1952) A Method for Measuring the Flow Point of Glass, J. Am. Cer. Soc. 35, 149
- Malkus, W. V. R. (1954) Discrete Transitions in Turbulent Convection, Proc. Roy. Soc. A.225, 185
- Malkus, W. V. R. (1954) The Heat Transport and Spectrum of Thermal Turbulence, Proc. Roy. Soc. A.225, 196
- Malkus, W. V. R. and Veronis, G. (1958) Finite Amplitude Cellular Convection, J. Fluid Mech. 4, 225
- Manring, W. H. and Bauer, W. C. (1964) Influence of Batch Preparation Process on the Melting and Fining of the Glass, Glass Ind. 45, 7, 354
- Mase, H. and Sasagawa, Y. (1973) Mathematical Modeling of Glass Tank Furnace, Automatic Control in Glass, IFAC Symposium, p93, West Lafayette, IN
- McKenzie, D. P., Roberts, J. M. and Weiss, N. O. (1974) Convection in the Earth's Mantle: Towards a Numerical Simulation, J. Fluid Mech. 62, 3, 465

- Millman, M. H. and Keller, J. B. (1969) Perturbation Theory of Nonlinear Boundary-Value Problem, *J. Math. Phy.* 10, 2, 342
- Oberbeck, A. (1888) Über die Bewegungserscheinungen der Atmosphäre (On the Phenomena of Motion in the Atmosphere), *Sitzungsber. d. Königlichen Preuss. Akad. d. Wiss.*, 383, Translated by C. Abbe in *Smithsonian Misc. Coll.*, (1891)
- Palm, E. (1960) On the Tendency Towards Hexagonal Cells in Steady Convection, *J. Fluid Mech.* 8, 183
- Pearson, J. R. A. (1958) On Convection Cells Induced by Surface Tension, *J. Fluid Mech.* 4, 489
- Pellew, A. and Southwell, R. V. (1940) On Maintained Convection Motion in a Fluid Heated from Below, *Proc. Roy. Soc.* A.176, 312
- Péyches, I. (1948) Convection Currents in a Glass Tank, *The Glass Ind.* 29, 1, 19
- Péyches, I. and Zortea, M. (1971) Glass Tanks as Models for Convection in the Upper Mantle, *J. Geophys. Res.* 76, 5, 1416
- Preston, E. and Turner, W. E. S. (1940) Fundamental Studies of the Glass Melting Process. The Effect of Particle Size and Temperature on the Rate of Glass Formation of a Pure Soda-Lime-Silica Glass, *J. Soc. Glass Tech.* 24, 124
- Pugh, A. C. P. (1968) A Method of Calculating the Melting Rate of Glass Batch and Its Use to Predict Effects of Changes in the Batch, *Glasteknisk Tidskrift* 23, 4, 95
- Rayleigh, Lord (1916) On Convection Currents in a Horizontal Layer of Fluids, When the Higher Temperature is on the Under Side, *Phil. Mag.* 6, 32, 529
- Reid, W. H. and Harris, D. L. (1958) Some Further Results on the Bénard Problem, *Phys. Fluids* 1, 2, 102
- Richter, F. M. and Parsons, B. (1975) On the Interaction of Two Scales of Convection in the Mantle, *J. Geophys. Res.* 80, 17, 2529
- Roberts, P. H. (1967) Convection in Horizontal Layers with Internal Heat Generation, *J. Fluid Mech.* 30, 1, 39
- Sani, R. (1968) An Extension and Convergence Proof of an Approximate Method due to Pellew and Southwell, *Z. Angew. Math. Mech.* 48, 65
- Schlüter, A., Lortz, D. and Busse, F. (1965) On the Stability of Steady Finite Amplitude Convection, *J. Fluid Mech.* 23, 1, 129
- Schwiderski, E. W. and Schwab, H. J. A. (1971) Convection Experiments with Electrolytically Heated Fluid Layers, *J. Fluid Mech.* 23, 1, 129

- Sparrow, E. M., Goldstein, R. J. and Jonsson, V. K. (1964) Thermal Instability in a Horizontal Fluid Layer: Effect of Boundary Conditions and Nonlinear Temperature Profile, *J. Fluid Mech.* 18, 513
- Stuart, J. T. (1960) On the Nonlinear Mechanics of Wave Disturbances in Stable and Unstable Parallel Flows, *J. Fluid Mech.* 9, 353
- Stuart, J. T. (1963) On the Cellular Patterns in Thermal Convection, *J. Fluid Mech.* 18, 481
- Torrance, K. E. and Turcotte, D. L. (1971) Thermal Convection with Large Viscosity Variations, *J. Fluid Mech.* 47, 1, 113
- Trier, W. (1965) Zusammenhang zwischen Temperaturfeld and Strömungsfeld bei Freier Konvektion in Glasschmelzen, *Glastechn. Ber.* 38, 282
- Tritton, D. J. (1977) Physical Fluid Dynamics, Van Nostrand Reinhold Co., 155-161
- Tritton, D. J. and Zarraga, M. N. (1967) Convection in Horizontal Layers with Internal Heat Generation Experiments, *J. Fluid Mech.* 30, 1, 21
- Tveitereid, M. (1978) Thermal Convection in a Horizontal Fluid Layer with Internal Heat Sources, *Int. J. Heat Mass Transfer*, 21, 335
- Tveitereid, M. and Palm, E. (1976) Convection due to Internal Heat Sources, *J. Fluid Mech.* 76, 481
- Van Dyke, M. D. (1975) Perturbation Methods in Fluid Mechanics, The Parabolic Press, Chapter VIII
- Veronis, G. (1963) Penetrative Convection, *Astrophys. J.* 137, 641
- Weber, J. E. (1973) On Thermal Convection between Non-uniformly Heated Planes, *Int. J. Heat Mass Transfer*, 16, 961
- Weber, J. E. (1978) On the Stability of Thermally Driven Shear Flow Heated from Below, *J. Fluid Mech.* 87, 1, 65
- Whitehead, J. A. and Chen, M. M. (1970) Thermal Instability and Convection of a Thin Fluid Layer Bounded by a Stably Stratified Region, *J. Fluid Mech.* 40, 3, 549
- Willis, G. E. and Deardroff, J. W. (1967) Development of Short-Period Temperature Fluctuations in Thermal Convection, *Phys. Fluids*, 10, 5, 1931
- Won, K. J. (1974) Simulation of Glass Melter Performance, S.M. Thesis, Department of Chemical Engineering, Massachusetts Institute of Technology, Cambridge

Zhuze, T. B., Mikhailova-Bogdanskaya, Z. A. and Pollyak, V. V. (1973),
A Study of the Stages of Melting of the Batch at Various Temperatures,
Glass and Ceramics, 30, 1, 6

BIOGRAPHICAL NOTE

The author was born in Seoul, Korea on March 9, 1944. After attending three elementary schools due to the Korean War, he received his high school education at Kyung-gi High School and graduated from it with First Class Honors in February, 1962. He entered the Engineering College of Seoul National University in the spring of the same year. In 1965, he was elected President of the Engineering College Student Council and then Chairman of the University General Student Council. As chairman, he had to weather the political turmoil in the academic society. He received his B.S. degree in Chemical Engineering in February, 1966. After three years' duty in the army, he was in the employ of the Korea Fertilizer Company from 1969 to 1971. On October 16, 1970, he married Myung-Shin RA of Seoul.

In September, 1971, the author entered the Chemical Engineering Department at M.I.T. He received the degree of S.M. in Chemical Engineering in 1974 and embarked upon his doctoral thesis. He coauthored two publications and is a member of the American Institute of Chemical Engineers and Sigma Xi.